

**COMBINATION OF NATURAL BETANIDIN DYE WITH SYNTHETIC
ORGANIC SENSITISER TOWARDS DYE-SENSITISED SOLAR CELL
APPLICATION**

Rene Costa

**A Dissertation Submitted in Partial Fulfilment of the Requirements for the Degree of
Doctor of Philosophy in Materials Science and Engineering of the Nelson Mandela
African Institution of Science and Technology**

Arusha, Tanzania

May, 2023

ABSTRACT

Betanidins belong to natural red-purple pigments betacyanins, which experimentally demonstrated good light adsorption in a visible range and might be suitable for the dye-sensitised solar cell (DSSCs). Instability is a well-known drawback of natural dyes, which impedes their use for DSSCs. A thermodynamic approach helps to understand the betanidin (Bd) instability which occurs due to spontaneous decarboxylation reaction with decarboxylated betanidin (dBd) formation. The study considers the improvement of the sensitizer's functionality via combination of natural Bd/dBd dyes and synthetic 4-(Diphenylamino)phenylcyanoacrylic acid (L0) dye. Novel complex D- π -A organic dyes, L0-Bd and L0-dBd with structural isomers, have been designed via esterification reactions. The DFT/B3LYP5/6-31G(d,p) approach has been used to compute geometry, vibrational spectra and thermodynamic characteristics of the individual isomers and their complexes with L0. Implementation of TD-DFT method aids in obtaining optoelectronic properties. The broader coverage of the solar spectrum with greater light-harvesting efficiency was achieved for the complexes compared to individual dyes. The dyes attachment to the semiconductor TiO₂ was simulated in terms of different adsorption modes to hydrogenated (TiO₂)₆ cluster. Binding energies and electronic spectra of the dye@TiO₂ systems were computed, and electron density distributions over frontier molecular orbitals analysed. Binding energy magnitudes varied within 15–21 eV for the dye@TiO₂ systems.

Keywords: betanidin, betanidin complex, decarboxylated betanidin complex, DFT/TD-DFT

DECLARATION

I, Rene Costa, do hereby declare to the Senate of the Nelson Mandela African Institution of Science and Technology that this dissertation is my original work and that it has neither been submitted nor concurrently submitted for a degree or similar awards in any other institution.



Rene Costa



Date

The above declaration is confirmed



Prof. Tatiana P. Pogrebnaya

09th May 2023

Date



Prof. Alexander M. Pogrebnoi

09th May 2023

Date

COPYRIGHT

This dissertation is copyright material protected under the Berne Convention, the Copyright Act of 1999 and other international and national enactments, in that behalf, on intellectual property. It must not be reproduced by any means, in full or in part, except for short extracts in fair dealing; for researcher private study, critical scholarly review or discourse with an acknowledgement, without a written permission of the Deputy Vice Chancellor for Academic, Research and Innovation, on behalf of both the author and the Nelson Mandela African Institution of Science and Technology.

CERTIFICATION

The undersigned certify that they have read and hereby recommend for submission to the Nelson Mandela African Institution of Science and Technology a dissertation entitled “Combination of natural betanidin dye with synthetic organic sensitiser towards dye sensitised solar cell application” in partial fulfilment of the requirements for the degree of Doctor of Philosophy in Materials Science and Engineering of the Nelson Mandela African Institution of Science and Technology.



Prof. Tatiana P. Pogrebnaya
(Supervisor 1)

09th May 2023

Date



Prof. Alexander M. Pogrebnoi
(Supervisor 2)

09th May 2023

Date

ACKNOWLEDGEMENTS

I take this opportunity to express my deep and sincere gratitude and thankfulness to my dearest tireless supervisors, Prof. Tatiana P. Pogrebnaya and Prof. Alexander M. Pogrebnoi, for their priceless advice, remarks, suggestions and guidance, proposed with extreme kindness. Heartfelt thanks should go to our research collaborators and expert in the area; first, Prof. Nuha Wazzan from the Chemistry Department, Faculty of Science, King Abdulaziz University, Jeddah, Saudi Arabia. Secondly, Dr. Ohoud S. Al-Qurashi from the Chemistry Department of the Faculty of Science, University of Jeddah, Jeddah, Saudi Arabia. Their kind support provides access to the King Abdulaziz University High-Performance Computing Centre (Aziz Supercomputer) <https://hpc.kau.edu.sa>.

I sincerely appreciate my employer, the Open University of Tanzania, for granting me a study leave. Furthermore, I gratefully acknowledge the support from WISE-Future <https://www.wisefutures.ac.tz/> of the ACE II, <https://ace2.iucea.org/> provided by the World Bank Group for the merit-based scholarship of Ph.D studies at Nelson Mandela African Institution of Science and Technology (NM-AIST), Arusha, Tanzania. Similarly, I would like to thank Prof. Revocatus Machunda (Former Dean, School of MEWES) and Dr. Thomas Kivevele (HoD, MESE Department) for providing a supportive environment to conduct my studies and for their leadership attributes. Furthermore, I wish to thank Mses. Analyce Ichwekeleza (Dean of Students), Victoria Ndossi, Silvia Ndakidemi (Students Welfare Office), Mr. Adam Mawenya, Mses. Leah Gonda and Joyce Martin for their dedicated assistance from the IT department. I again place my record and my sincere gratitude to Mr. Haji Chomba for his exceptional work in MEWES Dean's office for academic matters. I also owe the entire NM-AIST community. Other funders are much appreciated in supporting career development, starting from the University of California, Merced supporting the candidate June 2020 workshop. Secondly, the APS innovation fund and the US-Africa initiative for conference and workshop support to the candidate on June 14–18, 2021. Thirdly, Simons Foundations and Flatiron Institute fund the candidate for the conference from Monday, July 12th to Thursday, July 15th 2021. Fourthly, (a) Dyenamo AB from KTH Royal Institute of Technology, Sweden; (b) Pixel Voltaic, Portugal; (c) LEPABE, Portugal companies; (d) Department of Chemical Engineering, Faculty of Engineering, University of Porto, Portugal funds the support to the candidate to participate to the international solar power technologies conference <https://f1000research.com/documents/10-1041>. Fifthly, the 9th

IUPAC International Conference on Green Chemistry funds the candidate's support to participate in the Conference Proceedings <https://greeniupac2022.org/>. Sixthly, the IUMRS-ICYRAM 2022 supports the candidate to participate in the conference. Further details are at <https://www.iumrs-icyram2022.org/en/prg/index.php>, and more clarification is public at https://www.iumrs-icyram2022.org/en/prg/programList_poster.php?id=C. Last but not least, the 14th Green Chemistry Postgraduate Summer School appreciated the funds to support the candidate to participate in the Conference Proceedings.

I want to pass whole heartedly appreciation to my colleague, mentor and friend Dr. Geradius Deogratias who worked together from the beginning in this area. Furthermore, I sincerely thank colleagues Drs. Paul Lucas, Catherine Paschal, Eric Mutegoa, Faith Mpondo, Daniel S. Madulu and Edwin R. Ndibalema for their encouragements.

I also wish much appreciation to the colleagues Messrs. Melkizedeck Tsere and Nyanda Madili, who are mentees to the candidate. It is significant to receive mentees and colleagues to show interest in working on the projects to extend more understandings of the betalains materials to the DSSCs application. Furthermore, the candidate commits excellent appreciation to the new research collaborator Prof. Dr. Zaki S Safi, from the Chemistry Department, Faculty of Science, Al Azhar University-Gaza, Palestine State, accepted to work with Nyanda Madili and our future collaborations.

I wish to acknowledge my family's support and great love throughout this long commitment to being away from home.

DEDICATION

This work is dedicated to my late father, members of the family, colleagues and experts in the area.

TABLE OF CONTENTS

ABSTRACT	i
DECLARATION	ii
COPYRIGHT	iii
CERTIFICATION	iv
ACKNOWLEDGEMENTS	v
DEDICATION	vii
TABLE OF CONTENTS.....	viii
LIST OF TABLES.....	xiii
LIST OF FIGURES	xv
LIST OF APPENDICES	xx
LIST OF ABBREVIATIONS AND SYMBOLS	xxi
CHAPTER ONE	1
INTRODUCTION	1
1.1 Background of the problem	1
1.1.1 Renewable energy sources	1
1.1.2 The birth concept of photovoltaic solar cells	2
1.1.3 Generations of the photovoltaic solar cells	3
1.1.4 Nanotechnology for DSSCs fabrication.....	3
1.1.5 Structure of the DSSCs	4
1.1.6 Operation principle of the DSSCs.....	5

1.1.7	Dye (or photosensitiser) design	6
1.1.8	Figures of merit of DSSCs	10
1.1.9	Issues on the stability of DSSCs	16
1.1.10	Promising motivation.....	17
1.2	Statement of the problem	17
1.3	The rationale of the study	18
1.4	Research objectives.....	19
1.4.1	Main objective	19
1.4.2	Specific objectives	19
1.5	Research questions.....	19
1.6	Significance of the study.....	19
1.7	Delineation of the study	20
CHAPTER TWO		21
LITERATURE REVIEW		21
2.1	Introduction.....	21
2.2	Paradigm	22
2.2.1	Scientific research paradigm.....	23
2.2.2	The paradigm of choice in a materials science and engineering study	24
2.3	Applicability of betalains	25
2.3.1	Dyeing acrylic fabric.....	26
2.3.2	Medicinal issues.....	26

2.3.3	Natural dyes in the food industry (E162) and cosmetics	26
2.3.4	Dietary supplements.....	27
2.3.5	Photoprotectors	27
2.3.6	Beetroot pigment-based colourimetric sensors	28
2.3.7	Betalain-based biosensors	28
2.3.8	Functional plant-based food.....	28
2.3.9	Dye-sensitised solar cells	29
CHAPTER THREE		30
MATERIALS AND METHODS.....		30
3.1	Electronic structure prediction	30
3.1.1	Quantum mechanics, Schrödinger equation	30
3.1.2	Hartree-Fock method	33
3.1.3	Density functional theory.....	34
3.1.4	Kohn-Sham theory	36
3.1.5	Exchange–Correlation functionals.....	37
3.1.6	Plane-Wave functions and Brillouin zone sampling.....	39
3.1.7	Basis sets.....	41
3.2	Minima on potential energy surfaces	45
3.2.1	Empirical potential.....	45
3.2.2	Global search methods.....	46
3.2.3	Geometric optimisation.....	46

3.3	Computational software	47
3.3.1	Firefly code	47
3.3.2	Gaussian 16 code	49
3.3.3	VASP code.....	50
3.4	Investigated natural betacyanin (betanidin) and synthetic (L0) sensitisers	52
3.5	Dye design	53
3.6	Computational details	55
3.6.1	Computation of geometry and vibrational spectra.....	56
3.6.2	Calculation of the thermodynamic properties.....	56
3.6.3	A theoretical framework to study the betacyanins for DSSCs application.....	57
3.6.4	Solvation models.....	58
3.6.5	Electronic properties	60
3.6.6	Chemical molecular descriptors.....	61
3.6.7	Relationship between descriptors and thermodynamics	65
3.6.8	Charge transfer characteristics	66
3.6.9	Adsorption of the dyes on the TiO ₂ surface.....	70
CHAPTER FOUR.....		71
RESULTS AND DISCUSSIONS		71
4.1	General information on the betanidin geometrical isomers.....	71
4.1.1	Geometrical structure of the betanidin isomers and decarboxylated betanidin.....	71
4.1.2	Vibrational spectra of the betanidin and its decarboxylated isomer	74

4.1.3	Thermodynamics of chemical reactions of the betanidin conformational geometrical isomers	75
4.1.4	Optoelectronic properties of the betanidin conformational geometrical isomers	78
4.1.5	Betanidin conformational isomers (Bd–b, Bd–p) and dBd dye adsorption on TiO ₂ cluster	85
4.2	Designed betanidin complexes with L0 dye	92
4.2.1	The geometrical structure of the designed complexes	93
4.2.2	Vibrational spectra analysis of the betanidin complexes with L0	95
4.2.3	Thermodynamics of the chemical reactions of the betanidin with L0 dye.	97
4.2.4	Optoelectronic properties of the designed complexes	102
4.2.5	Designed betanidin complexes adsorption on the TiO ₂ cluster	113
CHAPTER FIVE		121
CONCLUSION AND RECOMMENDATIONS		121
5.1	Conclusion	121
5.2	Recommendations.....	122
REFERENCES		125
APPENDICES		158
RESEARCH OUTPUTS.....		162

LIST OF TABLES

Table 1:	The components of the research paradigm	24
Table 2:	Based on DSSCs, photo-electrochemical data for betalains	29
Table 3:	GTO contraction coefficients and exponential parameters used for the Ti atom in LANL2DZ (Frisch <i>et al.</i> , 2019).....	44
Table 4:	Selected geometrical parameters of the dye molecules: Bond distances in Å, bond angles and dihedral angles in degs.....	72
Table 5:	Thermodynamic characteristics of chemical reactions	77
Table 6:	Characteristics of electronic transitions $S_0 \rightarrow S_n$ in Bd-b, Bd-p and dBd computed with TD-DFT/B3LYP/6-31G(d,p) for a Vacuum, and DMSO, C ₂ H ₅ OH and H ₂ O solvents.....	80
Table 7:	Energies of the molecular orbitals $\varepsilon(\text{MO})$, excitation energies E_{ex} , energy gaps E_g and excited states oxidation potentials $E_{\text{ox}}^{\text{dye}*}$ of the selected states, DMSO solvent. The energies are in eV	83
Table 8:	Calculated ionisation potentials (IP_v , IP_{ad}), electron affinities (EA_v , EA_{ad}), hole extraction potentials (HEP), electron extraction potentials (EEP), hole and electron reorganisation energies (A_h , A_e); all values are in eV	83
Table 9:	Adsorption properties of the Bd-b@TiO ₂ and dBd@TiO ₂ complexes; connecting links between the dye site and TiO ₂ cluster, respective bond distances, O-Ti or N-Ti; electronic energies and binding energies of the complexes calculated at the B3LYP/6-31G(d,p)/LANL2DZ	87
Table 10:	Characteristics of electron transitions $S_0 \rightarrow S_n$ in the dye@TiO ₂ complexes, Bd-b@TiO ₂ and dBd@TiO ₂ , computed at the CAM-B3LYP/6-31G(d,p)/LANL2DZ with PCM for water.....	90
Table 11:	The selected geometrical parameters of the dye molecules: Bond distances in Å, bond angles, and dihedral angles in degs	94

Table 12:	Thermodynamic characteristics of the chemical reactions.....	98
Table 13:	The percentage contribution to the HOMO and LUMO from respective fragments of the dyes	103
Table 14:	Characteristics of the electronic transitions $S_0 \rightarrow S_n$ ($n = 1-15$) in L0, L0-1-Bd, L-2-Bd, L0-1-dBd and L0-2-dBd computed for a CH ₃ OH, H ₂ O, DMSO and CH ₃ CN solvents.....	105
Table 15:	Energies of the molecular orbitals $\varepsilon(\text{MO})$, excitation energies ΔE_{0-n} , energy gaps E_g and $ESOP_s$ of the selected transitions with oscillator strength $f \geq 0.1$ for the dyes in DMSO; all values are in eV	109
Table 16:	Ionisation potentials (IP_v , IP_{ad}); electron affinities (EA_v , EA_{ad}); hole and electron extraction potentials (HEP , EEP); hole, and electron and total reorganisation energies (A_h , A_e , A) of the L0 and designed complexes; all values are in eV.....	109
Table 17:	Dye@TiO ₂ adsorption links, the O-Ti bond distances ^a ; total electronic energies and binding energies of the studied systems calculated at the B3LYP/6-31G(d,p) for the dye molecules and LANL2DZ for Ti atoms.....	114
Table 18:	Characteristics of electronic transitions $S_0 \rightarrow S_n$ in the dye@TiO ₂ systems, L0@TiO ₂ , L0-1-Bd@TiO ₂ , L0-2-Bd@TiO ₂ , L0-1-dBd@TiO ₂ , and L0-2-dBd@TiO ₂	119

LIST OF FIGURES

Figure 1:	Atmospheric and sea level (AM 1.5G) solar irradiance spectra compared to a 5250 °C black body spectrum (Gabrielsson, 2014)	2
Figure 2:	Solar cell generations	4
Figure 3:	A typical dye-sensitised solar cell structure (Rosa <i>et al.</i> , 2017; Suhaimi <i>et al.</i> , 2015)	5
Figure 4:	A flowchart depicting the processes that occur in functioning DSSCs. Blue arrows represent helpful processes, whereas red arrows represent undesirable loses (Gabrielsson, 2014)	5
Figure 5:	Components of the dye design	10
Figure 6:	The five figures of merit of the DSSCs application	11
Figure 7:	Current–voltage characteristic curve (filled circles). The FF is equal to the area of the darkened zone bounded by the V_{\max} and J_{\max} multiplied by the area of the region bounded by the V_{oc} and J_{sc} . The blue curve (open circles) depicts power as a voltage function (Calogero <i>et al.</i> , 2015)	12
Figure 8:	Factor affecting the power conversion efficiency (η)	15
Figure 9:	The conceivable atomic combinations result in a large number of molecules that can be explored experimentally, theoretically, or computationally, most notably through high-throughput simulations. Figure from pictures (Polini <i>et al.</i> , 2013); experiments from (Acosta <i>et al.</i> , 2018); computational science and machine learning from (Mounet <i>et al.</i> , 2018); whole Figure from (Schleder <i>et al.</i> , 2019)	23
Figure 10:	Summarises the different beetroot pigment uses that may contribute to achieving sustainable development goals (SDGs)	25
Figure 11:	Representation of potential and pseudopotential (Payne <i>et al.</i> , 1992)	43
Figure 12:	Individual betanidin, decarboxybetanidin and L0 dyes	53

Figure 13:	Betanidin and L0 dye complex	54
Figure 14:	Decarboxylated betanidin and L0 dye complex.....	54
Figure 15:	The isomerisation reaction	55
Figure 16:	The research philosophy describes the fundamental tenets of the study	55
Figure 17:	Theoretical framework for the interconnectedness of the tools and variables.	58
Figure 18:	Optimised geometrical structures of the dye molecules	73
Figure 19:	IR spectra of betanidin molecules (top) and decarboxylated betanidin (bottom)	74
Figure 20:	The enthalpies $\Delta_r H^\circ(T)$ (Left) and entropies $\Delta_r S^\circ(T)$ (Right) of the decarboxylation reactions, $Bd-b \leftrightarrow dBd + CO_2$ (R2) and $Bd-p \leftrightarrow dBd + CO_2$ (R3)	76
Figure 21:	Thermodynamic characteristics: (a) of the isomerisation reaction $Bd-b \leftrightarrow Bd-p$ (b) pressure ratio p_{II}/p_I of the betanidin conformational isomers, p_I stands for $Bd-b$, p_{II} for $Bd-p$ (c) Gibbs free energies of decarboxylation reactions R2 and R3	77
Figure 22:	Frontier MOs of the considered dyes: Vacuum (top) DMSO solvent (bottom)	79
Figure 23:	UV-Vis spectra of the dyes, $Bd-b$, $Bd-p$ and dBd , simulated with TD- DFT/B3LYP5/6-31G(d,p) for a Vacuum, DMSO, C_2H_5OH and H_2O	82
Figure 24:	Energy level diagram of relevant MOs, excited state potentials E_{ox}^{dye*} and excitation energies ΔE_{0-1} for the dyes under study for the DMSO solvent. Valence and conduction bands of TiO_2 (Fujisawa <i>et al.</i> , 2017), redox potentials for electrolytes, I^-/I_3^- (Mishra <i>et al.</i> , 2009) and Spiro-OMeTAD (Nguyen <i>et al.</i> , 2014) for comparison.....	83
Figure 25:	Comparison of electronic energies for the dye molecules $Bd-b$, $Bd-p$ and dBd : (a) $-E_H$, IP_v and IP_{ad} (b) $-E_L$, EA_v , EA_{ad} and $ESOP$	84

Figure 26:	Optimised attachment modes for the Bd-b@TiO ₂ (at the top) and dBd@TiO ₂ (at the bottom) complexes.....	86
Figure 27:	The binding energies of the considered attachment modes between the dyes and hydrogenated (TiO ₂) ₆ semiconductor cluster as computed at the B3LYP/6-31G(d,p)/ LANL2DZ.....	87
Figure 28:	UV-Vis spectra of the complexes Bd-b@TiO ₂ (Top) and dBd@TiO ₂ (Bottom) simulated for different adsorption links at CAM-B3LYP/6-31G(d,p)/LANL2DZ with PCM for water	89
Figure 29:	The distribution patterns of the frontier and adjacent molecular orbitals involved in the S ₀ →S _n transition for the Bd-b@TiO ₂ calculated at the CAM-B3LYP/6-31G(d,p)/LANL2DZ with PCM for water	91
Figure 30:	The distribution patterns of the frontier and adjacent molecular orbitals involved in the S ₀ →S _n transition for the dBd@TiO ₂ calculated at the CAM-B3LYP/6-31G(d,p)/LANL2DZ with PCM for water	92
Figure 31:	Optimised geometrical structures of the complex dye molecules	93
Figure 32:	Optimised geometrical structure of the L0 dye molecule	93
Figure 33:	IR spectra of the betanidin complex dye molecules L0-1-Bd and L0-2-Bd	96
Figure 34:	IR spectra of the decarboxylated betanidin complex dye molecules L0-1-dBd and L0-2-dBd.....	96
Figure 35:	IR spectrum of the L0 dye molecule.....	97
Figure 36:	Thermodynamic characteristics of the reactions R1-R8: Enthalpies $\Delta_r H^\circ(T)$ (a) Entropies $\Delta_r S^\circ(T)$ (b) and Gibbs free energies $\Delta_r G^\circ(T)$ (c)	100
Figure 37:	Thermodynamic characteristics $\Delta_r H^\circ(T)$, $\Delta_r S^\circ(T)$ and $\Delta_r G^\circ(T)$ of isomerisation reactions for betanidin complexes L0-1-Bd↔L0-2-Bd (a) and decarboxylated betanidin complexes L0-1-dBd↔L0-2-dBd (b)	101

Figure 38:	Pressure ratio p_{II}/p_I of the betanidin complexes and decarboxy betanidin complexes isomers; p_I stands for either L0–1–Bd or L0–1–dBd, p_{II} for either L0–2–Bd or L0–2–dBd	101
Figure 39:	Frontier molecular orbitals (FMOs) of the dyes in DMSO solvent	102
Figure 40:	Representative fragments of the designed complex L0–2–Bd dye numbered with the Aomix calculation program (Gorelsky, 2017; Gorelsky & Lever, 2001)	103
Figure 41:	A bar graph of the percentage contribution to the HOMO and LUMO from different fragments of the considered dyes	104
Figure 42:	UV–Vis spectra of the dyes L0, L0–1–Bd, L0–2–Bd, L0–1–dBd and L0–2–dBd simulated at TD–DFT/B3LYP/6-31G(d,p) with PCM for DMSO	107
Figure 43:	Energy level diagram of relevant MOs, excited state potentials E_{ox}^{dye*} and excitation energies ΔE_{0-1} for the dyes under study for the DMSO solvent. Valence and conduction bands of TiO ₂ (Fujisawa <i>et al.</i> , 2017; Makoye <i>et al.</i> , 2020) redox potentials for electrolytes, I [–] /I ₃ [–] (Mishra <i>et al.</i> , 2009) and Spiro–OMeTAD (Nguyen <i>et al.</i> , 2014), are shown for comparison	110
Figure 44:	Comparison of electronic energies for the dye molecules L0, L0–1–Bd, L0–2–Bd, L0–1–dBd and L0–2–dBd: (a) $-E_H$, IP_v and IP_{ad} ; (b) $-E_L$, EA_v , EA_{ad} and $-ESOP$; (c) $-E_g$ and ΔE ; (d) ΔE_{0-n} vs $-E_g$	111
Figure 45:	Ratio of adiabatic to vertical values of IP and EA for the L0, L0–1–Bd, L0–2–Bd, L0–1–dBd and L0–2–dBd	111
Figure 46:	Comparison of reorganisation energies for electrons and holes in the L0, L0–1–Bd, L0–2–Bd, L0–1–dBd and L0–2–dBd	112
Figure 47:	Full electron donor-acceptor map; data for individual dyes Bd-b and dBd betanidin dyes	112

Figure 48:	Optimised attachment modes for the systems: L0@TiO ₂ , L0-1-Bd@TiO ₂ and L0-2-Bd@TiO ₂ (at the top) and L0-1-dBd@TiO ₂ and L0-2-dBd@TiO ₂ (at the bottom).....	115
Figure 49:	The binding energies of the considered attachment modes between the dyes and (TiO ₂) ₆ cluster as computed at the B3LYP/6-31G(d,p)/LANL2DZ	115
Figure 50:	The UV-Vis spectra of the betanidin complexes, L0-1-Bd@TiO ₂ (a), L0-2-Bd@TiO ₂ (b) and decarboxylated betanidin complexes, L0-1-dBd@TiO ₂ (c), L0-2-dBd@TiO ₂ (d), simulated for different adsorption links at CAM-B3LYP/6-31G(d,p)/LANL2DZ with polarisable continuum model (PCM) for water.....	117
Figure 51:	The distribution patterns of the frontier and adjacent molecular orbitals involved in the S ₀ →S _n transition for the L0@TiO ₂ , L0-1-Bd@TiO ₂ and L0-2-Bd@TiO ₂ calculated at the CAM-B3LYP/6-31G(d,p)/LANL2DZ with polarisable continuum model for water; H is the HOMO, L is the LUMO...	120
Figure 52:	The distribution patterns of the frontier and adjacent molecular orbitals involved in the S ₀ →S _n transition for the decarboxylated betanidin complexes L0-1-dBd@TiO ₂ and L0-2-dBd@TiO ₂ calculated at the CAM-B3LYP/6-31G(d,p)/LANL2DZ with polarisable continuum model for water; H is the HOMO, L is the LUMO.....	120

LIST OF APPENDICES

Appendix 1:	Optimised geometrical structure of the Bd-b, Bd-p and dBd dye molecules; Cartesian coordinates of atoms in Å.	158
Appendix 2:	Thermodynamic functions of the Bd-b, Bd-p, and dBd dyes in the gas phase	159
Appendix 3:	Total energies of the dyes in neutral and ionised states (a.u.)	161

LIST OF ABBREVIATIONS AND SYMBOLS

B3LYP	Becke's Three Parameters Gradient-Corrected Exchange Potential and The Lee–Yang–Parr Gradient–Corrected Correlation Potential
B3LYP5	Becke's Three Parameters Gradient-Corrected Exchange Potential and The Lee–Yang–Parr Five Gradient–Corrected Correlation Potential
BB	Bridging Bidentate
Bd	1-[(2E)-2-(2,6-Dicarboxy-2,3-dihydro-1H-pyridin-4-ylidene)ethylidene]-5,6-dihydroxy-2,3-dihydroindol-1-ium-2-carboxylate
BE	Binding Energy
BT	Bridging Tridentate
CAM–B3LYP	Coulomb–Attenuating Method Combined with B3LYP
CB	Conduction Band
CE	Counter Electrode
CPCM	Conductor–Like Polarizable Continuum Model
c–Si	Crystalline Silicon
dBd	2–decarboxy betanidin
DFT	Density Functional Theory
DFT–D3	Dispersion–Corrected Density Functional Theory Calculations
DMSO	Dimethyl sulfoxide
DSSCs	Dye–Sensitised Solar Cells
<i>EA</i>	Electron Affinity
<i>EA_a</i>	Adiabatic Electron Affinity
<i>EA_v</i>	Vertical Electron Affinity
ECP	Effective Core Potentials
<i>EEP</i>	Electron Extraction Potential
<i>ESOP</i>	Excited–State Oxidation Potential
FEDAM	Full–Electron Donor–Acceptor Map
FMOs	Frontier Molecular Orbitals
FTO	Fluorine–Doped Tin Oxide
GGA	Gradient–Correlated Approximation
<i>HEP</i>	Hole Extraction Potential
HOMO	Highest Occupied Molecular Orbital

ICT	Intramolecular Charge Transfer
<i>IP</i>	Ionisation Potential
<i>IP_a</i>	Adiabatic Ionisation Potential
<i>IP_v</i>	Vertical Ionisation Potential
IR	Infra-Red
ITO	Indium-Doped Tin Oxide
L0	(4-(diphenylamino)phenylcyanoacrylic acid
LANL2DZ	Los Alamos National Laboratory 2 Double Zeta
LHE	Light-harvesting Efficiency
M	Monodentate
MMFF94	Merk Molecular Force Field
PBE	Perdew-Burke-Ernzerhof
PCE	Power Conversion Efficiencies
PV	Photovoltaic
TCO	Transparent Conductive Oxides
TD-DFT	Time-Dependent Density Functional Theory
TPA	Triphenylamine
U	Coulombic Repulsion
UV-Vis	Ultraviolet-Visible
XC	Exchange-Correlation

CHAPTER ONE

INTRODUCTION

1.1 Background of the problem

Solar energy accounts for nearly all energy on Earth. Renewable energy sources are the most easily exploitable, limitless, silent and adaptable to massive uses (Lewis *et al.*, 2005). Photovoltaic (PV) technology turns sunlight directly into electricity without pollution, noise, or moving components, making it extremely durable and trustworthy; it is an elegant technique for harnessing the sun's energy (Grätzel, 2004; Pearce, 2002). The mechanism of photovoltaic devices is based on the charge separation principle, which occurs at the interface of two materials with distinctly different conduction mechanisms (Jasim, 2011). The history of photovoltaics began in the nineteenth century with the invention of the primitive photovoltaic cell made of selenium and a thin film of gold by Charles Fritts (Ludin *et al.*, 2014). Following Wilhelm Vogel's great work in 1873, the first panchromatic film, capable of converting realistic images to black and white, was developed after 1873. Vogel discovered a method for increasing the sensitivity of photographic emulsions and associated silver halide emulsions with dyes to produce black and white photographic films. However, due to their band gaps of 2.7–3.2 eV, silver halides are insensitive to a large portion of visible light. This accomplishment can be considered the first noteworthy investigation on dye sensitisation of semiconductors (Narayan, 2012; West, 1974).

1.1.1 Renewable energy sources

With a light output of 4×10^{24} W, the Sun, our nearest star, can maintain fusion reactions in its core (Williams, 2018). Black bodies with 5800 K temperatures have emission spectrums similar to this. Approximately 42% of this light is absorbed and scattered in the Earth's upper atmosphere, where just a minuscule percentage (1.74×10^7 W) of this enters our atmosphere (Kiehl & Trenberth, 1997). The amount of light reaching Earth's surface is still about 5000 times greater than all the energy we now use.

Latitude, altitude, time of year (and day), and weather all have an impact on the solar spectrum on the Earth's surface. Selected circumstances are represented, however, by standardised reference spectra. AM 1.5G is the most often used spectrum. The "1 Sun"

intensity of 1000 W/m^2 (or 100 mW/cm^2) can be achieved by integrating the AM 1.5 spectrum (Fig. 1). The AM 1 is a better representation of sunlight at the equator's zenith.

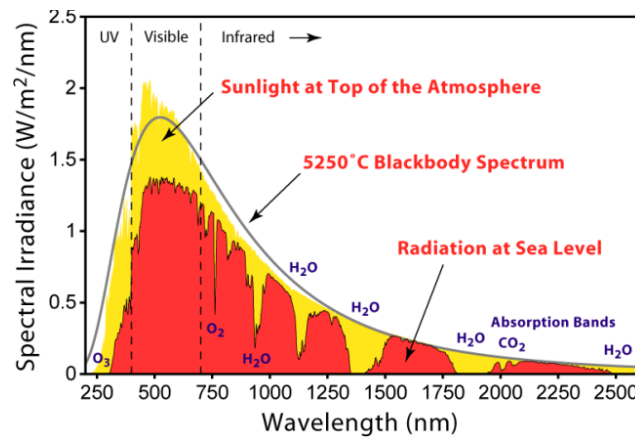


Figure 1: Atmospheric and sea level (AM 1.5G) solar irradiance spectra compared to a 5250 °C black body spectrum (Gabrielsson, 2014)

Using energy from renewable sources (such as solar thermal, geothermal, wind, and biomass) is one way to meet the world's rising energy needs. Because of its ability to meet global energy needs, solar has the potential to help us in a more sustainable future (Dhere, 2007; Hosseini & Wahid, 2020). As a bonus, solar power is ecologically benign and free to use. This gives people hope that solar energy will meet the world's energy needs now and in the future.

Semiconducting materials can be used to turn sunlight into useable electricity. Recent advances in photovoltaic technology, namely the creation of silicon solar cells, perovskite solar cells, and dye-sensitised solar cells (DSSCs), have led to a decrease in the cost of electricity and made the technology competitive with other power sources (Zhang *et al.*, 2020). The DSSCs employ nanocomposites of TiO_2 with organic or organic-inorganic (usually ruthenium complexes) dyes to generate electricity (Upadhyaya *et al.*, 2013). Creating devices that can convert and store solar energy is the focus of a great deal of scientific work in this area.

1.1.2 The birth concept of photovoltaic solar cells

Solar cells might be regarded as the leading invention in renewable energy due to recent advancements in power conversion efficiency and dramatic cost reductions (James & Contractor, 2018). In 1839, Becquerel noticed a current flowing between two silver electrodes in an electrolyte medium in response to light exposure; this was the first

observation of a photovoltaic phenomenon (Becquerel, 1839). Albert Einstein described the photoelectric effect in 1905 and was awarded the Nobel Prize in 1921 for his work (Jasim, 2011). In 1941, Russell Ohl invented the silicon solar cell. Bell Laboratories announced the manufacture of silicon solar cells with an efficiency greater than 6% in 1954 (Ludin *et al.*, 2014).

1.1.3 Generations of the photovoltaic solar cells

The term ‘photovoltaic’ derives from words ‘photo’, which means light, and ‘volt’, a unit of electrical measurement. Solar cells have been classified into three generations based on the material used to fabricate the cell, the power conversion efficiency (PCE), and the accompanying cost, as illustrated in Fig. 2. The majority of commercial solar cells are first-generation crystalline silicon solar cells (c-Si). In 1954, Chapin and colleagues discovered the c-Si (Chapin *et al.*, 1954). To date, c-Si solar panels have a PCE greater than 26% (Yoshikawa *et al.*, 2017), but polycrystalline solar panels have a PCE between 13% and 16%. The difference in PCEs between the two types of cells is attributable to the cleanliness of the silicon. Today, about 90% of the world’s solar systems are based on some forms of silicon. However, because of their complicated designs and extensive manufacturing procedures, c-Si panels are quite expensive; their cost per watt is also the highest (Saga, 2010). There are underlying health concerns related to the production of the c-Si, including inhalation of harmful fumes from dopant gases and vapours such as B_2H_6 , $POCl_3$, and PH_3 . For instance, poisonous gases P_2OCl_3 and Cl_2 can be created during the deposition of $POCl_3$ in a chamber. Other hazardous gases may be detected when HNO_3 , HF , or $NaOH$ are used to clean the reactor and wafer, and remove dopant oxides (Fthenakis, 2018).

1.1.4 Nanotechnology for DSSCs fabrication

One of the early difficulties in creating the DSSCs was the dye's low absorption capability. Due to the little amount of the dye on the TiO_2 , the dye might absorb less than 1% of incident light. Even if additional dye layers are formed on the TiO_2 , not all of the dye will touch the TiO_2 , resulting in low conversion efficiency. In order to address this issue, a nanoporous layer of TiO_2 with a surface area of approximately $300\text{ m}^2/\text{g}$ (formerly $10\text{ m}^2/\text{g}$) was produced (O'Regan & Grätzel, 1991). The cumulative effect of a variety of physical and chemical nanoscale characteristics determines the efficiency of a dye-sensitised solar cell. The critical issue is the dye-sensitisation principle for large band-gap semiconductor

electrodes. This is achieved by covering the internal TiO_2 electrode with dye molecules capable of absorbing the incident photons.

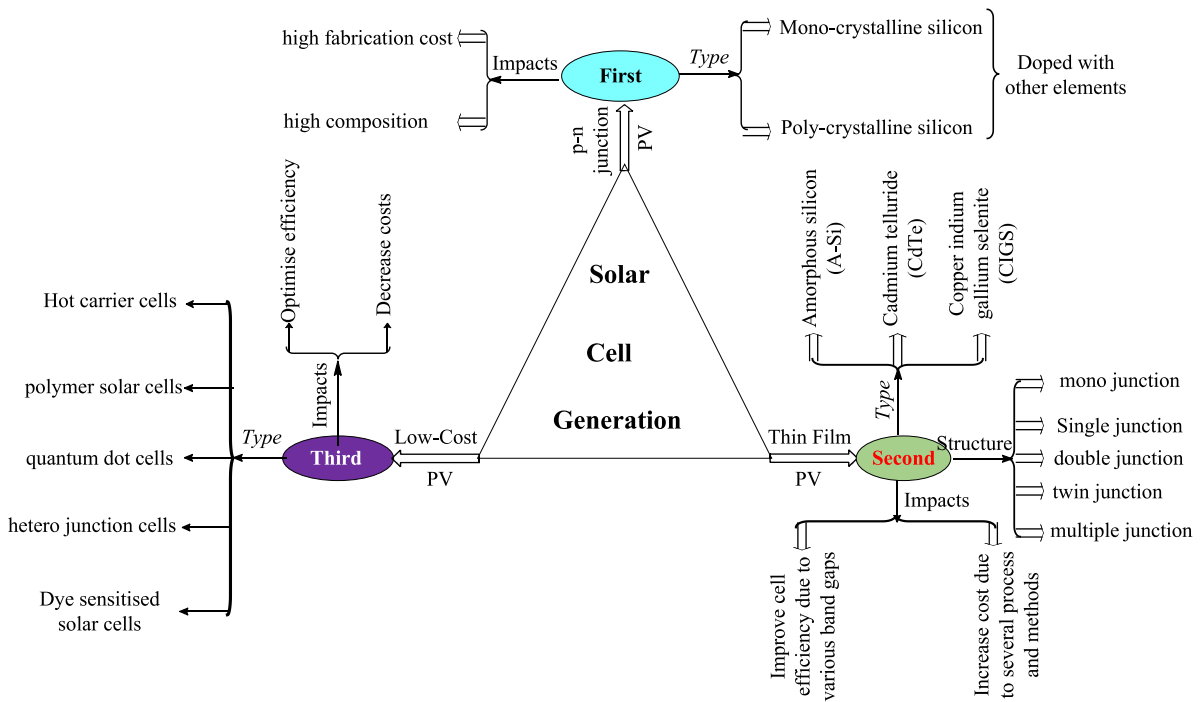


Figure 2: Solar cell generations

1.1.5 Structure of the DSSCs

The structure of a DSSC is depicted schematically in Fig. 3. The DSSCs are distinguished from other solar cell devices by their fundamental architecture and the physical processes that govern their operation. Compared to the first- and second-generation photovoltaic devices based on solid-state semiconductor materials, conventional DSSCs integrate liquid and solid phases. The DSSCs comprise a transparent conducting glass electrode (anode) that allows light to pass through it (Bauer *et al.*, 2002; Luque & Hegedus, 2011). Transparent glass substrates are commonly utilised as electrode substrates due to their low cost, availability, and great visible-spectrum transparency. The fluorine tin oxide F:SnO_2 coating provides a transparent conductive face. The titanium nanoparticle TiO_2 mesh serves as a dye container and facilitates electron transport within the cell. The TiO_2 particles are covered with dye molecules (light sensitisers), which convert photons to excited electrons and generate electricity. The dye is surrounded by an electrolyte layer (often iodide) that serves as a source of electrons to compensate for the loss. The counter electrodes (cathode) are commonly coated with graphite or platinum on the other side of the cell.

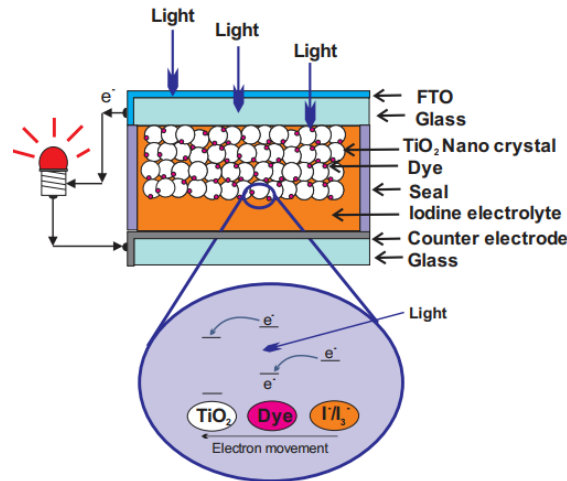


Figure 3: A typical dye-sensitised solar cell structure (Rosa *et al.*, 2017; Suhaimi *et al.*, 2015)

1.1.6 Operation principle of the DSSCs

As seen in Fig. 4, the process by which DSSCs create electrical current begins with the absorption of a photon by a dye molecule adsorbed to a mesoporous semiconductor, which induces it into an excited state (1). The excited dye molecule rapidly injects an electron from the excited state into the semiconductor's conduction band, therefore oxidising the dye (2). The electron is injected into the semiconductor and diffuses towards the (front) contact (3). After completing some external work, the electron is returned to the device's back contact, where it is used to reduce an oxidised species of the redox mediator (4). By donating an electron to an oxidised dye molecule, the reduced mediator diffuses to the working electrode and completes the circuit (5).

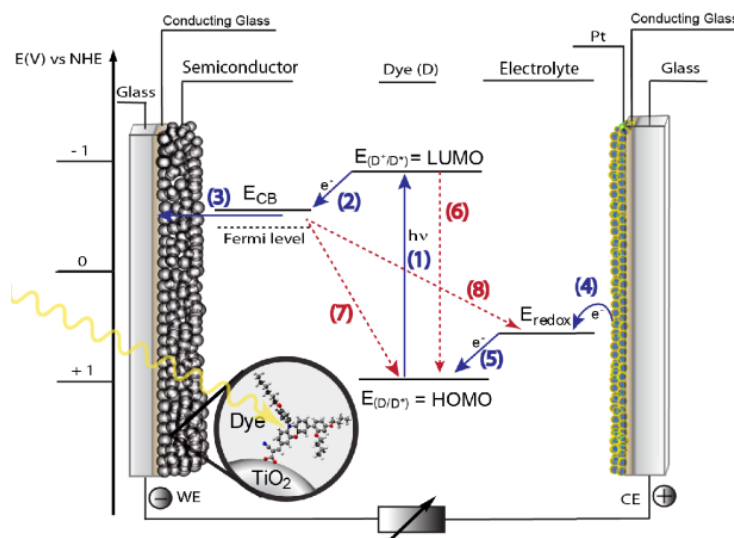


Figure 4: A flowchart depicting the processes that occur in functioning DSSCs. Blue arrows represent helpful processes, whereas red arrows represent undesirable losses (Gabrielsson, 2014)

While electron injection is a contentious matter, it generally refers to a highly fast process that occurs over a period of 10^{-13} – 10^{-10} s (Haque *et al.*, 2005; Koops *et al.*, 2009; Oum *et al.*, 2013). However, there exist dyes with substantially slower injection times (up to 10^{-7} s) (Morandeira *et al.*, 2007). The two competing relaxation reactions (6), fluorescence and internal conversion are typically substantially slower, occurring within 10^{-8} s (Gabrielsson, 2014). Electrons in the semiconductor's conduction band can recombine with one of two oxidised dye molecules on the surface (7) or oxidised redox species in the electrolyte (8). The former process, recombination to oxidised dye, happens on a timescale of 10^{-4} s and is primarily hindered by the dye regeneration process, which occurs on a time scale of 10^{-6} s (Gabrielsson, 2014). Although recombination to the oxidised redox mediator is one of the device's slowest processes, appearing on the 10^{-2} s timescale. The cell's voltage is defined by the difference between the semiconductor's quasi-Fermi level and the redox mediator's redox potential. The cell current output is controlled by the amount of photons absorbed by the dye at the working electrode, less the electrons lost in recombination processes.

1.1.7 Dye (or photosensitiser) design

In the dictionary, a dye is “a natural or synthetic material used to add or change the colour of something”. The dye's principal function in the DSSCs is to add colour; this straightforward definition accurately captures this. DSSCs absorb light and energy because of their colour. Absorption of light in the visible spectrum entails an electron travelling from a lower energy state to a higher one while absorbing the photon's energy. Since this absorbed energy must be transformed into electricity, the role of dyes is more complex than merely acting as light absorbers.

(i) Criteria for developing new dye for DSSCs

As a result, there are specific dye requirements and not all dyes can be utilised in DSSCs. Therefore, the following criteria are taken into account when developing a new dye for DSSCs:

- (a) Its absorption spectrum should be broad from the visible to the near-infrared regions of the solar spectrum.
- (b) To maximise light harvesting efficiency, its molar extinction coefficient (ϵ , $\text{M}^{-1} \text{cm}^{-1}$) must be as high as feasible.

- (c) There should be faster kinetics for the above processes than for their respective competitors.
- (d) The dye must be soluble in a solvent capable of adsorbing it to the semiconductor surface.
- (e) The dye should have a high resistance to desorption from the semiconductor.
- (f) The dye should have great photostability.
- (g) The dye should deposit a layer on the semiconductor that inhibits recombination between injected electrons and oxidised redox species.
- (h) The dye should be cheap and easy to synthesise.
- (i) The dye should be non-toxic as well as recyclable.
- (j) In order to inject an electron into the semiconductor's conduction band, the excited state reduction potential must be high enough, and the consequent oxidised state must be low enough to allow regeneration by the redox mediator.
- (k) When the dye is strongly anchored to the semiconductor surface, the electron injection channel is optimised.

(ii) Photo-electrochemical reactions

In the semiconductor/electrolyte interface of DSSCs, the photocurrent yield results from a competition between photo-electrochemical reactions.

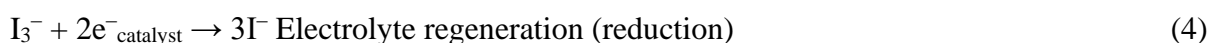
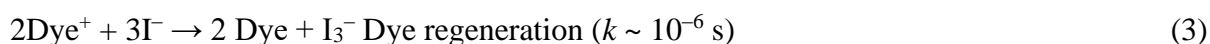
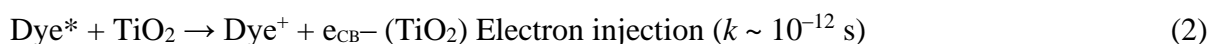
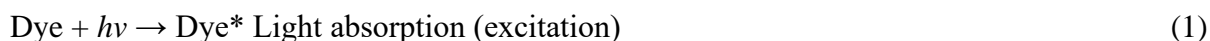
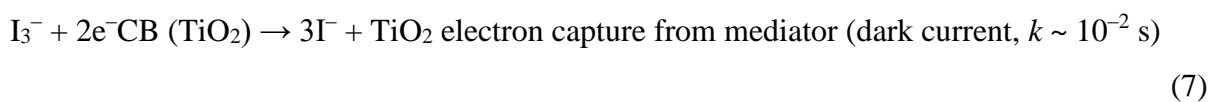
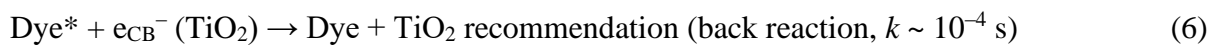
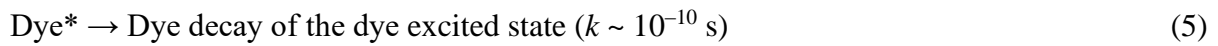


Figure 4 illustrates a sandwich-type solar cell's architecture and electron transfer mechanisms. When the dye molecules are lit, they absorb the incident photons ($h\nu$), creating electron-hole pairs (O'Regan & Grätzel, 1991). The photo-excited electrons in excited states

Dye* (Equation 1) which are energetically above the TiO₂ CB edge, are rapidly injected (Equation 2) into the TiO₂ CB (O'Regan & Grätzel, 1991) typical time constant k , around 10^{-12} s, under one sun illumination, i.e., irradiation power = 100 mW cm⁻², T = 25°C, light source spectral intensity = AM 1.5 global standard solar spectrum (Gray, 2003). The electronic density of TiO₂ increases due to the charge carrier transfer from the dye to the semiconductor oxide, resulting in an electrochemical potential difference (ΔV) between TiO₂ and the electrolyte (O'Regan & Grätzel, 1991).

The regeneration of oxidised dye molecules is performed by capturing electrons from the electrolyte mediator (Equation 3), which is sandwiched between the electrode and the catalyst for the reduction of I₃⁻ (Equation 4) (O'Regan & Grätzel, 1991). Thus, the entire cycle is regenerative (i.e., regenerate the oxidised sensitiser), and the overall balance is the conversion of photons to electrons without any permanent chemical transformation (Grünwald & Tributsch, 1997). Thus, perfect conditions should result in a stable cell capable of delivering photocurrent indefinitely. On the other hand, several “undesirable” processes impede electron transmission at the photoanode (Cherepy *et al.*, 1997). These loss mechanisms include the decay of the dye simulated to its ground state and the “re-capture” of injected electrons in the semiconductor CB by the oxidised dye or electrolyte species (Equation 5–7).



Thus, for DSSCs to be optimised, the electron injection (Equation 2) and dye regeneration processes by the electron donor mediator (Equation 3) must be faster than Dye* decay (radiative or non-radiative) (Equation 5) and the back reaction of the injected electron with the oxidised dye (Equation 6), respectively (O'Regan & Grätzel, 1991). In particular, the “dark current” is thought to be the primary mechanism of loss in DSSCs (Kalyanasundaram & Grätzel, 1998; Perera & Tennakone, 2003). Finally, “efficient” charge mediator regeneration at the CE (Equation 4) is critical; otherwise, the device's η may be limited (Kalyanasundaram & Grätzel, 1998; O'Regan & Grätzel, 1991). Therefore, a thorough understanding and knowledge of electron transfer kinetics are critical for identifying

materials that optimise the structure-function connection of DSSCs (Grätzel, 2006; Nazeeruddin *et al.*, 2001).

(iii) Natural sensitiser

In nature, some flowers, leaves, and fruits show various colours and consist of several pigments that can be readily extracted and used for DSSCs fabrication (Chang & Lo, 2010). Natural pigments have been considered as promising alternative sensitiser dyes for DSSCs because of their simple preparation technique, low cost, complete biodegradation, easy availability, purity grade, environmental friendliness, and most importantly, high reduction of noble metal, and chemical synthesis cost (Kishimoto *et al.*, 2005; Nishantha *et al.*, 2012; Sinha *et al.*, 2012). Plant pigmentation results from the electronic structure of pigments reacting with sunlight to change the wavelengths. The specific colour relies on the capacities of the viewer. The pigment can be described by the maximum absorption wavelength (λ_{\max}) (Davies, 2004).

The open circuit voltage (V_{oc}), the short circuit current (J_{sc}), the fill factor (FF), and the energy conversion efficiency (η) of DSSCs with natural sensitisers were used to evaluate their performance. Numerous pigments have been the topic of illustrious research. Numerous natural dyes, including chlorophyll II (Hao *et al.*, 2006; Kumara *et al.*, 2006), carotenoid (Gómez-Ortíz *et al.*, 2010; Kishimoto *et al.*, 2005; Rühle *et al.*, 2010), anthocyanin (Alhamed *et al.*, 2012; Chang & Lo, 2010), flavonoid (Davies, 2004; Sinha *et al.*, 2012; Sutthanut *et al.*, 2007) have studied to the application of DSSCs technology. Betacyanins are being investigated further in the current studies. Natural colourants are pigmentary molecules and can be derived primarily from plants but also from animals and minerals, with or without chemicals. Natural dyes include a hydroxyl group and are soluble in water (Wongcharee *et al.*, 2007). Numerous dyes lack a solubilising group; hence a temporary solubility group is formed during application (Rossetto *et al.*, 2002).

(iv) Synthetic sensitiser

Since dye has a vital role in absorbing and converting solar energy to electricity, numerous types of research have focused on the molecular engineering of several organic metal complexes and organic dyes. These complexes are also among the most effective sensitisers because of their high efficiency, excellent chemical stability, favourable photo-

electrochemical properties, and intense charge transfer absorption in the wide visible range (Hao *et al.*, 2006; Hernandez-Martinez *et al.*, 2012).

(v) Components of the dye design

The dye design is based on the three main categories to achieve good photosynthesiser in DSSCs application (Fig. 5). The category one (for isolated dye) and two (for complex dye) are considered to the present work. Category three (for dimer dye) is initially proposed for future work:

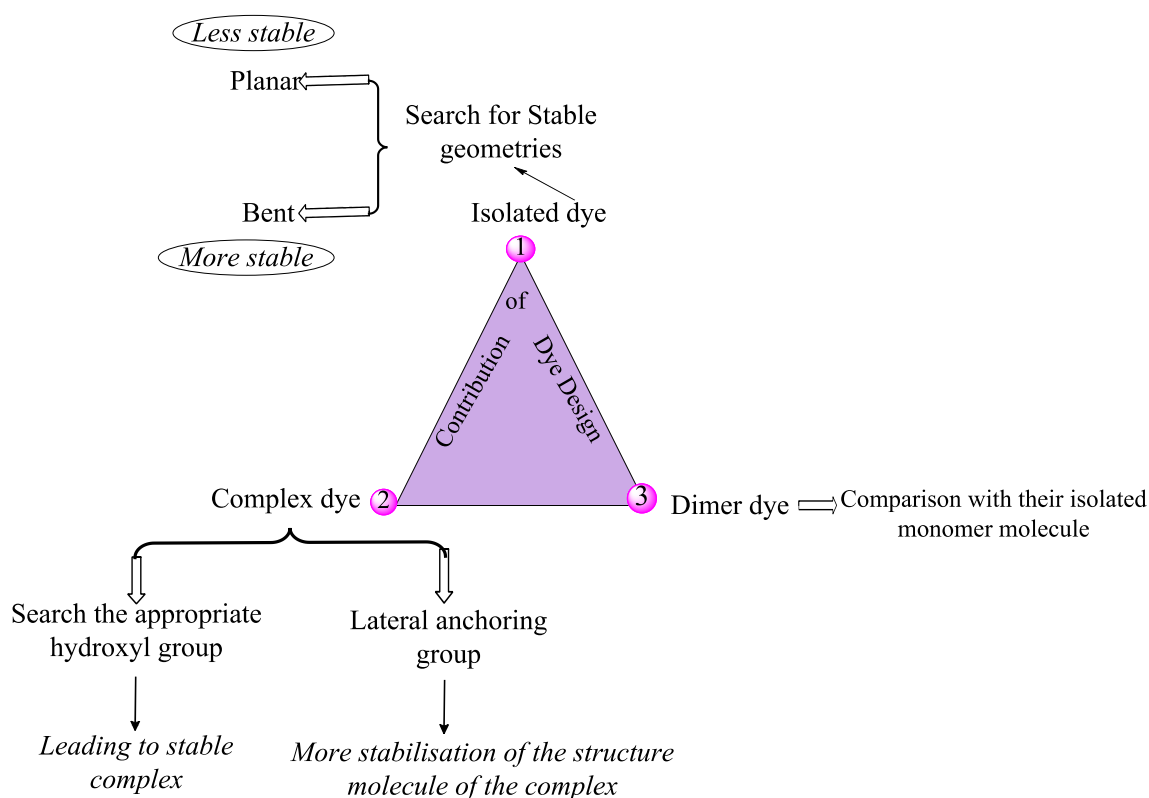


Figure 5: Components of the dye design

1.1.8 Figures of merit of DSSCs

For analytical chemists, figures of merit (Fig. 6) is a tool to characterise a method. Precision, accuracy, sensitivity, linear dynamic range, detection limit, and selectivity are the six figures of merit for analytical Chemist conceptions (Olivieri & Escandar, 2014).

A figure of merit is a term that refers to a quantity used to describe the performance of a device, system, or method compared to its alternatives. It is specified for specific materials or devices to ascertain their relative utility in a given application. Short-circuit photocurrent density (J_{sc}) (1), open circuit voltage (V_{oc}) (2), fill factor (FF) (3), incident photon conversion

efficiency (*IPCE*) (4), and energy conversion efficiency (η) (5) are summarised in Fig. 6 concerning DSSCs applications (Calogero *et al.*, 2015).

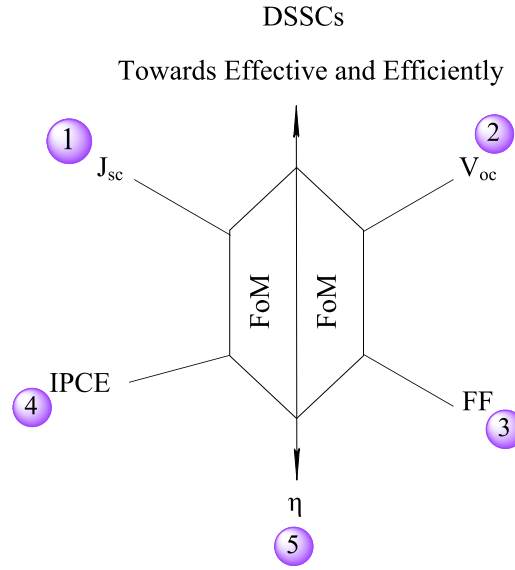


Figure 6: The five figures of merit of the DSSCs application

(i) Short-circuit photocurrent density (J_{sc})

Under 1 Sun, the short-circuit photocurrent density (J_{sc}) (Fig. 7) reflects the photocurrent per unit area (mA cm^{-2}) of the cell when it is short-circuited. The greater the J_{sc} , the greater the sensitiser's ability to absorb sunlight throughout abroad region of the solar spectrum and the greater its "efficiency" of injecting electrons into the semiconductor CB (Equation 1–3). Additionally, a high J_{sc} value is substantially correlated with the reduction rate of the oxidised dye (Equation 3). Indeed, the faster the oxidised dye is reduced, the smaller the dark current see (Equaion 6), which reduces the J_{sc} (Gray, 2003).

To obtain the photoelectric conversion efficiency, one must first determine the short-circuit current density (J_{sc}), which may be determined using the following equation (Fu *et al.*, 2018):

$$J_{sc} = e \int LHE(\lambda) \phi_{inj} \eta_{coll} \varphi_{ph,AM1.5G}(\lambda) d(\lambda) \quad (8)$$

where $LHE(\lambda)$ is available, $\varphi_{ph, AM1.5 G}$ is a standard reference for solar-radiation intensity in $\text{mA cm}^{-2} \text{ nm}^{-1}$. Meanwhile, Φ_{inj} denotes the injection efficiency (Ardo & Meyer, 2009), while η_{coll} denotes the efficiency of charge collecting (Haid *et al.*, 2012).

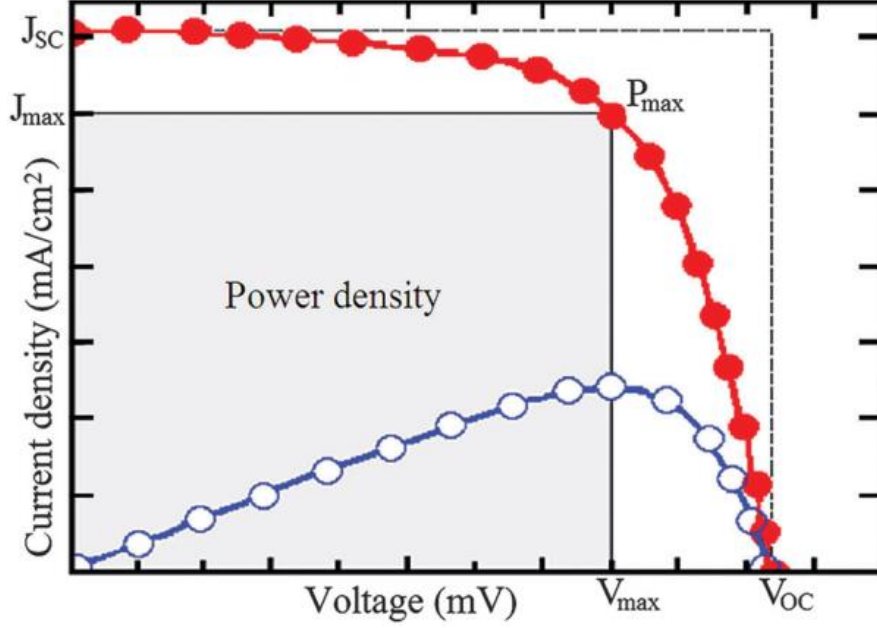


Figure 7: Current–voltage characteristic curve (filled circles). The FF is equal to the area of the darkened zone bounded by the V_{\max} and J_{\max} multiplied by the area of the region bounded by the V_{oc} and J_{sc} . The blue curve (open circles) depicts power as a voltage function (Calogero *et al.*, 2015)

(ii) Open circuit voltage (V_{oc})

The open circuit voltage (V_{oc}) is the electrical potential difference between the two terminals of the cell (photoanode and CE) when there is no current flowing. The maximum V_{oc} value of a DSSC (generally around 0.8-0.9 V) is equal to the difference between the semiconductor's quasi-Fermi level (E_F , -0.5 to -0.4 eV vs normal hydrogen electrode – NHE, for TiO_2) (Hagfeldt & Graetzel, 1995) and the charge mediator's redox potential (-0.4 V vs NHE, for I_3^-/I^- redox couple) (Hagfeldt & Graetzel, 1995). However, actual V_{oc} values are lower than theoretical values due to the recombination of injected electrons with the oxidised dye (Equation 6) and dark current (Equation 7). Indeed, for photo-electrochemical systems with regenerative capabilities (Gray, 2003). Therefore, after estimating the J_{sc} , the open circuit photovoltage (V_{oc}) can be calculated using either the standard model (Marinado *et al.*, 2010) (Equation 9) or the modified standard model (Equation 10) (Raga *et al.*, 2012).

$$V_{oc} = \frac{E_c + \Delta CB}{q} + \frac{k_B T}{q} \ln \left(\frac{n_c}{N_c} \right) - \frac{E_{redox}}{q} \quad (9)$$

where E_c denotes the semiconductor's conduction band edge, ΔCB denotes the shift of E_c caused by dye adsorbed on the semiconductor surface, q denotes the electron charge, n_c

denotes the number of electrons in the conduction band, N_C denotes the accessible density, and E_{redox} represents the reduction-oxidation potential.

As indicated in the study (Al-Qurashi & Wazzan, 2021), it was established that (Equation 9) ignores energy loss. The (Equation 10) accounts for the energy loss. The (Equation 9) being the standard model ignores energy loss, resulting in an incorrect value of η . The difference between V_{oc} and the lowest energy band gap of the donor/acceptor fragments is energy loss (Zhang *et al.*, 2017). Furthermore, through the electron injection process, the electron may recombine with the electrolyte or holes, lowering the semiconductor's Fermi energy and reducing V_{oc} . As a result, energy loss and recombination impact must be quantified in order to predict V_{oc} in the modified normal model (Ma *et al.*, 2014). Thus, the improved model may be compared to the previously developed model and available experimental data in further work.

$$V_{\text{oc}} = \frac{k_B T}{\beta'} \ln \frac{\beta' R_0 J_{\text{sc}}}{k_B T} \quad (10)$$

where β' is the charge transfer coefficient for recombination and equals 0.45 and R_0 is the recombination resistance, which may be approximated as (Wang *et al.*, 2006):

$$R_0 = \frac{\sqrt{\pi \lambda k_B T}}{q^2 d \gamma k_{\text{rec}} c_{\text{ox}} N_s} \exp \left(\gamma \frac{E_{\text{CBM}} - E_{\text{redox}}}{k_B T} + \frac{\gamma_{\text{tot}}}{4 k_B T} \right) \quad (11)$$

where d is the thickness determined experimentally to be 10 μm (Lin *et al.*, 2011); γ is the distribution of electron traps beneath the CB and has a value of ~ 0.3 (Ma *et al.*, 2014); c_{ox} is the acceptor species concentration ($\text{I}_3^- \sim 50 \text{ mmol L}^{-1}$); N_s is the total number of surface states contributing to recombination and is set to $\sim 10^5$; E_{CBM} is the CB shift after the dye is adsorbed on TiO_2 , and E_{redox} is the reduction-oxidation potential.

(iii) Fill factor (FF)

It is defined as the ratio of the following:

$$FF = \frac{P_{\text{max}}}{J_{\text{sc}} \cdot V_{\text{oc}}} \quad (12)$$

where P_{\max} denotes the cell's maximum power output per unit area, denoted by the product $(J_{\max}.V_{\max})$, the FF parameter describes how effectively the area under the current-voltage (J/V) curve fills in the maximum rectangle defined by the product $J_{sc}.V_{oc}$ in Fig. 7. The shape of this curve is a beneficial and straightforward instrument for characterising the DSSCs performance, specifically V_{oc} , J_{sc} and η).

(iv) Incident photon conversion efficiency

The photocurrent density generated in the external circuit per incoming monochromatic photon flux that impacts the cell is a measure of the cell's quantum efficiency at a specific excitation wavelength (λ) (Chapin *et al.*, 1954). The following equations are used to determine its value (as a function of λ) in the event of a short circuit (Calogero *et al.*, 2012).

$$IPCE = 1240 \text{ (ev nm)} \frac{J_{sc} [\text{mA cm}^{-2}]}{\lambda [\text{nm}].\Phi(\lambda) [\text{mW cm}^{-2}]} \quad (13)$$

The photon flux of monochromatic light is referred to as in $\Phi_{in}(\lambda)$. Therefore, one way to express IPCE is in terms of light harvesting efficiency [$LHE(\lambda)$], the quantum yield of electron injection Φ_{inj} from the excited state of sensitizer to semiconductor CB and collecting efficiency Φ_{coll} of an injected electron at the front electrode is as follows:

$$IPCE = LHE(\lambda)\Phi_{inj}\Phi_{coll} \quad (14)$$

when the $LHE(\lambda)$ is provided by:

$$LHE(\lambda) = 1 - 10^{-A} \quad (15)$$

where the exponent A is the dye absorbance or optical density, the product $(\Phi_{inj}\Phi_{coll})$, is the absorbed photon to current conversion efficiency [$APCE(\lambda)$] or internal quantum efficiency (IQE). Finally, Φ_{inj} is given by Nazeeruddin *et al.* (1993):

$$\Phi_{inj} = \frac{k_{inj}}{k_r + k_{nr} + k_{inj}} \quad (16)$$

where k_{inj} is the rate constant for Φ_{inj} into the semiconductor, while k_r and k_{nr} represent the radioactive and nonradiative rate constant, respectively. Thus, the IPCE is directly correlated to the absorption properties and the amount of adsorbed sensitizer on the semiconductor surface (or LHE) as well as the Φ_{inj} and Φ_{coll} .

(v) Energy conversion efficiency (η)

It is defined as the ratio of the electrical power output at its maximum (P_{\max}) to the energy of the incident light (P_{light}). It is the final determinant of DSSCs device performance, and its value is determined by a variety of photovoltaic parameters, as depicted in Fig. 8. The following equation can be used to forecast it:

$$\eta = \frac{P_{\max}}{P_{\text{light}}} = \frac{V_{\text{oc}} \cdot J_{\text{sc}} \cdot FF}{P_{\text{light}}} \quad (17)$$

(vi) Importance of figures of merit

The figure of merit is determined by the primary characteristic that makes something fit for a specific purpose. It helps to achieve efficiency and effectiveness of the device system. It also helps in interpreting the validity of the result. However, in a well-respected journal, a result without a reliability statement cannot be published or communicated because it is not a result (De Bièvre, 1997). Additionally, figures of merit are essential components of the analytical validation process. The development of new multiway analytical methods demands estimation of the corresponding analytical figures of merit to compare with previously existing methodologies as well as results and to report detection capabilities and other essential features (Olivieri & Faber, 2009). To the present work, it is of significance to further studies to search for the all-possible theoretical tools, including theories, formulas, calculations, and concepts, which can optimise for the prescribed figures of merits and allow a comparison with the experimental figure of merits.

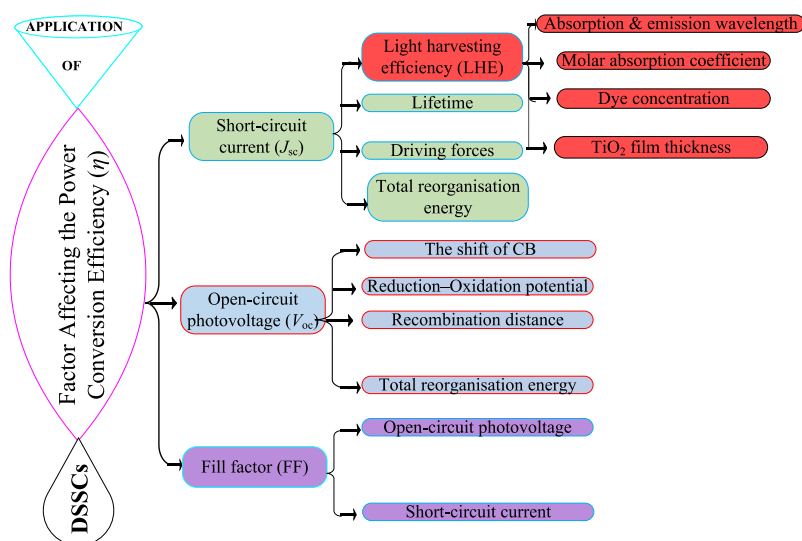


Figure 8: Factor affecting the power conversion efficiency (η)

1.1.9 Issues on the stability of DSSCs

Close scanning has been used to determine the stability of the four components of as DSSCs, namely the dye sensitiser, the counter electrode, the electrolyte, and the semiconducting oxide. A sensitiser for DSSCs capable of converting standard global AM 1.5 sunlight to energy should absorb all light with λ_{\max} below 920 nm. Thus, continued scientific study to improve future technology's efficiency and long-term stability is essential to deliver on the promises of future technology (Grisorio *et al.*, 2013). A DSSCs device must remain applicable for a minimum of 20 years without deteriorating performance. The photostability of the DSSCs sensitiser material must be sufficient to withstand numerous redox cycles without decomposition and contain attachment groups such as phosphate or carboxylate to rapidly graft it to TiO₂ oxide (Grätzel, 2004). The dye attachment group must create a layer spontaneously on top of the oxide coating. The photon absorption process disperses this molecular dye layer, and the dye molecule relaxes when the excited electron is injected into the mesoporous conduction band. However, because the absorption of a single dye monolayer is low, it is impossible to create a highly efficient sensitising device, assuming that smooth substrate surfaces are required to avoid the recombination loss mechanism associated with polycrystalline (rough) structures in solid-state photovoltaics. The charge recombination barrier exists because the dye molecule layer, an insulator in the ground state, separates the electron created in the semiconductor lattice from the positive charge carriers. Using nanocrystalline with thin films with a roughness factor greater than 1000 has become routine practice (Grätzel, 2003).

The structure of the dye employed as a sensitiser impacts the stability, performance, and efficiency of DSSCs, which occurs when the structure of the pigment has a longer R group, leading to the formation of a steric hindrance for the pigment molecules to build a link with TiO₂ surface. This technique efficiently stops the molecule from arraying on the semiconductor TiO₂ thin film, hence causing reduced electron transfer from the dye molecules to the TiO₂ conduction band (Ho *et al.*, 2011). The wavelength of the dye's absorption and intensity also affect the cell's stability and performance. The solvent used to extract natural dyes also affects the stability and performance of DSSCs (Aduloju *et al.*, 2011). The performance and stability of DSSCs sensitisers are determined using plant extracts from various species.

1.1.10 Promising motivation

Natural pigments can be employed as sensitisers in place of metal complexes or organic dyes in DSSCs. They are more environmentally friendly, less expensive, have a simple extraction technique, and are more commonly available than metal complexes or organic dyes. The primary disadvantages of DSSCs based on natural dyes are their inefficiency and instability. Therefore, additional research and development in these areas are required before these technologies may be put to practical use and become commercially viable. Because the efficiency remains relatively low despite repeated tries, the mixed dye system compensates for various probable types of interaction that may result in increased charge injection upon sensitisation. Undoubtedly, current output is restricted by the amount of “free” electrons accessible from exposed dyes. Increased photocurrent can be achieved by either providing dye additives that act as electron donors and form complexes with the dye or by adding co-adsorbents that inhibit electron recombination with the electrolyte, favouring charge injection. Simple adjustments and greater purification of existing natural pigments are easily accomplished by incorporating new techniques into the DSSCs construction process. This could open up new research avenues for improving the device’s efficiency and stability.

1.2 Statement of the problem

The DSSCs have gained widespread attention due to their advantageous characteristics, such as production costs, ease of fabrication process and tuneable optical properties. As a charge transfer mediator, a sensitiser plays a crucial role in solar cells. Therefore, great efforts were made to seek efficient dyes for advanced and stable DSSCs performance. Natural pigments were considered a promising alternative to synthetic sensitisers because of their simple preparation technique, low cost, availability and environmental friendliness. Betacyanins are natural red pigments that might suit the DSSC application. However, one of the drawbacks of these dyes is their low stability, which may lead to a deterioration of the solar cell.

The present study considers different conformational isomers of betanidin aimed at understanding the instability of the dyes through a thermodynamic approach. A combination of the betanidin natural dye and selected organic sensitiser L0 is proposed through a theoretical quantum chemical approach to improve the sensitisers' optoelectronic properties. It is essential to conceive the internal properties of the materials under investigation at the molecular level before embarking on experiments.

1.3 The rationale of the study

Betanidin belongs to the betalains pigments, which comprise high molar extension coefficients in the visible region and possess pH-reliant redox properties (Calogero *et al.*, 2010). In that sense, betalains pigments represent an additional class of dyes of potential interest. Similar to anthocyanins, betalains pigments demonstrate light absorption in the visible region and are antioxidant compounds (Azeredo, 2009; Calogero *et al.*, 2012; Stintzing & Carle, 2007). On the other hand, while in anthocyanins, there is the functional group (–OH), betalains contain the essential functional groups (–COOH) to bind better to the TiO₂ nanoparticle (Calogero *et al.*, 2010; Calogero *et al.*, 2012; Qin & Clark, 2007; Zhang *et al.*, 2008). The stronger electronic coupling and rapid forward and reverse electron transfer reaction due to the interaction of the TiO₂ nanoparticle films and (–COOH) (Calogero *et al.*, 2012) is of significance compared to that of (–OH) groups.

The distinctive performance embedded from different geometrical structure isomer to either bent or planar. This variation resulted in a significant change of molecular properties to the different spectro-electrochemical and optoelectronic properties. Therefore, the interpretation of physicochemical properties was essential. That is why the thermodynamic and optoelectronic properties were investigated. The betanidin with bent structure was selected for further studies at the molecular level. The structure was tried to be improved by forming the complex with synthetic L0 dye through an esterification reaction. A thorough understanding of the stable geometrical structure and feasible thermodynamic functions of the materials at the molecular level is of significance. It enables the explanation of the unique properties and phenomena of existing bent (non-planar) or planar materials and the design of new materials with desired properties. The present findings from simulation and modelling studies demonstrate a relationship between the unique properties of materials and their molecular structure. Further progress in the study considers the dimerisation of the betanidin through etherification and esterification to the formation of oxane and acid anhydride complex to the dimerised product.

1.4 Research objectives

1.4.1 Main objective

To investigate betanidin conformers and design their complexes with selected organic sensitiser L0 in order to improve optoelectronic properties towards dye-sensitised solar cell application.

1.4.2 Specific objectives

- (i) To examine the isomerisation and decarboxylation reactions of the betanidin molecules aimed at the dyes' instability analysis through a thermodynamic approach.
- (ii) To design complexes through a combination of the betanidin and L0 dye.
- (iii) To investigate geometrical structure, vibrational and electronic spectra and thermodynamic properties of the betanidin and decarboxylated betanidin and the designed complexes with the L0 dye.

1.5 Research questions

- (i) Which isomers of the betanidin may occur and what is their thermodynamic stability?
- (ii) Which combination between the betanidin and L0 dyes will bring to complexes with improved optoelectronic properties?
- (iii) What are geometrical structures, vibrational and electronic spectra and thermodynamic properties of the dyes?

1.6 Significance of the study

The present study helps to understand the limited information from the practical experiments which were previously conducted and offers the desired properties to further proposed experimental investigations. Also, there is insufficient information for the theoretical simulation and modelling of the betacyanins; for example, the reorganisation energy was unreliable (Qin & Clark, 2007). Qin and Clark (2007) confirm the reason for the unavailability of optoelectronic properties of betacyanins. The present work provides a possible way to obtain the stable bent conformer. The study helps to acquire optoelectronic

properties of betacyanins. It is based on theoretical work due to the reliable data of the reorganisation energies.

However, the main material is from plant products such as betacyanin is being improved with synthetic dye L0 in one of the strategies via specific objective two; both are organic materials. Organic dyes are easy to synthesise compared to inorganic dye materials. The molar extinction coefficients of organic dyes are higher than metal-based dyes. Using both natural betacyanins and L0, which offer environmentally friendly materials, significantly avoids the risk of exposure to poisonous materials like ruthenium.

1.7 Delineation of the study

In order to propose the desired properties to the materials, the investigation of the stable feasible conformers, their thermodynamic functions, optical and electrochemical features is need. The research on these stated essential properties of the materials was carried out using computational approaches. The obtained results were compared with the benchmark available information for critical significance analysis of the particular property. Generally, this dissertation is divided into five chapters. Chapter one consists of the background information, statement of the research problem, the study's rationale, objective, research questions, and significance. Chapter two presents the literature review, which details the betalain's stability to the DSSCs application. Chapter three presents the theoretical tools, methods and techniques used to investigate the isolated dyes and the proposed complex to the energy technology application. Chapter four presents the results and discussions, which are detailed into four sections which are as follows.

Firstly, the study searched the two stable equilibrium betanidin molecular structures planar and bent. The bent structure succeeded in further optoelectronic properties investigations. Secondly, combining the synthetic dye L0 with betanidins predicts improvement of the optoelectronic properties compared to individual betanidins. The combination was analysed based on the two available positions of the (–OH) group present at the betanidin backbone of the molecular structure. Chapter five marks the conclusion and recommendations for the conducted study.

CHAPTER TWO

LITERATURE REVIEW

2.1 Introduction

Betalains as vegetable dyes symbolise one more class of water-soluble (Brockington *et al.*, 2015; Timoneda *et al.*, 2019), to be light absorbers in DSSC technology due to great interest experienced for their scientific potentiality (Calogero *et al.*, 2010; Hernandez-Martinez *et al.*, 2011). The attained betalains dye belongs to Caryophyllales, and some Basidiomycota plants help to define the colour of their flowering plants (Cronquist & Takhtadzhian, 1981; Strack *et al.*, 2003). The basic structure of betalains is made up of four groups of compounds. This may lead to discrepancies in the dye's photochemistry and photophysics: betalamic acid, betacyanins, betaxanthins and indicaxanthin. Nevertheless, betalains illustrate the class of materials to which the mentioned four groups belong. Anthocyanins have not yet been found in betalains containing pigment plants, although they are widespread in the most variety of plants. The vegetable dye from the plants, for instance, purple corn, elderberry, red oranges, blueberries, red cabbage, blackberries, mango, grapes, red onion, eggplant (aubergine), black rice and red radicchio are the most important sources of the anthocyanins (Calogero *et al.*, 2012).

Moreover, in the order of Caryophyllales plants, red beetroots (*Beta vulgaris*) and cacti fruits belong to the genus *Opuntia*. The order is the outstanding acknowledged source of betalains. Therefore, betanin from betacyanins and indicaxanthin from betaxanthins are their primary pigments (Felker *et al.*, 2008; Hempel & Böhm, 1997). The other discovery of the novel sources characterised the contents of the betalains, for instance, the tubers from *Ullucus tuberosus* (Svenson *et al.*, 2008) or the betalain consisting of berries of *Rivina humilis* (Khan *et al.*, 2012). In 2017, multiple shades of quinoa grains (*Chenopodium quinoa*) were reported to possess betacyanins and betaxanthins (Escribano *et al.*, 2017).

Since both betalains and anthocyanins belong to the group of nitrogenous plant pigments (Piattelli *et al.*, 1964; Wyler & Dreiding, 1957) but are never found in the same plant. The colour properties of the betalains proved to be a novel family of pigments different from the anthocyanins, although both are nitrogenous plant pigments (Piattelli *et al.*, 1964; Wyler & Dreiding, 1957). However, fifteen years ago, the first natural fluorescence of the betalains was reported (Gandía-Herrero *et al.*, 2005c), and light emission was exhibited in the plant

tissues that contain them, along with flowers (Gandía-Herrero *et al.*, 2005a; Gandía-Herrero *et al.*, 2005b). The promising bioactive properties of the betalains are also achieved in recent years. The betalains purified from beetroot were revealed from early investigations to have strong free radical scavenging capacity (Escribano *et al.*, 1998). The following research showed the existence of an intrinsic activity extant in all betalains (Gandía-Herrero *et al.*, 2010; Gliszczyńska-Świgło *et al.*, 2006), modulated explicitly by structural factors. The introduction of the betalains fluorescence announces new fields and development on the existing fields in the ongoing research due to the applications of these pigments. Since the phenomenon was first discovered (Gandía-Herrero *et al.*, 2005c), the overtaking of the initial expectations has been realised. The fluorescence will contribute to understanding photophysics, charge transfer, and optoelectronic properties to develop the DSSCs technology.

2.2 Paradigm

We have observed the development of massive amounts of theoretical and experimental data, as depicted in Fig. 9, in various fields of knowledge over the previous three decades. Such a wealth of data is conceivable in computational materials science due to the success of density functional theory and the rapid development of computational capabilities. On the other hand, advancements in instrumentation and electronics have made it possible for experiments to generate vast amounts of data. As a result of the high-throughput (HT) method, we have amassed a massive amount of theoretical and experimental data; the logical next step is the development of unique tools capable of extracting knowledge from such data. Among these tools, the discipline of statistical learning originated the term “machine learning” techniques, which are currently guiding research toward a new paradigm of data-driven science.

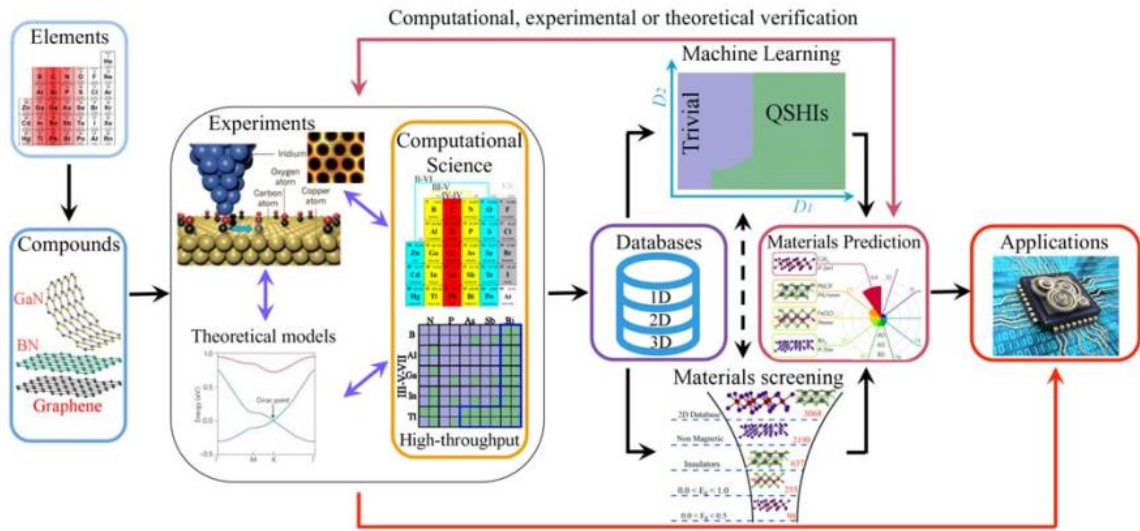


Figure 9: The conceivable atomic combinations result in a large number of molecules that can be explored experimentally, theoretically, or computationally, most notably through high-throughput simulations. Figure from pictures (Polini *et al.*, 2013); experiments from (Acosta *et al.*, 2018); computational science and machine learning from (Mounet *et al.*, 2018); whole Figure from (Schleder *et al.*, 2019)

2.2.1 Scientific research paradigm

The paradigm of scientific research aids in the definition of scientific research philosophy. Additionally, the scientific research paradigm is defined by a definite technique comprised of numerous steps. After completing the processes mentioned above, the researcher establishes a connection between the research objective and the research questions. The phrase paradigm is synonymous with the concept of ‘normal science’. Materials Scientists working inside the same paradigm framework adhere to the same rules and standards for scientific practice. That is how the scientific community sustains itself.

A new research paradigm is being developed concerning how we generate knowledge. According to Thomas Kuhn (Kuhn, 1962), a paradigm is an established technique of questioning the world and integrating knowledge shared by many scholars in a discipline at any time (Kuhn, 1962). The scientific research paradigm is the way of thinking or approaching the research, the research process, and the method of execution. It is not a methodology but rather a philosophy that guides the research process, i.e., drives it in a specific direction. All research paradigms are defined by ontology, epistemology, and methodologies (Alghamdi & Li, 2013; Creswell, 2007; Guba & Lincoln, 1994), as illustrated in Table 1.

Table 1: The components of the research paradigm

C/N	Component	The theoretical and methodological principles on which specialised study is based:
1	Ontology	The existence theory is a concept about the nature of reality based on a particular paradigm assumption about reality and truth. The dye molecule has a unique geometry; the challenge is determining which geometry is stable under which conditions. It marks the start of our investigation into the stable geometry of the betanidin dye molecule.
2	Epistemology	The theory concerns how the materials researcher can acquire knowledge about the phenomena of interest to them, specifically with analyses of what distinguishes a reasonable certainty from an opinion. After obtaining the stable conformer, the possibility of other conformers was investigated. Additional improvement to the dye molecule occurs via the design of dye complex molecules.
3	Research Methodology	It encompasses the systematic methods, procedures, and tools used to collect and analyse data. Numerous computational methods and tools have been considered. It includes softwares such as Firefly, Gaussian and VASP that employ a variety of analytical methodologies. It helps to account for the varied thermodynamic and optoelectronic properties.

2.2.2 The paradigm of choice in a materials science and engineering study

Novel materials allow for developing technical applications essential for resolving societal problems. No matter how hard it is to measure the historical influence of materials discoveries, from the Stone Age through the Bronze and Iron Ages and until the present silicon technologies, it is easy to appreciate their impact on society (Jain *et al.*, 2016). In addition, two-thirds of all advances in computation were enabled by materials research, which also altered other industries, such as energy storage (Magee, 2012).

There is an estimated 20 years delay between the invention and commercialisation of new technologies based on innovative materials (Eagar, 1995). It is also difficult to replace

materials once they are integrated into an existing process because of the high costs of establishing large-scale manufacturing infrastructures (Curtarolo *et al.*, 2013). That is evident in the semiconductor industry, where silicon is a constant reminder. Because of this, introducing new materials for a particular sector is becoming increasingly critical to its success, and various new technical niches need new materials.

2.3 Applicability of betalains

As a source of betalains product, beetroot is one of the essential vegetables obtained in a taproot portion of the beet plant. Therefore, it has been researched to provide applications in several industries (Fig. 10) likely to dyeing acrylic fabric, medicinal issues, food and cosmetics, dietary supplements, photoprotectors, sensors, functional food and dye-sensitised solar cells (DSSCs), to mention but a few discussed in this review. All these applications benefit from the best conformational structure of the betalains products they offer. Therefore, the studies of the conformer structures concerning activity are significant.

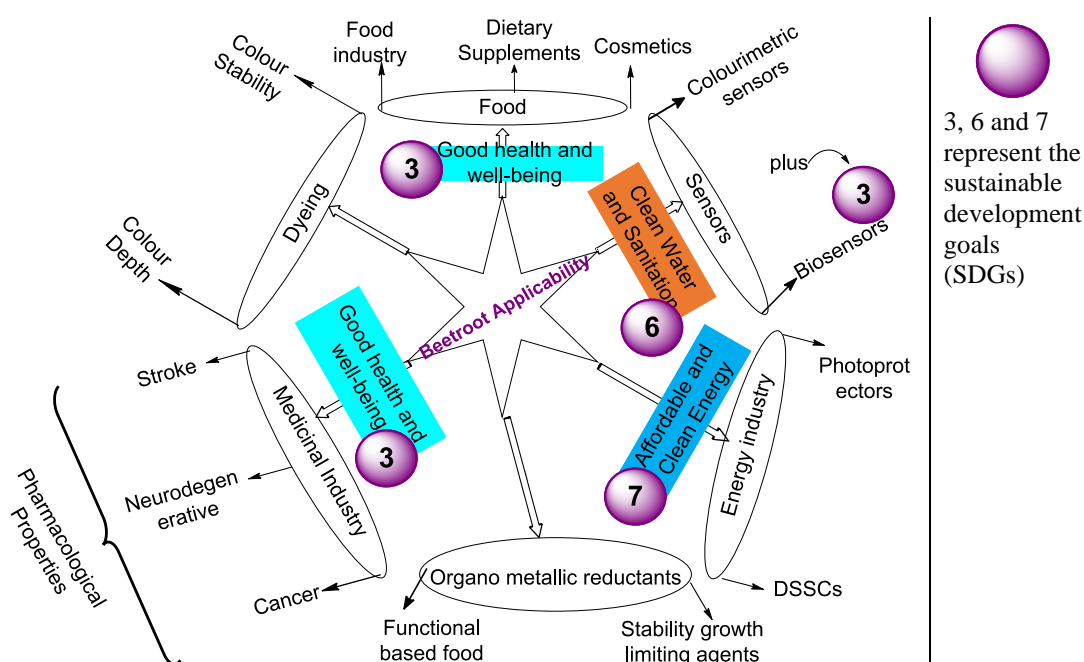


Figure 10: Summarises the different beetroot pigment uses that may contribute to achieving sustainable development goals (SDGs)

2.3.1 Dyeing acrylic fabric

Natural betanin dye can hold against synthetic alternatives regarding colour depth, shade, and fastness. A study by Guesmi *et al.* (2012) evaluated the effect of dye bath pH, salt concentration, dyeing time, and temperature on the dyeing of betanin on modified acrylic fabrics. Conventional heating was used to dye modified acrylic fabric in a dye bath containing sodium chloride (0-15 g/L) and a dye concentration of 30 mg/L with a 40:1 liquor ratio.

2.3.2 Medicinal issues

Betanin has been shown to have antioxidant properties in biological lipids, such as lipoproteins of low density, whole cells, and membranes (Vieira Teixeira da Silva *et al.*, 2019). In addition, Betanin has attracted researchers for its anti-inflammatory and hepatic safety activities in whole cells (Khan, 2016). In addition, betanin regulates the redox-mediated signal transduction pathways essential for inflammatory responses, and it has also been shown to have antiproliferative effects on human tumour cell lines (Gentile *et al.*, 2004; Kapadia *et al.*, 2011; Reddy *et al.*, 2005). Furthermore, betanin promotes the translocation of the antioxidant response element (erythroid 2-related factor 2 (Nrf2)) from the cytosol to the nuclear domain in both tumoral and healthy human hepatic cell lines. This element regulates the mRNA and protein levels of antioxidant/detoxifying enzymes, including heme oxygenase-1, NAD(P)H quinone dehydrogenation-1 and glutathione S-transferase (Krajka-Kuźniak *et al.*, 2013). Anti-diabetic properties are also present due to their ability to regulate the activity of liver enzyme markers (Amjadi *et al.*, 2018; Dhananjayan *et al.*, 2017; Sutariya & Saraf, 2017).

2.3.3 Natural dyes in the food industry (E162) and cosmetics

Using natural plant extracts containing betacyanin pigment as a safe alternative to synthetic food colourants is rising. For example, beetroot powder with high betanin content is allowed as a natural red food colourant in the United States under Title 21 of the Code of Federal Regulations, Part 73.40, and under the E-162 code of the European Union (Rahimi *et al.*, 2019a). Several factors can affect the stability and appearance of food products, including the presence and composition of betacyanin degradation products. Low acidic and neutral foods can be dyed with betalains, stable at pH between 3 and 7. Ascorbic acid can also help to keep them stable.

In contrast, anthocyanins in the colouration of such foods are impossible because of their instability at pH levels above 3. Additionally, ascorbic acid promotes anthocyanin degradation. For these reasons, betalain pigments appear preferable to anthocyanins when colouring vitamin C-rich foods or products (Kezi & Sumathy, 2014; Kujala *et al.*, 2002). Dairy products, tomato soup, sauce, paste, desserts, jams and jelly beans can benefit from beetroot extract to bring out the red colour. They are also used to keep meat fresh and prevent it from going bad (Martínez *et al.*, 2006). However, a membrane process is required for commercial red beet application because of the unpleasant flavour of beetroot extract due to their geosmin and pyrazine derivatives content (Stintzing & Carle, 2007).

2.3.4 Dietary supplements

Betalains are also considered natural dietary supplements because of their health benefits (Fu *et al.*, 2020). Results showed that betalain-rich extracts (betalain-rich red beet supplement and betacyanin-rich *Opuntia strica* supplement) affected atherosclerotic risk factors in patients with coronary heart disease. In the 48 patients studied, glucose levels, total cholesterol, homocysteine, triglyceride, and low-density lipoprotein (LDL) were lower. In addition, supplements containing betalain and betacyanins, taken at a safe dose of 50 mg each for two weeks, reduced systolic and diastolic blood pressure (Rahimi *et al.*, 2019b). Quinoa (*Chenopodium quinoa* Willd) has been used in various food and nutraceutical products over the past two decades. Quinoa supplementation has been shown to significantly impact humans' cardiovascular, gastrointestinal, and metabolic health in clinical trials (Graf *et al.*, 2015).

2.3.5 Photoprotectors

Betanin's photophysical properties in aqueous and alcoholic solutions were analysed, and the formation of betanin electronically excited species was investigated. In water, betanin has a short S_1 state lifetime (π, π^*) (6.4 ps), primarily due to the efficient $S_1 \rightarrow S_0$ radiationless relaxation, which probably requires a great geometric change. Photoproduct formation and intersystem crossing have been reported to be nearly non-existent between S_1 and T_1 systems. In order to support the idea that betanin is a photoprotector in vivo, a rapid light-to-heat conversion was observed in the absence of triplet excited state formation (Wendel *et al.*, 2017; Wendel *et al.*, 2015). The phenolic moiety in the betanin structure enables the colourimetric detection of reactive oxygen species. Betanin is an efficient quencher of singlet

oxygen when dissolved in deuterated water. Betanin's ability to scavenge $^1\text{O}_2$ corroborates its photoprotective properties (Wendel *et al.*, 2016).

2.3.6 Beetroot pigment-based colourimetric sensors

Copper ions detection in drinking water was developed. Additionally, this resulted in an Android-based smartphone application for quantitative and visual colourimetric analysis being developed. When the Cu^{2+} concentration in drinking water increased, the red beet pigment solution gradually changed colour from bright purple to orange-red as it chelated Cu^{2+} and formed a complex. This detection system had a linear range of 4 to 20 μM and a detection limit of 0.84 μM (Cao *et al.*, 2019).

2.3.7 Betalain-based biosensors

Biosensors based on betalain are being developed that are inexpensive, environmentally friendly, and easy to use. *Bacillus* species are good examples of the importance of early detection. As a result of the 2001 anthrax attack, the highly virulent *B. anthracis* has been classified as a bioterrorism agent (Sanderson *et al.*, 2004). In addition, *B. cereus*, a food-borne pathogen, poses a threat (Gould, 1977). Therefore, efforts have been made to use betanin as a ligand in the new europium (III) complex, which is sensitive to calcium dipicolinate CaDPA (the major component of the bacterial spore core). Betanin was converted into a water-soluble, non-luminescent orange complex when Eu (III) ions were present. The $[\text{Eu}(\text{betanin})^+]$ aqueous solution turns magenta when CaDPA is added. The CaDPA detection limit is approximately $2.06 \times 10^{-6} \text{ mol L}^{-1}$. It is also sensitive to CaDPA but not to other aromatic, pyridinic and acidic ligands structurally similar to CaDPA (Gonçalves *et al.*, 2013; Guerrero-Rubio *et al.*, 2020).

2.3.8 Functional plant-based food

Researchers are considering using beetroot extracts as a mild alternative to organometallic reductants such as NaBH_4 and as stabilising agents (growth-limiting). The bottom-up synthesis of metal nanoparticles led to a wide range of particle sizes and shapes (Fernandes *et al.*, 2016).

2.3.9 Dye-sensitised solar cells

As an alternative to dyes made from ruthenium complexes, natural plant pigments have been tested in solar cell applications (Calogero *et al.*, 2012; Shahid *et al.*, 2013) for their affordability, speed, low energy consumption, and environmental friendliness, as illustrated in Table 2. Betanin, 2,17-bidecarboxy-betanin, vulgaxanthin I, extracted from red beetroot extract, and betanidin-6-O-(6',6''-di-O-E-4-coumaroyl)- β -sophoroside from Bougainvillea were also tested for use in dye-sensitised solar cells (DSSCs). When TiO₂ electrodes are immersed in an acidic solution at pH \sim 3 containing betalains, the carboxylic groups in betalains serve as anchoring groups for the betalains, enabling the construction of DSSCs. Betacyanin and betaxanthin-based DSSCs have a quantum yield of electron injection of about 50% and 70%, respectively. For betaxanthin-based DSSCs, the total sunlight conversion efficiency was due to a blue-shifted absorption band. In this process, only two electrons are injected from betanin to TiO₂ (Knorr *et al.*, 2014; Knorr *et al.*, 2015).

Table 2: Based on DSSCs, photo-electrochemical data for betalains

Betalains (Fruits and Vegetables)	J_{sc} (mA cm ⁻²)	V_{oc} , mV	η	References
Red beet	2.90	400	0.44	Zhang <i>et al.</i> (2002)
	2.42	440	0.67	Zhang <i>et al.</i> (2008)
	13.91	360	2.71	Sandquist and McHale (2011)
Red turnip	9.50	425	1.70	Calogero <i>et al.</i> (2010)
Sicilian Indian fig.	2.70	375	0.50	Calogero <i>et al.</i> (2010)
Wild sicilian prickly pear	9.40	350	1.26	Calogero <i>et al.</i> (2010)
Wild sicilian prickly pear	8.80	389	2.06	Calogero <i>et al.</i> (2012)
Bougainvillea	2.10	300	0.36	Calogero <i>et al.</i> (2010)
Red Bougainvillea glabra (RBG)	2.34	260	0.45	Hernandez-Martinez <i>et al.</i> (2011)
Violet Bougainvillea spectabilis (VBG)	1.86	230	0.31	Hernandez-Martinez <i>et al.</i> (2011)
Purified red BG	2.33	260	0.49	Hernandez-Martinez <i>et al.</i> (2011)
Red Bougainvillea spectabilis (RBS)	2.29	280	0.48	Hernandez-Martinez <i>et al.</i> (2011)
Bougainvillea spectabilis (BS)	1.88	250	0.35	Hernandez-Martinez <i>et al.</i> (2011)
Bougainvillea spectabilis (BS)	2.34	260	0.45	Hernandez-Martinez <i>et al.</i> (2011)

CHAPTER THREE

MATERIALS AND METHODS

3.1 Electronic structure prediction

The materials sciences and engineering area's susceptible demands nowadays are the properties' use, understanding, and prediction. They consider tracking how to synthesise materials of marked and target required properties. The field of computational chemistry/biology/physics methods is essential for predicting the properties and characteristics of the various phase structure of the materials like liquids, gaseous, and solids, to mention a few. The methods provide a high level of accuracy of the predicted properties. They contribute to the popularity of computational methods in diversified disciplines linked with energy, health, waste and environmental pollution (Andreoni & Yip, 2020). Multiscale materials modelling is acquired in several schemes considering its ability to connect a system's descriptions at numerous length scales; from the atomic to the molecular level, like the electronic structure's description to the microscopic scale→mesoscopic scale→macroscopic scale (Andreoni & Yip, 2020). The linking between theory and experiment will likely prompt cost-effective investigations so society can pay off the gain obtained in materials designed and innovation. This dissertation comprises research questions, computation and simulation, and then achieved materials demonstrate desirable properties which can further be imposed in the physical environment through experiments.

3.1.1 Quantum mechanics, Schrödinger equation

In the early 19th Century, the discovery of exciting phenomena like energy quantisation and wave-particle duality of light was considered. Suddenly, many considerable contributions were endorsed in quantum mechanics' evolution; Erwin Schrödinger contributed in 1926. He recommended that a physical system is illustrated thoroughly by a wave function Ψ . Although typically no physical property perhaps peaked straight from Ψ , the product between Ψ and its complex conjugate Ψ^* ($\Psi^*\Psi = |\Psi|^2$) suggests a probability density. However, the probability of obtaining a particle specified by Ψ in a volume element dr is accorded by:

$$\rho(r) = |\Psi(r)|^2 dr \quad (18)$$

By bearing in mind the normalisation criterion, the probability of obtaining a particle within the region must be equal to a unit.

$$\int |\Psi|^2 d\tau = \langle \Psi | \Psi \rangle = 1 \quad (19)$$

where the integral about $d\tau$ signifies the integration over the entire space, and the wave function can be achieved by solving the time-independent Schrödinger equation:

$$\hat{H}\Psi = E\Psi \quad (20)$$

where \hat{H} are the Hamiltonian or energy operator and consists of kinetic and potential energy terms; E is the system's total energy. In order to simulate a chemical system consisting of N interacting electrons and M nuclei, the Schrödinger equation's solution cannot be found via analytical methods. Instead, the many-body wave function $\Psi(\{r_i\}, \{R_A\})$ is used to interpret quantum state of the system. This wave function Ψ be influenced by the electronic coordinates $\{r_i\}$ and the nuclear coordinates $\{R_A\}$ and is the solution of the time-independent Schrödinger equation (Schrödinger, 1926). The Hamiltonian is expressed as:

$$\hat{H} = \hat{T}_e + \hat{T}_A + \hat{V}_{Ae} + \hat{V}_{ee} + \hat{V}_{AA} \quad (21)$$

with:

N : number of electrons

M : number of the nucleus

r_i : electronic coordinate

R_A : nuclear coordinate

M_A : a mass of the nucleus A

Z_A : atomic number of the nucleus A

$$\hat{T}_e = -\sum_{i=1}^N \frac{\hbar^2 \nabla_i^2}{2m_e} : \text{kinetic energy of electrons}$$

$$\hat{T}_A = -\sum_{A=1}^M \frac{\hbar^2 \nabla_A^2}{2M_A} : \text{kinetic energy of nuclei}$$

$$\hat{V}_{Ae} = -\sum_{i=1}^N \sum_{A=1}^M \frac{e^2 Z_A}{|\mathbf{r}_i - \mathbf{R}_A|} : \text{attractive energy between electrons and nuclei}$$

$$\hat{V}_{ee} = \sum_{i=1}^N \sum_{j>1}^N \frac{e^2}{|\mathbf{r}_i - \mathbf{r}_j|} : \text{repulsive energy between electrons}$$

$$\hat{V}_{AA} = \sum_{A=1}^M \sum_{B>A}^M \frac{e^2 Z_A Z_B}{|\mathbf{R}_A - \mathbf{R}_B|} : \text{repulsive energy between the nuclei}$$

Hence the Schrödinger equation can be expressed as:

$$\left[-\sum_{i=1}^N \frac{\hbar^2 \nabla_i^2}{2m_e} - \sum_{A=1}^M \frac{\hbar^2 \nabla_A^2}{2M_A} - \sum_{i=1}^N \sum_{A=1}^M \frac{e^2 Z_A}{|\mathbf{r}_i - \mathbf{R}_A|} + \sum_{i=1}^N \sum_{j>1}^N \frac{e^2}{|\mathbf{r}_i - \mathbf{r}_j|} + \sum_{A=1}^M \sum_{B>A}^M \frac{e^2 Z_A Z_B}{|\mathbf{R}_A - \mathbf{R}_B|} \right] \Psi = E\Psi \quad (22)$$

The raised Schrödinger equation is challenging to deal with it. Therefore, it is unavoidable to propose beneficial approximations to meet an approximate solution to this equation. One of the approaches is termed to be the Born-Oppenheimer approximation (Born & Oppenheimer, 1927). This approach depends on the evidence that the nuclei are much more abundant than the electrons (about 1800 times more massive), and the kinetic energy of nuclei is much lesser than the electron's kinetic energy. Later the nuclear kinetic energy was conceivably ignored when determining the electronic problem. This approach approves us to alienate the kinetic energy of the electrons and the nucleus in solving the electrons' dynamics in a “frozen” nuclei configuration. The total wave function thus develops into:

$$\Psi(\{r_i\}, \{R_A\}) = \Psi(\{r_i\}) \times \Psi(\{R_A\}) \quad (23)$$

$$H_e \Psi(\{r_i\}) = E_e \Psi(\{r_i\}) \quad (24)$$

where:

$$H_e = -\sum_{i=1}^N \frac{\hbar^2 \nabla_i^2}{2m_e} - \sum_{i=1}^N \sum_{A=1}^M \frac{e^2 Z_A}{|\mathbf{r}_i - \mathbf{R}_A|} + \sum_{i=1}^N \sum_{j>1}^N \frac{e^2}{|\mathbf{r}_i - \mathbf{r}_j|} + \sum_{A=1}^M \sum_{B>A}^M \frac{e^2 Z_A Z_B}{|\mathbf{R}_A - \mathbf{R}_B|}$$

Though solving this equation is crucial, more simplification is desired to avoid a hard time. The considered electrons in the system are acquainted with complying with the anti-symmetry property and the Pauli Exclusion Principle via Slater Determinant (Slater, 1929). Hence the wave function Ψ is not noticeable and $|\Psi(\vec{x}_1, \vec{x}_2, \dots, \vec{x}_N)|^2 d\vec{x}_1 d\vec{x}_2 \dots d\vec{x}_N$ is the probability of finding an electron at a given point in space $d\vec{x}_1 d\vec{x}_2 \dots d\vec{x}_N$. Therefore, the electrons are identical, and the exchange of the two electrons changes only the sign of the wave function:

$$\Psi(\vec{x}_1, \vec{x}_2, \dots, \vec{x}_N) = -\Psi(\vec{x}_2, \vec{x}_1, \dots, \vec{x}_N) \quad (25)$$

Nevertheless, the probability stands invariable:

$$|\Psi(\vec{x}_1, \vec{x}_2, \dots, \vec{x}_N)|^2 = |\Psi(\vec{x}_2, \vec{x}_1, \dots, \vec{x}_N)|^2 \quad (26)$$

The appointed wave functions (spin orbitals) for some electrons can be reported as $\chi_i(x_i)$. In this situation, the N-electron system is conceivably expressed by an anti-symmetrised product ϕ_{SD} (Slater Determinant) which is expressed as:

$$\phi_{SD} = \frac{1}{\sqrt{N!}} \begin{vmatrix} \chi_1(x_1) & \chi_2(x_1) & \cdots & \chi_N(x_1) \\ \chi_1(x_2) & \chi_2(x_2) & \cdots & \chi_N(x_2) \\ \vdots & \vdots & \ddots & \vdots \\ \chi_1(x_N) & \chi_2(x_N) & \cdots & \chi_N(x_N) \end{vmatrix} \quad (27)$$

3.1.2 Hartree-Fock method

Determining the N-body wave function and the system's energy is troublesome. In this examination, the Hartree-Fock method (HF) method (Brillouin, 1934; Fock, 1930; Hartree & Hartree, 1935; Slater, 1930) is familiarised to facilitate the prediction by calculating each electron's energy in the equated static field. The Fock Hamiltonian can be expressed as:

$$f_i = -\frac{1}{2} \nabla_i^2 - \sum_k^{core} \frac{Z_k}{r_{ik}} + V_i^{HF} \quad (28)$$

Hartree-Fock potential, V_i^{HF} revealing the average repulsive potential of one electron to the other N-1 electrons. It can be expressed as:

$$V_i^{HF}(\vec{x}_1) = \sum_i^N (\hat{J}_i(\vec{x}_1) - \hat{K}_i(\vec{x}_1)) \quad (29)$$

of which \vec{x}_1 is the position of one electron, \vec{J}_i is the coulomb operator and \vec{K}_i is the exchange contribution to the Hartree-Fock potential:

The coulomb operator is illustrated as follows:

$$\vec{J}_i(\vec{x}_1) = \int |\chi_j(\vec{x}_2)|^2 \frac{1}{r_{12}} d\vec{x}_2 \quad (30)$$

and \hat{K} is specified when it is operating on a spin-orbital:

$$\hat{K}_j(\vec{x}_1) \chi_i(\vec{x}_1) = \int \chi_j^*(\vec{x}_2) \frac{1}{r_{12}} \chi_i(\vec{x}_2) d\vec{x}_2 \chi_i(\vec{x}_1) \quad (31)$$

Thus, the HF potential V_i^{HF} is non-local and certain of the spin orbitals, which are initially unspecified. In order to determine V_i^{HF} , a Hartree-Fock Self-Consistent Field (HF-SCF) process is arranged to be considered. The preliminary set of spin orbitals χ_i is guessed and utilised to produce a new one V_i^{HF} . So herewith, the HF potential and new spin orbitals are determined. This process is recurrent up to the outcome and satisfies the convergence criteria. Meanwhile, the HF is not regarded as the dynamic correlation between electronic movements; the HF energy always exceeds total energy.

3.1.3 Density functional theory

Density functional theory (DFT) does not employ the electrons' N-body wave functions, although the electrons' total density uses it as a fundamental quantity. Electron density is a physical characteristic; albeit the number of electrons increases, it is effortless to be calculated. More notably, the DFT approach overcomes the Hartree-Fock method's principal drawback, which neglects the electron correlation. The DFT is used to solve problems on molecular structures, vibrational frequencies, global energies, thermochemistry, hydrogen bonds, weakly bound systems, magnetic properties, electrical properties, thermodynamic properties, optoelectronic properties, and chemical reactivity, to mention a few. Since the HF actual electronic wave function is based on $3N$ variables, high memory is required to resolve

the issue. Instead of that, using electronic density, $\rho(\mathbf{r})$, in the DFT function of only three variables would be highly advantageous to define the system due to the Hohenberg-Kohn theorem.

Hohenberg and Kohn suggested with the main idea of the first fundamental DFT theorem that: “the external potential of the system $V_{\text{ext}}(\vec{r})$ is a unique function of the electronic density $\rho(\vec{r})$ because of the presence of nuclei”. So only the electron density decides the Hamiltonian, and thus all ground-state properties. In many-body, the Hamiltonian fixes the system's ground state, which means it defines the ground-state wavefunction of many-body. Hence, the above theorem ensures that the ground-state density is also functional. The density functionals $\rho(\mathbf{r})$ determine, therefore, both kinetic and electron-electron interaction energies.

$$E = E[\rho], \quad \Psi = \Psi[\rho]. \quad (32)$$

Moreover, as a result, the energy is a functional of ρ such that $E_0 = E[\rho_0(\mathbf{r})]$, and therefore,

$$E[\rho(\mathbf{r})] = \langle \Psi[\rho(\mathbf{r})] | \hat{H} | \Psi[\rho(\mathbf{r})] \rangle \quad (33)$$

Resulting in the Born-Oppenheimer approximation, we have:

$$E_{\text{el}}[\rho] = \int \rho(\mathbf{r}) V_{\text{ext}} d\mathbf{r} + F_{\text{HK}}[\rho] \quad (34)$$

where $F_{\text{HK}}[\rho] = T[\rho] + V_{\text{ee}}[\rho]$ refers to the universal functional in that, regardless of the external potential involved, it is called Hohenberg-Kohn and has the same dependency on electron densities for any system. In contrast, T and V_{ee} are the kinetic energy and electron-electron interaction operator, respectively.

Hohenberg-Kohn's second theorem to the variation principle in the DFT analogue states that: the functional $F_{\text{HK}}[\rho]$, which provides the system ground state energy, provides the lower energy only if the input density is the correct ground state density. That is to say, any test density ρ' in the external potential, V_{ext} , which results in a better approximation of the ground-state electron density by any lower energy density.

$$E[\rho'] = \int \rho'(\mathbf{r}) V_{\text{ext}} d\mathbf{r} + T[\rho'] + V_{\text{ext}}[\rho'] \geq E_0 \quad (35)$$

The second theorem is valid for the ground state; it considers precise functionals. Hence, when used in accordance with the first theorem, the exact wave function can be identified in a variable direction if precise functionals are used. Though system-independent and therefore universally true, the problem is that the functional form of F_{HK} is unknown.

3.1.4 Kohn-Sham theory

Kohn and Sham (1965) have suggested the Schrödinger equation solution method. The interactive system is replaced with a non-interactive system, provided the electronic ground states are similar. Density $\rho(\mathbf{r})$ can be defined as all the energy contributions. The energy is the lowest only if the density is in its fundamental state $\rho(\mathbf{r})=\rho_0(\mathbf{r})$ and is the same as the ground state. Kohn and Sham proposed introducing a hypothetical system using non-interacting electrons and the same electronic density as the existing system to simplify the task of seeking universal functionality. This reference system is defined using one electron known as Kohn-Sham (KS) orbitals because of the non-interacting electrons.

$$\hat{H}_R \psi_i(\mathbf{r}) = \varepsilon_i \psi_i(\mathbf{r}) \quad (36)$$

The Hamiltonian that does not interact can be described as:

$$\hat{H} = -\frac{1}{2} \nabla^2 + v_R(\mathbf{r}) \quad (37)$$

The reference potential $v_R(\mathbf{r})$ ensures that the system is densely equivalent to the real system.

$$\rho(\mathbf{r}) = \sum_{i=1}^N |\psi_i(\mathbf{r})|^2 \quad (38)$$

The kinetic energy of the electrons is well known in the reference system after the introduction of orbitals, the energy of the referential system can be represented as:

$$E_R[\rho] = \underbrace{-\frac{1}{2} \sum_{i=1}^N \langle \psi_i | \nabla^2 | \psi_i \rangle}_{T_s[\rho]} + \int v_R(\mathbf{r}) \rho(\mathbf{r}) d\mathbf{r} \quad (39)$$

The resulting expression for the real system's energy can be written using kinetic energy and estimated electron-electron interactions with simple Coulombic repulsion (or Hartree term) as a first approximation of the reference system.

$$E[\rho] = T_s[\rho] + \frac{1}{2} \iint \frac{\rho(\mathbf{r})\rho(\mathbf{r}')}{|\mathbf{r}-\mathbf{r}'|} d\mathbf{r}d\mathbf{r}' + \int v_{\text{ion}}(\mathbf{r})\rho(\mathbf{r})d\mathbf{r} + E_{\text{xc}} \quad (40)$$

where the exchange-correlation functional, $E_{\text{xc}}[\rho]$, is defined by the reference kinetic energy and Hartree term as the error of energy approximation.

$$E_{\text{xc}}[\rho] = T_e[\rho] - T_s[\rho] + U_{\text{ee}}[\rho] - \frac{1}{2} \iint \frac{\rho(\mathbf{r})\rho(\mathbf{r}')}{|\mathbf{r}-\mathbf{r}'|} d\mathbf{r}d\mathbf{r}' \quad (41)$$

The following is the reference potential describing the reference system from the expressions of the energy of the real systems and the reference:

$$v_{\text{R}}(\mathbf{r}) = \underbrace{\int \frac{\rho(\mathbf{r}')}{|\mathbf{r}-\mathbf{r}'|} d\mathbf{r}'}_{v_{\text{H}}(\mathbf{r})} + v_{\text{ion}}(\mathbf{r}) + \underbrace{\frac{\partial E_{\text{xc}}[\rho]}{\partial \rho}}_{v_{\text{xc}}(\mathbf{r})} \quad (42)$$

As shown, the reference potentials are density-dependent; hence, the Kohn-Sham equations must be solved in a self-consistent approach from an initial guess of $\rho(\mathbf{r})$. The DFT theory is exact so far, though it has no approximation. The exchange-correlation term $E_{\text{xc}}[\rho]$ is the only unknown term. It is significant for the various approximation to be under consideration, and the following section discusses various approximations.

3.1.5 Exchange–Correlation functionals

As stated above, the $E_{\text{xc}}[\rho]$ functional involves non-classical contributions to the energy potential due to electron-electron interaction and the difference between the actual system and non-interacting system kinetic energy. It is noticeable that different approximations are applied to these exchange-correlation functionals. The new functional development is a continuous and active field of study. Several methods are under suggestions for the calculation of the exchange and correlation term $E_{\text{xc}}[\rho]$, for instance, local density approximation (LDA) and the generalised gradient approximation (GGA).

(i) The local density approximation

When considering that electrons are a uniform gas for the electron, it is presumed that the charging density varies little by little on the atomic scale and that the inhomogeneous electronic structures should be regarded as homogeneous locally. The energy of exchange-correlation can be defined as for the spin-unpolarised system.

$$E_{xc}^{LDA}[\rho] = \int \rho(\mathbf{r}) \varepsilon_{xc}(\rho) d\mathbf{r} \quad (43)$$

Vosko, Wilk and Nusair (VWN) (Vosko *et al.*, 1980) have produced Monte Carlo's calculations for a uniform electron gas as an LDA functional example. The exchange-correlation energy of the local spin density (LSDA) may be written for the polarised spin system as follows:

$$E_{xc}^{LSDA}[\rho_\alpha, \rho_\beta] = \int d\mathbf{r} \rho(\mathbf{r}) \varepsilon_{xc}(\rho_\alpha, \rho_\beta) \quad (44)$$

where ρ_α and ρ_β represent the electronic spin densities, it gives reasonable precision to estimate the molecular properties of the structure, like frequencies of vibrations and charge moment's geometrical structure, to mention a few. However, when the density varies quickly, energy specifics, for instance, binding energy, energy barriers etc., prove to be poorly approximated.

(ii) The generalised density approximation

The proposed generalised density approximation (GGA) solves the previous problem. It enhances the LDA approach in a system, taking into account non-local electron effects in functional systems, and the system is a non-uniform electron gas. The exchange-correlation term can be written according to ρ and $\nabla\rho$ as follows:

$$E_{xc}^{GGA}[\rho] = \int \varepsilon_{xc}(\mathbf{r}) [\rho(\mathbf{r}) + \bar{\nabla}\rho(\mathbf{r})] d^3\mathbf{r} \quad (45)$$

The different approximations for the above equation are available to the GGA family, such as BLYP, PW91, and PBE, to mention a few. However, GGA typically provides better outputs than LDA, such as total energies, atomisation energies, energy barriers and structural energy disparities, since GGA allows for a more considerable fluctuation.

The PBE functional through Perdew, Burke and Ernzerhof realise exchange-correlation functional) (Perdew *et al.*, 1996) is an improving GGA function. It has a simple derivation with fundamental parameters. The functional is better working with molecules and solids, including metals, and our work in progress provides significant findings.

(iii) A meta generalised density approximation

The meta-GGA functionalities strengthen marginally with the GGA functionalities with a further dependency on the kinetic energy density of Kohn Sham:

$$\tau(r) = \sum_i \frac{1}{2} |\nabla \phi_i(r)|^2$$

$$E_{xc}^{meta-GGA}[\rho] = \int \varepsilon_{xc}(r) [\rho(r) + \bar{\nabla} \rho(r) + \tau(r)] d^3 r \quad (46)$$

One of the most frequently used meta-GGA functions is the TPSS function (the interchange-relation function developed by Tao, Perdew, Staroverov and Scuseria) (Tao *et al.*, 2003).

(iv) The hybrid functionals

Electronic self-interaction leads to inadequate representation of exchange parts of previously presented functionals when defining the exchange component in HF. However, there are weak results directly combining the correlation component from DFT and the HF exchange part. This problem would be avoided by the hybrid functionals that mix DFT and HF and combine both methods' exchange and correspondence portions. Perhaps the B3LYP (Kim & Jordan, 1994; Stephens *et al.*, 1994) is the most regularly used hybrid functional. It is represented as:

$$E_{xc}^{B3LYP} = E_x^{LDA} + a_0(E_x^{HF} - E_x^{LDA}) + a_x(E_x^{GGA} - E_x^{LDA}) + E_c^{LDA} + a_c(E_c^{GGA} - E_c^{LDA}) \quad (47)$$

where E_x^{GGA} and E_c^{GGA} are the generalised gradient approximation exchange and correlation functionals; E_c^{LDA} is the local density approximation to the correlation functional; a_0 is set to 0.20; a_x is set to 0.72; a_c is set to 0.81.

3.1.6 Plane-Wave functions and Brillouin zone sampling

The system is modelled using the periodic boundary conditions (PBC) by replicating three-dimensional unit-cell atoms. As the total energy and forces converge, the model is assumed to be stable. In the plane-wave basis set, the electronic density is defined. The theorem of the Bloch is as follows:

$$\Psi_k(\vec{R} + \vec{T}) = e^{i\vec{k}\vec{T}} \Psi_{\vec{k}}(\vec{R}) \quad (48)$$

where;

$\Psi_{\vec{k}}(\vec{R})$: electronic wave function

\vec{R} : vector in the direct space

\vec{T} : vector in the reciprocal space

k : a set of three quantum numbers (k_x, k_y, k_z)

The quantum numbers are substantially continuous in a finite solid. However, cut-off energy limits the set to a sphere in reciprocal space.

$$E_{cut-off} > \frac{\hbar^2 |k + T|^2}{2m} \quad (49)$$

where; m : is a mass of one electron

The cut-off energy must not be set too high or too small to produce a good result for a fair cost of computation time. The functions of the Bloch's are already commonly specified in the Brillouin zone by an infinite number of \vec{k} points. The Bloch function $\Psi_{i,R}$ equation for each \vec{k} point is required to be solved. The total energy of the system for each B point is an integral part of the band energy:

$$E = \sum_i \frac{1}{\Omega_{BZ}} \int E_{i,k} g_i(\vec{k}) d\vec{k} \quad (50)$$

where Ω_{BZ} represents the Brillouin zone's volume and $g_i(\vec{k})$ is the state i 's electronic occupation at the point \vec{k} . This equation is approximated to the next discrete one in order to simplify the calculation.

$$E = \sum_i \sum_k \omega_{\vec{k}} E_{i,k} g_i(\vec{k}) \quad (51)$$

where $\omega_{\vec{k}}$ represents the factor corresponding to each \vec{k} point.

The Monkhorst and Pack (1976) methodology were used to discretise the Brillouin zone in our VASP calculations. This algorithm automatically produces the points. It turns the system of an infinite number of electrons into a finite number of bands, depending on the number of electrons in a unit cell.

3.1.7 Basis sets

A variety of convenient yet physically driven sets of one-electron functions extend the molecular electronic wavefunctions without exception. However, since the substantial amount of expansion functions influence computational effort, it is crucial to restrict as many functions as possible without affecting the accuracy of the wave function.

(i) Atomic-centred basis sets

It is possible to construct atomic or molecular orbitals via atom-localised basis functions. The expansion of the orbitals as a linear combination with specific coefficients of such functions is essential. Two principal types define them: Slater-type orbitals (STOs) and Gaussian-type orbitals (GTOs) (Davin, 2009).

In the following form, STOs are represented:

$$\eta^{STO} = N r^{n-1} e^{-\zeta r} Y_{lm}(\Theta, \phi) \quad (52)$$

where N is normalisation factor; ζ is the exponent; r, Θ , and ϕ are the spherical coordinates; Y_{lm} is the angular momentum part; n is the principal; l is the angular quantum number; m is the magnetic quantum number.

For the GTOs, the following form can be expressed:

$$\eta^{GTO} = N x^l y^m z^n e^{-\alpha r^2} \quad (53)$$

of which N is the normalisation factor, and x, y and z are Cartesian coordinates. The STOs usually have a cusp at $r=0$, and a strong exponential decay is achieved for higher values of r. These properties lead to a similar definition of the hydrogen atomic orbit. By comparison, the GTOs do not display the $r=0$ cusp and easily decay for higher r values. However, the product of two GTOs is a third, which is not the case with STOs. This property prevents the issue of the computationally expensive of the four-centre-two-electron integrals. The combination of

multiple GTOs can be approximated to the STO, typically more effective than using STOs directly. In order to describe each nuclear orbit, the number of contracted functions (CGF) is described as a level of complexity or precision. For instance, a linear combination of 3 CGF representing an STO constitutes the STO-3G basis set. Double-zeta and triple-zeta basis sets typically provide reasonable precision and system definition.

The valence electrons are vital since they are most active in chemical reactions. A flexible definition of valence electrons is, therefore, appropriate. The treatment of the core and valence orbitals differently results from the split valence basis sets' development. The 6-31G basis set that follows the X-YZG nomenclature is the most frequently used split valence basis set. X signify the number of primitives GTOs at ease with the description of one single contracted Gaussian function of the core. Y and Z (for better precision, more can be added) signify the number of primitives GTOs explaining the valence orbitals. It consists of two functions for 6-31G, one containing three primitives and the other having only one.

There can be additions to the basis sets via polarisation functions/diffuse functions. For example, atom bonding allows the electronic cloud to deform, termed polarisation occurring around each atom. In order to do so, the basis set is replaced with functions with higher angular momentum. For instance, the addition of a p function to H allows polarisation. Likewise, a d-function may be added to the basis sets with *p*-valence orbitals and *f*-functions for *d*-valence orbitals. The included polarisation functions can be better defined for more precise results. For instance, a hydrogen atom with 6-31G basis set p and d polarisation functions conceivably added, and the basis set enhancing 6-31G(d,p). A symbol “+” (such as 6-31+G or 6-31++G) speaks for diffuse functions, which defines the portion of the atomic orbitals distant from the nuclei that can have a crucial role example, in second or third-row transition metals when considering anions and diffuse electronic clouds.

(ii) Pseudopotential basis sets

The overlong computational times involved in calculations are difficult for systems that include heavy elements. It is another fact that these atoms' inner core is substantial for transition metals (mostly heavy elements). Hence, the number of basis functions used to describe them will be extensive. However, we know that most solids' physical and chemical properties depend more on the electrons in valence and less on the core electrons. These basis functions can be replaced with an effective core potential (ECP) to overcome this problem.

The ECP models the effects on valence electrons of the nucleus and electrons from the inner shell as an average effect. This ECP reduces large computations and has some relativistic effects on the system studied (Jensen, 2013). This situation happens since relativistic atomic simulations provide these basis functions. The ECP eliminates the core electrons and the strong, attractive nuclear potential from the previous fact and replaces them with a weaker pseudopotential that operates on a set of pseudo-wave functions rather than the proper valence wave functions.

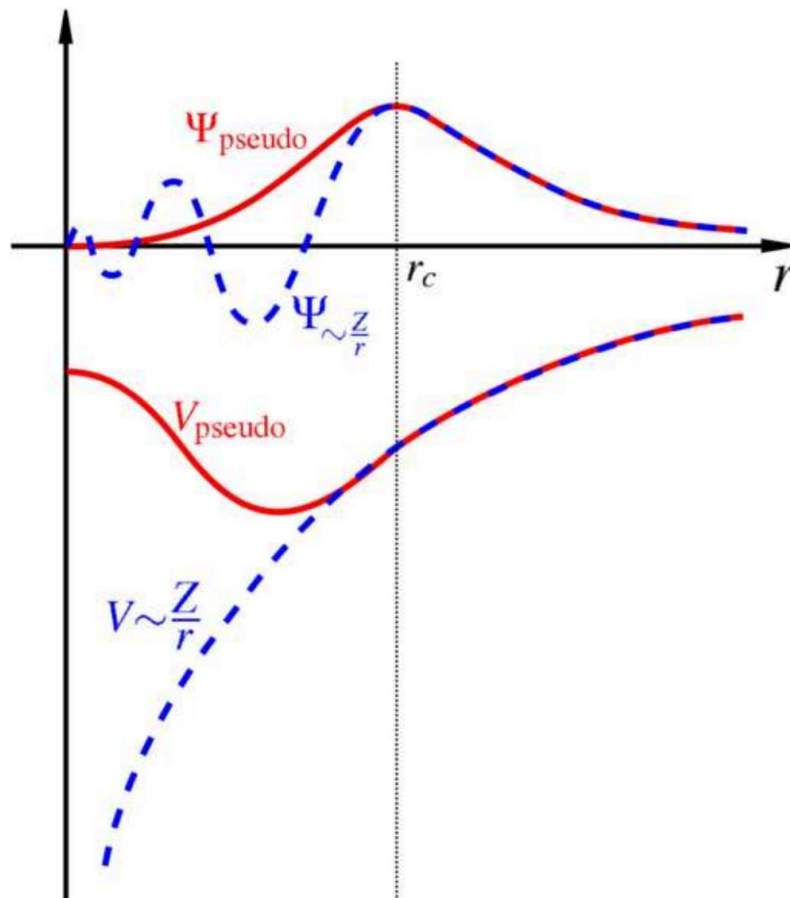


Figure 11: Representation of potential and pseudopotential (Payne *et al.*, 1992)

LANL2DZ is a double-zeta basis used most often in the research of heavy metals (mostly transition metals) (Cramer, 2013). This LANL2DZ consists of Los Alamos pseudopotential and double zeta valence basis set. Figure 11 briefly represent the understanding of the pseudopotential function. With its contractual coefficients and exponential parameters, the GTO valence basis sets in the GTO part of the LANL2DZ basis set are optimised for the above pseudopotential. Table 3 lists these parameters for the Ti atom. In addition, several pseudopotentials exist, such as orthogonalized plane wave (OPW); ultra-soft pseudopotential (USPP); norm-conserving pseudopotentials (NCPP); and projected augmented waves (PAW).

Table 3: GTO contraction coefficients and exponential parameters used for the Ti atom in LANL2DZ (Frisch *et al.*, 2019)

Atomic number	Valence electrons	Angular Momentum	Power of R	Exponent	Coefficient	S0-Coefficient
22	12	D and up	1	265.3263909	-10.00000000	0.00000000
			2	47.7687815	-51.84278160	0.00000000
			2	11.8903334	-9.14291450	0.00000000
		S-D	0	81.4730696	3.00000000	0.00000000
			1	72.6496724	19.48255790	0.00000000
			2	31.8128213	207.33492790	0.00000000
			2	6.1664468	235.67445010	0.00000000
			2	5.8268347	-166.87843870	0.00000000
		P-D	0	50.2966943	5.00000000	0.00000000
			1	63.5089754	5.53488220	0.00000000
			2	26.0996084	177.84193840	0.00000000
			2	5.6022573	107.42071530	0.00000000
			2	5.2171069	-71.90659020	0.00000000

The convergence of USPP and PAW schemes requires relatively small numbers of plane waves. The method of the projector augmented waves (PAW) used in our calculations suggested by Blöchl (1994) and is carried out in the VASP software by Kresse and Furthmüller (1996b), Kresse and Joubert (1999). The PAW method is used to explain (Blöchl, 1994) the wave function of all electrons $|\Psi^{AE}\rangle$ is represented as:

$$|\Psi^{AE}\rangle = |\Psi_v^{PS}\rangle + \sum_i c_i (|\varphi_i^{AE}\rangle - |\varphi_i^{PS}\rangle) \quad (54)$$

where Ψ_v^{PS} is the pseudo-function of valence electrons, φ_i are the local functions stated in the space centred in the core of atoms.

For Ψ_v^{PS} it can be expressed as:

$$\Psi_v^{PS} = \sum_i \langle p_i | \Psi_v^{PS} \rangle \varphi_i^{PS} \quad (55)$$

Because of this situation, the all-electron wave function is feasible to be expressed as:

$$|\Psi^{AE}\rangle = |\Psi_v^{PS}\rangle - \sum_i |\varphi_i^{PS}\rangle \langle p_i | \Psi_v^{PS} \rangle + \sum_i |\varphi_i^{AE}\rangle \langle p_i | \Psi_v^{PS} \rangle \quad (56)$$

The projector augmented waves (PAW) pseudopotentials are easier to construct than other pseudopotentials, such as ultra-soft pseudopotentials. It keeps these forms for all the electrons and provides better results for alkaline and transition metals.

3.2 Minima on potential energy surfaces

There is an exponential increase in the number of stable structures within the atomic nanocluster. These most stable structures are referred to as low-lying isomers (or molecular clusters conformers) by exploring the system's possible potential energy surface (PES), also known as the energy landscape. Concerning the nuclear parameters, the PES corresponds to the molecular energy of the nanocluster system. The PES in 3D space can be contrasted with a mountain, hill, valley or basin-like landscape. The "basins" in the PES are the local energy minima and the lowest is the global minimum. Any minimum on the PES meeting agreed with coordinates for which the system is regarded as stable.

The molecular energy evaluation uses an electronic structure calculation based on the previously mentioned quantum mechanical methods and empirical/semi-empirical force fields. The following section explains, for example, the GUPTA empirical potential adapted for metallic systems. Because of how extensive PES scanning can decide the configurations in all possible ways too challenging for a computer, methods were suggested in the literature. Most of those presented in the next sections could effectively find the relevant local minimum called "global optimisation" or "global search algorithms".

3.2.1 Empirical potential

There are two leading families, the first principle and empirical methods, to assess potential energy. The first principle methods solve the Schrödinger equation as an approximate operating method and have previously been implemented. Molecular energy is often derived from an empirical force field that depends upon the atom's position and the empirical parameters. Therefore, with these empirical force fields, the system's energy is calculated very quickly if accessible, even if most of the empirical results often do not have total agreement with their "first principle". The following empirical methods are widely used: Morse potential, Coulomb-Born-Mayer potential, Z potential, Lennard-Jones potential, and GUPTA potential (Zhang & Dolg, 2015). The GUPTA Nouemo *et al.* (2016) potential enables simulations of up to three hundred atoms to be carried out on small workstations. This GUPTA potential has been used extensively in the simulation of metallic clusters (Garzón *et al.*, 1998; Michaelian *et al.*, 1999). Results are consistent with those provided by the first-principles methods. With only four adjustable parameters, the GUPTA potential

models the many-body clusters. Compared to DFT methods, the results can be obtained in a very short time. The energy can be expressed as follows:

$$V_{cluster} = \sum_i^N \{V^r(i) - V^m(i)\} \quad (57)$$

With repulsive pair energy:

$$V^r(i) = \sum_j^N A(a,b) e^{-p(a,b) \left(\frac{r_{ij}}{r_0(a,b)} - 1 \right)} \quad (58)$$

and attractive many-body energy:

$$V^m(i) = \sqrt{\sum_i^N \zeta^2(a,b) e^{-2q(a,b) \left(\frac{r_{ij}}{r_0(a,b)} - 1 \right)}} \quad (59)$$

where a and b are two types of atoms in the cluster, r_{ij} is the distance between two atoms, i and j. A, r_0 , ζ , p and q are the four adjustable parameters fitted to the experimental values of the cohesive energy, lattice parameters and independent elastic constants for the bulk metals at 0 K.

3.2.2 Global search methods

In general, four major types of global methods exist: Molecular Dynamics, Monte Carlo, Basin Hopping and Genetic Methods (Christmann, 1988; Papoian *et al.*, 2000), which were not used in this work.

3.2.3 Geometric optimisation

Local optimisation through local search method begins from the initial structure, which follows an iterative process until the best structure is found. The most stable structure should have as close to zero internal forces as possible, and the sum of all internal forces should be minimised. It is realised by calculating the forces for each atom based on the Hellmann-Feynman theory:

$$\frac{dE_\lambda}{d\lambda} = \int \psi_\lambda^* \frac{d\hat{H}_\lambda}{d\lambda} \psi_\lambda dV \quad (60)$$

where E_λ is the energy of the system, \hat{H}_λ is the Hamiltonian operator depending on λ , ψ_λ is the Eigen-wavefunction of Hamiltonian, and dV is the integration over the wavefunction. Suppose the forces identified in the first step are above the threshold. In that case, the algorithm leads the system to different coordinates with or without calculating the energy's second derivatives. The process is repeated until the force converges. Algorithms that use more Newton, conjugate, or combined gradients are the most popular or regularly used algorithms. For example, as implemented in the Gaussian 09 package, the Berny algorithm (Schlegel, 1982) uses BFGS search (Broyden-Fletcher-Goldfarb-Shanno) (Grossmann, 1981) as local optimisation for GUPTA empirical potential. In contrast, the conjugate gradient method (Press *et al.*, 2007) in the VASP package is employed (see the IBRION keyword detailed in the next section).

3.3 Computational software

Within this dissertation, the open-source software package, i.e., Firefly 8.2.0 code and the commercial software package (i.e., Gaussian 16 code and VASP code) are used to realise our DFT calculations. These three codes and their input/output setting are briefly introduced in this chapter.

3.3.1 Firefly code

The Firefly version (Granovsky, 2013; Schmidt *et al.*, 1993) supports all GAMESS software package features up to the October 25th, 1999 release of GAMESS (US). There are many features added to GAMESS since 1999 that also have been implemented into Firefly. The RHF, UHF, ROHF, GVB or MCSCF case wavefunctions are available from *ab initio* SCF. The Møller-Plesset (MP) perturbation theory and configuration interaction (CI) allow correlation corrections to be applied. MCQDPT2 can determine the correlation corrections for MCSCF wavefunctions. The electronic excited states can also be described with singles (CIS), RPA (i.e., TD-HF) and TD-DFT configuration. The support is provided for effective core capabilities and a range of DFT functionals. Geometry optimisation can be performed with HF, MP2, CI, DFT, and MCSCF gradients. Hessians can be computed for wavefunctions calculated using RHF, ROHF, and GVB methods, and numerical Hessians are available for all methods that support analytic gradients. Finally, number gradients and Hessians double numbers are available for all methods.

(i) Firefly input files

Firefly input may be upper or lowercase. In Firefly, there are three kinds of input groups. (a) A pseudo-name list, free format, group driven by keyword. This first category covers nearly all input groups. (b) The free format group does not follow the rules (such as keywords). Only \$DATA, \$ECP, \$POINTS and STONES are examples of this category. (c) Well-structured data. The user is never typed; instead, some earlier Firefly execution generates this data in the correct format. Every input group starts with a \$ sign in Column 2, followed by a group name. For each group in category 2 or 3, the group name should be the only item on the input line. Finally, a \$END ends for all input groups. The \$END must appear in column 2 and be the only item in this input line for any group from categories 2 and 3. Groups of type 1 can have the input keyword in the same line as their group's name, and \$END can be found anywhere. Due to the unique names of each group, the groups can be presented in any order. Indeed, several category 1 groups occurrences are permitted. If the programme defaults are appropriate, most groups may be omitted. An exception, which is always necessary, is \$DATA.

(ii) Firefly output files

The default on-screen printing is the main output. The output can be sent to the file (firefly.exe >dye.out 2>&1). Otherwise, the -o parameter can be used (firefly.exe -o dye.out). The different keywords in Firefly may modify the amount of information printed. The most important and relevant keyword in \$CONTRL is NPRINT. The PUNCH file contains several calculated data. Many of these data are formatted and can be copied to the second run input. The data punched would include, for example, information on the geometry, basis set information, the constant force matrix, orbitals, etc. The multiple functions are available in the IRCDATA file. For instance, molecular geometries discovered during an IRC run are present. In addition, it contains restart data from hessian numerical calculations and Raman. The programme controls the time of the CPU and stops if the time is short. The data are deposited in the computer's hard drive in a punch-out format. So, restarts can be made easily. The orbitals are currently placed in the punch file of all SCF modules when the number of iterations is achieved. These orbitals may restart the stop-iterations in conjunction with the GUESS = MOREAD option. Furthermore, suppose the \$CONTRL TIMLIM option is used to set a time limit slightly below the job batch time. In that case, Firefly stops when the time

required to finish another full iteration is insufficient, and the current orbital is punched in the current batch time.

3.3.2 Gaussian 16 code

The Gaussian 16 is the latest Gaussian code version. It is used incredibly commonly in the field of quantum chemistry. It can employ a variety of methodologies, such as centred atomic orbitals, HF, post-HF, and DFT. To read more, visit their official website at <https://gaussian.com/>. The purchase of a new Gaussian license includes the *Exploring Chemistry with Electronic Structure Methods* textbook, which introduces chemical compounds and reactions using electronic structure methods. The textbook's authors also launched a website containing the input files from the book and some instructional videos. The web address is <http://expchem3.com/>, and this website, along with the textbook, can be a useful tool for researchers, especially new researchers, to learn how to use the software.

(i) Gaussian 16 input files

Only a single input file is necessary to run the Gaussian code. For the calculation, the first line provides the number of processors used; the second line provides the system's memory amount. In the third line, beginning with the symbol '#,' the route section includes the keyword used in the Gaussian calculation separated by spaces. The code "P" after a # symbol controls a more detailed output file. In our computation, we use the following keywords:

The Gaussian code 16 for reading the ECP and the basis sets specified in the input file are used for heavy atoms such as Ti, et cetera. The GFinp keyword can be added or modified by the current basis set in the appropriate form in a standard basis set. The "SCF" keyword controls the self-consistent field process itself. There are two keywords, 'Maxcycle' and 'Conver', within the brackets after SCF. The maximum number of SCF cycles is indicated in the 'maxcycle', generally set to 1999. The 'Conver' is the set of conditions under which SCF converges. As the system needs to converge accurately, the SCF matrix must satisfy both $<10^{-N}$ root mean square change in the density matrix and $<10^{-(N-2)}$ maximum change in the density matrix. The 'Conver', in our case, is usually set at 8 for complete geometric optimisation. If you write or complete all keywords, you add an empty line to specify the complete research path (or route section).

A title line whose purpose is to show the calculation name follows the route segment, and another blank line has the end of the title line. The next line's description contains the total electronic charge and the system's multiplicity. Each atom of the system shall be written in a row in the corresponding sequence without a blank line by its atomic symbols and the three initial cartesian coordinate numbers. In the last portion of the Gaussian input file, each type of atom's basis set appears.

(ii) Gaussian 16 output files

The system SFC energy for each ionic step is given in the output file of Gaussian 16. The final total energy and the system's optimised geometric configuration are obtained once the convergence criterion is met or the maximum cycle number is reached.

3.3.3 VASP code

The Vienna *ab initio* simulation package (VASP) is a FORTRAN language computer programme for first-principle atomic-scale modelling (Kresse & Furthmüller, 1996a; Kresse & Hafner, 1993, 1994; Kresse & Joubert, 1999). The periodic systems can be created with VASP from repeated unit cells in three-dimensional space. Furthermore, one can determine a given system's electronic ground state by utilising either density functional theory or the Hartree-Fock method. The 'VASP the GUIDE' (Kresse *et al.*, 2018) provides details on input features.

(i) VASP input files

The four main input files are available from VASP: POSCAR, POTCAR, INCAR and KPOINT. The starting lattice geometry and ionic positions are included in POSCAR. The first line is a comment line that can be a calculation title. The second line is a universal scaling factor that calculates both lattice vectors and atomic coordinates. Whether the total volume is negative, interpret them as the total cell volume. The third, fourth and fifth lines are the vectors that define the system unit cell. The sixth line provides the chemical elements of the system with their atomic symbols. The atom species in the sixth line corresponds to the number of atoms in the seventh line written in the sixth line. The eighth line is optional, and if it is written as 'Selective Dynamics', it is supplied with extra flags 'T' and 'F' that allow the coordinate (s) of that atom to change during the ionic optimisation (using T) or not (using F). When select dynamics is not the eighth line, all systems atoms can change their coordinates

by default during optimisation. The eight lines set out the atom coordinates in cartesian or direct coordinates. The Cartesian coordinates are used if the coordinates are written with the word 'C' or 'Cartesian'. The direct coordinates are used when it is written "Direct" or "D". The following lines are the three atomic coordinates. The coordinate number gives those three numbers in the Cartesian mode. In the Cartesian mode (or orbital mode), these three numbers are the positions of atoms provided in terms of their coordinate number. These three numbers are given values in the direct mode, paired with the three basic vectors, written in the third, fourth and fifth lines. The coordinates line should be compatible with the sixth line that shows the atomic symbols.

The POTCAR is a list containing pseudopotentials for each atom in the system. The VASP package provides the pseudopotentials for certain atomic species. When there are more than one species in the system, all the pseudopotentials of atoms should be combined in the POTCAR file. For example, this can be done in the UNIX system with the 'cat' command to get a POTCAR file together. The atom's pseudopotentials should be in the same order as POSCAR file atoms, in which the atomic symbols of the system are represented in the sixth line.

INCAR is the main input file containing most calculation keywords, for instance, cut-off energy, smearing parameters, convergence parameters, et cetera. The following keywords are used for a normal SCF geometry improvement of a specific cell size unit: (a) IBRION = 2, which is used to relax the ions into their ground condition by a conjugate gradient algorithm; (b) NSW = 100, 100 is the maximum ionic steps performed; (c) PREC = The default for three sets of parameters is normal in our case (NGX, NGY, NGZ; NGXf, NGYf, NGZf and ROPT); (d) LREAL = AUTO, real space projection, fully automated operator optimisation; (e) The electronic minimisation algorithm is specified in ALGO = FAST. For the initial stage, Davidson (IALGO = 38) is used, then VASP switches over to RMM-DIIS (IALGO = 48); (f) The DOSCAR and PROCAR are written in LORBIT = 10; (g) ISMEAR = 0, Gaussian smearing applied; (h) The width of the smearing in eV is determined by SIGMA = 0.01; (i) GGA = PE, carries out GGA calculations with pseudopotentials of Perdew-Burke-Ernzerhof; (j) ENCUT = 500, Plane Wave Basis Cut-off energy set in eV. The basis set includes all plane waves with kinetic energy smaller than ENCUT; (k) Calculation of the ISIF = 2, stress and force tensor; unchangeable ions, cell shape and volume remain the same; (xii) ISPIN = 2, allows spin-polarisation calculations; (l) ISPIND = 2, makes spin calculations

polarised; (m) POTIM = 0.5, step width scaling constants; (n) The ionic relaxing loop break status is defined by the EDIFFG = -0.02 . If all forces are small, then the $|\text{EDIFFG}|$ relaxation will stop; (o) The global break condition of the electronic SC-loop is set by EDIFF = 0.001; (p) If the total (free) energy change and the band structure changes energy (change of eigenvalues) between two levels are both smaller and smaller than that of EDIFF, electronic degrees of freedom will be discontinued.

In the Brillouin zone for sampling, the KPOINT file shows the coordinates and weights for k-points. We used automatic k-mesh generation in our case. The first line is simply a comment line. The second line of zero decides to use an automatic k-point generation. The second line shows how to generate the Monkhorst-Pack method in our case.

(ii) VASP output files

The VASP code produces three main outputs: CONTCAR, OUTCAR, and OSZICAR. The CONTCAR file is updated each time, and ionic steps are made. The relationship between lattice geometry and ionic positions has been optimised. It has the same format as the POSCAR and is usually written directly. The OUTCAR is the most important output file of VASP. This file contains the most calculation output data. It includes the following parts: get information from INCAR, POTCAR, and POSCAR files; calculate results of the nearest neighbour distance and symmetry analysis of the system; get information on analysed and detailed INCAR keyword; get detailed job information; get lattice, k-points and ionic positions information; get basis set information; get non-local pseudopotential information and detailed information of each electronic step during the optimisation; get eigenvalues; get charge; get energy and stress tensor; get the timing. The OSZICAR file is the simplified OUTCAR file version, which contains information for each electronic step in one line. This file can easily find the number of iterations, total energy, and total energy change.

3.4 Investigated natural betacyanin (betanidin) and synthetic (L0) sensitizers

The natural dyes betanidin (Bd) and decarboxylated Bd (dBd), belong to betacyanins family, synthetic dye is (4-(diphenylamino)phenylcyanoacrylic acid (L0). The two-dimensional molecular structures are shown in Fig. 12.

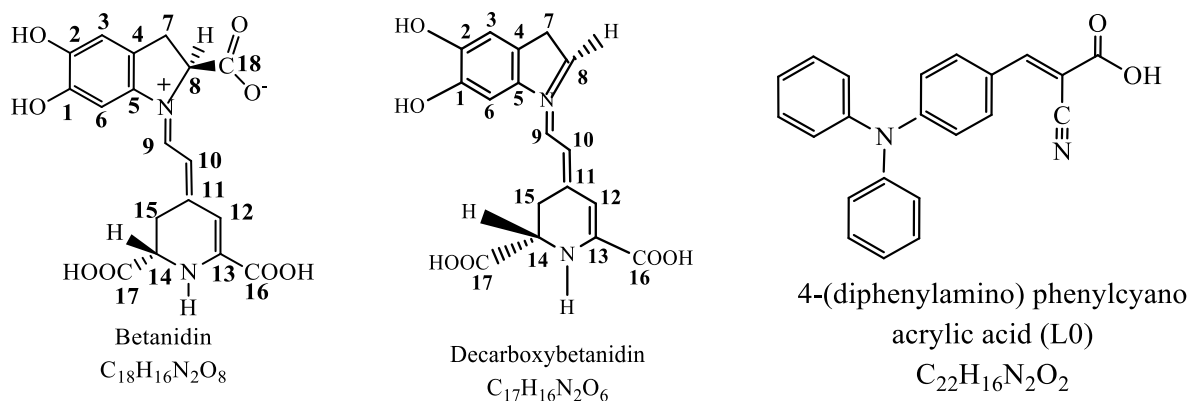


Figure 12: Individual betanidin, decarboxybetanidin and L0 dyes

3.5 Dye design

The molecule of betanidin structure provides two different reaction paths, due to the C_2 or C_1 carbon atoms through which the L0 attachment may occur (Fig. 13). The reaction between hydrogen ion (H11) of L0 dye with the hydroxyl group of betanidin (Bd) and 2-decarboxy betanidin (dBd) is reaction route one (1) at C_2 and the reaction route two (2) at C_1 (Fig. 14). Both the reaction routes can generate the complex products according to schemes E1–E3; Fig. 15 show isomerisation reactions for the two Bd isomers as well as dBd isomers.

We have examined the possible reaction schemes and ensured true energy minimum without the presence of imaginary frequencies for each participant. The use of the scheme and other thermodynamic functions suitable to determine the convenient reaction path to the product's complex development is inevitable. The CO_2 loss at C_2 and the hydroxyl group of the betacyanin molecule combined with L0 propose the various likely schemes. The methods and procedures implemented by previous works (Ioannidis & Kulik, 2015; Ismael, 2012; Makoye *et al.*, 2020; Vovna *et al.*, 2012; Becke, 1993; Lee *et al.*, 1988; Myrseth *et al.*, 2002). The dye design considers the research philosophy as addressed in Fig. 16. The fundamental tenets cover searching firstly and identifying the stable geometries; secondly, design a complex dye from the obtained stable geometry dye of the bent structure; thirdly, analyse the effect of solvent and thermodynamic properties.

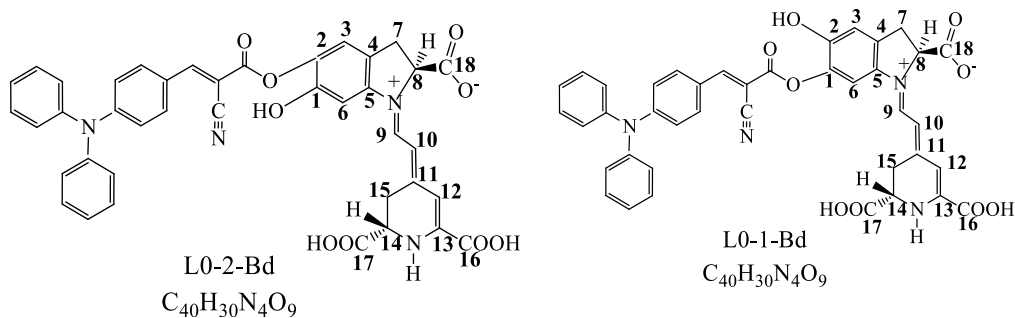


Figure 13: Betanidin and L0 dye complex

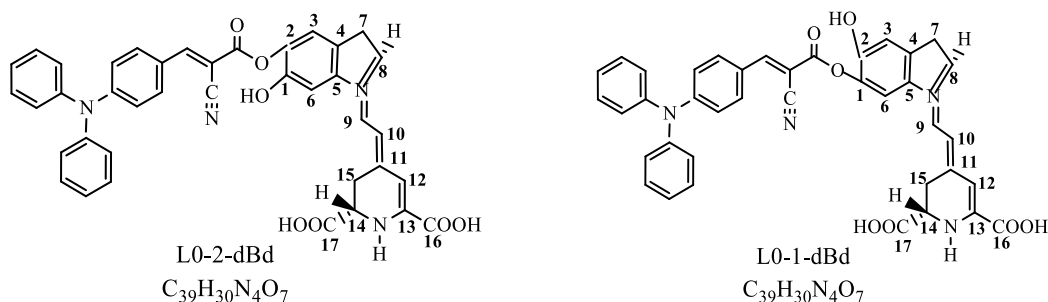
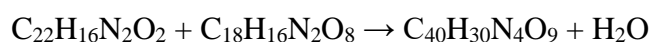


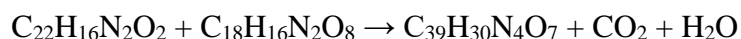
Figure 14: Decarboxylated betanidin and L0 dye complex



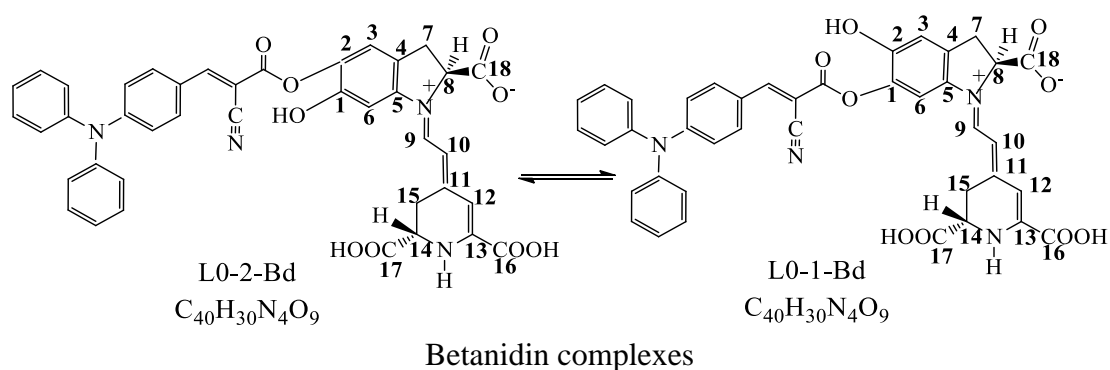
Equation E1: Formation of the betanidin complex with ester group at the betanidin's C₂ or C₁ carbon. The formed complex is due to the reaction of L0 and betanidin, and another product is water



Equation E2: Formation of the decarboxylated betanidin complex with ester group at the betanidin's C₂ or C₁ carbon. The formed complexes are due to L0 and decarboxylated betanidin, and another product is water



Equation E3: Formation of decarboxylated betanidin complex with ester group at C₂ or C₁ of the betanidin. The formed complexes are due to L0 and betanidin's reaction; other products are CO₂ and water



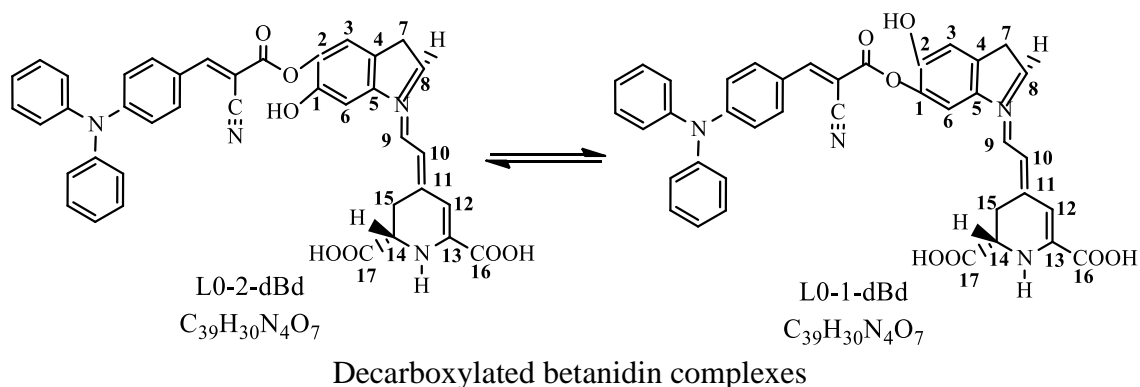


Figure 15: The isomerisation reaction

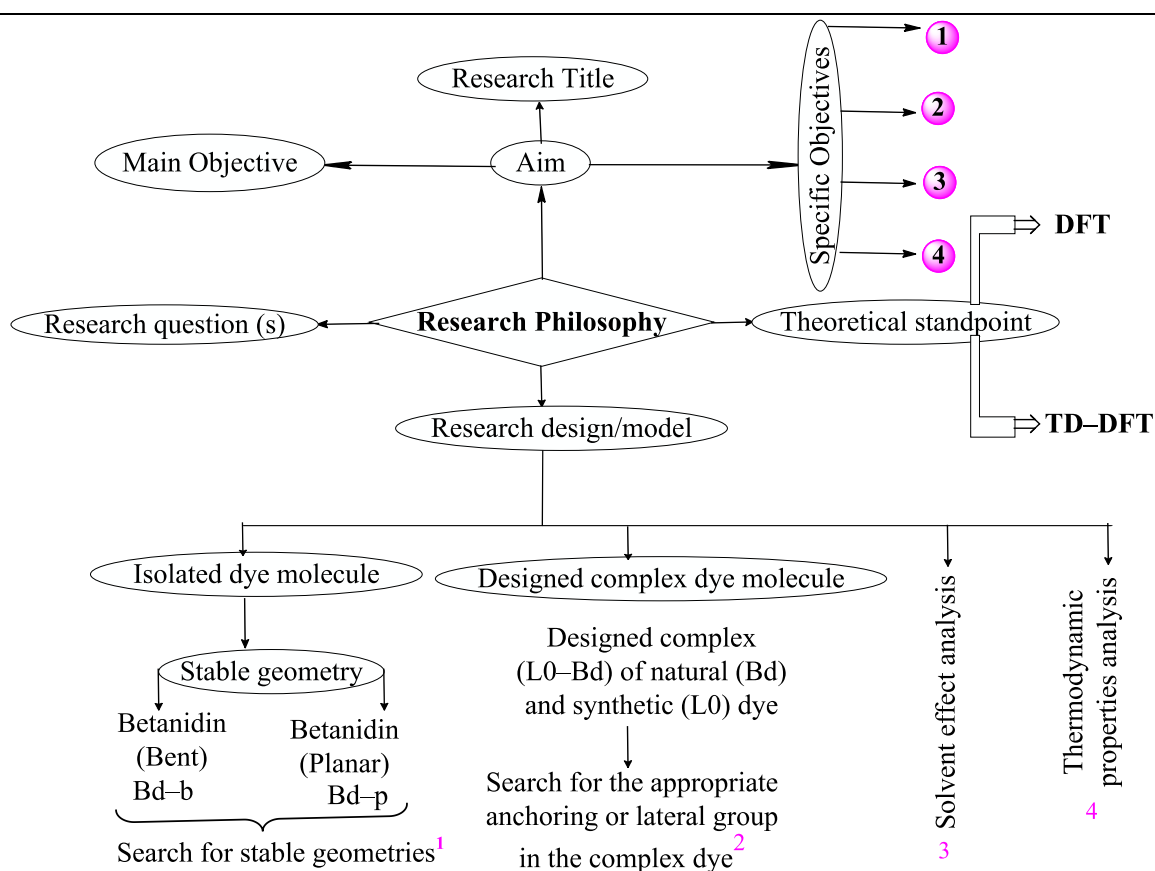


Figure 16: The research philosophy describes the fundamental tenets of the study

3.6 Computational details

The geometrical structure was obtained from the initial atomic coordinates of the individual and the designed complex dyes to investigate their properties. The optimisation calculations of the structure help to realise the stable equilibrium geometry of the molecule through the existences of real frequencies, accounting for vibrational spectra of the feasible dye molecule. The evaluation of the electronic properties, chemical descriptors, charge transfer properties, and the dye's adsorption to the semiconductor characteristics is significant typical parameters for the DSSCs application.

3.6.1 Computation of geometry and vibrational spectra

The ChemSpider database shows the original molecular geometries of the selected dyes. Betanidin, L0 and decarboxylated betanidin are the individual dyes under consideration. The slight modification of the ChemSpider geometries (by rotation of hydroxyl groups) was done without distorting a given design for the rapid formation of intramolecular hydrogen bonds. Chemcraft (Zhurko & Zhurko, 2015) was implemented for this change. Avogadro software helps to achieve bending Bd-b and planar Bd-p shape molecules by using auto-optimisation with the universal force field (UFF) via molecular mechanics (MM) (Hanwell *et al.*, 2012). Input coordinates were obtained for all 3 individual molecules, Bd-b, Bd-p and dBd, using the GAMESS input generator. Avogadro software (Hanwell *et al.*, 2012) was used for design the complex dye molecular structures. The betanidin structure offers two different reaction pathways through the C₂ or C₁ carbon-connected hydroxyl group (Fig. 14 and 15). The interaction between the L0 dye, its hydrogen ion (H11), and the betanidin hydroxyl group forms a complex dye joined with an ester group. The density functional theory (DFT) with hybrid functional B3LYP5 (Becke, 1993; Lee *et al.*, 1988) and the basis set 6-31G(d,p) were used to optimise geometry and to calculate the vibrational spectra of the dye molecules. To the best of our knowledge, the functional proposed results are reliable for calculating of structural and optical properties of organic dye molecules (Ioannidis & Kulik, 2015; Ismael, 2012; Makoye *et al.*, 2020; Vovna *et al.*, 2012). An absence of imaginary frequencies indicates that the optimised structures match the lowest energy on the potential energy surfaces.

3.6.2 Calculation of the thermodynamic properties

Optimised geometric parameters and vibrational frequencies were applied in determining thermodynamic functions of the species in the gas phase: entropies $S^\circ(T)$, enthalpy increments $H^\circ(T) - H^\circ(0)$ and reduced Gibbs free energies $\Phi^\circ(T)$ calculated in "rigid rotor-harmonic oscillator" approximation through the OpenThermo software (Tokarev, 2007–2009). Furthermore, energies of chemical reactions, $\Delta_r E$, have been obtained through the total energies of products and reactants:

$$\Delta_r E = \sum E_{i_prod} - \sum E_{i_react} \quad (61)$$

The enthalpies of the reactions, $\Delta_r H^\circ(0)$, have been calculated through the expression:

$$\Delta_r H^\circ(0) = \Delta_r E + \Delta_r \varepsilon \quad (62)$$

$$\Delta_r \varepsilon = \frac{1}{2}hc(\sum \omega_{i_prod} - \sum \omega_{i_react}) \quad (63)$$

where $\Delta_r \varepsilon$ is zero-point vibration energy (ZPVE); h represents the Plack's constant, c is the speed of light in free space, $\sum \omega_{i_prod}$ and $\sum \omega_{i_react}$ are the sums of the vibration frequencies of the products and reactants, respectively. The thermodynamic properties of the reactions $\Delta_r H^\circ(T)$, $\Delta_r G^\circ(T)$, $\Delta_r S^\circ(T)$ and $\Delta_r \Phi^\circ(T)$ are calculated from classical thermodynamic expressions:

$$\Delta_r H^\circ(T) = \Delta_r H^\circ(0) + \Delta_r [H^\circ(T) - H^\circ(0)] \quad (64)$$

$$\Delta_r G^\circ(T) = \Delta_r H^\circ(T) - T\Delta_r S^\circ(T) \quad (65)$$

$$\Delta_r \Phi^\circ(T) = -\frac{\Delta_r G^\circ(T) - \Delta_r H^\circ(0)}{T} \quad (66)$$

$$\Delta_r \Phi^\circ(T) = -\frac{\Delta_r [H^\circ(T) - H^\circ(0)] - T\Delta_r S^\circ(T)}{T} \quad (67)$$

3.6.3 A theoretical framework to study the betacyanins for DSSCs application

The electronic structure problem was identified, and a numerical solution was required to understand characteristics of the betacyanin dye molecule. It is a Density functional theory that was considered. It is because the foundation of understanding the *ab initio* electronic structure follows the Hohenberg-Kohn-Sham theorem, which states that the energy of the ground electronic states is a unique functional of the electron density. Understanding and predicting the properties like UV-Vis absorption/emission characteristics, optoelectronic properties, and the route to synthesise materials of target properties is required.

The B3LYP5 functional implemented in Firefly software was selected because of being efficiency in predicting properties of the organic molecules close to experimental values. The CAM-B3LYP was taken because B3LYP5 failed to study adsorption of the dye to TiO₂ cluster through Firefly, so studies shifted to Gaussian Software with this functional reported to work better for UV-Vis absorptions and optical properties (Deogratias *et al.*, 2019; Zhang *et al.*, 2018). From our observations, we found that in Firefly Software, B3LYP5 for the isolated systems in TD-DFT produced findings closer to the experimental when compared to the CAM-B3LYP. Therefore, we propose that further studies may work to compare these

functional in one package software system. In order to understand the approach to the study, the research questions, as well as the components of the research paradigm, were the helpful tool for the interconnectedness of the framework (Fig. 17).

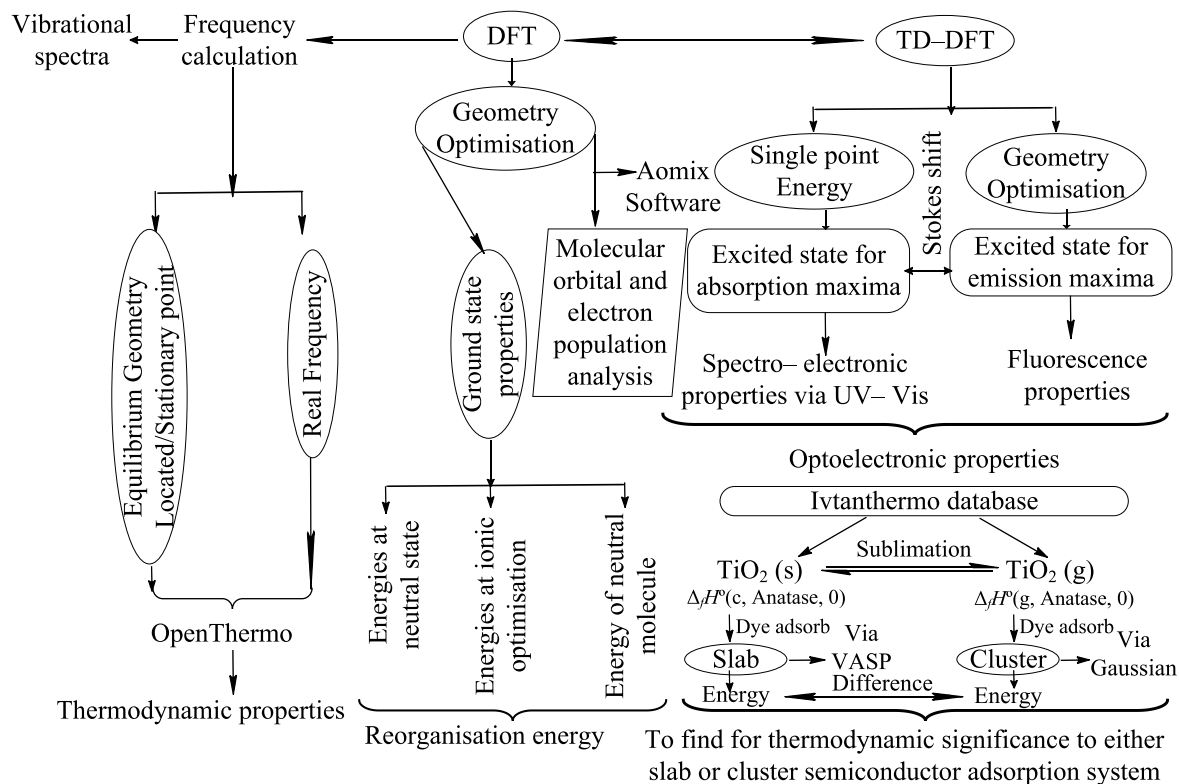


Figure 17: Theoretical framework for the interconnectedness of the tools and variables

3.6.4 Solvation models

Quantum chemical packages usually deal with molecules in gas phase as isolated species that do not interact with each other. Whereas this creates a simplistic environment for calculation, the system's chemical environment's impact is not taken into account. These effects can be significant for biologically relevant molecules, as almost all biologically happen in solution (Cramer, 2013). Solvation has been investigated extensively with various theoretical methods on the electronic states of multiple molecules (DeFusco *et al.*, 2011). The theoretical studies by DeFusco *et al.* (2011) and Ren *et al.* (2012) demonstrate these effects by altering the two lowest energy bands of the altered solvation position in their selected molecules in the UV absorption spectrum. Both studies found that when calculating the absorption spectrum in solution, the lowest energy spectral band of molecules was moved to a shorter wavelength. In contrast, the calculated aqueous absorption molecule spectrum showed a significant shift in the second-lowest spectral band's position to a longer wavelength (DeFusco *et al.*, 2011; Ren

et al., 2012). Changes in spectral absorption band lengths result from a solvent shift, so these changes are referred to as bathochromic or hypsochromic shifts.

In addition to being affected by solvent-induced changes in absorption bands, solvation can also affect bands. An increase in spectral band absorption intensity is known as the hyperchromic shift. In contrast, a decrease in absorption intensity is called a hypochromic shift (Das, 2012). In recent years, extensive research has been undertaken to develop models for studying solvation effects. The two main types of such approaches can be divided into explicit and implicit models.

(i) Explicit solvation model

Some discrete solvent molecules circle the solution in explicit solvation models (Lewars, 2003). Although this method provides a detailed and precise description of the solvent-solvent interactions, it is costly computationally because of the increased system size. The calculations of statistical mechanical averages are responsible for a substantial proportion of computational demand. The system contains numerous molecules and requires statistical averages to check its balance properties. The system is large, which generally restricts the use of explicit solvent models to Monte Carlo and Molecular Dynamics simulations (Skyner *et al.*, 2015).

(ii) Implicit solvation model

Implicit models decrease the calculating costs by replacing each solvent molecule with continuous medium. The medium surrounds a cavity in which the system is located in an implicit continuum model (Skyner *et al.*, 2015). The cavity shape is closer to the system studied, but its precise dimensions depend on the continuum's specific model. Only a few parameters define the continuum. It usually has characteristics such as the dielectric constant or surface voltage and values that correspond to the ideal solvent. Implicit models provide an average representation of solute-solvent interactions and are not appropriate for studies in which explicit solvent behaviour is important (Cramer, 2013).

The polarisable continuum model (PCM) is a commonly used model for electrostatic interactions, an implicit method. The PCM advantages are that they can represent a statistically averaged (continuous) solvent to achieve significant results in one calculation. The PCM models are advantageous to model reactivity and spectroscopy of various solvents

with different polarities (Tomasi *et al.*, 2005). Solvent water molecules preferably orientate their negative dipoles towards the solution's positive charge in a solvent-solute system, where atom Q (solute) has a positive charge. The orientation is less than its mean thermal fluctuations for only one water molecule. There is only a slight preference. The cavity in PCM consists of superimposed spheres with radii scaled to the Van der Waals atom. The solution's overall form of the cavity is defined as each sphere being an atomic centre. There are cavity regions with which solvent cannot interact, so a solvent-accessible surface area (SASA) around the cavity is outlined (Tomasi & Mennucci, 2002). Only the dielectric constant defines the continuum and its degree of polarisation. The solvent polarisation takes place in a self-consistent fashion. The charge density of the solute leads to dielectric continuum polarisation.

In turn, it polarises the solution and forms a reaction field (Tomasi & Mennucci, 2002). These response fields can be calculated using point charge, given that the charge spreads across the cavity surface. The SASA is divided into small fragments called tesserae, and the point charge is determined at each fragment (Tomasi *et al.*, 2005). In conjunction with TD-DFT, PCM models frequently include solvent effects in excited states' studies. For example, Han *et al.* (2015) used a variant PCM, IEFPCM, to investigate various complexes with heterocyclic carbene platinum (II) complexes for photophysical properties.

Non-electrostatically contributions to solvation-free energy are not experimentally measurable in continuum models for non-electronic interactions like electrostatic components in solvation-free energy. Therefore, some effects could be more susceptible than others to the solubility of experimental systems. Following this, several neutral model systems were developed. For example, for calculating cavitation-free energy through solvation energy observation for noble gases, specific model components like Pierotti (1976) were used to develop a model formula based on the theory of scaled particles. Another is atomic surface tension, which uses the atomic or group-specific and proportionate area of the atomic surface to assess non-electrostatic components of solvation-free energy. The present study uses the PCM model in its calculations and most of the findings agree with the previous reported data.

3.6.5 Electronic properties

The electronic excitations were studied through the time-dependent density functional theory (TD-DFT). This TD-DFT is an extension of DFT used to study the system's excited state

properties (Nogueira *et al.*, 2003). These obtained properties will help us to understand the desired performance of the molecule. The Gaussian 16 (GW16) package version (Frisch *et al.*, 2019) and Firefly software are applicable only for individual dye in an excited state, geometry optimisation and frequency calculation. The ground state's geometries were optimised using the DFT/B3LYP5 and DFT/B3LYP methods. The B3LYP5 performs an analysis using Firefly software. The ground state for B3LYP was optimised for both Gaussian and Firefly software, while the CAM-B3LYP functional was applied via Gaussian. Frequency calculations were carried out to ensure that optimised geometric structures on the potential energy surfaces represent real minima. The experimental spectra for natural sensitisers were taken from (Zhang *et al.*, 2008), while spectra for synthetic dyes were measured by Marinado *et al.* (2009).

The TD-DFT calculations contribute to achieving emission data at B3LYP/LANL2DZ alongside optimised excited state structures. For each system, formatted checkpoint files with B3LYP/LANL2DZ were created for viewing molecular orbitals (MOs). Solvation has also been studied in the PCM, the default version in GW16, to calculate CPCM/TD-DFT on CAM-B3LYP/LANL2DZ to simulate UV-Vis spectra for excitation energies of the designed dye materials. The calculation of CPCM in GW16 was done with water as a solvent.

3.6.6 Chemical molecular descriptors

A descriptor represents a particular type of feature, such as either chemical, physical, topological or energetic attributes of a chemical structure. The form and derivation of these descriptors can vary significantly to their features. A descriptor is generally a vector of individual numerical values (features) in an ordered list, each encoding specific information concerning a single molecule (Leach & Gillet, 2007). It contains the essential details about a particular molecule. Information like electrophilicity; chemical hardness; chemical softness; chemical potential; electronegativity, and net electrophilicity can be more straightforward. In general, the information can usually be either the molecular weight or the count of a particular atom type or the prediction of relevant experimental quantities. However, semi-empirical or quantum chemists may derive them from complex or isolated molecular modelling attempts. There is a clear difference in the cost of calculating various descriptors. Descriptors with higher refinement levels and, consequently, more useful molecular discrimination are often subject to higher computational costs. Different molecular descriptors and several software pieces can be used to calculate those (Leach & Gillet, 2007).

(i) Global properties

Global properties are characteristics of a molecule or a subsystem that apply at a macroscopic level.

Electronegativity

Electronegativity is an earlier idea initiated in 1932 by Pauling (1932; 1960), which describes how an atom can attract electrons in a molecule. Thermodynamics arguments regarding bond energies have quantified this concept by Pauling and led to the idea of property scaling as the square root of energy. Some years later, Mulliken (1934) suggested a rather simple definition of electronegativity, the arithmetic mean value of ionisation energy and EA .

This definition leads to the homogeneous property. Pauling and Mulliken's scales are most commonly used to compare the electronegativity of elements. Gordy, Allred-Rochow, Sanderson, and many other researchers have proposed other definitions of electronegativity. Most Chemists consider Pauling's scale the best electronegativity scale, even though it is less well-founded than Mulliken's. It should be pointed out that these scales do not match precisely as the scale of Mulliken is homogenous to energy, whereas Pauling's is homogenous to a square root of energy. Others are still different in terms of their dimensions, such as forces or other physical quantities or dimensionless. The theory cannot be explained in the linear connections between the electronegativity of Mulliken and the one suggested by Pauling in the past (Hinze & Jaffe, 1962; Pritchard & Skinner, 1955).

However, the conversion factor must be proportional to a square root of the energy factor that can be obtained through a contribution from conversion to this factor if a linear relationship is recognised between Mulliken's and Pauling's scales. Komorowski (1987) achieved promising results for a collection of bonds and molecules in which the hardness of the van de Waals radius was estimated.

Electronegativity is a chemical potential, a concept that originated in the work of Gyftopoulos and Hatsopoulos (1968). Interestingly, the definition of the Equation 68 is the finite difference approximation from that of a partial energy derivative E versus the number of electrons (Iczkowski & Margrave, 1961) also pointed out. Therefore, this expression can be naturally obtained within the context of DFT by identifying electronegativity (Parr *et al.*, 1978), χ to minus the chemical potential, μ :

$$\chi = -\mu = -\left(\frac{\partial E}{\partial N}\right) \quad (68)$$

The idea of orbital electronegativities is rather old (Hinze & Jaffe, 1962) and (Liu & Parr, 1995) have later discussed it.

Hardness and softness

Hardness, h , is the second derivative of the number of electrons concerning mass number; corresponding to the global softness, S , is equal to its inverse. Considering the energy variation when an electron is added or removed from the system, finite differences are approximated:

$$\chi = \frac{IP + EA}{2} \quad (69)$$

$$\eta = IP - EA \quad (70)$$

$$S = \frac{1}{h} = \frac{1}{1 - EA} \quad (71)$$

IP and EA are the vertical energy of ionisation and electron affinity, respectively, according to the partial derivative's continuous external potential:

$$IP = E(N = N_0 - 1) - E(N = N_0) \quad (72)$$

$$EA = E(N = N_0) - E(N = N_0 + 1) \quad (73)$$

N_0 is the amount of electrons in the system's ground conditions (usually neutral but charged). Therefore, a small size atom favours hardness. The atom size was introduced in the definitions of electronegativity (i.e., Gordy $[Z/r]$ (Gordy, 1946a, 1946b), Allred-Rochow $[Z/r^2]$ (Allred & Hensley, 1961; Allred & Rochow, 1958) and before any relationship between electron negativity and hardness.

(ii) Electrophilicity

Electrophilicity (Carey & Sundberg, 2007; Carruthers *et al.*, 2004; Lowry & Richardson, 1987) is one of the key concepts to streamline a wide range of organic reactions. Its

connection to the acidity and oxidation of Lewis increases its field of applicability. It provides adequate information on the structure, properties, reactivity, dynamics of many electrons systems, their aromatic and toxicity (Chattaraj & Giri, 2009; Chattaraj & Roy, 2007; Domingo *et al.*, 2007; Domingo *et al.*, 2008). Since both electrons and nuclei are contained in molecules, the electrophile (also a nucleophile) faces attractive and repulsive forces during the reaction. This also applies to a molecule for an atom/group. It would be a net electrophilicity (electrophilicity of a system relative to its nucleophilicity) explaining any species' electrophilic power. Precisely, a species' net electrophilicity measures the electron's acceptance power compared to its electron-donation power. Inspired by Maynard *et al.* (1998) work and Parr *et al.* (1999) have provided an electrophilicity (ω) described as:

$$\omega = \frac{\mu^2}{2h} = \frac{\chi^2}{2h} \quad (74)$$

where μ is the chemical potential (negative of the electronegativity, χ) of a density normalisation Lagrange multiplier defined via the below expressions (Chattaraj, 2009; Geerlings *et al.*, 2003; Parr, 1980; Parr *et al.*, 1978):

$$\mu = -\chi = \left(\frac{\partial E}{\partial N} \right)_{v(r)} \approx -\frac{IP + EA}{2} \approx \frac{E_{\text{HOMO}} + E_{\text{LUMO}}}{2}$$

and h is the hardness given by Parr and Pearson (1983) and Pearson (1997):

$$h = \left(\frac{\partial^2 E}{\partial N^2} \right)_{v(r)} \approx IP - EA \approx E_{\text{LUMO}} - E_{\text{HOMO}} \quad (75)$$

In this N-electron system with total energy E , and the external potential $v(\mathbf{r})$, IP is the ionisation potential, and EA is the electron affinity. At the same time, E_{HOMO} and E_{LUMO} are the energies of the highest-occupied and lowest-unoccupied molecular orbitals. In a significant and ground-breaking work Gazquez *et al.* (2007) have defined electron-donating (ω^-) and electron-accepting (ω^+) powers as:

$$\omega^- = \frac{(\mu^-)^2}{2h} \quad (76)$$

$$\omega^+ = \frac{(\mu^+)^2}{2h^+} \quad (77)$$

where the directional derivatives μ^\pm and h^\pm are associated. The definitions, as reported by Gazquez *et al.* (2007) of (ω^-) and (ω^+) are two different terms that have been defined as:

$$\omega^- = \frac{IP^2}{2(IP - EA)} \quad (78)$$

$$\omega^+ = \frac{EA^2}{2(IP - EA)} \quad (79)$$

Hence, by using an alternative interpolation of energy:

$$\omega^- = \frac{(3IP + EA)^2}{16(IP - EA)} \quad (80)$$

$$\omega^+ = \frac{(IP + 3EA)^2}{16(IP - EA)} \quad (81)$$

It should be noted that a greater value ω^+ corresponds to an improved ability to receive charges, whereas a smaller value of ω^- is a better electron donor of a system. The decision to compare ω^+ with $(-\omega^-)$ considers the balance of comparison between ω^+ and ω^- as a way to see how a system will behave. A method, therefore, proposes that the net electrophilicity be defined as follows:

$$\Delta\omega^\pm = \omega^+ - (-\omega^-) = \omega^+ + \omega^- \quad (82)$$

Note that this quantity could be defined and kept intact by other means, for instance

$$(\omega^+ - (1/\omega^-)).$$

3.6.7 Relationship between descriptors and thermodynamics

Due to their potential impact on these model molecules' physical-chemical behaviour, theoretical analysis was extended into the global reactivity indexes. The reactivity indexes analysed included hardness (h), electrophilicity (ω), electron-accepting power (ω^+), and electron-donating power (ω^-). Absolute hardness is an important factor in Pearson's hard and soft acids and bases (*HSAB*). It shows that electrons are expected to flow from the low electronegative (*EN*) system to that of the high *EN*. It is also apparent that resistance to deformation or change is the common meaning of hardness.

The thermal chemistry process corresponds well to h , ω^+ , ω^- (Torres-García *et al.*, 2011). The lower hard molecules produce the most negative Gibbs free reaction energy, while the highest-hardness molecules correspond to the least thermodynamically favoured reactions. It appears important to remember at this time, given that the charging process stabilises the system's greater values so that the electrons can be received more easily. On the other hand, charge donation processes destabilise the system, indicating a greater capacity for electrons (Torres-García *et al.*, 2011) to be denoted to a smaller value of a given system. Consequently, these calculated reactivity indexes explain the available information on the different model reactions and the thermodynamic and thermo-chemical feasibility.

3.6.8 Charge transfer characteristics

The individual isolated of natural and synthetic dyes, as well as of newly designed dyes, are metal-free organic molecules constituted by the donor (D), π -bridge (π) and acceptor (A) moieties known as D- π -A character. The structure like these characters has caused an intramolecular charge transfer (ICT) from the subunit D to A when a dye absorbs the light (Dai *et al.*, 2015; Patel *et al.*, 2011; Wenger *et al.*, 2010; Zeng *et al.*, 2010a). The presence of the symmetrical axial conjugate group with the donor contributes to the shift in red in the charging transfer transition. With the high coplanarity of the dye molecule, higher E_{ox} charging characteristics are easily experienced, and the best photovoltaic performance is to be achieved (Fernandes *et al.*, 2017; Wang *et al.*, 2017).

The study analyses the possibility of charge transfer from donor to acceptor on electronic excitation; the dyes' electronic structure was simulated with the Gaussian package. The assessments were achieved by obtaining the following parameters: ionisation potential, reorganisation energy for electron affinities, injection of electrons and regeneration of electrons. The electron transfer from the donor part to the acceptor part once excited indicates the electrons can efficiently transfer from the donor part to the acceptor part once excited, resulting in fast electron injection from the LUMO of the dyes to the CB of the TiO₂. The axial-symmetric conjugate allows an efficient transfer of charge that is not hampered by the stereoscopic effect and leads to an effective charge transfer. Because the dihedral angle decreases, the inclined plane angle increases, as does the coplanarity among the donor and π -bridge; both are favourable for charge transfer.

(i) Ionisation potential, electron affinity and reorganisation energies

The designed dyes' anionic and cationic states are measured to evaluate the ionisation potential and electron affinities. A single point energy calculation was performed, which accepted geometries for the ions the same as those optimised for neutral molecules in the ground electronic state. The minimum energies were included on the potential energy surface. The electron was added or removed from the system, followed by open-shell calculations. When the electron is added or removed, the *IP* or *EA* is the difference between reference and open-shell energies. The *IP* or *EA* are categorised to be vertical and adiabatic termed as *IP_v* or *IP_{ad}* and *EA_v* or *EA_{ad}* through the following expressions:

$$IP_v = E^+(g_0) - E^0(g_0) \quad (83)$$

$$IP_{ad} = E^+(g_+) - E^0(g_0) \quad (84)$$

$$EA_v = E^0(g_0) - E^-(g_0) \quad (85)$$

$$EA_{ad} = E^0(g_0) - E^-(g_-) \quad (86)$$

$$HEP = E^+(g_+) - E^0(g_+) \quad (87)$$

$$EEP = E^0(g_-) - E^-(g_-) \quad (88)$$

where $E^0(g_0)$ is the energy of the neutral molecule in the ground state; $E^+(g_0)$ and $E^-(g_0)$ are the energies of cationic and anionic states at the optimised geometry of the neutral molecule; $E^+(g_+)$ and $E^-(g_-)$ are the energies of the cationic and anionic states at the optimised geometries of the respective cation and anion; $E^0(g_+)$ and $E^0(g_-)$ are the energies of the neutral molecule at the optimised geometries of the respective cation and anion. The total energies of neutral and ionised species are also taken into account.

The energy difference between an anion optimised in the neutral state, and an anion optimised in the anion state is the *electron extraction potential (EEP)* (Ulahannan *et al.*, 2020). The energy difference between the cation optimised in the cation and the anion optimised in the anion state is the *hole extraction potential (HEP)* (Ulahannan *et al.*, 2020).

In charge transfer processes, dye molecules' reorganisation occurs in neutral and ionised states. The reorganisation energies of holes λ_h and electrons λ_e can be evaluated as follows:

$$A_h = IP_v - HEP \quad (89)$$

$$A_e = EEP - EA_v \quad (90)$$

All these parameters are linked to intermolecular charge transfer, electrons and holes between the dye molecules and the dye and environment.

(ii) Electron injection and electron regeneration

The CT process is electron injection from the excited state of sensitiser towards the conduction band of the semiconductor of TiO₂, as well as the regeneration of the dyes in the ground state (Megala & Rajkumar, 2016). The oxidised dyes and the electrolyte and their discrepancies in potential contribution to the driving force work out the return of electron collection and dye regeneration (Megala & Rajkumar, 2016). This potential difference must be suitable to provide an adequate driving force for fast and efficient regeneration of the dye ground state. These situations intend to lower the charge recombination between the oxidised dye and the semiconductor of TiO₂, where the photoexcited electrons are injected (Irfan & Al-Sehemi, 2012; Zhang *et al.*, 2013). The better oscillator strength (*f*) and electron injection ability from the excited states of the dye to the CBE of the semiconductor is thoughtfully relevant to electron injection efficiency (Wang *et al.*, 2013). The free energy change for the electron injection (ΔG_{inj}) influences the electron injection rate and enhances the current density J_{SC} in DSSC. The electron injection of the dye molecules (ΔG_{inj}) can be estimated as the difference between the oxidation potential of the dye in the excited state and the edge of the conduction band of the TiO₂ semiconductor through Equation 92 (Li *et al.*, 2017; Naik *et al.*, 2017; Zhang *et al.*, 2012). It is acknowledged that the decay process from the first excited state (S_1) to the ground state (S_0) is vital for injecting the excited electron into the CB of TiO₂.

The excited state decay to the ground state is longer than the injection time as a prerequisite for the electron to reach CB. This situation will provide efficient charge transfer for the injection ahead of a radioactive or photochemical reaction. The longer excited-state lifetime τ for the sensitiser considered here will likely facilitate charge transfer. The τ value parameter of the dye derivatives in S_1 can be calculated by employing the Equation 91 retrieved straight from Einstein transition probabilities (Deogratias *et al.*, 2019; Li *et al.*, 2019; Wazzan & Irfan, 2018; Xu *et al.*, 2019):

$$\tau = \frac{1.499}{\Delta E^2 \cdot f} \quad (91)$$

where ΔE is the vertical excitation energy (in cm^{-1}) at the λ_{max} and f is the oscillator strength of the electronic state with the adsorbed dye molecule from the λ_{max} (Li *et al.*, 2015; Zeng *et al.*, 2010b). An efficient charge transfer (injection) from the excited state to the semiconductor is required. As the electron injection time should be shorter than the excited state decay to the ground state, it acts as the prerequisite before the radioactive or photochemical reaction occurs to have an efficient injection (Arunkumar *et al.*, 2018; Hardin *et al.*, 2012; Listorti *et al.*, 2011).

Sensitisers with longer excited-state lifetimes, τ , are expected to exhibit better charge transfer efficiency with a low possibility of charge recombination, resulting in high efficiency of the cell (Deogratias *et al.*, 2019). The free energy of the electron injection can be assessed through the TiO_2 CB and excited state oxidation potential of the dye $E_{\text{ox}}^{\text{dye}*}$:

$$\Delta G_{\text{inj}} = E_{\text{CB}}(\text{TiO}_2) - E_{\text{ox}}^{\text{dye}*} = E_{\text{CB}} - (E_{\text{ox}}^{\text{dye}} + E_{0-0}) \quad (92)$$

To the proposed dye, LUMOs energy levels lie above the edge of the CB, so we expect efficient charge injection. An assessment $E_{\text{ox}}^{\text{dye}*}$ is performed by dealing with electron injections from the unrelaxed excited states. As Koopman's theorem suggests, the $E_{\text{ox}}^{\text{dye}*}$ is withdrawn from the oxidation potential of the ground state $E_{\text{ox}}^{\text{dye}}$ and the vertical excitation energy. In a restricted (or closed) system, the HOMO energy is associated with the potential of the first oxidation (Obasuyi *et al.*, 2019) (i.e., $-E_{\text{HOMO}}^{\text{dye}} = E_{\text{ox}}^{\text{dye}}$). Now the $E_{\text{ox}}^{\text{dye}*}$ is expressed (Arunkumar *et al.*, 2018; Ramkumar & Manidurai, 2017) as:

$$E_{\text{ox}}^{\text{dye}*} = E_{\text{ox}}^{\text{dye}} + \Delta E \quad (93)$$

where ΔE is the first excitation energy corresponding to λ_{max} . It is a prerequisite condition which is well-known that the stated association is only logical if the entropy change all along the light absorption process can be neglected (Obasuyi *et al.*, 2019; Preat *et al.*, 2009) and in this study, we conclude consistently the same. The free energy of the dye regeneration ΔG_{reg} can be determined through the following expression (Deogratias *et al.*, 2019):

$$\Delta G_{\text{reg}} = E_{(I^-/I_3^-)} - E_{\text{ox}}^{\text{dye}} \quad (94)$$

where $E_{(I^-/I_3^-)}$ is the redox potential of the electrolyte in solvent (−4.83 eV) (Mishra *et al.*, 2009).

3.6.9 Adsorption of the dyes on the TiO₂ surface

Furthermore, we have simulated the adsorption of the dyes on the TiO₂ surface using DFT/B3LYP in Gaussian 16 (Frisch *et al.*, 2019). The LANL2DZ pseudopotential with 12 valence electrons (Hay & Wadt, 1985) has been described a titanium atom (Table 3) during complex optimisation and a basis set of 6–31G(d,p) for lighter atoms C, N, O and H was used. The complexes' electronic spectra are simulated using the hybrid CAM–B3LYP functional. Based on Syzgantseva *et al.* (2011), it became clear that hydrogenated (TiO₂)_nH, n = 1–10, had greater stability than corresponding naked clusters on the compromise between the computational cost and the results accuracy. During our work, the hydrogenated cluster was tried to complex the isolated dyes by various adsorption modes; either carboxylic acid or phenols groups were separated from the hydrogen atom during the composition. The entire optimisation has been carried out without structural constraints, and vibrational frequencies have been established to confirm that the complexes' geometry on potential surfaces corresponds to minima.

CHAPTER FOUR

RESULTS AND DISCUSSIONS

4.1 General information on the betanidin geometrical isomers

Betacyanins, from the chemical point of view, originate when betalamic acid reacts with the 3,4-dihydroxyphenylalanine. Betanin marks the presence of glycosylation, whereas betanidin results (Bartolotta & Calogero, 2020) due to the deglycosylation reaction. Experimental spectra of the red-purple betacyanins (i.e., betanin and betanidin) demonstrate intensive light absorption in the visible range (Bartolotta & Calogero, 2020; Jackman & Smith, 1996; Strack *et al.*, 2003; Zhang *et al.*, 2008). To the best of our knowledge, limited information on the use of betacyanins in DSSCs has been published, see, e.g., reference (Zhang *et al.*, 2008). The novelty of our work relates to the information on structural, thermodynamic, and optoelectronic properties of the betanidin dyes towards DSSCs application. The non-planar and planar conformational isomers of the betanidin are investigated. Moreover, through a thermodynamic approach, we consider isomerisation and decarboxylation reactions of the betanidin dyes aimed at the dye's instability analysis. In addition, we have attempted to model the attachment of the dye to the TiO₂ semiconductor.

4.1.1 Geometrical structure of the betanidin isomers and decarboxylated betanidin

According to the IUPAC nomenclature, the name of the betanidin is (C₁₈H₁₆N₂O₈) is 1-[(2E)-2-(2, 6-Dicarboxy-2, 3-dihydro-1H-pyridin-4-ylidene)ethylidene]-5, 6-dihydroxy-2, 3-dihydroindol-1-ium-2-carboxylate. The optimised structures of two conformational betanidin isomers, bent (Bd-b) and planar (Bd-p) as well as decarboxylated betanidin, dBd, are shown in Fig. 18. The selected geometrical parameters, bond lengths, valence and dihedral angles are given in Table 4; the Cartesian coordinates of atoms are listed in Appendix 1. The detachment of the CO₂ from the conformers, either Bd-b or Bd-p, leads to the equivalent configurations of the dBd with the same minimum energy. Between the two Bd conformers, the bent one appeared more stable by 8.3 kJ mol⁻¹ compared to its planar counterpart. The higher stability of Bd-b is apparently attributed to forming the intramolecular hydrogen bond O4-H4...O7 with bond lengths 1.007 Å, 1.678 Å and an angle of 170°. It is well known from the literature, e.g., (Pawar *et al.*, 2011; Rostkowska *et al.*, 1998; Todkary *et al.*, 2006; Vessecchi *et al.*, 2012) that intramolecular hydrogen bonds favour the stabilisation of molecules. Worth to note the Bd-p conformer is called 'planar'

conditionally due to coplanarity between the three rings of the molecule, whereas the CO₂-fragment locates almost perpendicular to the neighbouring five-membered ring.

Table 4: Selected geometrical parameters of the dye molecules: Bond distances in Å, bond angles and dihedral angles in degs

Moiety	Parameter	Bd-b	Bd-p	dBd	Qin and Clark (2007)
Benzenoid ring	C1-C2	1.415	1.414	1.411	1.419
	C4-C5	1.396	1.396	1.393	1.395
	H1-O1	0.970	0.970	0.970	
	H1...O2	2.110	2.110	2.111	
	O1-H1...O2	114.2	114.3	114.5	
Five-membered cycle with N1	N1-C8	1.486	1.462	1.350	1.484
	C7-C8-N1	104.5	105.3	112.0	
	C5-N1-C8	108.6	109.1	108.3	
	C4-C7-C8-N1	20.3	16.0	1.4	
Central moiety	N1-C9	1.315	1.324	1.365	1.331
	C9-C10	1.432	1.411	1.405	1.395
	C10-C11	1.373	1.379	1.382	1.397
	N1-C9-C10-C11	133.3	176.5	173.9	
	C8-C18	1.618	1.671	NA	1.541
	C18=O7	1.266	1.240	NA	1.205
	C13-N2-C14	116.9	117.8	115.3	
	N1-C8-C18	109.6	110.3	NA	
	H4-O4	1.007	0.973	0.972	
	H4...O7	1.678	NA	NA	
	H4-O4...O7	169.6	NA	NA	
Six-membered ring with N2	N2-C13	1.352	1.368	1.395	1.335
	N2-C14	1.453	1.445	1.448	1.450
	C13-N2-C14	116.9	117.8	115.3	
	C13-N2-C14-C15	47.6	46.4	53.7	
	C12-C13-N2-C14	7.0	17.5	26.2	

We can distinguish the bending of the betanidin structure *via* the central chain N1-C9-C10-C11 parameters: this twisted angle equals 133° in the Bd-b but close to the straight in the other two molecules; elongation of the outmost bonds, N1-C9 and C10-C11, by ~0.01–0.05 Å and shrinkage of the middle one C9-C10 by ~0.02–0.03 Å (Table 4). Worth to note that the elongation of the bond C8-C18, from 1.62 Å in Bd-b to 1.67 Å in Bd-p, seems facilitates the CO₂ detachment from the latter. The benzenoid ring is planar in all three molecules. At the same time, cycles containing nitrogen, five- and six-membered, are non-planar: the dihedral angles C4-C7-C8-N1 are 20.3°, 16.0° and 1.4° in the Bd-b, Bd-p and dBd, respectively, and C12-C13-N2-C14 are 7°, 17.5° and 26.2°, respectively; thus, the heterocycles are slightly bent in both conformers as well as in dBd. Comparison of our calculated geometrical parameters with results Qin and Clark (2007) obtained for the betalains molecules theoretically by similar DFT approach in Table 4. As is seen, our bond

lengths of the central chain in the three dye molecules generally accord well with respective values from the literature of Qin and Clark (2007).

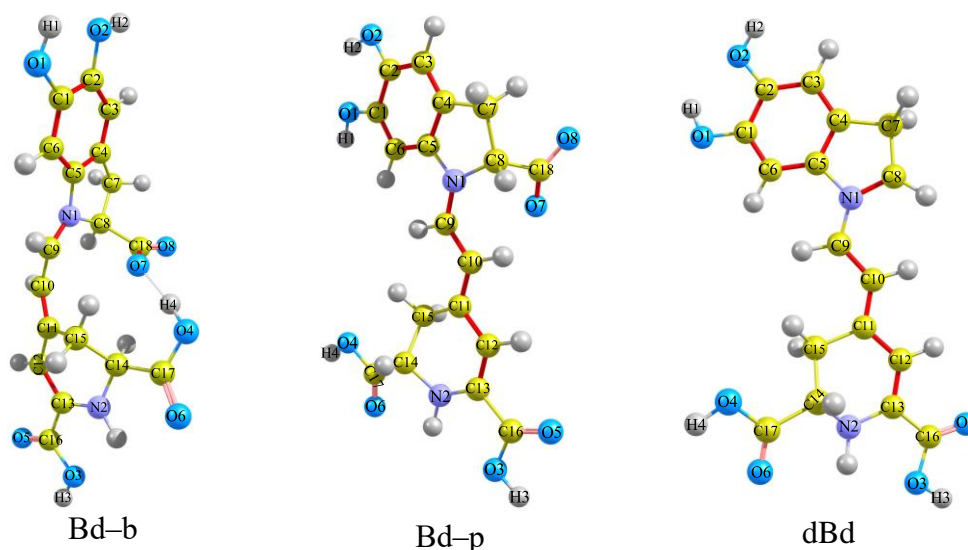


Figure 18: Optimised geometrical structures of the dye molecules

The position of proposed anchoring groups $-\text{COOH}$ and $-\text{CO}_2$ is essential for electron injection to the semiconductor. The respective dihedral angles θ have been analysed in detail for the optimised configurations of the dye molecules. In the vicinity of the nitrogen-containing six-membered ring, the angles θ , which link to the carboxylic groups, are in the range 10° – 15° ($\text{O6}=\text{C17}-\text{C14}-\text{N2}$), 3° – 7° ($\text{H4}-\text{O4}-\text{C17}-\text{C14}$), 0 – 3° ($\text{O3}-\text{C16}-\text{C13}-\text{N2}$) and 0 – 2° ($\text{O5}=\text{C16}-\text{C13}-\text{C12}$) in the Bd-b, Bd-p and dBd molecules. In the five-membered ring linked to the $-\text{CO}_2$ group, the angles $\text{O7}-\text{C18}-\text{C8}-\text{N1}$ are 13° and 36° for the Bd-b and Bd-p, respectively. The carboxylic groups have promising good dipole interactions with TiO_2 through bidentate chelate or bridging coordination to the surface (Finnie *et al.*, 1998; Hwang *et al.*, 2008; Park *et al.*, 2013). The lower θ reflects increased electronic interaction between the dye and semiconductor and helps to facilitate efficient electron injection through the π - π stacking of the dye molecule (Ahn *et al.*, 2006). From the above-analysed dihedral angles, the bent structure has lower θ values; thus, the Bd-b isomer is expected to show better sensitising properties among the three dyes. We do not consider the $-\text{OH}$ as the best candidate to bind with TiO_2 because the benzenoid ring acts as electron-withdrawing and stabilising the electronegativity of the hydroxyl oxygen atom through inductive effects (i.e., I effect). The electron delocalisation in the benzenoid ring structure occurs through the mesomeric effect (i.e., +M effect). In comparing these two effects, we understand that in our materials, the positive mesomeric impact dominates over the negative inductive effect. Therefore, these two $-\text{OH}$ at C_1 and C_2 of the benzenoid ring (Fig. 18) act as activating groups performing the role

of electron donors while the central chain C5–N1–C9–C10–C11–C12–C13–N2 acts as π -linker to the dye system leaving the –COOH as the anchoring groups and thus achieve D– π –A system.

4.1.2 Vibrational spectra of the betanidin and its decarboxylated isomer

In the IR spectra of the three dye molecules (Fig. 19), four regions may be observed, three of which — the low-frequency region (200–1000 cm^{-1}), the central part (1000–2000 cm^{-1}) and the high-frequency range (3500–4000 cm^{-1}) — look-alike in general.

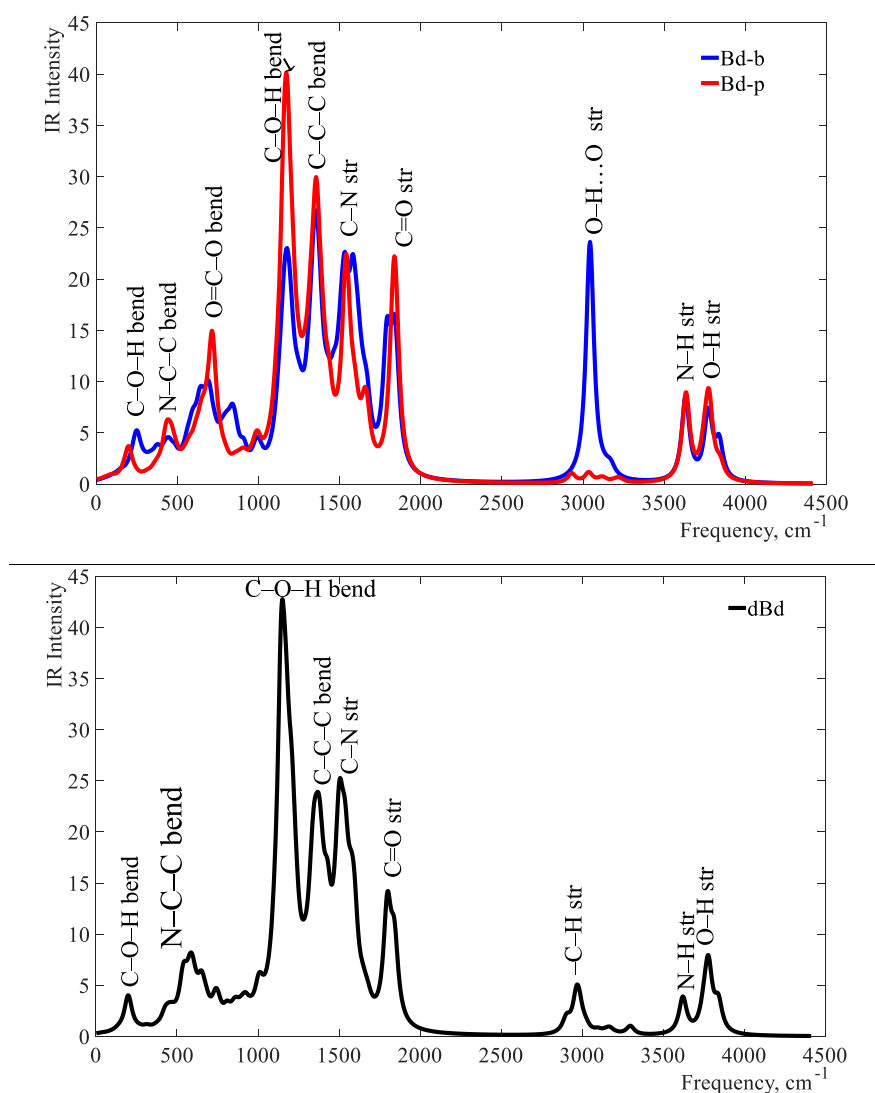


Figure 19: IR spectra of betanidin molecules (top) and decarboxylated betanidin (bottom)

However, a dissimilarity is seen in the region at the $\sim 3000 \text{ cm}^{-1}$. In the low-frequency range, bands are assigned to twisting and bending vibrations of cycles. The central part contains mostly C–O–H bending modes at 1140–1180 cm^{-1} and stretching vibrations of heavier atoms

(C–C, C=C, C–O, C=O, C–N and C=N) at 1500–1800 cm^{-1} . The high-frequency part corresponds to C–H, O–H and N–H stretching modes. The distinction between the spectra relates to the structural particularities of the molecules. In the Bd–b spectrum, the most intensive peak at 3043 cm^{-1} corresponds to the stretching vibration of the O4–H4...O7 group, which is found neither in the Bd–p nor in dBd. The intensive bands at 1790 cm^{-1} in Bd–b and 1840 cm^{-1} in Bd–p is assigned to the vibrations of the CO₂–a group linked to carbon C8; the difference of 50 cm^{-1} is apparently to the shortage in the respective C18=O7 bond, from 1.266 Å in the bent structure to 1.240 Å in the planar one. These two peaks in both betanidin molecules overlap the bands of C=O stretching vibrations (1828–1846 cm^{-1}) of the carboxylic groups COOH. As the latter is available in the dBd, the intensive band at 1798–1841 cm^{-1} is also found in the spectrum.

4.1.3 Thermodynamics of chemical reactions of the betanidin conformational geometrical isomers

(i) Isomerisation reaction of betanidin conformational geometrical isomers

The isomerisation reaction of the Bd molecule C₁₈H₁₆N₂O₈ has been considered:



The thermodynamic characteristics of the reaction, energy $\Delta_r E$, ZPVE $\Delta_r \epsilon$, enthalpy $\Delta_r H^\circ$, entropy, $\Delta_r S^\circ$ and Gibbs free energy, $\Delta_r G^\circ$, are presented in Table 5. In addition, the thermodynamic functions of the species in the gas phase: molar heat capacities $C_p^\circ(T)$, entropies $S^\circ(T)$, reduced Gibbs free energies $\Phi^\circ(T)$ and enthalpy increments $H^\circ(T) - H^\circ(0)$ are given in Appendix 2.

The bent conformer has lower energy and is more stable than the planar. The entropy of the reaction is positive, which is apparently due to a distinctive ordering of the Bd–b. The bent conformer seems less flexible as its lowest frequency is about 26 cm^{-1} whereas it is 15 cm^{-1} for the Bd–p. The elongation of the C8–C18 bond, mentioned above, brings to the loosening motion of the CO₂ moiety and sufficient entropy increase of the planar structure. The Gibbs free energy $\Delta_r G^\circ(298 \text{ K})$ is slightly negative, apparently due to the contribution of the entropy factor. The temperature dependences of the thermodynamic characteristics of the isomerisation reaction are shown in Fig. 21a. As is seen with temperature rise, the enthalpy and entropy of the reaction are slightly changing. The Gibbs free energy becomes more

negative, indicating the spontaneous reaction towards the planar isomer. The partial pressure ratio of two isomers p_{II}/p_I has been calculated for a temperature range from 298 to 600 K:

$$\ln \frac{p_{II}}{p_I} = \frac{\Delta_r \Phi^\circ(T)}{R} - \frac{\Delta_r H^\circ(0)}{RT} \quad (95)$$

The value p_{II}/p_I appeared to be 1.5 at room temperature, increasing to ~ 11 at 600 K (Fig. 21b). It implies that the isomer II (Bd-p) is more abundant than Bd-b; thus, despite the less energetic stability of the planar conformer, the higher entropy brings to its prevalence.

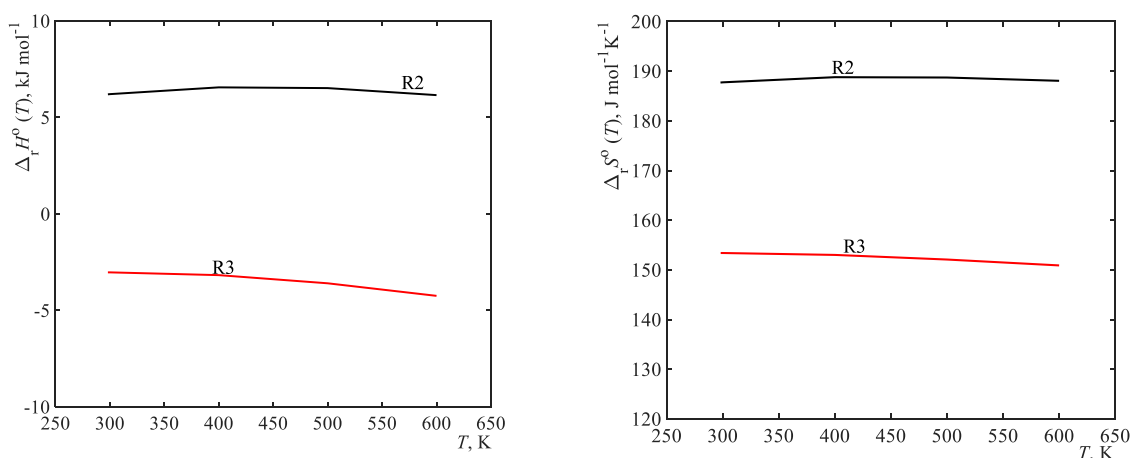


Figure 20: The enthalpies $\Delta_r H^\circ(T)$ (Left) and entropies $\Delta_r S^\circ(T)$ (Right) of the decarboxylation reactions, Bd-b \leftrightarrow dBd + CO₂ (R2) and Bd-p \leftrightarrow dBd + CO₂ (R3)

(ii) Decarboxylation reactions of the betanidin conformational geometrical isomers

Decarboxylation reactions of betanidin have been considered for both conformers:



Thermodynamic characteristics are given in Table 5. The enthalpies of the reactions indicate that reaction R2 is endothermic while R3 is exothermic. The difference between $\Delta_r H^\circ$ of R2 and R3 equals the enthalpy of the isomerisation reaction R1. The thermodynamic properties calculated from ambient temperature to 600 K are shown in Fig. 20. The values $\Delta_r H^\circ(T)$ and $\Delta_r S^\circ(T)$ demonstrated no change practically with temperature increase while the Gibbs free energy, $\Delta_r G^\circ(T)$ became more negative as seen in Fig. 21c. For both isomers, the decarboxylation reaction is spontaneous. Therefore, betanidin is expected to undergo decomposition with CO₂ release and dBd formation.

Table 5: Thermodynamic characteristics of chemical reactions

No.	Reaction	$\Delta_r E$, kJ mol^{-1}	$\Delta_r \varepsilon$, kJ mol^{-1}	$\Delta_r H^\circ(0)$, kJ mol^{-1}	$\Delta_r H^\circ(298)$, kJ mol^{-1}	$\Delta_r S^\circ(298)$, $\text{J mol}^{-1} \text{K}^{-1}$	$\Delta_r G^\circ(298)$, kJ mol^{-1}
R1	Bd-b \leftrightarrow Bd-p	8.3	-1.2	7.1	9.2	34.3	-1.0
R2	Bd-b \leftrightarrow dBd + CO ₂	13.7	-11.9	1.9	6.2	187.7	-49.8
R3	Bd-p \leftrightarrow dBd + CO ₂	5.4	-10.6	-5.2	-3.0	153.4	-48.8

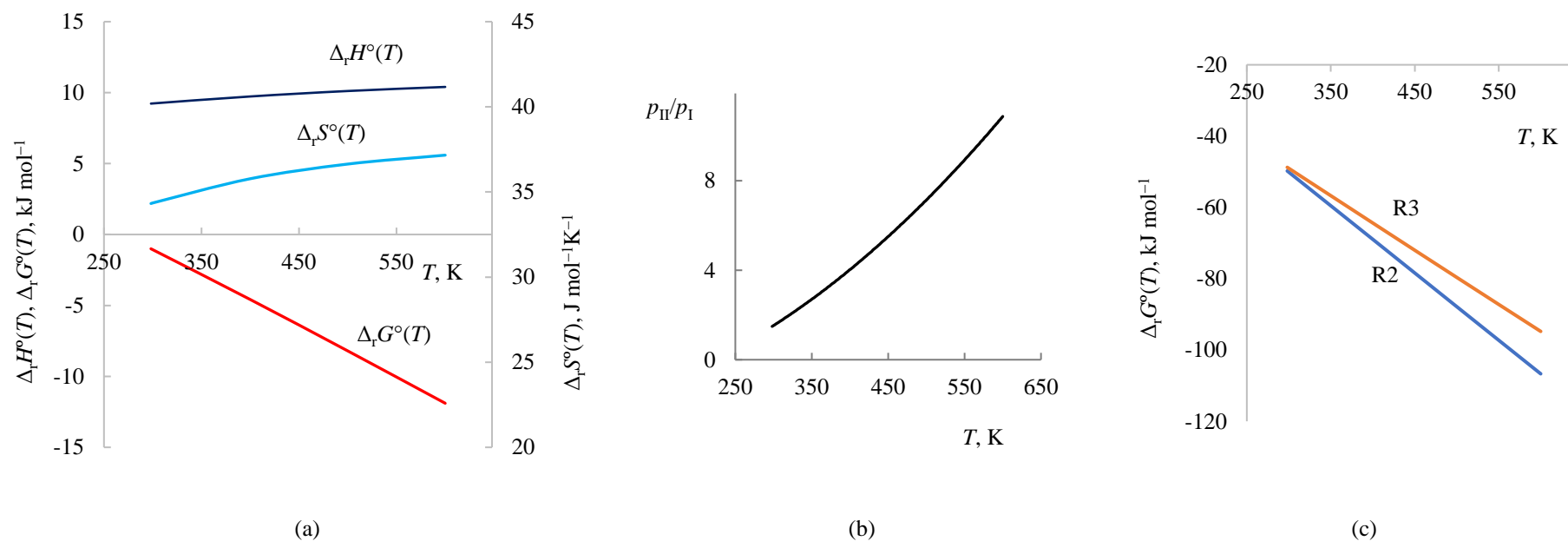


Figure 21: Thermodynamic characteristics: (a) of the isomerisation reaction Bd-b \leftrightarrow Bd-p (b) pressure ratio p_{II}/p_I of the betanidin conformational isomers, p_I stands for Bd-b, p_{II} for Bd-p (c) Gibbs free energies of decarboxylation reactions R2 and R3

4.1.4 Optoelectronic properties of the betanidin conformational geometrical isomers

(i) Frontier molecular orbitals of the Bd-b, Bd-p and dBd dyes molecules

A suitable electron density distribution over frontier molecular orbitals (FMOs), HOMO and LUMO, is essential for the charge transfer facilitation (Saravanan *et al.*, 2014) from the dye molecule to semiconductor surface and lessening chances of electron-hole recombination. Furthermore, knowing the dye parts responsible for electron transfer helps identify probable anchoring groups to metal oxide attachment. For the functional materials, we expect the LUMO electron density to concentrate on the electron acceptor, and a part of that acts as an anchoring group; such electron density will allow for secure binding with the semiconductor. The FMOs of the dyes are shown in Fig. 22; the calculated energies of HOMO, LUMO and energy gaps are indicated.

As is seen in all three molecules, there is no distinct redistribution of electron density between the HOMO and LUMO, except for the Bd-p carboxylic group being more populated with electrons in the LUMO. Also, some electron density shift to the benzenoid ring occurs in the LUMOs in the dBd (Fig. 22). Let us compare the FMOs isosurfaces between vacuum and solution. The respective MOs look alike the Bd-p and dBd, whereas a dissimilarity in the benzenoid ring population can be noted in the HOMOs of the Bd-p. The carboxylic groups, populated with electrons in LUMOs, can participate in intermolecular charge transfer. The non-planar moiety would control aggregation due to the interruption of the π - π^* stacking (Hagberg *et al.*, 2006).

Hence, the bent structure of the Bd-b is highly probable to prevent the dye aggregation; the π - π^* transition allows smoother electron delocalisation from the benzenoid to the extended conjugated part. As a result, the energy gap E_g decreases in series Bd-b \rightarrow Bd-p \rightarrow dBd while the HOMO and LUMO energies ascend in the same order, except for Bd-p LUMO in DMSO. A noticeable change in respective energies from betanidins to decarboxylated betanidin was observed. It is attributed to CO₂ detachment. The situation leads to the variation of the π -conjugated and anchoring groups and significantly affects the HOMO and LUMO energies.

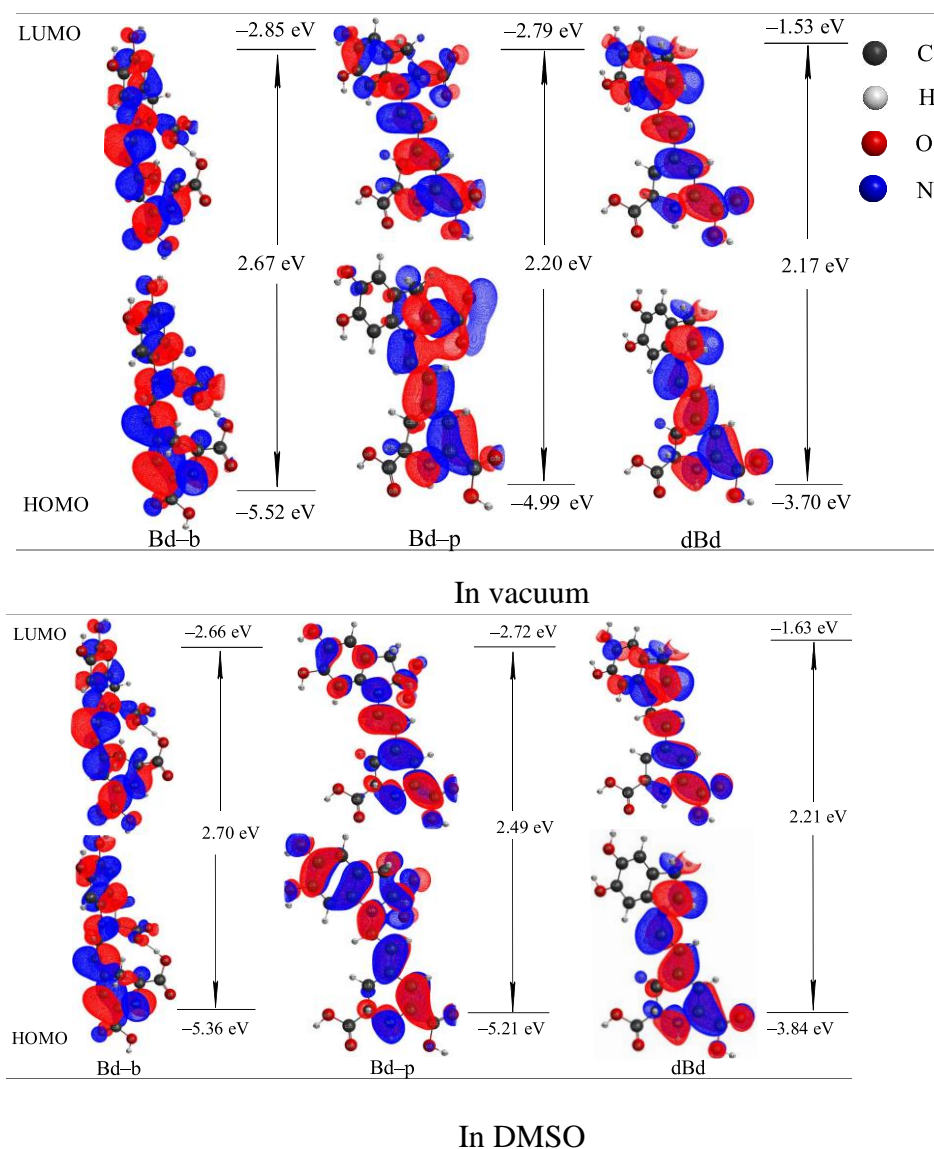


Figure 22: Frontier MOs of the considered dyes: Vacuum (top) DMSO solvent (bottom)

(ii) Electronic transitions and UV-Vis spectra of the Bd-b, Bd-p and dBd dye molecules

The DSSC is a photoelectric conversion device where the dye should have a high potential to absorb solar radiation to cover the whole visible and near-IR range. The TD has computed electronic spectra of the dyes-DFT/6-31G(d,p) method for vacuum and solvents, polar aprotic (DMSO) and polar protic (C_2H_5OH and H_2O); spectral band intensities were evaluated through oscillator strengths. The absorption properties were stipulated in terms of light-harvesting efficiencies, $LHE = 1 - 10^{-f}$ where f is the oscillator strength at a distinct wavelength. Higher values of the LHEs are desirable to maximise the photocurrent response (Janjua, 2017). Characteristics of electronic spectra, excitation energies ΔE_{0-n} , wavelengths λ ,

oscillator strengths f , LHEs and transition configurations are presented in Table 6; among the transitions, $S_0 \rightarrow S_n$, $n = 1-25$, those with $f > 0.1$ are taken into account. The simulated UV-Vis spectra of the dyes in a vacuum and solvents are shown in Fig. 23.

Table 6: Characteristics of electronic transitions $S_0 \rightarrow S_n$ in Bd-b, Bd-p and dBd computed with TD-DFT/B3LYP5/6-31G(d,p) for a Vacuum, and DMSO, C₂H₅OH and H₂O solvents

Dye	Medium	n	ΔE_{0-n} , eV	λ , nm	f	LHE, %	MOs contribution, %
Bd-b	Vacuum	1	2.35	527	0.361	56	H→L; 88
		2	2.54	489	0.134	26	H-1→L; 85
		4	2.99	415	0.101	21	H-2→L; 74
	DMSO	1	2.46	504	0.598	75	H→L; 99
	C ₂ H ₅ OH	1	2.46	505	0.595	75	H→L; 99
	H ₂ O	1	2.46	504	0.599	75	H→L; 99
Bd-p	Vacuum	3	2.32	536	0.388	59	H→L; 78
		4	2.69	460	0.643	77	H-2→L; 56
	DMSO	1	2.55	487	0.968	89	H→L; 100
	C ₂ H ₅ OH	1	2.53	488	0.959	89	H→L; 100
		2	2.78	446	0.077	16	H-1→L; 97
	H ₂ O	1	2.55	487	0.972	89	H→L; 100
dBd	Vacuum	1	2.44	508	0.626	76	H→L; 92
		2	2.74	452	0.280	47	H→L+1; 88
		3	3.22	383	0.143	28	H→L+2; 78
	DMSO	1	2.52	492	0.875	87	H→L; 101
		2	3.03	409	0.173	33	H→L+1; 86
		5	3.62	342	0.105	22	H-1→L; 76
	C ₂ H ₅ OH	1	2.52	492	0.869	86	H→L; 100
		2	3.03	410	0.174	33	H→L+1; 86
		5	3.63	342	0.105	24	H-1→L; 76
	H ₂ O	1	2.52	492	0.877	87	H→L; 102
		2	3.04	408	0.172	33	H→L+1; 86
		5	3.62	342	0.105	22	H-1→L; 76

For each dye molecule, in the spectrum for a vacuum, there are two intensive peaks seen in the visible range; Bd-b 527 and 489 nm, Bd-p 536 and 460 nm and dBd 508 and 452. Spectra of dye solutions in water, ethanol and DMSO look alike; only one intensive peak at 487–505 nm, and this excitation originates mostly from H→L transition. In solutions, the blue shift of spectral bands is seen compared to a vacuum; 22–23 nm (Bd-b), 48–49 nm (Bd-p) and 16 nm (dBd). When transferred from a vacuum to solution, the most substantial decrease of λ_{\max} for Bd-p can be explained by more distinct electron density redistribution between the HOMO and LUMO (Fig. 23). Worth to note that our simulated spectra of betanidin are in accordance with the experimental findings (Starzak *et al.*, 2012; Zhang *et al.*,

2008) where the UV–Vis spectra of aqueous beet extract were measured and a broadband 450–600 nm assigned to the betanin and betanidin pigments.

(iii) Charge transfer properties of the betanidin (Bd-b, Bd-p) conformational geometrical isomers and dBd dye molecules

A dye sensitizer requires appropriate energy levels of FMOs to possess the efficient performance of a DSSC. Therefore, the HOMO energy E_H should be more negative than the redox potential of the electrolyte (I^-/I_3^- , -4.83 eV (Mishra *et al.*, 2009) or spiro-OMeTAD, 5.05 eV (Nguyen *et al.*, 2014) and LUMO energy E_L should be above the conduction band energy of the semiconductor (TiO_2 , -4.05 eV (Fujisawa *et al.*, 2017). Drawing the frontier MOs energy levels with valence and conduction band edge of a substrate and the electrolyte redox level is considered the simple route to this alignment. However, it is more appropriate to represent excited states through excited states oxidation potentials (*ESOPs*) E_{ox}^{dye*} (Madili *et al.*, 2018; Makoye *et al.*, 2020; Oprea *et al.*, 2011). Therefore, the values E_{ox}^{dye*} have been obtained as sums of the occupied MOs and relevant excitation energies, as identified in Table 7. For the first excited state, the *ESOPs* values attained through the HOMO energies and the first excitation energies:

$$E_{ox}^{dye*} = E_H + \Delta E_{0-1} \quad (96)$$

The energy level diagram of the most relevant MOs of the species (dyes) in the DMSO solution is shown in Fig. 24. As observed, all considered dyes meet the criterion of the energy level alignment for the electron injection to be proper photosensitizers when a TiO_2 semiconductor is used because the *ESOP* levels lie above the conduction band edge of TiO_2 , allowing electron transfer to the substrate. To the side of occupied MOs, the HOMO levels of the betanidin conformers lie below the redox level of the I^-/I_3^- or spiro-OMeTAD electrolytes releasing electrons to the pigment molecule. However, the dBd does not satisfy the criterion on the dye regeneration as the HOMO energy lies above the redox potential of the electrolytes. Excitation energies have a substantial effect on DSSCs performance. Therefore, sensitizers with lower excitation energy are beneficial to facilitate light absorption in longer wavelength ranges. Regarding the first excitation energy ΔE_{0-1} , i.e., 2.46 (Bd-b), 2.55 (Bd-p) and 2.52 eV (dBd), all three dyes have an equal probability of sensitizing the semiconductor. Therefore, from the energy level diagram, one can conclude that the two conformers (Bd-b and Bd-p) are better candidates than dBd as sensitizers for the DSSCs.

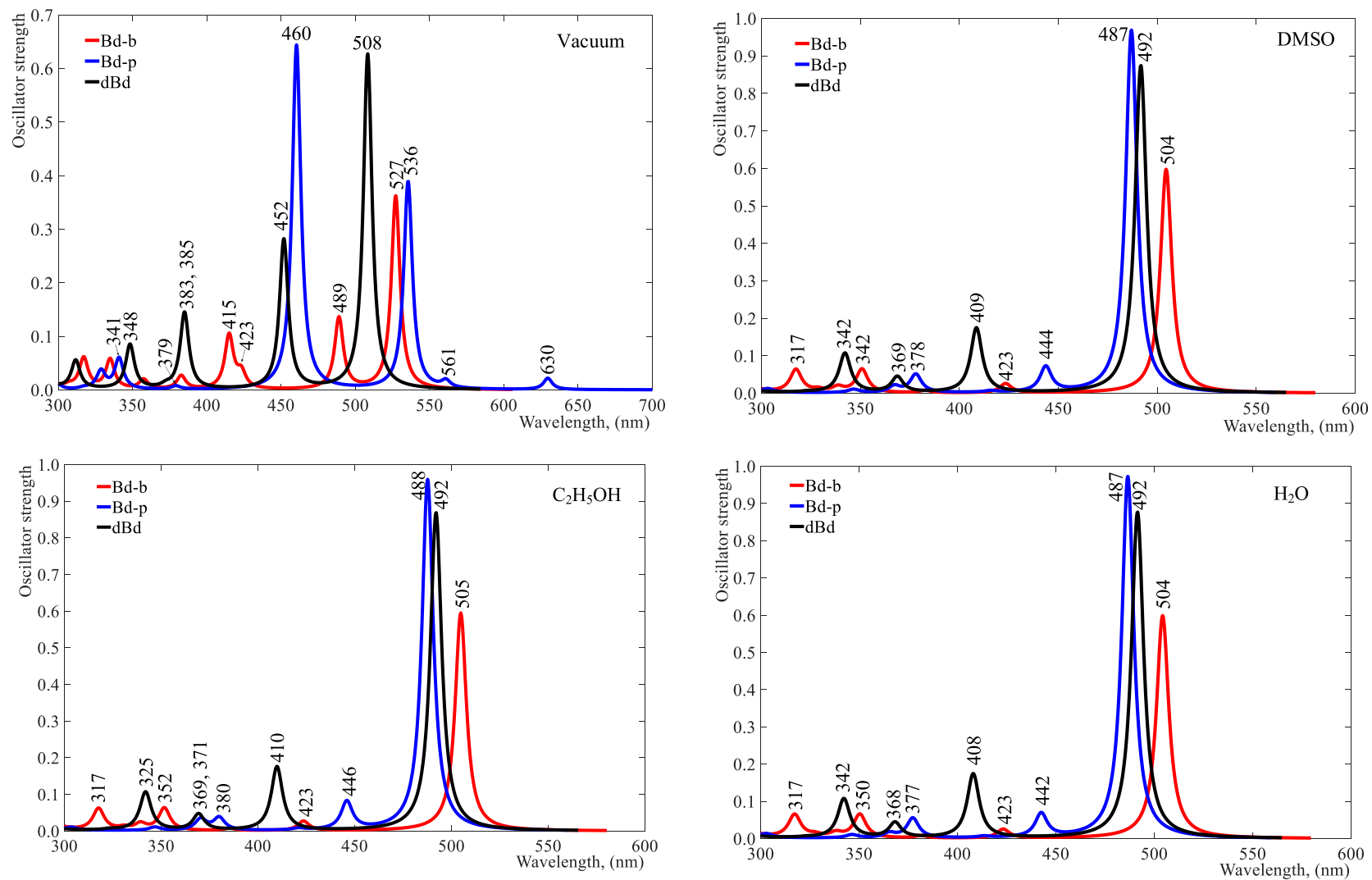


Figure 23: UV-Vis spectra of the dyes, Bd-b, Bd-p and dBd, simulated with TD-DFT/B3LYP5/6-31G(d,p) for a Vacuum, DMSO, C₂H₅OH and H₂O

Table 7: Energies of the molecular orbitals $\varepsilon(\text{MO})$, excitation energies E_{ex} , energy gaps E_{g} and excited states oxidation potentials $E_{\text{ox}}^{\text{dye}^*}$ of the selected states, DMSO solvent. The energies are in eV

Dye	MO	$\varepsilon(\text{MO})$	Transition	E_{ex}	E_{g}	$E_{\text{ox}}^{\text{dye}^*}$
Bd-b	101, H	-5.36	H→L	2.46	2.70	-2.90
	102, L	-2.66				
Bd-p	101, H	-5.21	H→L	2.55	2.49	-2.66
	102, L	-2.72				
dBd	90, H	-3.84	H→L	2.52	2.21	-1.31
	89, H-1	-5.62	H→L+1	3.03	3.50	-0.80
	91, L	-1.63	H-1→L	3.62	3.99	-1.99
	92, L+1	-0.34	H-1→L+1	4.82	5.28	-0.80

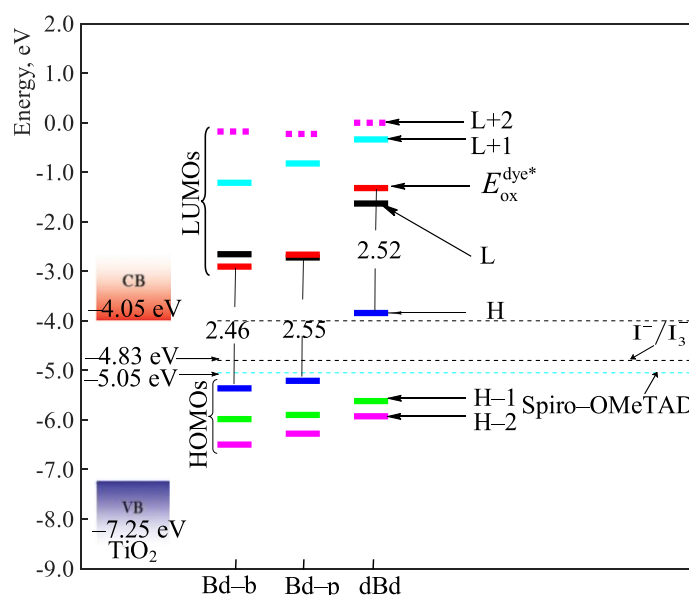


Figure 24: Energy level diagram of relevant MOs, excited state potentials $E_{\text{ox}}^{\text{dye}^*}$ and excitation energies ΔE_{0-1} for the dyes understudy for the DMSO solvent. Valence and conduction bands of TiO_2 (Fujisawa *et al.*, 2017), redox potentials for electrolytes, I^-/I_3^- (Mishra *et al.*, 2009) and Spiro-OMeTAD (Nguyen *et al.*, 2014) for comparison

Table 8: Calculated ionisation potentials (IP_{v} , IP_{ad}), electron affinities (EA_{v} , EA_{ad}), hole extraction potentials (HEP), electron extraction potentials (EEP), hole and electron reorganisation energies (λ_{h} , λ_{e}); all values are in eV

Dye	IP_{v}	IP_{ad}	HEP	EA_{v}	EA_{ad}	EEP	λ_{h}	λ_{e}
Bd-b	6.89	6.69	6.44	1.52	1.94	2.44	0.45	0.93
Bd-p	6.40	NA ^a	NA ^a	1.47	1.84	2.20	NA ^a	0.73
dBd	5.09	4.85	4.64	0.26	0.62	1.06	0.45	0.80

^aFor the Bd-p cation. Optimisation of geometry resulted in the system comprising the decarboxylated betanidin cation and CO_2 .

The results demonstrate that during the optimisation procedure of dye ionic forms, the bent isomer Bd-b undergoes safe hole and electron reorganisation. In contrast, the Bd-p cationic form is to decompose into the dBd-cation and CO_2 . The stability of the Bd-b ionic forms is apparently attributed to the intramolecular hydrogen bonding. Based on the DFT analysis,

Qin and Clark (2007) found that betanidin's low-frequency and very flat potential energy surface led to larger artificial displacements and a failure in reorganisation energy. With our designed Bd-p, we have also failed to obtain the hole reorganisation energy due to automated CO₂ detachments from the cationic dye system; in this aspect, we agree well with the findings in reference (Qin & Clark, 2007).

The ionisation potentials of the Bd-b and dBd molecules appeared to be rather low and comparable with those of typical organic molecules used in DSSCs (Tripathi & Prabhakar, 2018). Among the three dyes, the dBd has the lowest *IP* and *EA* values; hence it is a good electron donor but a poor electron acceptor. The reorganisation energies for holes, $\lambda_h = 0.45$ eV, are lower than for electrons, $\lambda_e = 0.73$ – 0.93 eV (Table 8), which indicates higher hole mobilities. Worth to note that both types of reorganisation energies of dyes considered are rather high compared to typical charge transport materials (~ 0.2 – 0.3 eV) (Lin *et al.*, 2005; Tripathi & Prabhakar, 2018).

A bar diagram in Fig. 25 also compares the relevant electronic energies. The value of minus HOMO energies ($-E_H$) are considerably less by 1.1–1.5 eV than *IP*s, while the magnitudes of LUMO energies ($-E_L$) are greater than electron affinities, being comparable to respective *ESOP*s. Regarding the electronic energy properties, like suitable energy levels of E_H or E_L with reduced energy gaps, lower first excitation energies, lower *IP* and higher *EA* values, the results help argue that the dye is appropriate for DSSC. Generally, from our analysis, the dyes cannot be ranked in a particular order because one demonstrates better donor properties but a poor acceptor and vice versa.

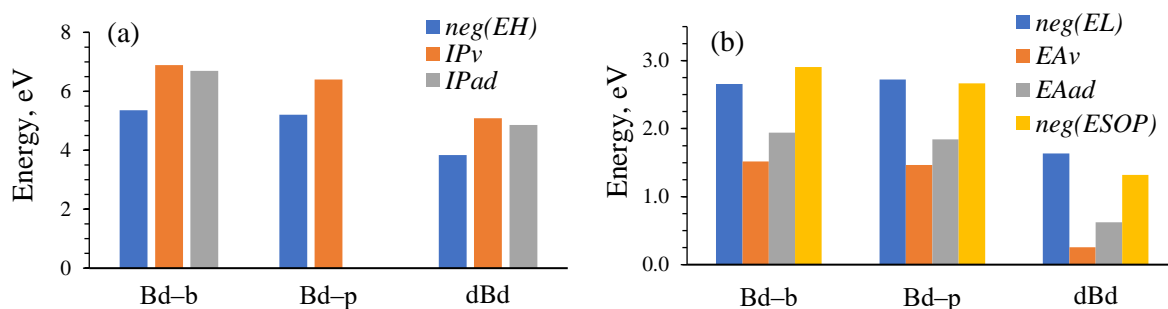


Figure 25: Comparison of electronic energies for the dye molecules Bd-b, Bd-p and dBd: (a) $-E_H$, IP_v and IP_{ad} (b) $-E_L$, EA_v , EA_{ad} and $ESOP$

4.1.5 Betanidin conformational isomers (Bd-b, Bd-p) and dBd dye adsorption on TiO₂ cluster

(i) Bd-b, Bd-p and dBd dye molecules adsorption modes and their binding energies

The dye adsorption on the TiO₂ surface was designed via possible connecting links, including CO₂, carboxylic groups, the dihydropyridine nitrogen atom and the benzenoid hydroxyls. According to the results presented in reference (Zhang *et al.*, 2018), the bidentate adsorption demonstrated stronger binding than other adsorption modes, mono-, bidentate bridged or chelating. The smaller bond length and more negative BE value indicate higher stability of the dye@TiO₂ complex. The Ti-O bond distance in the range of 2.05–2.10 Å or less was commented that the dye interacts strongly with the TiO₂ (Chen *et al.*, 2009; Pastore & De Angelis, 2010). Therefore, in our simulation, the aim was to investigate the bidentate bridged modes. In each case, the dye hydrogen atom was detached from the anchoring group and bound to the (TiO₂)₆ cluster (Fig. 26). During the planar Bd-p@TiO₂ complex simulation, the CO₂ group, disconnected simultaneously, resulting in the dBd@TiO₂ system formation. So, we considered further only two types of complexes, Bd-b@TiO₂ and dBd@TiO₂. Worth to mention that upon optimisation of the Bd-b@TiO₂ system, the tridentate coordination was identified without being intended. From our computation by the B3LYP/6–31G(d,p)/LANL2DZ method, the total energy of the TiO₂ cluster was established to be –1253.5231 au, and those of dehydrogenated individual dyes Bd-b –1406.8589 au and dBd –1218.2723 au, and that of the hydrogen atom 0.5003 au. For the considered links between the dye site and TiO₂ cluster, the calculated adsorption energies and bond lengths are shown in Table 9.

The binding energies obtained in the present work are negative, indicating thermodynamically favourable attachment of the dye to the TiO₂ cluster. In most cases, the dBd@TiO₂ complexes reveal shorter bond lengths than those in the Bd-b@TiO₂ except for the N2@TiO₂ link. The histogram in Fig. 27 compares the binding energies in the dye@TiO₂ complexes. The BE magnitudes vary within 14–20 eV in the considered attachment modes and differ irregularly throughout the respective links. The C18@TiO₂ system demonstrates the strongest adsorption, proving that the CO₂ group is most feasible for binding to the semiconductor.

Concluding this section, it is worth to comment our rather big BE magnitudes. We suggest that the binding energies are greatly influenced by the accepted adsorption modes in which the dehydrogenated dyes are bound to the $(\text{TiO}_2)_6$ cluster. According to the study on betalains (including betanidin) by Oprea *et al.* (2012), where protonated and deprotonated dyes were investigated, the proton affinity of the dyes was assessed in the range of 12–13 eV. Following these findings, we anticipate that dye dehydrogenation contributes to a great extent to our BE values. This suggestion is supported by studies (Deogratias *et al.*, 2020; Zhang *et al.*, 2018). Therefore, our reported magnitudes of the binding energies between the dyes and TiO_2 should be considered qualitative values appropriate for comparative analysis of the adsorption links.

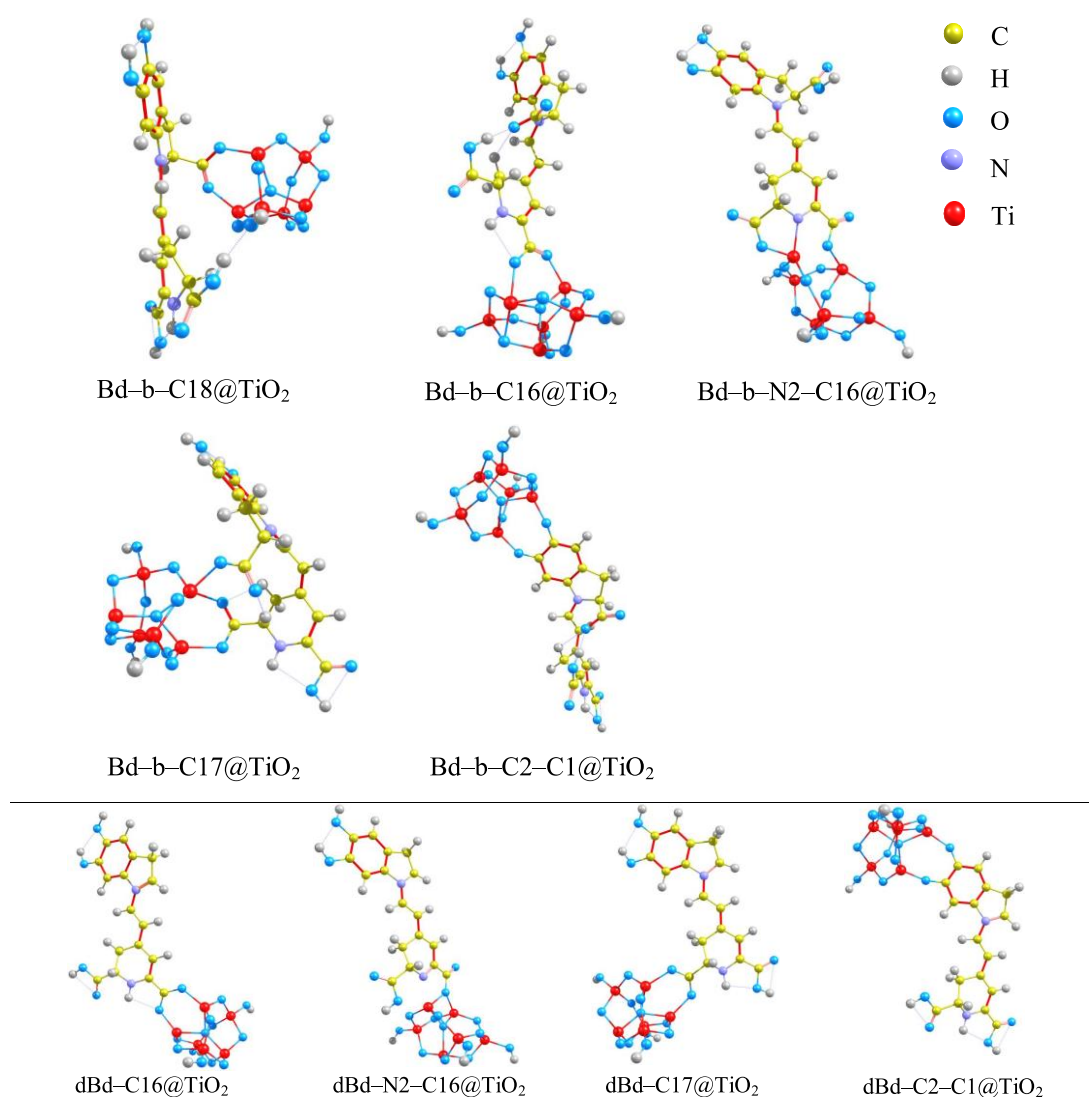


Figure 26: Optimised attachment modes for the Bd-b@TiO₂ (at the top) and dBd@TiO₂ (at the bottom) complexes

Table 9: Adsorption properties of the Bd-b@TiO₂ and dBd@TiO₂ complexes; connecting links between the dye site and TiO₂ cluster, respective bond distances, O–Ti or N–Ti; electronic energies and binding energies of the complexes calculated at the B3LYP/6–31G(d,p)/LANL2DZ

Connecting link	Bond distance, Å	Attachment mode	$E_{\text{dye@TiO}_2}, \text{au}$	BE, eV
Bd-b@TiO₂				
C16–O@TiO ₂	2.011	bidentate	–2660.5094	–17.08
C16=O@TiO ₂	2.004			
C18–O@TiO ₂	2.015	bidentate	–2661.1420	–20.68
C18=O@TiO ₂	2.003			
C2–O@TiO ₂	1.798	bidentate	–2659.9301	–14.93
C1–O@TiO ₂	1.855			
N2@TiO ₂	2.092	tridentate	–2659.9948	–16.69
C16–O@TiO ₂	2.067			
C17=O@TiO ₂	1.909			
C17–O@TiO ₂	2.094	tridentate	–2660.5210	–17.40
C17=O@TiO ₂	2.043			
C18–O@TiO ₂	2.063			
dBd@TiO₂				
C16–O@TiO ₂	1.967	bidentate	–2471.9385	–17.50
C16=O@TiO ₂	1.962			
C2–O@TiO ₂	1.849	bidentate	–2471.3483	–15.06
C1–O@TiO ₂	1.796			
N2@TiO ₂	*	bidentate	–2471.3390	–14.81
C16–O@TiO ₂	2.065	bridged		
C16–O@TiO ₂	2.066			
C17–O@TiO ₂	2.004	bidentate	–2471.9275	–17.20
C17=O@TiO ₂	2.006			

*In the N2@TiO₂ link, the distance N2–Ti is 2.167 Å which is longer than accepted for bond lengths

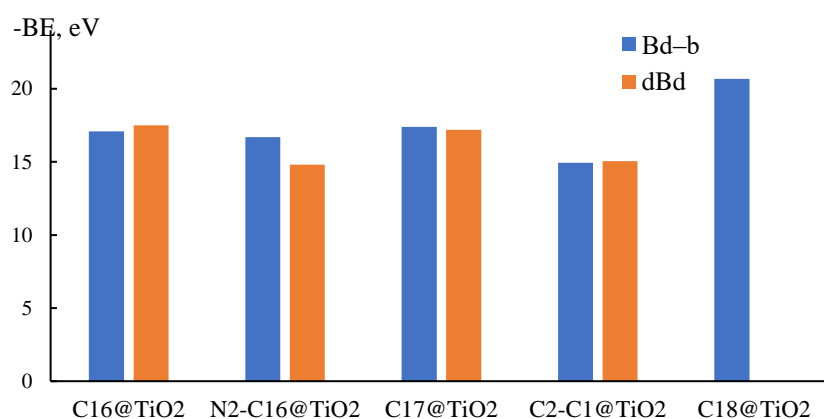


Figure 27: The binding energies of the considered attachment modes between the dyes and hydrogenated (TiO₂)₆ semiconductor cluster as computed at the B3LYP/6–31G(d,p)/ LANL2DZ

(ii) Electronic spectra of the Bd–b, Bd–p, and dBd dye@TiO₂ complexes

For considered Bd–b@TiO₂ and dBd@TiO₂ adsorption modes, electronic transitions $S_0 \rightarrow S_n$ ($n = 1-20$) have been computed at the TD–DFT/CAM–B3LYP/6–31G(d,p)/LANL2DZ level of theory (Table 10); the simulated UV–Vis spectra of the complexes are compared between each other and with individual dyes in Fig. 28. In most cases, the dye@TiO₂ complexes reveal lower excitation energies and higher spectral maxima than respective isolated dyes. The band position corresponded to λ_{\max} ranges from 416 to 490 nm for the Bd–b@TiO₂ and 508–883 nm for dBd@TiO₂, depending on the connecting link. In the Bd–b@TiO₂ spectra, for the C16, N2–C16, and C17 cases, the bands are slightly red-shifted, by ~30 nm, regarding the individual dye, while the Bd–b–C18@TiO₂ link exhibits a noticeable (by 60 nm) blue shift, and the C2–C1–O@TiO₂ shows the same maxima position as in respective pure dye spectrum. For the decarboxylated dBd@TiO₂ system, quite intensive absorption maxima are seen for the four considered links, similar to the Bd–b@TiO₂; all bands are red-shifted regarding the individual dBd dye spectrum.

If comparing the UV–Vis spectra of the two systems, betanidin Bd–b@TiO₂ and decarboxylated dBd@TiO₂, for the latter, the bands are intensive and noticeably red-shifted. This finding accords well with the literature data (Herbach *et al.*, 2006; Subalakshmi *et al.*, 2017), where it was reported that the decarboxylation should not change or destabilise the chromophore structure, but it retains the chromatic characteristics of the betacyanin.

The prior experimentally measured UV–Vis spectra of the beet extract in water before and after dipping a TiO₂ film in the extract looked alike (Zhang *et al.*, 2008). In our simulated spectra, a noticeable change from individual dye to the complex, i.e., red or blue peak shift, originates probably from the adopted model of the dye adsorption, that is, the deprotonation of the dye via intentional detachment of the hydrogen and representing the semiconductor surface by the (TiO₂)₆ cluster. The radical of the dye forms a bond between its oxygen or nitrogen atom and titanium atoms of the hydrogenated (TiO₂)₆ cluster. Adsorption of the dye to the TiO₂ cluster broadens and shifts the spectral bands compared to individual dyes. We anticipate that in a real situation of dye adsorption, the dye molecules can link by different sites on the TiO₂ surface, and each option contributes an intensive absorption peak in the spectrum. Therefore, overlapping the peaks should result in intense broadband. This speculation accords well with experimental spectra of dyes on the TiO₂ film compared with

narrower bands of pure dye solution, see, for example (Calogero *et al.*, 2010; Oprea *et al.*, 2012).

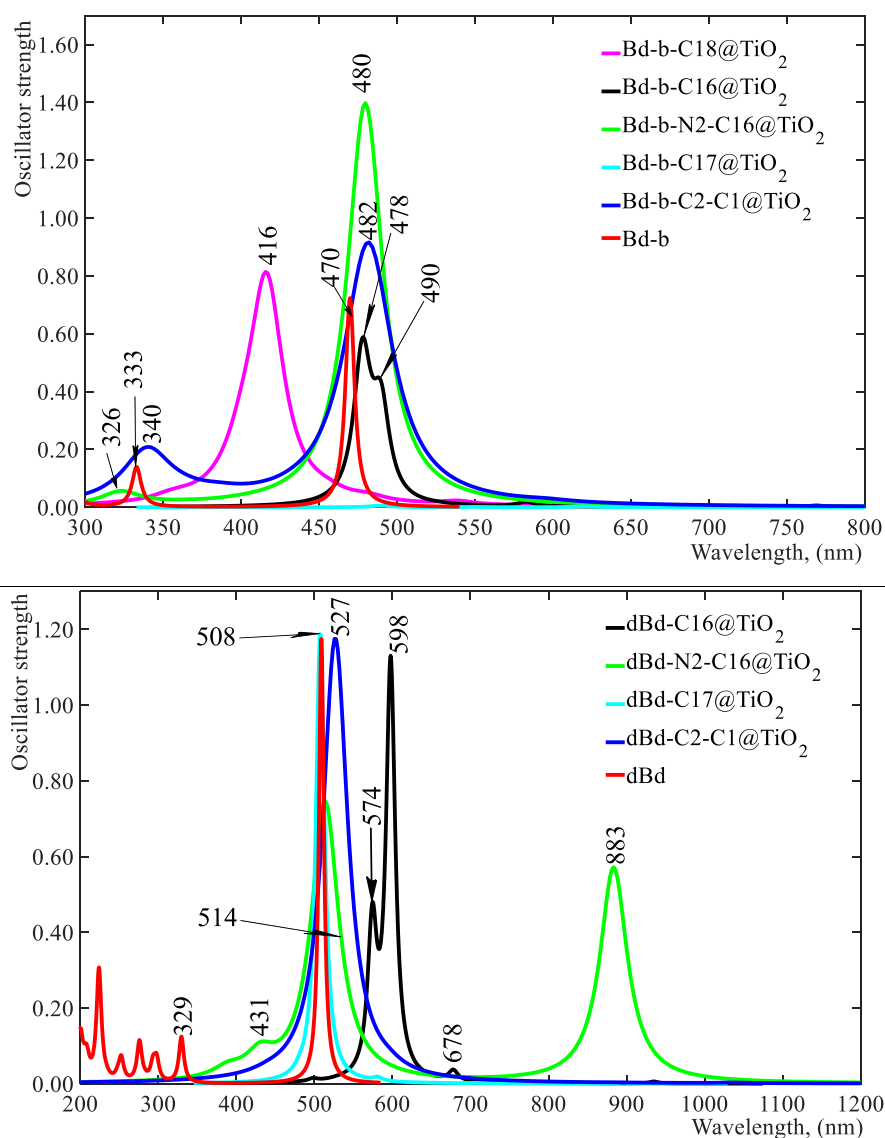


Figure 28: UV-Vis spectra of the complexes Bd-b@TiO₂ (Top) and dBd@TiO₂ (Bottom) simulated for different adsorption links at CAM-B3LYP/6-31G(d,p)/LANL2DZ with PCM for water

Table 10: Characteristics of electron transitions $S_0 \rightarrow S_n$ in the dye@TiO₂ complexes, Bd-b@TiO₂ and dBd@TiO₂, computed at the CAM-B3LYP/6-31G(d,p)/LANL2DZ with PCM for water

System	<i>n</i>	ΔE_{0-n} , eV	λ , nm	<i>f</i>	LHE, %	MOs Contribution, %
Bd-b@TiO₂						
C18@TiO ₂	14	2.98	416	0.762	82.7	H→L+15; 19
	15	3.09	401	0.112	22.7	H→L+5; 31
C16@TiO ₂	18	2.53	490	0.315	51.5	H-1→L; 12
	20	2.59	478	0.509	31	H-1→L; 31
N2-C16@TiO ₂	6	2.58	480	1.397	96	H→L; 42
	16	3.81	326	0.024	5.4	H→L+1; 29
C17@TiO ₂	13	2.00	620	0.003	0.7	H→L+5; 12
	19	2.53	490	0.006	1.3	H→L; 32
C2-C1@TiO ₂	7	2.57	482	0.911	87.7	H→L; 41
	19	3.64	340	0.137	27	H-2→L; 19
	20	3.67	338	0.046	10	H-1→L+6; 20
dBd@TiO₂						
C16@TiO ₂	14	2.07	598	1.098	92	H→L; 32
	16	2.16	574	0.388	59	H→L; 14
N2-C16@TiO ₂	5	1.40	883	0.569	73	H→L; 92
	10	2.41	514	0.741	82	H→L; 3
	12	2.88	431	0.056	12	H-3→L; 24
C17@TiO ₂	18	2.44	508	1.187	93.5	H→L+4; 49
C2-C1@TiO ₂	9	2.35	527	1.176	93.3	H→L+7; 20

(iii) Frontier molecular orbital analysis of the Bd-b, Bd-p, and dBd dye@TiO₂ systems

Most probable (with higher oscillator strength) electronic excitations $S_0 \rightarrow S_n$ have been assigned to transitions between the frontier and adjacent MOs, i.e., $H-\delta \rightarrow L+\delta$, ($\delta = 0, 1, 2, 3, 4, 5, 6 \dots 20$), for the Bd-b@TiO₂ and dBd@TiO₂ complexes (Table 10); graphical representation of the MO charge densities are shown in Fig. 29 and 30. The following MOs contributions can be viewed; for the Bd-b@TiO₂, $H \rightarrow L+15$ (C18@TiO₂), $H-1 \rightarrow L$ (C16@TiO₂), $H \rightarrow L$ (N2-C16@TiO₂, C2-C1@TiO₂), and for dBd@TiO₂, $H \rightarrow L$ (for C16@TiO₂ and N2-C16@TiO₂), $H \rightarrow L+4$ (C17@TiO₂) and $H \rightarrow L+7$ (C2-C1@TiO₂). Generally, the distribution patterns of the relevant MOs involved in the $S_0 \rightarrow S_n$ transitions confirm that HOMOs expand over the dye structure. In contrast, unoccupied orbitals are mostly located on the dye anchoring groups bound to the TiO₂ cluster. Such electron density distribution favours an effective intermolecular charge transfer from the dye to the semiconductor. In the dye@TiO₂ complexes, the FMOs assure a reasonable expectation that betanidin binds to the TiO₂ through carboxylic groups at C8 and C13 that agrees with the theoretical interpretation of the visualised transitions by Sandquist and McHale (2011) in

terms of an easy approach to the LUMO to the TiO_2 surface and the HOMO being isolated which helps prevailing an electron injection over sprout recombination. Our isodensity surfaces of the most relevant MOs not only show electron density distribution over the different moieties of the dye@ TiO_2 complexes but reveal the electron movements to the respective anchoring groups at either C8 or C13 and support an efficient electron injection from the dye to TiO_2 achieved well to these positions rather than any other anchor or lateral group.

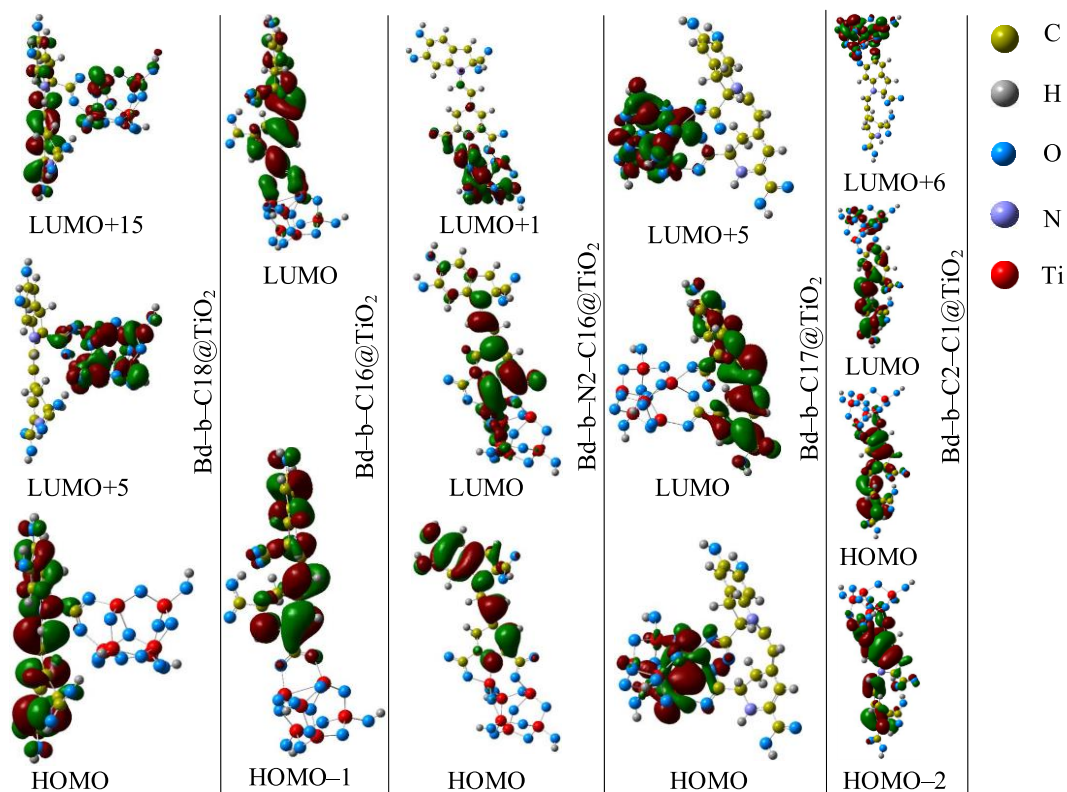


Figure 29: The distribution patterns of the frontier and adjacent molecular orbitals involved in the $S_0 \rightarrow S_n$ transition for the Bd-b@ TiO_2 calculated at the CAM-B3LYP/6-31G(d,p)/LANL2DZ with PCM for water

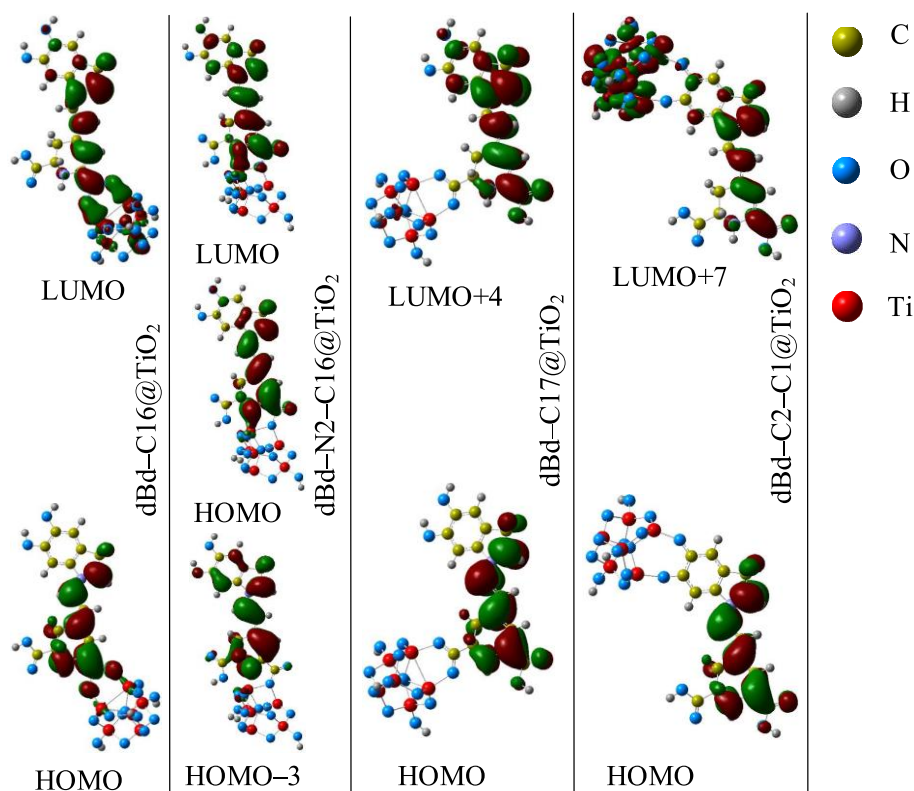


Figure 30: The distribution patterns of the frontier and adjacent molecular orbitals involved in the $S_0 \rightarrow S_n$ transition for the dBd@TiO₂ calculated at the CAM-B3LYP/6-31G(d,p)/LANL2DZ with PCM for water

4.2 Designed betanidin complexes with L0 dye

The work reports four novel complex D- π -A organic dyes. In the designed complexes, the triphenylamine part of the L0 unit is employed as the electron donor, an ester group formed is adopted as a bridge towards the π -spacer of the betanidin, carboxyl and hydroxyl groups are utilised as the electron acceptor units. Betanidin has those appropriate functional groups, which promote strong anchoring to the TiO₂ surface via bi-dentate chelation (Park *et al.*, 2013; Sreeja & Pesala, 2020), enhancing the charge transfer rate to the TiO₂ anode. Furthermore, a lateral chain might favour the dye attachment on the TiO₂ surface (Hao *et al.*, 2009; Ooyama *et al.*, 2007). According to Gou *et al.* (2014), the hydroxyl group shows relevance as a lateral anchoring group, likewise the carboxylic group. In addition, to achieve a significant charge transfer rate, the adsorption of the dye on the TiO₂ was enhanced by the lateral anchoring group (Liyanage *et al.*, 2013). In our study, we have analysed how the position of lateral groups influences the thermodynamic and optoelectronic properties of engineered complexes and their binding to TiO₂.

4.2.1 The geometrical structure of the designed complexes

Assumed esterification reactions between the synthetic dye L0 and natural dye Bd result in two types of isomeric complexes L0–Bd: L0–1–Bd and L0–2–Bd; similarly, two isomers arise for the decarboxylated betanidin complexes L0–dBd: L0–1–dBd and L0–2–dBd. The optimised structures of the complexes and L0 are shown in Fig. 31 and 32; the selected geometrical parameters are indicated in Table 11. The vibrational spectra demonstrated the absence of imaginary frequencies, thus confirming the equilibrium structures. The IR spectra are analysed and displayed in Fig. 33–35.

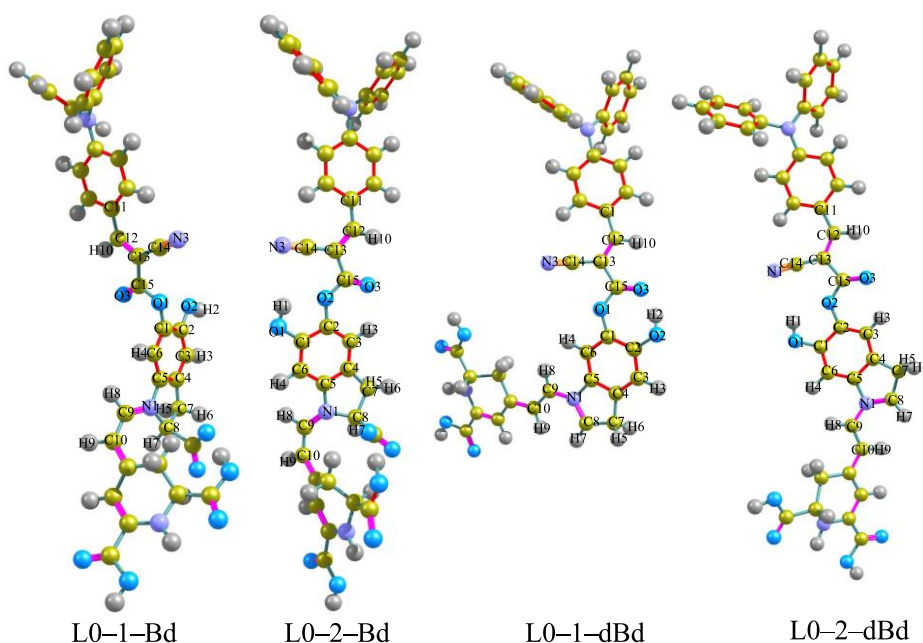


Figure 31: Optimised geometrical structures of the complex dye molecules

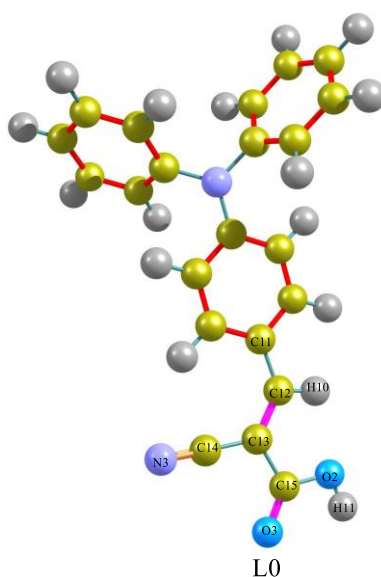


Figure 32: Optimised geometrical structure of the L0 dye molecule

Table 11: The selected geometrical parameters of the dye molecules: Bond distances in Å, bond angles, and dihedral angles in degs

Moiety	Parameter	L0-1-Bd	L0-2-Bd	L0-1-dBd	L0-2-dBd	L0	Bd	dBd
Bd moiety six-membered ring	C1-C2	1.408	1.415	1.412	1.413		1.415	1.411
	C5-C4	1.395	1.395	1.396	1.394		1.396	1.393
	H1-O1		0.971		0.971		0.970	0.970
	C1-O1		1.353		1.355		1.358	1.360
	H1...O2		2.115		2.116		2.110	2.111
	C2-O2	1.357		1.351			1.371	1.375
	O1-H1...O2		111.9		111.9		114.2	114.5
Bd moiety five-membered cycle with N1	N3-C8	1.497	1.498	1.350	1.350		1.486	1.350
	C7-C8-N1	103.3	103.3	112.2	112.1		104.5	112.0
	C5-N1-C8	109.2	109.3	108.0	108.2		108.6	108.3
	C4-C7-C8-N1	18.2	18.2	0.66	1.15		20.3	1.4
L0 moiety bonds	C11-C12	1.440	1.437	1.436	1.437	1.444		
	C12=C13	1.370	1.371	1.373	1.371	1.369		
	C14-C13	1.427	1.426	1.427	1.426	1.430		
	C14≡N3	1.165	1.166	1.165	1.166	1.165		
	C12-H10	1.089	1.089	1.088	1.089	1.087		
Ester group with adjacent bonds	C1-O1	1.389		1.404				
	C2-O2		1.390		1.392			
	C15-O1	1.374		1.349		1.361		
	C15-O2		1.366		1.364			
	C15=O3	1.210	1.212	1.226	1.212	1.214		
	C13-C15	1.485	1.485	1.477	1.486	1.485		

Between the two Bd complex conformers, the L0–2–Bd appeared more stable by 21 kJ mol⁻¹ compared to L0–1–Bd. The higher stability of the L0–2–Bd is likely attributed to a more favourable orientation of the Bd hydroxyl group towards the ester linkage. To the side of the decarboxylated betanidin complexes, they are comparable by energy; the L0–1–dBd is slightly lower by ~2 kJ mol⁻¹, which is caused by the hydrogen bond O2–H2...O3 formation with parameters 0.98 Å, 1.72 Å and 156° (Table 11). The ester linkage of the betanidin L0–Bd complexes is seen via the C–O–C bridge with distances C–O 1.37 Å, O–C 1.39 Å in both complexes and angles 117° (L0–1–Bd) and 126° (L0–2–Bd). In the L0–1–Bd, the central part, which includes the benzenoid ring of the TPA, C–O–C bridge, and benzenoid and five-membered cycles of the Bd, is twisted; the Bd rings are turned by 103° with respect to the rest part. In the L0–2–Bd, the three constituents of the central fragment are coplanar; the D– π –A coplanarity helps the intramolecular charge transfer from the donor to the anchoring group (Deogratias *et al.*, 2019). As for L0–dBd, the structural features resemble those of the L0–Bd; the central part of the L0–1–dBd is twisted while the coplanarity of the L0–2–dBd even is more expressed than of L0–2–Bd. The interruption of the π – π^* stacking (Saravanan *et al.*, 2014) needs to be controlled to reduce dye aggregation through non-planar moiety existence. Among our four designed molecules, the L0–1–Bd and L0–1–dBd dyes are expected to be more resistant against aggregation when being absorbed on the semiconductor surface.

4.2.2 Vibrational spectra analysis of the betanidin complexes with L0

The IR spectra of the five dye molecules, one individual L0 and four complexes, are shown in Fig. 33–35. In the low-frequency region (200–1000 cm⁻¹), bands are assigned to the twisting and bending vibrations of cycles, whereas O–H bending and Ar–C–H out-of-plane vibrations are highly distinguished. The moderate region (1000–2600 cm⁻¹) contains C–O stretching of the ester group near 1100 cm⁻¹, Ar–C–H, C–H, N–H bending modes at 1195–1610 cm⁻¹, and the stretching vibrations at 1700–2600 cm⁻¹ for C=O, C \equiv N. The high-frequency peaks (2600–3800 cm⁻¹) are in good agreement with associated functional groups vibrations in the individual betanidin dyes investigated in Section 4.1. At the same time, most of the L0 molecule vibrations are reproduced in the spectra of the complexes. The observed spectral distinction between the L0–Bd, and L0–dBd complexes is evidence relating to the structural peculiarities of the molecules. For instance, in the spectra of the L0–Bd, the peak near 2600 cm⁻¹ originates from the hydrogen bond between the CO₂ and carboxylic group of the Bd moiety; apparently, this vibration is unavailable in the decarboxylated molecules. For the L0–

dBd complexes, unlike other molecules, a rather intensive band at $\sim 3500\text{ cm}^{-1}$ corresponds to the OH...O bond near the ester linkage. In the complexes via C_2 (L0-2-Bd and L0-2-dBd), a noticeable peak at 3750 cm^{-1} relates to the hydroxyl near the ester group, whereas in the complexes via C_1 (L0-1-Bd and L0-1-dBd), smaller peaks can be assigned to O-H vibrations of the carboxylic group.

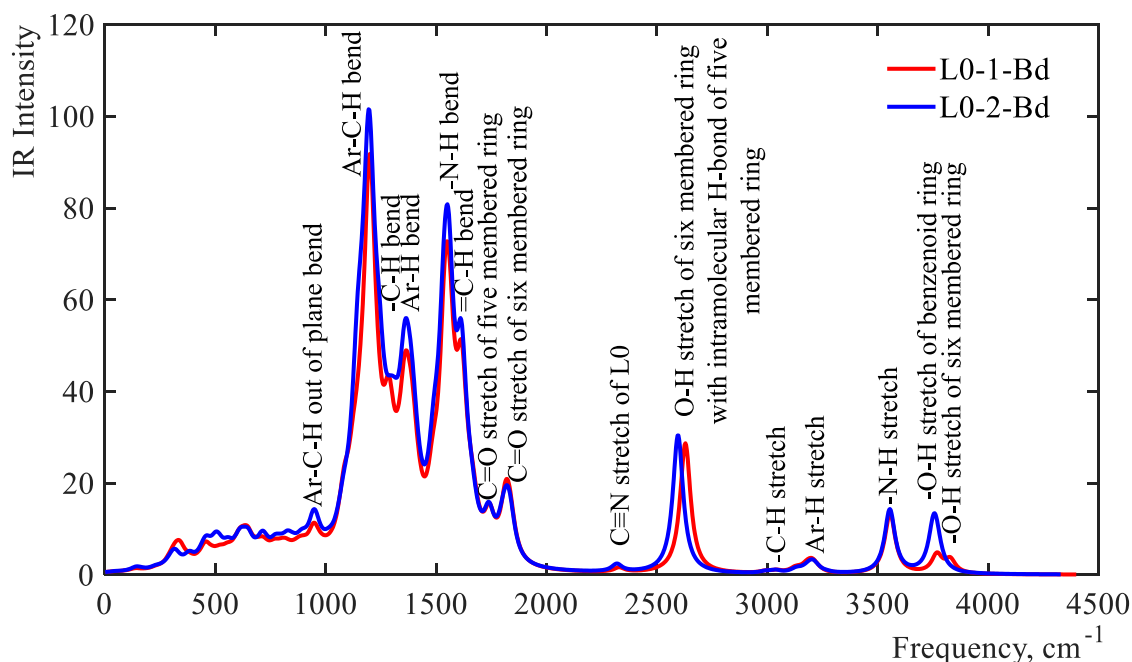


Figure 33: IR spectra of the betanidin complex dye molecules L0-1-Bd and L0-2-Bd

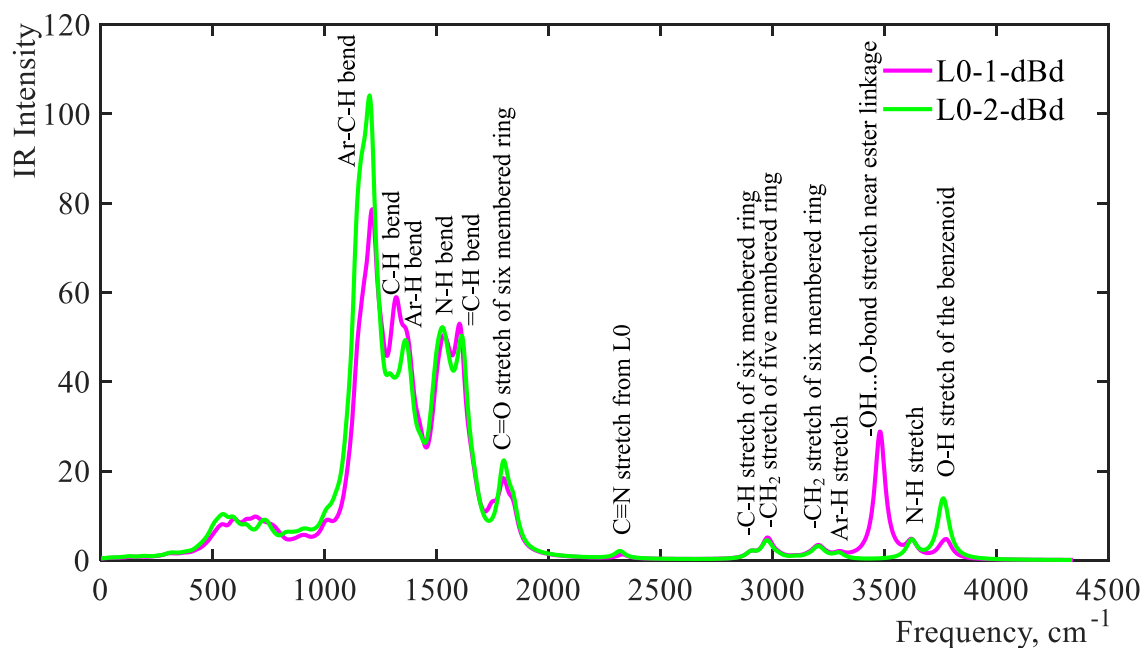


Figure 34: IR spectra of the decarboxylated betanidin complex dye molecules L0-1-dBd and L0-2-dBd

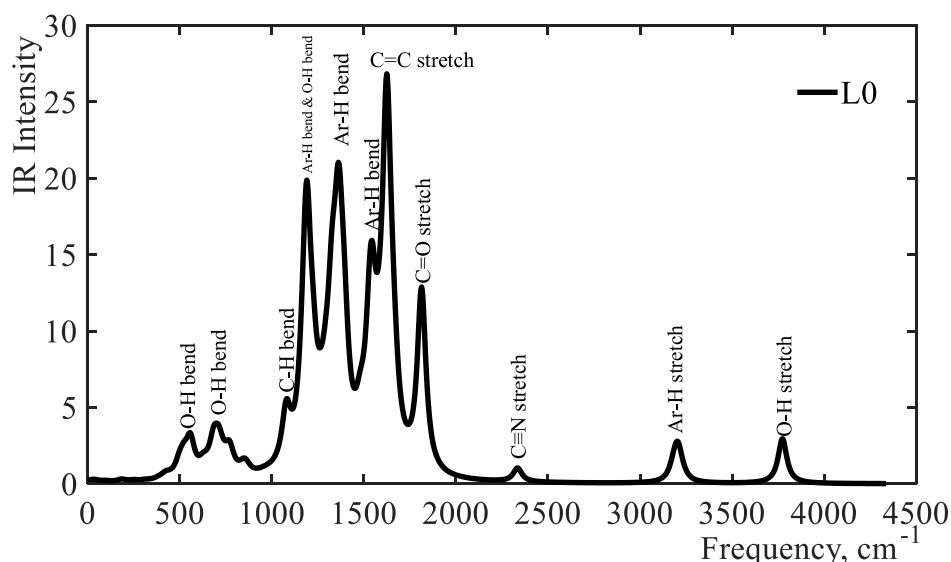


Figure 35: IR spectrum of the L0 dye molecule

4.2.3 Thermodynamics of the chemical reactions of the betanidin with L0 dye.

(i) Reactions of the betanidin complex formation with L0

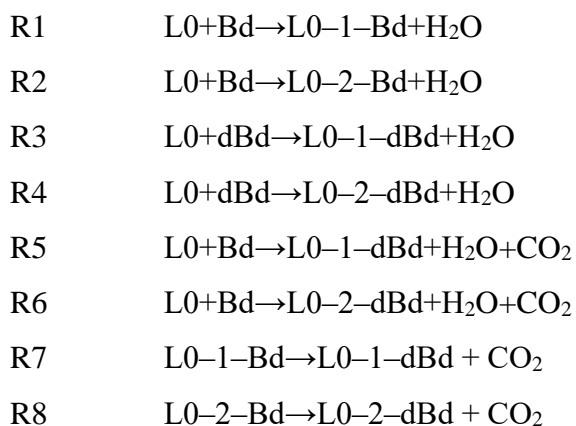
The reactions of the complexes formed may be categorised into three groups according to Schemes S1–S5 (Table 12); the first group, S1 comprises reactions R1 and R2 of the betanidin complexes formation from the L0 and Bd; the second group S2 concerns reactions R3 and R4 of the decarboxybetanidin complexes formation from L0 and dBd; and the third group S3 relates to the reactions R5 and R6 leading to the L0–1–dBd and L0–2–dBd from L0 and Bd. Thermodynamic characteristics of the reactions, energies $\Delta_r E$, zero-point vibration energies $\Delta \epsilon$, enthalpies $\Delta_r H^\circ$, entropies $\Delta_r S^\circ$, and Gibbs free energies $\Delta_r G^\circ$, are summarised in Table 12. In addition, thermodynamic functions of the gaseous species, molar heat capacities $C_p^\circ(T)$, entropies $S^\circ(T)$, reduced Gibbs free energies $\Phi^\circ(T)$, and enthalpy increments $H^\circ(T) - H^\circ(0)$ are calculated within RRGO approximation for temperature range from ambient temperature to 600 K in Appendix 2.

As is seen, the complexes formation reactions are endothermic except for the R2, which is slightly exothermic at room temperature. The Gibbs free energies $\Delta_r G^\circ(298)$ are positive for the esterification reactions R1–R4 but negative for R5 and R6, producing the L0–dBd complexes with H_2O and CO_2 release. The spontaneity of the reactions R5 and R6 is attributed to a significant entropy increase. Our previous work revealed the spontaneous decay of betanidin into dBd and CO_2 (Section 4.1.3).

Table 12: Thermodynamic characteristics of the chemical reactions

Schemes	No.	Reaction	$\Delta_r E$, kJ mol ⁻¹	$\Delta_r \epsilon$, kJ mol ⁻¹	$\Delta_r H^\circ(0)$, kJ mol ⁻¹	$\Delta_r H^\circ(298)$, kJ mol ⁻¹	$\Delta_r S^\circ(298)$, J mol ⁻¹ K ⁻¹	$\Delta_r G^\circ(298)$, kJ mol ⁻¹
S1	R1	L0+Bd→L0-1-Bd+H ₂ O	18.9	-8.5	10.5	15.3	-14.8	19.7
	R2	L0+Bd→L0-2-Bd+H ₂ O	-1.9	-7.1	-9.1	-4.7	-25.4	2.8
S2	R3	L0+dBd→L0-1-dBd+H ₂ O	15.5	-7.8	7.8	12.3	-27.5	20.5
	R4	L0+dBd→L0-2-dBd+H ₂ O	17.5	-8.5	9.0	14.4	-14.3	18.6
S3	R5	L0+Bd→L0-1-dBd+H ₂ O+CO ₂	29.3	-19.6	9.7	18.3	160.2	-29.5
	R6	L0+Bd→L0-2-dBd+H ₂ O+CO ₂	31.2	-20.3	10.9	20.4	173.5	-31.3
S4	R7	L0-1-Bd→L0-1-dBd + CO ₂	10.32	-11.2	-0.8	3.2	175.0	-49.0
	R8	L0-2-Bd→L0-2-dBd + CO ₂	33.1	-13.2	19.9	25.3	198.8	-34.0
S5	R9	L0-1-Bd↔L0-2-Bd	-20.9	1.3	-19.5	-20.0	-10.6	-16.9
	R10	L0-1-dBd↔L0-2-dBd	2.0	-0.7	1.2	2.1	13.3	-1.9

Formation of L0–dBd complexes may be proposed via channels R7 and R8, which can be considered a combination of the reactions R5, R1, and R6, R2, respectively; R7=R5–R1 and R8=R6–R2. According to most negative values of $\Delta_r G^\circ$, the routes R7 and R8 are predicted to be most spontaneous than other reactions. Temperature dependences $\Delta_r H^\circ(T)$, $\Delta_r S^\circ(T)$, and $\Delta_r G^\circ(T)$ have been computed for the reactions R1–R8, and the plots are displayed in Fig. 36.



The values of the $\Delta_r H^\circ(T)$ and $\Delta_r S^\circ(T)$ show a very slight ascending by 1–2 kJ mol^{–1} with temperature increase, while the $\Delta_r G^\circ(T)$ values of reactions R1–R4 also slightly increase; at the same time, reactions R5–R8, which lead in the decarboxylated betanidin complexes with carbon dioxide release, demonstrate considerable growth of spontaneity; the Gibbs free energy becomes more negative by ~50 kJ mol^{–1}.

(ii) Isomerisation reactions of the betanidin complex isomers

Isomerisation reactions between two betanidin complexes L0–1–Bd and L0–2–Bd and decarboxylated complexes L0–1–dBd and L0–2–dBd, have been considered; the reactions are denoted as R9 and R10 in Table 12. The structural formulas of the isomers are shown in Figs. 8–9. As indicated in Table 12, the betanidin complex L0–2–Bd formed through the C₂–linkage of the betanidin moiety has lower energy and thus is more stable energetically than the L0–1–Bd. The Gibbs free energy $\Delta_r G^\circ(298)$ is negative, attributed to the exothermicity of the reaction. To the side of decarboxybetanidin complexes, L0–1–dBd and L0–2–dBd is comparable by energetic stability. The entropy of the reaction R10 is positive, $\Delta_r S^\circ(298) = 13.3 \text{ J mol}^{-1} \text{ K}^{-1}$, the second isomer of greater entropy, which may be explained by a contribution of lower frequencies and hence its higher structural flexibility. The temperature dependences of the thermodynamic characteristics of the isomerisation reactions are shown in Fig. 36. For both reactions, with temperature rise, the enthalpy does not practically change,

and the entropy $\Delta_r S^\circ(T)$ governs the $\Delta_r G^\circ(T)$, which slightly raises for the R7 and decreases for the R8.

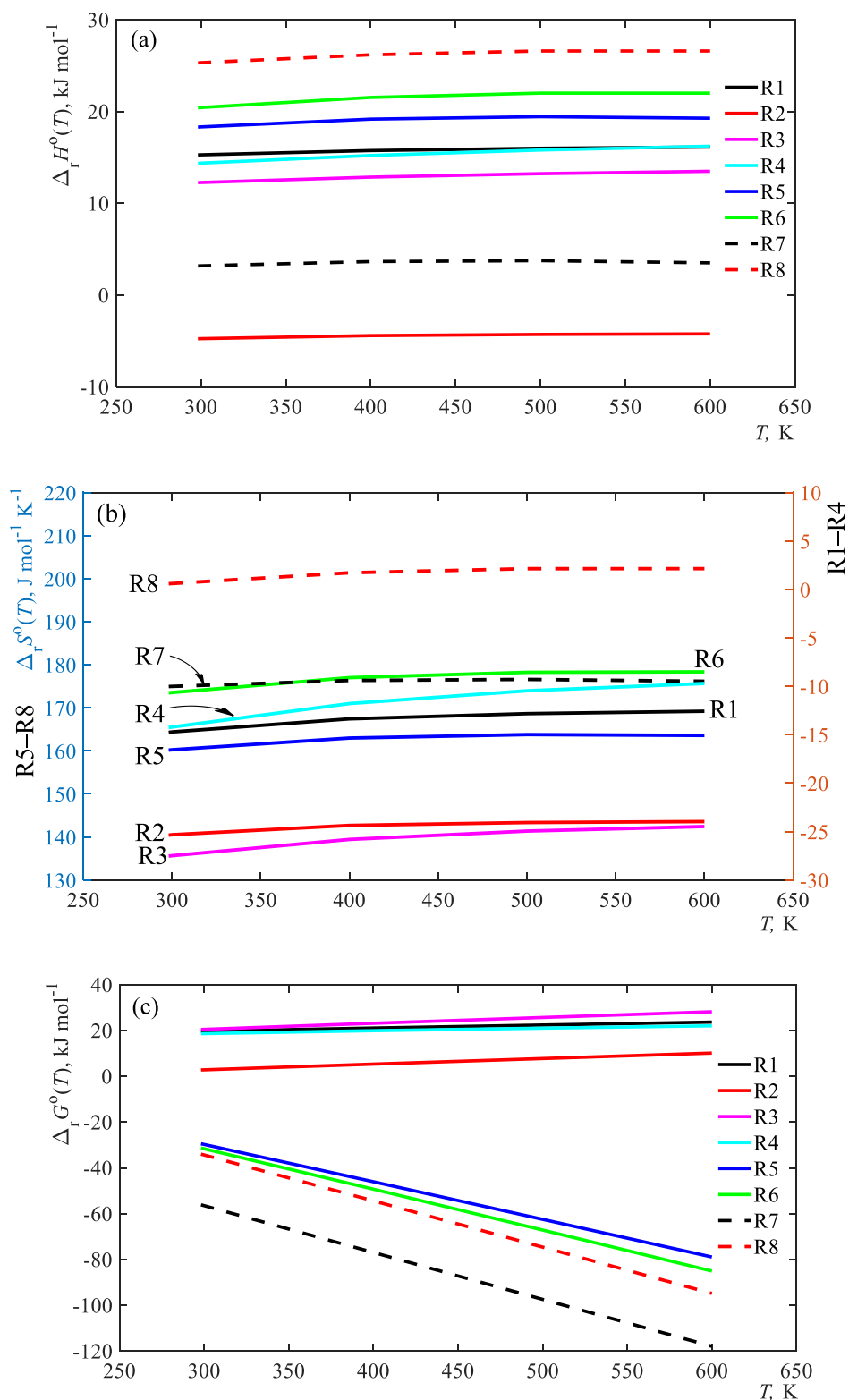


Figure 36: Thermodynamic characteristics of the reactions R1–R8: Enthalpies $\Delta_r H^\circ(T)$ (a) Entropies $\Delta_r S^\circ(T)$ (b) and Gibbs free energies $\Delta_r G^\circ(T)$ (c)

Therefore, entropy is the critical factor for the dye isomer to predominate. The partial pressure ratios p_{II}/p_I for the L0-Bd and L0-dBd complexes have been calculated for the temperature range from 298 to 600 K as indicated in Equation 95 where p_I stands for L0-1-Bd (or L0-1-dBd) and p_{II} stands for L0-2-Bd (or L0-2-dBd).

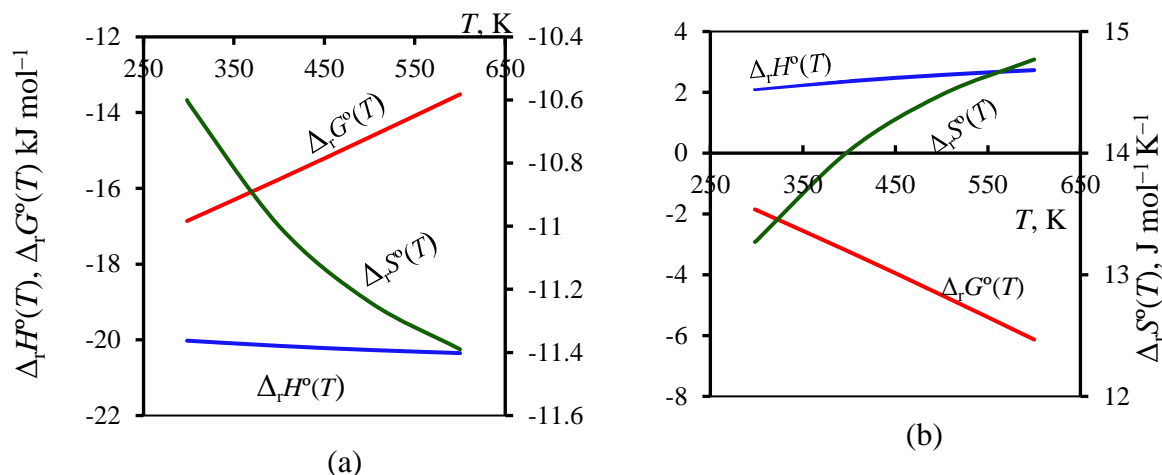


Figure 37: Thermodynamic characteristics $\Delta_r H^\circ(T)$, $\Delta_r S^\circ(T)$ and $\Delta_r G^\circ(T)$ of isomerisation reactions for betanidin complexes L0-1-Bd ↔ L0-2-Bd (a) and decarboxylated betanidin complexes L0-1-dBd ↔ L0-2-dBd (b)

The values of the p_{II}/p_I appeared to be about 900 for R7 and 2 for R8 at ambient temperature and decreased up to 15 for R7 and increased up to 3 for R8 at 600 K (Fig. 38). It points towards that the betanidin complex L0-2-Bd is much more abundant than isomer L0-1-Bd due to the stronger energetic stability of the former but shows poor entropy contribution for its prevalence. On the other hand, the decarboxylated isomer L0-2-dBd is more abundant than L0-1-dBd, and thus despite the less energetic stability, the higher entropy brings to its prevalence.

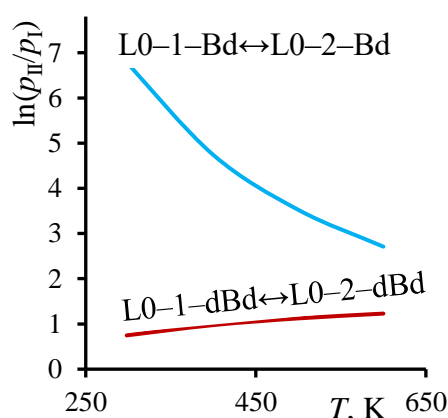


Figure 38: Pressure ratio p_{II}/p_I of the betanidin complexes and decarboxy betanidin complexes isomers; p_I stands for either L0-1-Bd or L0-1-dBd, p_{II} for either L0-2-Bd or L0-2-dBd

4.2.4 Optoelectronic properties of the designed complexes

(i) Frontier molecular orbital analysis of the betanidin complexes dyes

The electron density spatial distribution over frontier molecular orbitals (FMOs) is analysed in Fig. 39. The analysis demonstrates that in individual L0 molecule and L0-Bd complexes, the HOMO electrons are distributed over the triphenyl rings. In contrast, LUMO electrons, including anchoring groups, are delocalised in the betanidin part. In contrast, in the decarboxylated L0-dBd complexes, the HOMO electrons are delocalised over the decarboxybetanidin part, whereas LUMO electrons are concentrated on the triphenyl rings. From a common understanding of a sensitizer, HOMO electrons should be concentrated on the donor part and LUMO electrons on the acceptor moiety. The presence of the LUMO charge density in anchoring (i.e., acceptor) groups favours the ultra-fast charge injection from the sensitizer to the semiconductor (Zhang *et al.*, 2018) as satisfied for the L0, L0-1-Bd, and L0-2-Bd, but not for the decarboxylated complexes where the LUMO extends over the triphenyl rings leaving lack of charge density at the betanidin anchoring groups which may restrict dye-semiconductor electron coupling and hence weaken electrons injection. We have identified the lower HOMO-LUMO energy gap in the decarboxylated L0-dBd complex molecules, 1.44 eV (L0-1-dBd) and 1.52 eV (L0-2-dBd), compared to the L0-Bd complexes and individual dye L0 (Fig. 39). Both L0-dBd molecules demonstrate the intramolecular hydrogen bonding between the ester linkage and hydrogen atom of the dBd fragment (Fig. 31); one can suggest this additional H-bond favours the lower energy gap and, therefore, the charge transferability in the complexes.

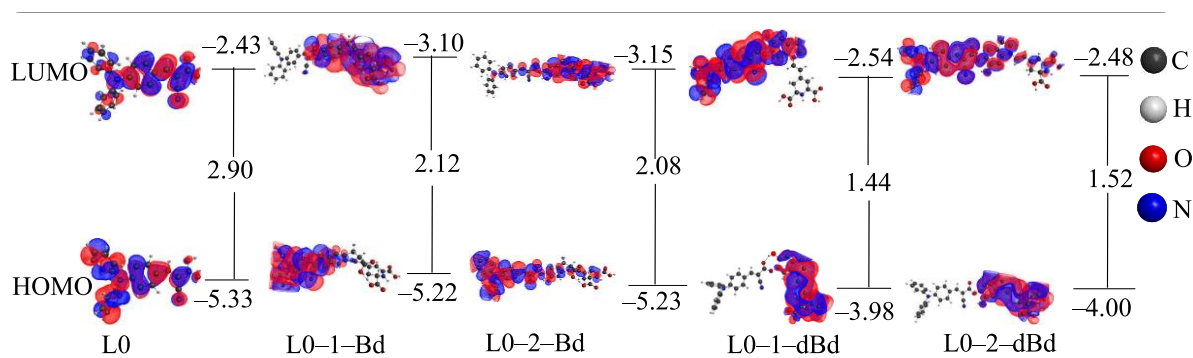


Figure 39: Frontier molecular orbitals (FMOs) of the dyes in DMSO solvent

Table 13: The percentage contribution to the HOMO and LUMO from respective fragments of the dyes

Dye	MO	Fragments and their percentage contribution, %		
		L0 moiety	Bd moiety	Ester group
L0-1-Bd	HOMO	97.86	0.46	1.68
	LUMO	0.01	99.97	0.02
L0-2-Bd	HOMO	89.94	8.35	1.72
	LUMO	1.43	97.65	0.91
L0-1-dBd	HOMO	0	100	0
	LUMO	67.72	16.23	16.06
L0-2-dBd	HOMO	0	100	0
	LUMO	65.38	17.27	17.35

In order to understand the HOMO and LUMO distribution over different parts of the complex molecule in detail, the designed complex structure has been divided into three main fragments. Namely, L0 moiety, Bd moiety, and ester group (Fig. 40). The percentage contribution from each part of the FMO of the dyes is counted as shown in Fig. 40 and Table 13. The L0 moiety contribution to the HOMO is higher in the L0-1-Bd (98%) than in the L0-2-Bd (90%), whereas it appears to be zero in the decarboxylated complexes. To the side of Bd moiety, its supply to LUMO is 100% in L0-Bd while only 16–17% in L0-dBd complexes. The ester group acts as a π -spacer to bridge the electron from one moiety to another, accumulating a small electron density on either HOMO or LUMO of the dyes. Therefore, the contribution of the electrons from the molecular fragments confirms that electron injection to the semiconductor can occur via the betanidin moieties in the L0-Bd. At the same time, one can expect a poor electron injection for the decarboxylated complexes because of the lack of electrons in the acceptor groups in the LUMO.

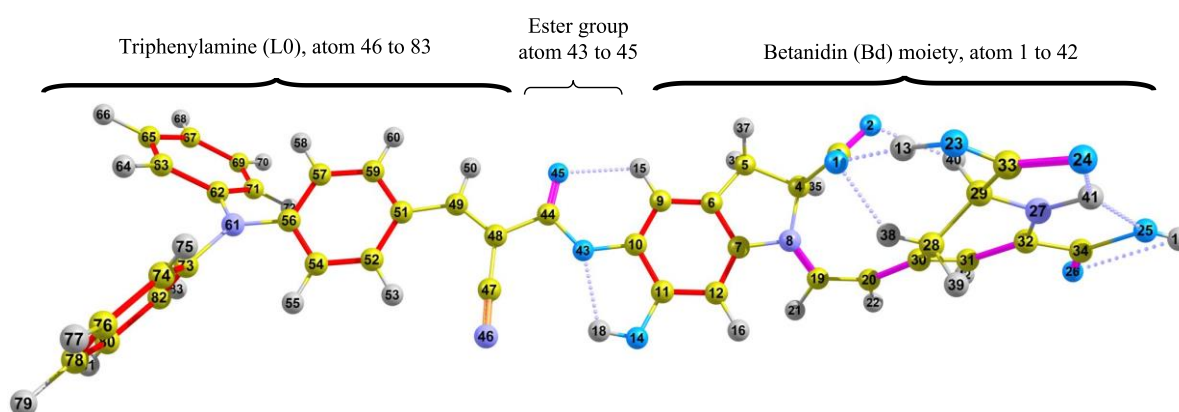


Figure 40: Representative fragments of the designed complex L0-2-Bd dye numbered with the Aomix calculation program (Gorelsky, 2017; Gorelsky & Lever, 2001)

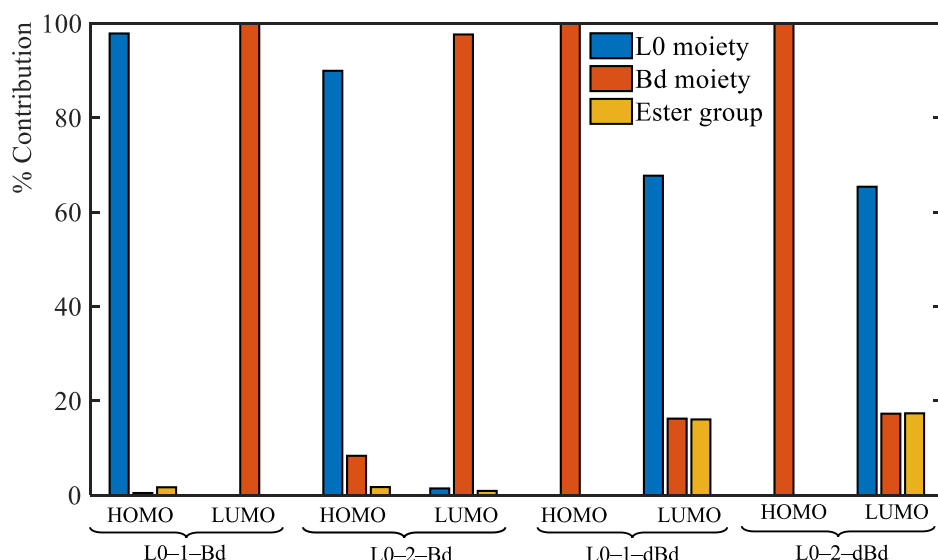


Figure 41: A bar graph of the percentage contribution to the HOMO and LUMO from different fragments of the considered dyes

(ii) Electronic transitions and UV-Vis spectra of the betanidin complexes

A DSSC performance is assisted by broader coverage of the solar spectrum and greater light-harvesting efficiency (LHE) of the sensitiser. For the escalation of photocurrent response, higher values of the LHEs of the sensitiser are preferable (Janjua, 2017). The electronic spectra of the L0 dye and designed sensitisers have been simulated for different solvents, polar aprotic (DMSO/CH₃CN), and polar protic (H₂O), and the spectral intensities are evaluated through oscillator strengths. The spectral properties — wavelengths λ , transition configurations, oscillator strengths f , LHEs, and excitation energies ΔE_{0-n} — are indicated in Table 14, the transitions $S_0 \rightarrow S_n$, $n = 1-15$, with $f > 0.1$ being considered. The LHEs are computed through the oscillator strengths f , $LHE = 1 - 10^{-f}$. The simulated electronic spectra of the considered dyes in the DMSO are demonstrated in Fig. 42. The two most intensive groups of peaks in the visible range, 453–466 nm, and 503–518 nm, seen in the L0-Bd, and L0-dBd complexes' spectra besides the lower edge at 453 nm coincide with the maximum of the L0.

Significant peaks in our simulated spectra of the complexes relate to electronic transitions to the second $S_0 \rightarrow S_2$ or third $S_0 \rightarrow S_3$ excited states. The λ_{\max} values in the ascending order together with the electronic transition configurations are as follows: L0 453 nm ($H \rightarrow L$) < L0-1-Bd 503 nm ($H-1 \rightarrow L$) < L0-1-dBd 505 nm ($H-1 \rightarrow L$) < L0-2-dBd 513 nm ($H-1 \rightarrow L$) < L0-2-Bd 518 nm ($H-1 \rightarrow L$). Therefore, an essential red-shift of λ_{\max} , more than 50 nm, is observed from the original L0 to the designed complexes; also, a significant increase of the oscillator strengths can be noticed in the complexes compared to L0.

Table 14: Characteristics of the electronic transitions $S_0 \rightarrow S_n$ ($n = 1-15$) in L0, L0-1-Bd, L-2-Bd, L0-1-dBd and L0-2-dBd computed for a CH₃OH, H₂O, DMSO and CH₃CN solvents

Dye	Solvent	n	ΔE_{0-n} , eV	λ , nm	f	LHE, %	MOs contribution, %
L0	CH ₃ OH	1	2.74	453	0.718	82	H→L; 99
		5	4.18	297	0.277	47	H-3→L; 79
		8	4.38	283	0.185	35	H→L+2; 67
	H ₂ O	1	2.73	454	0.717	81	H→L; 99
		5	4.17	297	0.278	47	H-3→L; 79
		8	4.38	283	0.188	35	H→L+2; 70
	DMSO	1	2.74	453	0.717	81	H→L; 99
		5	4.18	297	0.278	47	H-3→L; 79
		8	4.38	283	0.186	35	H→L+2; 69
	CH ₃ CN	1	2.74	453	0.718	81	H→L; 99
		5	4.18	297	0.278	47	H-3→L; 79
		8	4.38	283	0.186	35	H→L+2; 68
L0-1-Bd	CH ₃ OH	2	2.46	503	1.046	91	H-1→L; 93
		3	2.74	453	0.647	77	H→L+1; 93
	H ₂ O	2	2.47	503	1.056	91	H-1→L; 93
		3	2.73	454	0.634	77	H-1→L+1; 92
	DMSO	2	2.46	503	1.050	91	H-1→L; 93
		3	2.74	453	0.641	77	H→L+1; 92
	CH ₃ CN	2	2.46	503	1.046	91	H-1→L; 93
		3	2.74	453	0.644	77	H→L+1; 93
L0-2-Bd	CH ₃ OH	1	1.90	653	0.116	23	H→L; 100
		2	2.39	518	1.205	94	H-1→L; 88
		3	2.69	460	0.530	70	H→L+1; 88
	H ₂ O	1	1.89	655	0.113	23	H→L; 100
		2	2.39	518	1.223	94	H-1→L; 87
		3	2.69	461	0.515	69	H→L+1; 88
	DMSO	1	1.90	654	0.114	23	H→L; 100
		2	2.39	518	1.214	94	H-1→L; 88
		3	2.69	460	0.522	70	H→L+1; 88
	CH ₃ CN	1	1.90	653	0.115	23	H→L; 100
		2	2.39	518	1.209	94	H-1→L; 88
		3	2.69	460	0.526	70	H→L+1; 88
L0-1-dBd	CH ₃ OH	2	2.46	505	0.865	86	H→L+1; 90
		3	2.66	466	0.859	86	H-1→L; 77
		4	2.73	454	0.210	38	H→L+2; 81
		6	3.16	392	0.198	37	H→L+4; 76
	H ₂ O	2	2.46	505	0.869	86	H→L+1; 90
		3	2.66	466	0.881	87	H-1→L; 79
		4	2.74	453	0.185	35	H→L+2; 83
		6	3.17	392	0.201	37	H→L+4; 77
	DMSO	2	2.46	505	0.867	86	H→L+1; 90
		3	2.66	466	0.871	87	H-1→L; 78
		4	2.74	453	0.197	36	H→L+2; 82
		6	3.16	392	0.200	37	H→L+4; 77
	CH ₃ CN	2	2.46	505	0.866	86	H→L+1; 90

Dye	Solvent	n	ΔE_{0-n} , eV	λ , nm	f	LHE, %	MOs contribution, %
L0-2-dBd		3	2.66	466	0.864	86	H-1→L; 78
		4	2.73	453	0.204	38	H→L+2; 81
		6	3.16	392	0.199	37	H→L+4; 76
	CH ₃ OH	2	2.41	514	1.105	92	H→L+1; 89
		3	2.68	463	0.963	89	H-1→L; 88
		4	2.87	432	0.227	41	H→L+2; 77
	H ₂ O	2	2.42	513	1.121	92	H→L+1; 86
		3	2.68	463	0.940	89	H-1→L; 88
		4	2.87	432	0.234	42	H→L+2; 77
	DMSO	2	2.42	513	1.113	92	H→L+1; 89
		3	2.68	463	0.951	89	H-1→L; 88
		4	2.87	432	0.231	41	H→L+2; 77
	CH ₃ CN	2	2.41	513	1.088	92	H→L+1; 89
		3	2.68	463	0.958	89	H-1→L; 88
		4	2.87	432	0.229	41	H→L+2; 77

In addition, both the FMOs and adjacent molecular orbitals might contribute to the LHEs of the dye materials that are not limited only by H→L. If we compare the spectral maxima of the designed complexes with λ_{max} of pure betanidin, 504 nm (Bd-b), 487 nm (Bd-p), and 492 nm (dBd) as seen from Section 4.1.4 for the DMSO solvent, the peaks for the complexes are slightly red-shifted. Also, some increases in the oscillator strengths can be noticed. Thus, one can conclude that in the spectra of the complexes, the two most prominent peaks in the visible range originate apparently from the individual L0 and betanidin dyes. At the same time, shorter wavelengths come from the L0, and longer wavelengths come from the betanidin constituents. Therefore, the combination of two individual dyes appeared to successfully improve the UV-Vis spectra of the designed sensitizers, which is highly desirable for the DSSCs performance. As for the solvent influence on the position and intensity of the major peaks, the spectra in the CH₃OH, H₂O, DMSO, and CH₃CN look quite alike (Fig. 42); hence no solvent effect is observed. Our findings accord well with the experimental data on the UV-Vis spectra of beetroot juice and extract in methanol, ethanol and water (Devadiga & Ahipa, 2020; Dumbravă *et al.*, 2012), where the band's position and intensity appeared to be similar under different solvents. For the synthetic dye L0, the measured UV-Vis spectrum in the CH₃OH demonstrated the λ_{max} assigned to 433 nm (Tiwari & Pal, 2015). In our simulated spectra of the L0, the λ_{max} is 453 nm, which is higher by 20 nm, i.e., 5% deviation.

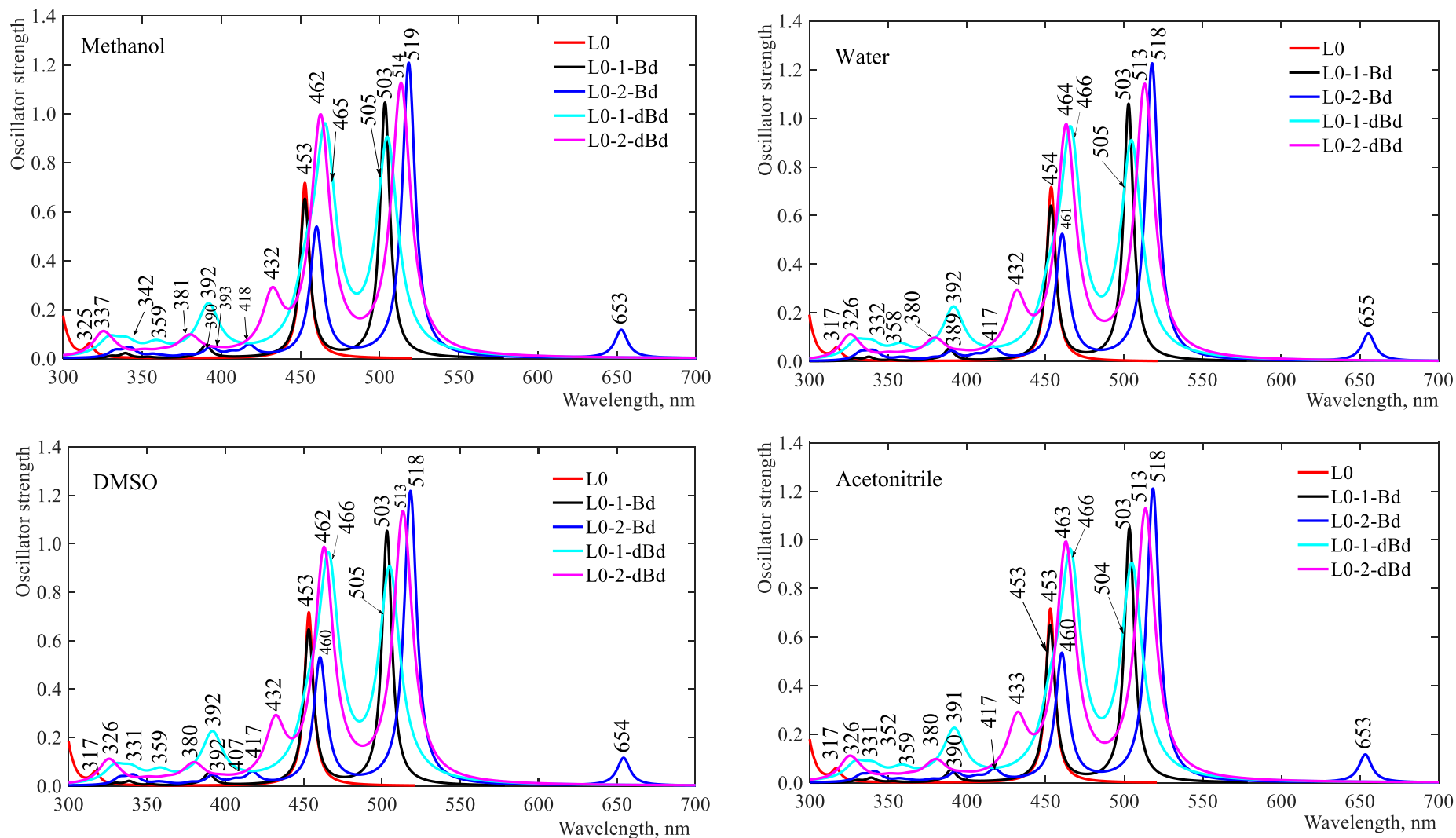


Figure 42: UV-Vis spectra of the dyes L0, L0-1-Bd, L0-2-Bd, L0-1-dBd and L0-2-dBd simulated at TD-DFT/B3LYP/6-31G(d,p) with PCM for DMSO

(iii) Energy level alignment of the betanidin complexes dyes

The power conversion efficiency of DSSCs depends on the appropriate energy level alignment of a dye to provide good electron injection and dye regeneration (Li *et al.*, 2019; Makoye *et al.*, 2020). The diagram of the frontier and adjacent MOs energy levels, the valence and conduction band edges of a substrate, and the redox level of electrolytes are shown in Fig. 43. Excited states of the molecules can be represented through excited states oxidation potentials (*ESOPs*) (Madili *et al.*, 2018; Makoye *et al.*, 2020; Oprea *et al.*, 2011), which have been obtained as the sum of energies of the occupied MOs and relevant excitation energies. The calculated energies of the frontier and adjacent MOs, excitation energies ΔE_{0-n} , energy gaps E_g and *ESOPs* are indicated in Table 15. The obtained results point out that for the L0 and L0-Bd complexes, values of the E_g are greater by 0.14–0.50 eV than particular excitation energies; that is, the *ESOPs* are lower than the energies of respective unoccupied MOs. However, for the H→L+1 transition in the L0-dBd complexes, the E_g appeared to be less than ΔE_{0-2} .

In agreement with reasonable photosensitiser requirement, a LUMO of a dye should lie above the conduction band edge of the semiconductor TiO₂ (−4.05 eV) (Fujisawa *et al.*, 2017; Makoye *et al.*, 2020) to provide electron injection into the substrate from the excited photosensitiser. The level of the HOMO should lie below the redox potential of the electrolyte I[−]/I₃[−] (−4.83 eV) (Mishra *et al.*, 2009) or spiro-OMeTAD (−5.05 eV) (Nguyen *et al.*, 2014) for the dye regeneration by acquiring electrons from the electrolyte. As is observed in Fig. 43, all considered dyes meet the criteria of the energy level alignment for the electron injection to be proper photosensitisers when TiO₂ semiconductor is used due to LUMO levels lie above the conduction band of the TiO₂, and the *ESOPs* levels approach very close to the CB edge allowing electron transfer to the substrate.

To the side of occupied MOs, for the L0 and betanidin complexes, L0-Bd, their HOMO levels lie below the redox level of the I[−]/I₃[−] or spiro-OMeTAD electrolyte, which allows electron transfer to the pigment molecule from the electrolyte. On the contrary, in the decarboxylated betanidin complexes L0-dBd, their HOMO levels lie above the redox potential of the electrolyte; hence the L0-dBd complexes do not satisfy the requirement for sensitiser regeneration. Therefore, the obtained energy level diagram designates that betanidin complexes L0-Bd might be better candidates for the DSSCs than individual L0 and decarboxylated L0-dBd dyes.

Table 15: Energies of the molecular orbitals $\varepsilon(\text{MO})$, excitation energies ΔE_{0-n} , energy gaps E_g and $ESOPs$ of the selected transitions with oscillator strength $f \geq 0.1$ for the dyes in DMSO; all values are in eV

Dye	MO	$\varepsilon(\text{MO})$	Transition	ΔE_{0-n}	E_g	$E_g - \Delta E_{0-n}$	$ESOP$
L0	89, H	-5.33	H \rightarrow L	2.74	2.90	0.16	-2.59
	86, H-3	-6.96	H-3 \rightarrow L	4.18	4.53	0.35	-2.78
	90, L	-2.43	H \rightarrow L+2	4.38	4.95	0.57	
	92, L+2	-0.38					
L0-1-Bd	185, H	-5.22	H-1 \rightarrow L	2.46	2.60	0.14	-3.24
	184, H-1	-5.70	H \rightarrow L+1	2.74	2.89	0.15	-2.48
	186, L	-3.10					
	187, L+1	-2.33					
L0-2-Bd	185, H	-5.23	H \rightarrow L	1.90	2.08	0.18	-3.33
	184, H-1	-5.73	H-1 \rightarrow L	2.39	2.58	0.19	-3.34
	186, L	-3.15	H \rightarrow L+1	2.69	2.83	0.14	-2.54
	187, L+1	-2.40					
L0-1-dBd	174, H	-3.98	H \rightarrow L+1	2.46	2.16	-0.30	-1.52
	173, H-1	-5.35	H-1 \rightarrow L	2.66	2.81	0.15	-2.69
	175, L	-2.54	H \rightarrow L+2	2.74	3.24	0.50	-1.24
	176, L+1	-1.82	H \rightarrow L+4	3.16	3.43	0.27	-0.82
	177, L+2	-0.74					
	178, L+4	-0.55					
L0-2-dBd	174, H	-4.00	H \rightarrow L+1	2.42	2.17	-0.25	-1.58
	173, H-1	-5.33	H-1 \rightarrow L	2.68	2.85	0.17	-2.65
	175, L	-2.48	H \rightarrow L+2	2.87	3.27	0.40	-1.13
	176, L+1	-1.83					
	177, L+2	-0.73					

Table 16: Ionisation potentials (IP_v , IP_{ad}); electron affinities (EA_v , EA_{ad}); hole and electron extraction potentials (HEP , EEP); hole, and electron and total reorganisation energies (λ_h , λ_e , λ) of the L0 and designed complexes; all values are in eV

Dye	IP_v	IP_{ad}	HEP	EA_v	EA_{ad}	EEP	λ_h	λ_e	λ
L0	6.66	6.59	6.52	0.75	1.07	1.39	0.14	0.64	0.78
L0-1-Bd	6.40	6.29	6.20	1.79	2.18	2.69	0.20	0.90	1.10
L0-2-Bd	6.39	6.28	6.11	1.94	2.21	2.63	0.28	0.69	0.97
L0-1-dBd	4.95	4.70	4.47	1.34	1.70	2.08	0.48	0.74	1.22
L0-2-dBd	4.95	4.70	4.47	1.35	1.65	1.98	0.48	0.64	1.11

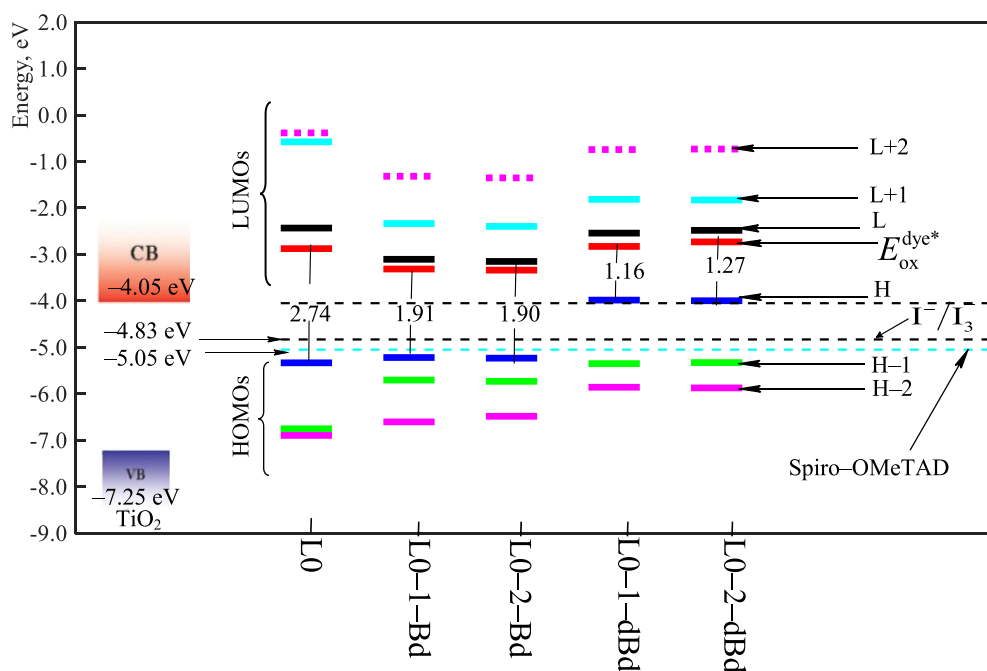


Figure 43: Energy level diagram of relevant MOs, excited state potentials $E_{\text{ox}}^{\text{dye}}$ and excitation energies ΔE_{0-1} for the dyes under study for the DMSO solvent. Valence and conduction bands of TiO_2 (Fujisawa *et al.*, 2017; Makoye *et al.*, 2020) redox potentials for electrolytes, I^-/I_3^- (Mishra *et al.*, 2009) and Spiro-OMeTAD (Nguyen *et al.*, 2014), are shown for comparison

(iv) Ionisation potential, electron affinities and reorganisation energies

Fundamental characteristics, ionisation potential (IP) and electron affinity (EA), are directly linked to the electrons and holes formation in optoelectronic materials. The IP is to be small so that electron detachment would lead to a hole formed in the HOMO. At the same time, the EA , as the energy released when an electron is added to the molecule, should be high to enable efficient electron admittance into the LUMO level. The reorganisation of dye molecules in neutral and ionised states was considered via geometry optimisation in those states. Along with vertical and adiabatic IP and EA , the hole and electron extraction potentials (HEP , EEP), as well as hole and electron reorganisation energies (A_h , A_e), have been determined using the information in Appendix 3; these parameters are shown in Table 16. A comparison of electronic energies for the dye molecules was performed through a bar graph (Fig. 44). The IP_v , IP_{ad} , and HEP values rise in the order $\text{L0-dBd} < \text{L0-Bd} < \text{L0}$ and follow the sequence of the HOMO energy magnitudes in accordance with Koopmans' theorem. The electron affinities EA_v , EA_{ad} and $EEPs$ increase in $\text{L0} < \text{L0-dBd} < \text{L0-Bd}$. The adiabatic to vertical IP ratio is close to one for all dye molecules, while the ratio EA_{ad}/EA_v lies in the range of 1.14–1.43 (Fig. 45).

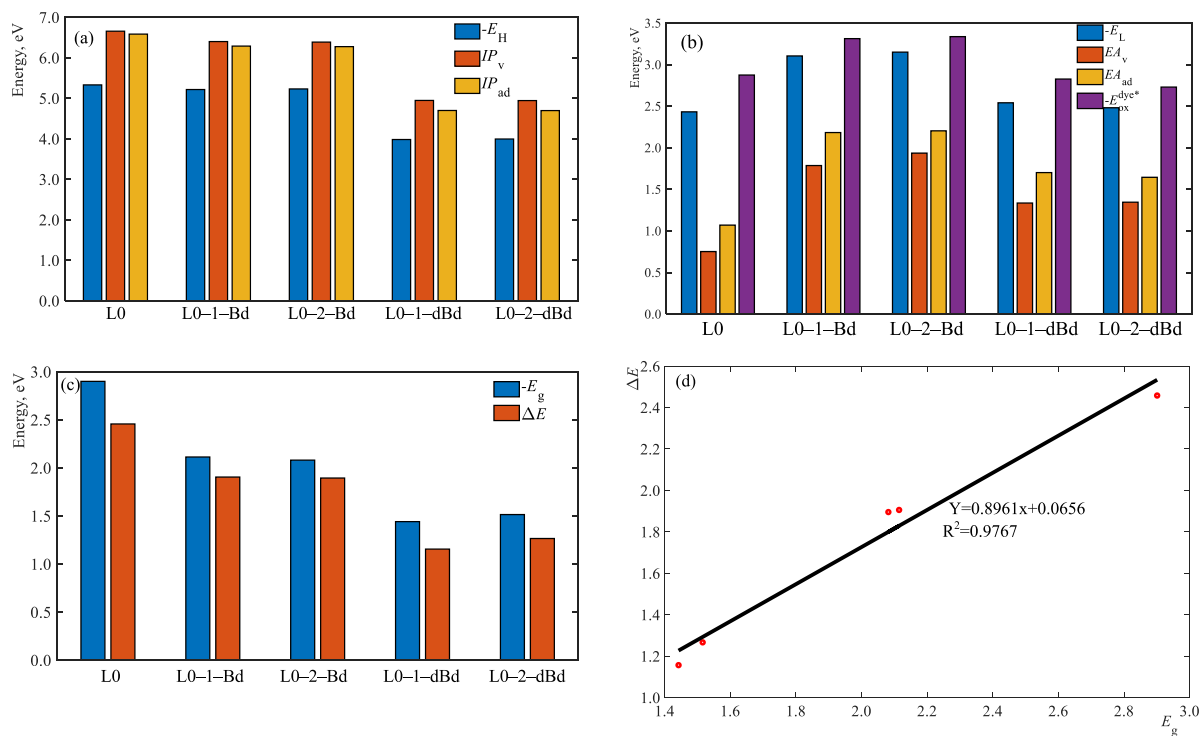


Figure 44: Comparison of electronic energies for the dye molecules L0, L0-1-Bd, L0-2-Bd, L0-1-dBd and L0-2-dBd: (a) $-E_H$, IP_v and IP_{ad} ; (b) $-E_L$, EA_v , EA_{ad} and $-ESOP$; (c) $-E_g$ and ΔE ; (d) ΔE_{0-n} vs $-E_g$

For the considered dyes, reorganisation energies are less for holes than for electrons, $\lambda_h < \lambda_e$ (Fig. 46), indicating higher hole mobility. The latter might yield higher PCE for the L0-Bd complexes than the other dyes. Based on the Marcus electron transfer theory (Anderson & Lian, 2004; Marcus, 1965), the lower values of reorganisation energies result in a higher rate constant of charge transfer (Tripathi & Prabhakar, 2020).

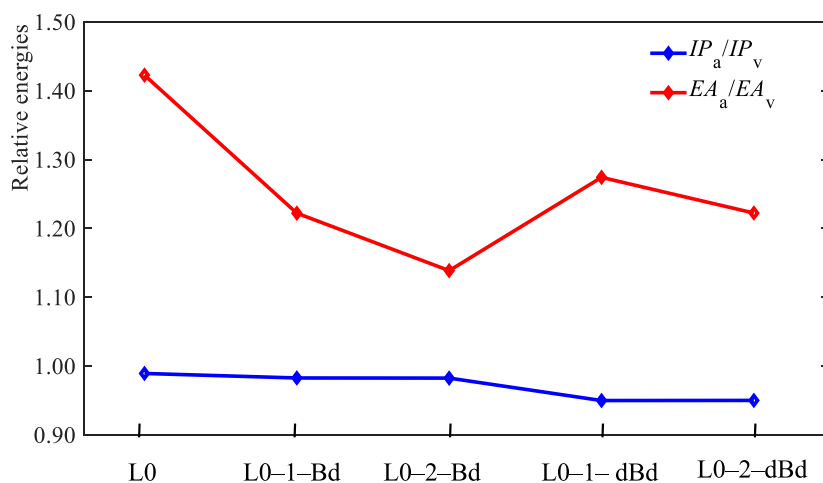


Figure 45: Ratio of adiabatic to vertical values of IP and EA for the L0, L0-1-Bd, L0-2-Bd, L0-1-dBd and L0-2-dBd

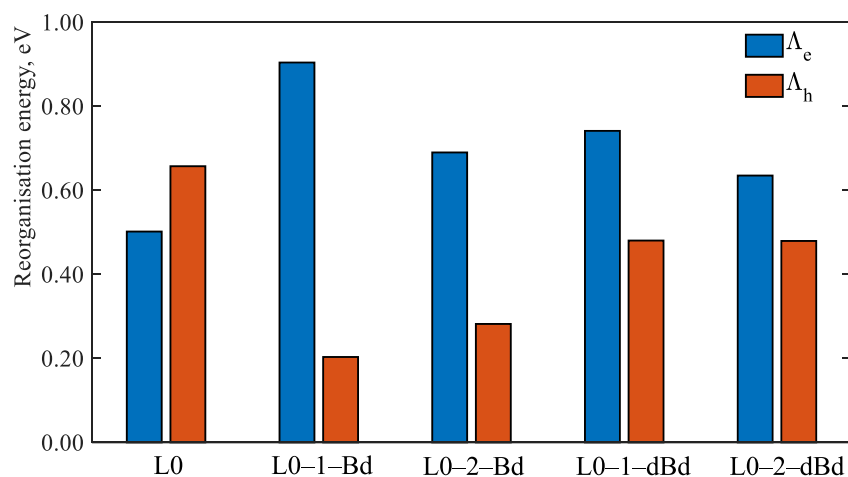


Figure 46: Comparison of reorganisation energies for electrons and holes in the L0, L0-1-Bd, L0-2-Bd, L0-1-dBd and L0-2-dBd

Ionisation potential and electron affinity are necessary for elucidating whether molecules are more or less reactive (Deogratias *et al.*, 2019). Therefore, it is worth establishing a relationship between IP and EA values for the dyes under study with reference data for Na and F atoms, respectively, through relative electron donation RIP and electron acceptance REA indices (Martínez *et al.*, 2009):

$$RIP = \frac{IP_v(\text{dye})}{IP_v(\text{Na})} \quad (97)$$

$$REA = \frac{EA_v(\text{dye})}{EA_v(\text{F})} \quad (98)$$

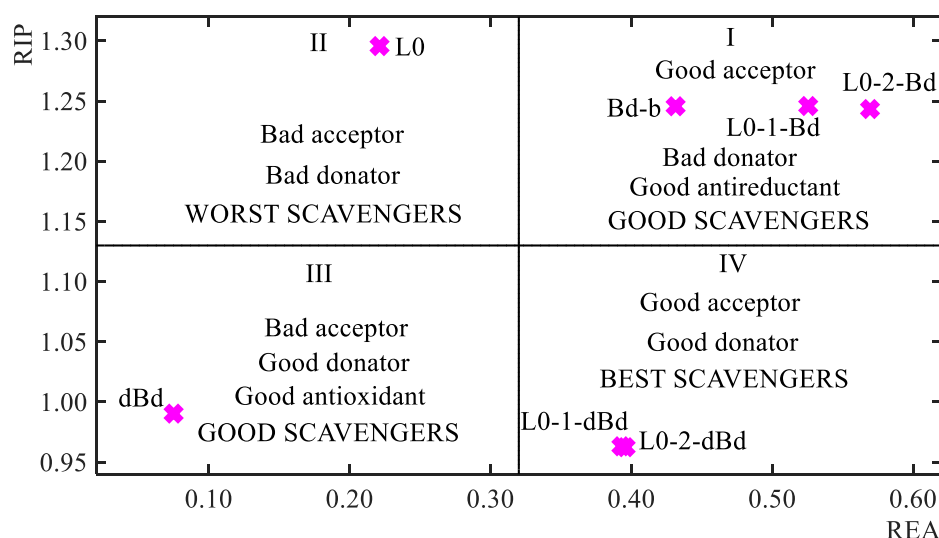


Figure 47: Full electron donor-acceptor map; data for individual dyes Bd-b and dBd betanidin dyes

Using these values, *RIP* vs *REA*, it is desirable to construct a full electron donor-acceptor map (FEDAM) (Martínez *et al.*, 2009). It allows allocating the considered dyes regarding their electron-donating or electron-accepting capabilities, as shown in Fig. 47. Among the considered dyes, the decarboxylated designed complexes L0–1–dBd and L0–2–dBd are located in quadrant IV, thus demonstrating the remarkable capability of being good photon energy scavengers. The acceptor tendency is associated with the COOH group of the six-membered ring of betanidin. In contrast, the donor tendency is achieved by the triphenylamine part of the L0 within the dye complex. The challenge of the decarboxylated complexes is in the electron regeneration as per the energy level alignment diagram (Fig. 43). The problem of the poor regeneration may be caused by unsuitable electron density distribution in the frontier MOs, that is, the poor percentage contribution of the L0 moiety fragment in the HOMO, as indicated in Table 13 and Fig. 47. Therefore, the donation and acceptance of the electrons by the decarboxylated betanidin complexes L0–1–dBd and L0–2–dBd is expected to be non-spontaneous due to failing of the electron regeneration. On the other hand, we suggest that a large contribution (about 80–90%, Table 14) of the H–1 MO to the intensive electronic transition at 463 nm might increase the regeneration ability of the L0–dBd complexes. As a whole, Fig. 41 indicates an improvement of the complexes compared to the original dyes; the Bd–b is improved in quadrant I for being a good acceptor, dBd and L0 shift from quadrant III and II, respectively, to quadrant IV.

4.2.5 Designed betanidin complexes adsorption on the TiO₂ cluster

The dye complexes' attachment to the TiO₂ cluster is simulated in terms of different possible adsorption modes and their binding energies (BE). The electronic spectra of the dye@TiO₂ systems have been computed, and electron density distributions over FMOs analysed.

(i) Betanidin complex adsorption modes and binding energies

Adsorption of the dye complexes L0–Bd and L0–dBd on the TiO₂ was considered through the CO₂, carboxylic, or ester groups; the semiconductor surface was imitated by the (TiO₂)₆ cluster based on the study by Syzgantseva *et al.*, (2011) during the dye attachment, the dye hydrogen atom was detached from the anchoring group. It was linked to the (TiO₂)₆ cluster. According to the literature (Zhang *et al.*, 2018), the bidentate bindings were stronger than other adsorption modes, mono- or bidentate chelating. The smaller the bond length and greater the BE magnitude means that the dye@TiO₂ system is more stable; for example, the

Ti–O bond distance in the range 2.05–2.10 Å or less was commented that the dye interacts strongly with the TiO₂ (Chen *et al.*, 2009; Pastore & De Angelis, 2010). Our simulation aimed at the bidentate adsorption modes and compared the designed complexes and individual dyes, L0, Bd or dBd. From our calculations via the B3LYP/6–31G(d,p)/LANL2DZ method, the total energies of the interacting species were established to be as follows: (TiO₂)₆ cluster –1253.5231 au, dehydrogenated L0 dye –1107.9433 au and complexes, L0–1–Bd –2438.3757 au, L0–2–Bd –2438.3834 au, L0–1–dBd –2249.7901 au and L0–2–dBd –2249.7894 au. The considered links between the dye site and (TiO₂)₆ cluster are shown in Fig. 48. The calculated adsorption energies and bond lengths are indicated in Table 17. In addition, the histogram (Fig. 49) compares the binding energies of the dye@TiO₂ systems.

Table 17: Dye@TiO₂ adsorption links, the O–Ti bond distances^a; total electronic energies and binding energies of the studied systems calculated at the B3LYP/6–31G(d,p) for the dye molecules and LANL2DZ for Ti atoms

System	D1	D2	D3	$E_{\text{dye@TiO}_2}$, au	BE, eV	BE, eV
L0@TiO ₂	1.993	1.986	–	–2361.6020	–17.3	
L0–1–Bd–C18@TiO ₂	2.038	1.944	–	–3692.6143	–19.5	–20.7
L0–1–Bd–C16@TiO ₂	2.023	2.012	–	–3692.0065	–16.6	–17.1
L0–1–Bd–C17@TiO ₂	2.022	2.019	–	–3691.9932	–16.2	–17.4
L0–2–Bd–C18@TiO ₂	2.018	2.002	–	–3692.6331	–19.8	–20.7
L0–2–Bd–C16@TiO ₂	2.011	2.004	–	–3692.0034	–16.3	–17.1
L0–2–Bd–C17@TiO ₂	2.045 ^b	–	–	–3692.0231	–16.8	–17.4
L0–2–Bd–ester@TiO ₂	–	–	1.877 ^b	–3692.5841	–18.4	
L0–1–dBd–C16@TiO ₂	1.964	1.960	–	–3503.4345	–16.9	–17.5
L0–1–dBd–C17@TiO ₂	2.050	2.002	–	–3503.4655	–17.8	–17.2
L0–2–dBd–C16@TiO ₂	1.965	1.960	–	–3503.4345	–16.9	–17.5
L0–2–dBd–C17@TiO ₂	2.005	2.004	–	–3503.4222	–16.6	–17.2
L0–2–dBd–ester@TiO ₂	–	–	1.879 ^b	–3503.9706	–17.9	

^aThe O–Ti distances D1, D2 correspond to C–O@TiO₂, C=O@TiO₂ bonds of the carboxylic groups and D3 corresponds to the C=O@TiO₂ bond of the ester group. ^bIndicated links are monodentate.

For the dye@TiO₂ systems, the obtained BE values are negative, indicating thermodynamically favourable attachment of the dyes to the TiO₂ cluster. For similar carboxylic links via C16 or C17 atoms, the decarboxylated L0–dBd@TiO₂ systems reveal shorter bond lengths and slightly greater BE magnitudes than L0–Bd@TiO₂. An exceptional monodentate C17@TiO₂ link can be noticed for the L0–2–Bd, whereas the alike link for the L0–1–Bd and decarboxylated complexes corresponds to the bidentate mode of attachment. As for the ester@TiO₂, the linkage is proved to occur only for L0–2–Bd and L0–2–dBd complexes, whereas for L0–1–Bd@TiO₂ and L0–1–dBd@TiO₂ systems upon optimisation, computation failed with error to achieve convergence.

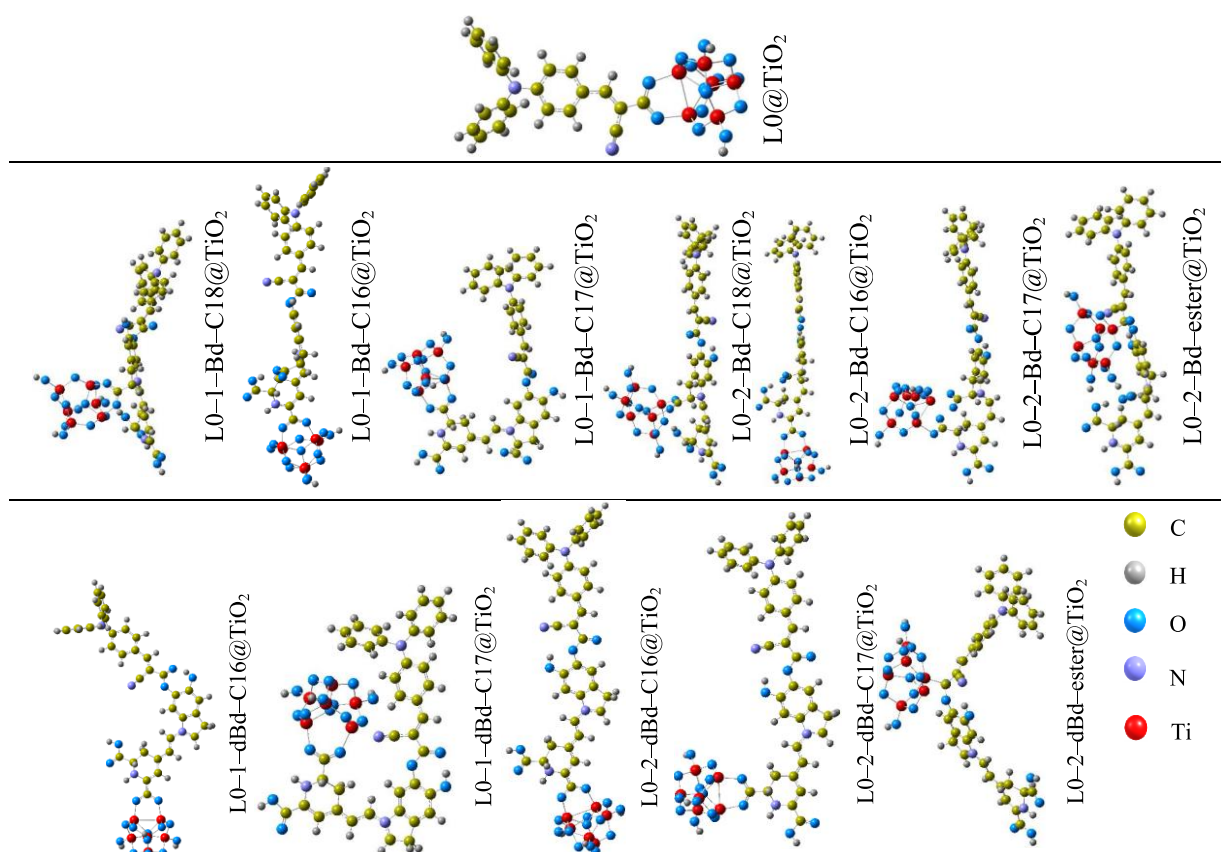


Figure 48: Optimised attachment modes for the systems: $L0@TiO_2$, $L0-1-Bd@TiO_2$ and $L0-2-Bd@TiO_2$ (at the top) and $L0-1-dBd@TiO_2$ and $L0-2-dBd@TiO_2$ (at the bottom)

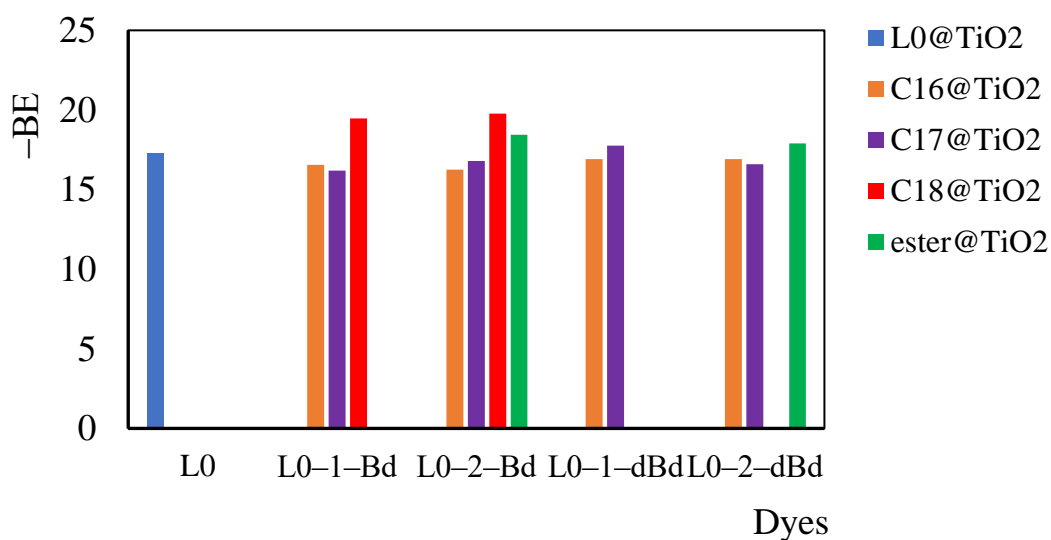


Figure 49: The binding energies of the considered attachment modes between the dyes and $(TiO_2)_6$ cluster as computed at the B3LYP/6-31G(d,p)/LANL2DZ

The link through the CO₂ group, available in the L0–Bd@TiO₂ systems, turns out strong with the highest BE magnitude of about 20 eV and this result complies with the data for the Bd@TiO₂ complexes reported in Section 4.1. Therefore, the C18@TiO₂ systems for individual Bd dye and designed L0–Bd@TiO₂ complexes show the strongest attachment that confirms the CO₂ group is most feasible for binding to the semiconductor; that might give a chance of the betanidin complexes' strengthening against decarboxylation. Hence, the insertion of the TiO₂ into the systems can favour their stabilisation. Consequently, it would be interesting to consider kinetics of the reactions R5–R8 (Table 12) under two conditions, before and after TiO₂ dipping into the dye solution.

Regarding the individual dye systems Bd@TiO₂ and dBd@TiO₂ modelled at a similar theoretical approach in Section 4.1, their binding stability is systematically higher than for respective carboxylic or CO₂ links of the designed L0–Bd@TiO₂ and L0–dBd@TiO₂ systems that are the BE trends retain. The links originating from the Bd (or dBd) sites reproduce their attachment features in the L0–Bd@TiO₂ (or L0–dBd@TiO₂) systems; at the same time, it seems reasonable that the complexes, being larger than original molecules, attach weaker to the semiconductor. It is worth mentioning the study on betalains (including betanidins) by Oprea *et al.* (2012), in which protonated and deprotonated dyes were investigated. The dyes' proton affinity was assessed in the 12–13 eV range. In Section 4.1 on the individual betanidin Bd and dBd dyes at the TiO₂ cluster, the BE magnitudes varied within 15–21 eV and in the present work, from 16 to 20 eV. Following these findings, our rather big BE magnitudes are greatly influenced by the accepted adsorption modes in which the dehydrogenated dyes are bound to the (TiO₂)₆ cluster, resulting in electrostatic interaction between the constituents.

(ii) Electronic spectra of the betanidin complex dye@TiO₂

For the considered dye@TiO₂ adsorption modes, the electronic transitions $S_0 \rightarrow S_n$ ($n=1-20$) have been computed at the TD–DFT/CAM–B3LYP/6–31G(d,p)/LANL2DZ level of theory (Table 18). In Fig. 50, the simulated UV–Vis spectra of the systems are compared between each other as well as with isolated complexes and individual dye L0. In most cases, the dye@TiO₂ systems reveal lower excitation energies than respective isolated dyes. Therefore, the most probable electronic transitions (with $f > 0.1$) in the visible region corresponding to 462 nm (L0–1–Bd@TiO₂), 418–493 nm (L0–2–Bd@TiO₂), 572–599 nm (L0–1–dBd@TiO₂) and 415–601 nm (L0–2–dBd@TiO₂) depending on the connecting link.

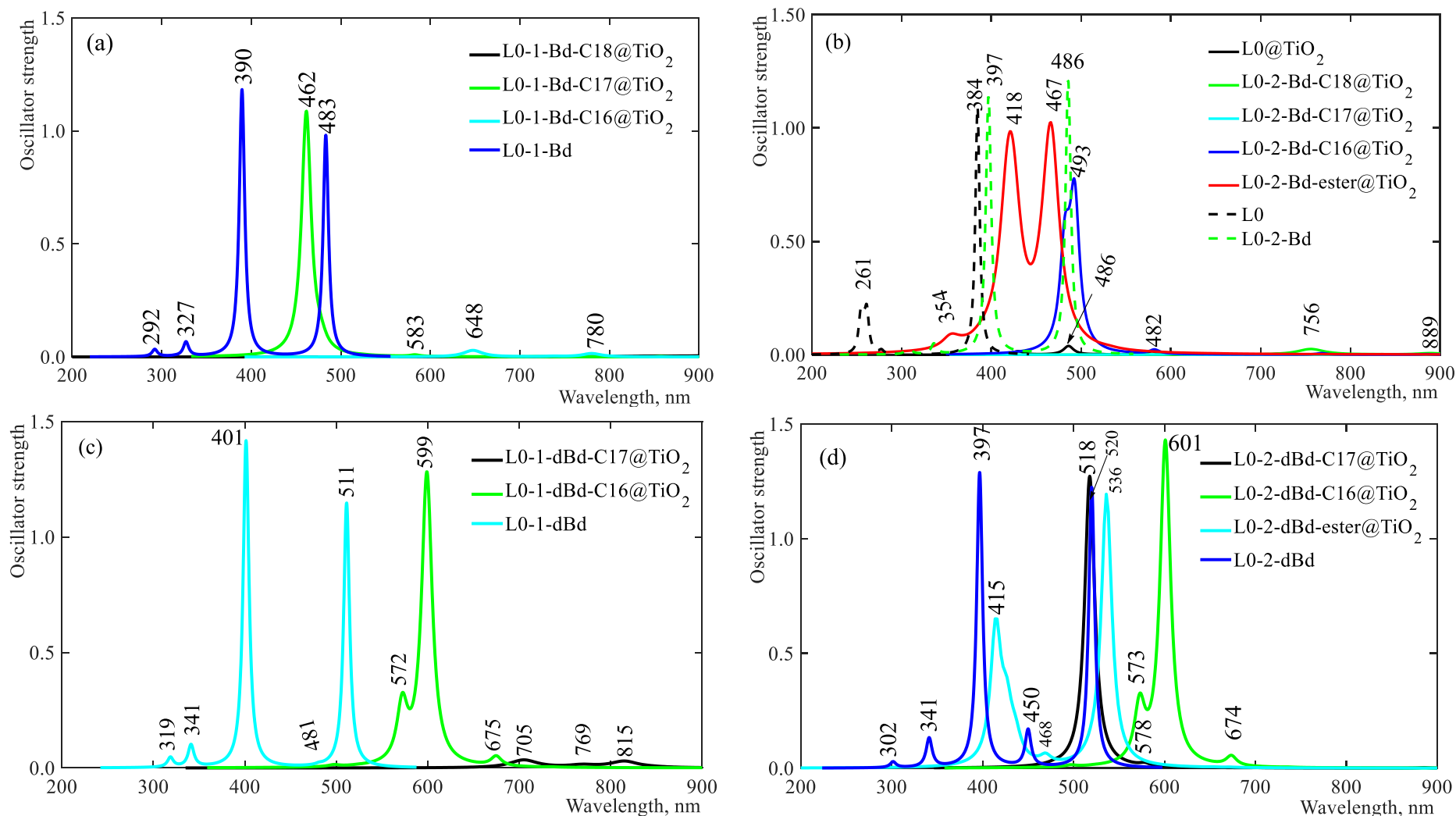


Figure 50: The UV-Vis spectra of the betanidin complexes, L0-1-Bd@TiO₂ (a), L0-2-Bd@TiO₂ (b) and decarboxylated betanidin complexes, L0-1-dBd@TiO₂ (c), L0-2-dBd@TiO₂ (d), simulated for different adsorption links at CAM-B3LYP/6-31G(d,p)/LANL2DZ with polarisable continuum model (PCM) for water

For the L0–1–Bd@TiO₂, only one peak at 462 nm is observed (that is for the C17@TiO₂ link), while for the pure complex L0–1–Bd, two peaks, 390 and 483 nm, are seen in Fig. 50a; these spectra are somehow alike to those of the L0–1–dBd–C16@TiO₂ (599 nm) and L0–1–dBd (401 and 511 nm), see Fig. 50c. For the L0–2–Bd@TiO₂ different links, the peaks correspond to the C16@TiO₂ (493 nm) and ester linkage (418, 467 nm); the latter two are similar to those of the pure complex L0–2–Bd, 397 and 486 nm (Fig. 50b). In L0–1–Bd@TiO₂ and L0–2–Bd@TiO₂ spectra, for the C18@TiO₂ mode, no noticeable peak is seen; maxima at longer wavelengths 460–490 nm originates from the betanidin and those at shorter λ around 400 nm come from the L0 dye. Regarding the decarboxylated systems L0–2–dBd@TiO₂, for the ester linkages, intensive peaks are observed at 415, 536 nm that is with the small red shift to the pure L0–2–dBd, 387 and 518 nm (Fig. 50d); in general, the spectra resemble those of the L0–2–Bd@TiO₂ and pure L0–2–Bd, respectively. Also, a similarity can be seen in the spectra for the link C16@TiO₂ in the decarboxylated complexes L0–1–dBd and L0–2–dBd is the occurrence of the split intensive peaks at 572–601 nm.

The present findings in Section 4.2 agree with the results of the original betanidin dyes reported in Section 4.1. Furthermore, the simulated spectra confirmed that the Bd and dBd dye's attachment to the TiO₂ cluster resulted in a slight broadening and red shifting of the spectral bands compared to the individual dyes. Also, our present results accord well with the literature data (Herbach *et al.*, 2006; Subalakshmi *et al.*, 2017) that the decarboxylation should not change or destabilise the chromophore structure, but it retains the chromatic characteristics of the betacyanin. Moreover, previously measured experimentally, UV–Vis spectra of betalain pigments in water before and after dipping TiO₂ film looked likewise (Zhang *et al.*, 2008), indicating a poor interaction between the dye extract and the film.

(iii) Frontier molecular orbital analysis of the betanidin complex dye@TiO₂ systems

Most probable electronic excitations $S_0 \rightarrow S_n$ (i.e., those with greater oscillators strengths) are assigned to transitions between frontier and adjacent MOs, e.g., $H-\delta \rightarrow L+\delta$, ($\delta = 0, 1, 2, 3, 4, 5, 6 \dots 20$), for the considered L0–Bd@TiO₂ and L0–dBd@TiO₂ different links (Table 18); graphical representation of the MO charge densities is shown in Fig. 51–52. For effective sensitisation, the electron density of the highest occupied orbitals should be located on or nearby the dye's anchoring group, while that of the lowest unoccupied MOs distributed close to the semiconductor area. This condition is well realised for decarboxylated systems L0–1–dBd–C17@TiO₂, L0–2–dBd–ester@TiO₂ and up to some extent for L0–1–dBd–

C16@TiO₂, whereas for other adsorption modes, the electron density distribution over systems moieties does not predict promotion of efficient electron transfer promotion from the dye to semiconductor. However, an involvement of adjacent MOs in electron transitions leads to an improvement of electron allocation and hence more efficient sensitisation and subsequent dye regeneration.

Table 18: Characteristics of electronic transitions $S_0 \rightarrow S_n$ in the dye@TiO₂ systems, L0@TiO₂, L0-1-Bd@TiO₂, L0-2-Bd@TiO₂, L0-1-dBd@TiO₂, and L0-2-dBd@TiO₂

System	n	ΔE_{0-1} , eV	λ , nm	f	LHE, %	MOs contribution, %
L0@TiO ₂	17	2.55	486	0.0383	8.4	H→L+4; 17
L0-1-Bd-C18@TiO ₂	13	1.13	1102	0.0052	1.2	H→L+2; 16
	16	1.32	941	0.0025	1.7	H→L+5; 11
L0-1-Bd-C17@TiO ₂	14	2.13	583	0.0065	1.49	H→L+8; 17
	20	2.69	462	1.0828	91.7	H-2→L; 45
L0-1-Bd-C16@TiO ₂	16	1.59	780	0.0149	3.4	H→L+8; 9
	19	1.91	648	0.0289	6	H→L+1; 36
L0-2-Bd-C18@TiO ₂	15	1.39	889	0.0065	1.49	H→L+9; 15
	18	1.64	756	0.0250	5.6	H→L; 38
L0-2-Bd-C17@TiO ₂	14	2.06	602	0.0029	0.67	H→L+5; 12
L0-2-Bd-C16@TiO ₂	19	2.52	493	0.6508	77.7	H-2→L; 22
L0-2-Bd-ester@TiO ₂	8	2.66	467	0.8367	85.4	H-1→L; 42
	11	2.96	418	0.5438	71.4	H→L+2; 10
	19	3.51	354	0.0265	5.9	H→L+4; 7
L0-1-dBd-C17@TiO ₂	17	1.52	815	0.0275	6.1	H-1→L+1; 20
	18	1.61	769	0.0101	2.3	H-1→L+2; 20
	19	1.76	705	0.0336	7.4	H-1→L+1; 13
L0-1-dBd-C16@TiO ₂	10	1.84	675	0.0416	9.1	H-1→L+1; 18
	14	2.07	599	1.2680	94.6	H→L+1; 36
	17	2.17	572	0.2466	43.3	H-1→L+7; 11
L0-2-dBd-C17@TiO ₂	14	2.14	578	0.0104	2.4	H-1→L+8; 15
	19	2.39	518	1.2565	94.5	H→L+5; 42
L0-2-dBd-C16@TiO ₂	10	1.84	674	0.0426	9	H-1→L+1; 11
	14	2.06	601	1.4164	96.2	H→L; 19
	17	2.16	573	0.2453	43.2	H-1→L+7; 11
L0-2-dBd-ester@TiO ₂	8	2.31	536	1.1912	93.6	H→L+5; 43
	18	2.99	415	0.5952	74.6	H-1→L; 12

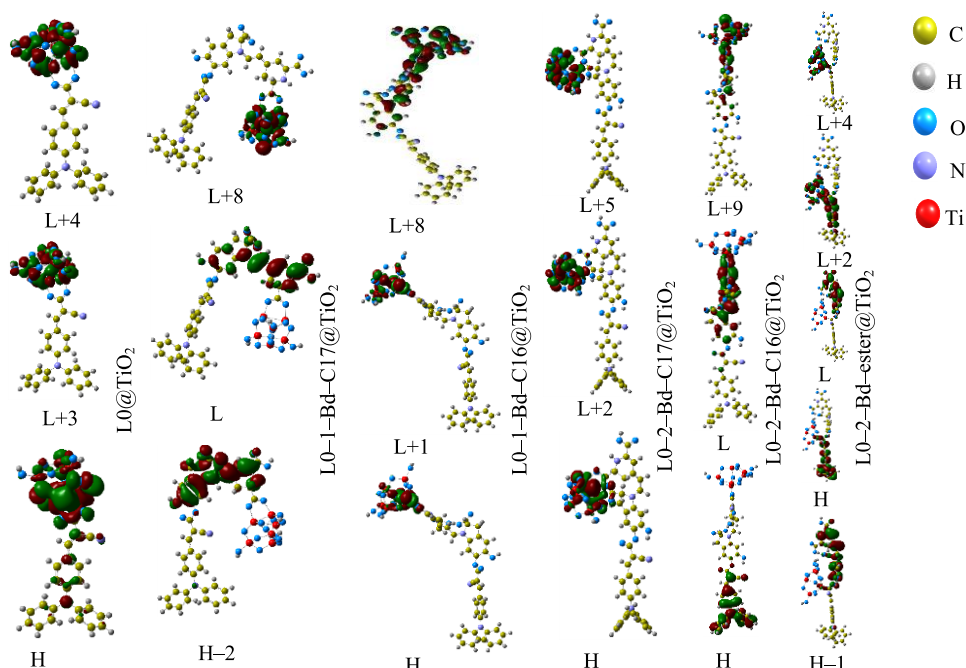


Figure 51: The distribution patterns of the frontier and adjacent molecular orbitals involved in the $S_0 \rightarrow S_n$ transition for the $L0@TiO_2$, $L0-1-Bd@TiO_2$ and $L0-2-Bd@TiO_2$ calculated at the CAM-B3LYP/6-31G(d,p)/LANL2DZ with polarisable continuum model for water; H is the HOMO, L is the LUMO

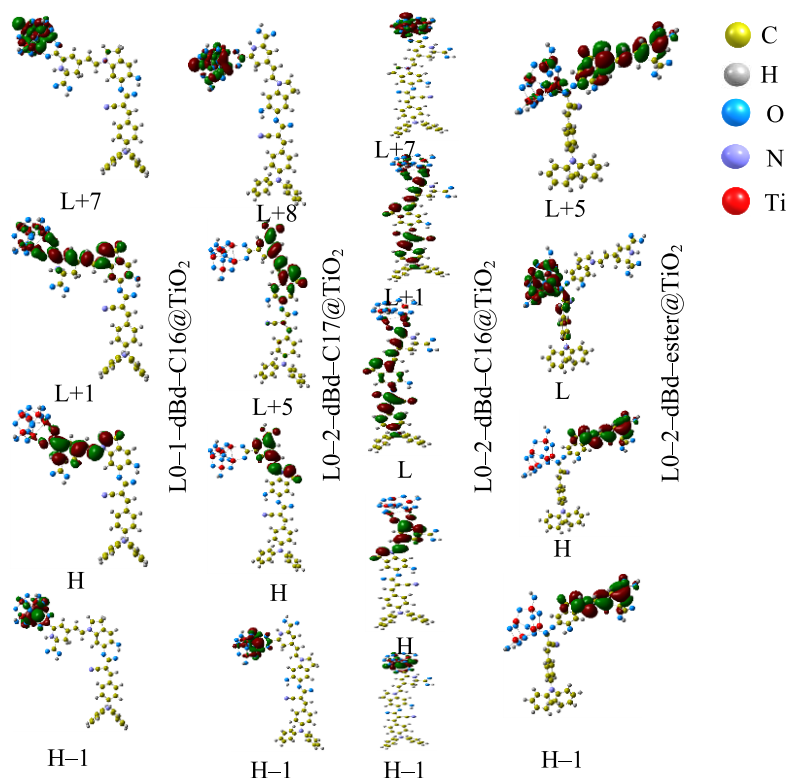


Figure 52: The distribution patterns of the frontier and adjacent molecular orbitals involved in the $S_0 \rightarrow S_n$ transition for the decarboxylated betanidin complexes $L0-1-dBd@TiO_2$ and $L0-2-dBd@TiO_2$ calculated at the CAM-B3LYP/6-31G(d,p)/LANL2DZ with polarisable continuum model for water; H is the HOMO, L is the LUMO

CHAPTER FIVE

CONCLUSION AND RECOMMENDATIONS

5.1 Conclusion

Theoretical work on modification of the betanidin molecules has been conducted using quantum chemical approaches towards the dye-sensitised solar cell applications. First, the alteration was based on achieving intramolecular bonding, resulting in the bent structural form rather than the planar one. Second, because the betanidin molecule has carboxylic groups throughout, the availability of additional electron donor species via the hydroxyl groups at C₁ and C₂ was advantageous. The donor dye of choice was triphenylamine (TPA) or L0 as a synthetic dye molecule that combines with betanidin molecules at C₁ and C₂ to generate the complex dyes L0-1-Bd and L0-2-Bd, respectively. The stability and feasibility of the associated processes were calculated and analysed using thermodynamic functions, and the results were compared to molecular descriptors for further interpretations. Thirdly, thermodynamic, optoelectronic, spectro-electrochemical, and chemical reactivity parameters of betacyanins-based molecular-engineered dyes revealed promising results.

The structural parameters, thermodynamic and optoelectronic properties of betanidin isomers, bent Bd-b, planar Bd-p, and decarboxylated betanidin dBd were investigated. Due to the hydrogen bond formation, the bent structure is more stable energetically than the planar one. At the same time, according to the thermodynamic approach, the planar isomer appeared to be more abundant in the gas phase equilibrium because of the entropy factor. Both betanidin isomers demonstrated instability undergoing spontaneous decomposition into the dBd and CO₂. Regarding the optoelectronic and charge transfer properties, a strong absorption band at 460–530 nm is revealed in the simulated UV-Vis spectra of the dyes. According to the energy level alignment diagram, the dyes meet the requirement for electron injection into the conduction band of the TiO₂ semiconductor. Both betanidin dyes are suitable for regeneration, whereas the dBd does not satisfy the criterion on the regeneration as its HOMO energy lies above the redox potential of the electrolytes. The dye's attachment to the hydrogenated TiO₂ cluster has been simulated and analysed. The determined binding energies and isosurfaces of relevant MOs involved in most probable electronic transitions testify that suitable localisation of the electrons favours increasing the binding strength of the dye with the TiO₂ cluster. Therefore, we anticipate that the optoelectronic properties of natural

betanidin dyes might be improved via the introduction of spacers or linkers and modification through esterification or other reactions.

The metal-free organic sensitisers, the betanidin complexes L0-Bd and decarboxylated betanidin complexes L0-dBd, were designed through esterification reactions between the individual dyes L0 and Bd or dBd. The complexes gained improved optoelectronic properties like expanded UV-Vis spectra, favourably including the most intensive bands from the two constituents, near 400 nm from the L0 and around 500 nm from Bd or dBd. Calculated enthalpies and Gibbs free energies of chemical reactions show that the L0-dB complexes are predicted to decompose with CO₂ release and L0-dBd formation. Following the energy level diagram obtained, the L0-Bd complexes satisfy the requirement to sensitise the TiO₂ semiconductor and be regenerated by the electrolyte I⁻/I₃⁻, while the L0-dBd dyes do not show the regeneration ability. Therefore, according to electrochemical properties, the L0-Bd complexes are more appropriate sensitisers but prone to decompose with CO₂ detachment.

Nevertheless, from our simulations of the dye adsorption to the TiO₂, the attachment mode via the CO₂ group reveals the strongest binding compared to other modes. Hence, routine utilisation of the TiO₂ semiconductor in a DSSC might favour the system's stabilisation. Consequently, it would be interesting to consider the L0-Bd complexes' decomposition kinetics under two conditions, before and after TiO₂ dipping into the dye solution. The decarboxylated L0-dBd complexes are stable but may challenge regeneration. The involvement of adjacent MOs could overcome this obstacle to electronic transitions confirmed by the TD-DFT computations. On the other hand, we anticipate that the energies of the frontier and adjacent MOs might be adjusted through structural modification of the complexes by introducing certain spacers or linkers.

5.2 Recommendations

The obtained thermodynamic, spectro-electrochemical, optoelectronic, and chemical reactivity properties indicate that the designed betacyanins sensitisers may offer several opportunities to improve the dye-sensitised solar cell power conversion efficiency. The theoretical research of the chromophore structures of the betacyanins has been stacked (Qin & Clark, 2007) due to the planar structure of the betanidin, which produce critical detachment of CO₂. The present findings unlock the existing stack concepts after critical modification and analysis of another geometrical structure, the bent structure. The combining of other dyes to

the betacyanins was thought to be implemented. Despite the findings and efforts presented in this work, further study may be carried out and recommended on the basis of theoretical and experimental approaches:

- (i) The initiative was implemented to improve the desired properties through a complex design based on synthetic L0 dye donor materials. Therefore, the recommendation of the betacyanin dimer complex design for betanidin and decarboxylated betanidin through dimerisation to obtain a dimer molecule may be considered beneficial to avoid much dependence on synthetic materials.

Dimerisation of the betacyanin (betanidin/decarboxylated betanidin)

This dimer formation will offer the possibility for the engineered inclusion of a modified pi-spacer with both characteristics of transferring electrons and donating them to the benzenoid ring.

Phenyl betalains and their derivatives (pBeet and OxiBeet)

Betacyanins have a number of potential dye materials which have never been tested for energy harvesting and other crucial applications. However, these materials' preliminary potential properties have been found and published in recent years. Many betalain pigment materials need to be well understood through their chromophore structure. It will allow its screening of available potential properties towards the sustainable application. Investigations of the phenyl betalains and their derivatives should be aimed at understand of the structural conformers, their stability and the role of pi-spacers.

- (ii) Based on the theoretical data published by Qin and Clark (2007), the experimental UV–Vis absorption measurements reported by Zhang *et al.* (2008), and the properties of the L0 dye reported by Marinado *et al.* (2010), the present work was carried out to deepen the sensitiser's understandings. The designed complexes, and the existing betacyanins conformers experimental measurement ought to be taken into account for future studies. Firstly, the synthesis of the proposed, designed dyes is to be realised. Secondly, the experimental of the UV–Vis absorption and emission spectra are to be measured and compared with theoretically predicted parameters. Thirdly, considering

indoor and outdoor tool kit tests for the designed materials is inevitable. Fourthly, it is desirable to test the designed dyes with the pi-spacers.

Since the pBeet and OxiBeet have been investigated, their test for energy harvesting has never been realised either theoretically or experimentally; this is the promising gap. It is this gap which needs urgently recovered not only from a theoretical standpoint but also from an experimental perspective on the energy harvesting applications.

- (iii) Assessment through a review of the betalains conformers' structure, synthesis, properties, characterisation, stability issues towards dye-sensitised solar cells and application is essential.

REFERENCES

- Acosta, C. M., Ouyang, R., Fazzio, A., Scheffler, M., Ghiringhelli, L. M., & Carbogno, C. (2018). Analysis of topological transitions in two-dimensional materials by compressed sensing. *arXiv preprint arXiv*, 1–10.
- Aduloju, K. A., Shitta, M. B., & Simiyu, J. (2011). Effect of extracting solvents on the stability and performances of dye-sensitized solar cell prepared using extract from *Lawsonia Inermis*. *Fundamental Journal Modern Physics*, 1(2), 261–268.
- Agrawal, A., & Choudhary, A. (2016). Perspective: Materials informatics and big data: Realization of the “fourth paradigm” of science in materials science. *APL Materials*, 4(5), 1–11. <https://doi.org/10.1063/1.4946894>.
- Ahn, T. K., Kim, K. S., Kim, D. Y., Noh, S. B., Aratani, N., Ikeda, C., Osuka, A., & Kim, D. (2006). Relationship between two-photon absorption and the π -conjugation pathway in porphyrin arrays through dihedral angle control. *Journal of the American Chemical Society*, 128(5), 1700–1704. <https://doi.org/10.1021/ja056773a>.
- Al-Qurashi, O. S., & Wazzan, N. (2021). Prediction of Power Conversion Efficiencies of Diphenylthienylamine-Based Dyes Adsorbed on the Titanium Dioxide Nanotube. *ACS Omega*, 6(13), 8967–8975. <https://doi.org/10.1021/acsomega.0c06340>.
- Alghamdi, A. H., & Li, L. (2013). Adapting design-based research as a research methodology in educational settings. *International Journal of Education and Research*, 1(10), 1–12.
- Alhamed, M., Issa, A. S., & Doubal, A. W. (2012). Studying of natural dyes properties as photo-sensitizer for dye sensitized solar cells (DSSC). *Journal of Electron Devices*, 16(11), 1370–1383.
- Allred, A. L., & Hensley, A. L. (1961). Electronegativities of nitrogen, phosphorus, arsenic, antimony and bismuth. *Journal of Inorganic and Nuclear Chemistry*, 17(1), 43–54.
- Allred, A. L., & Rochow, E. G. (1958). A scale of electronegativity based on electrostatic force. *Journal of Inorganic and Nuclear Chemistry*, 5(4), 264–268.

- Amjadi, S., Ghorbani, M., Hamishehkar, H., & Roufegarinejad, L. (2018). Improvement in the stability of betanin by liposomal nanocarriers: Its application in gummy candy as a food model. *Food Chemistry*, 256, 156–162.
- Anderson, N. A., & Lian, T. (2004). Ultrafast electron transfer at the molecule-semiconductor nanoparticle interface. *Annual Review of Physical Chemistry*, 56(1), 491–519.
- Andreoni, W., & Yip, S. (2020). *Handbook of Materials Modeling: Applications: Current and Emerging Materials*. Springer Cham. <https://doi.org/10.1007/978-3-319-50257-1>.
- Ardo, S., & Meyer, G. J. (2009). Photodriven heterogeneous charge transfer with transition-metal compounds anchored to TiO₂ semiconductor surfaces. *Chemical Society Reviews*, 38(1), 115–164. <https://doi.org/10.1039/B804321N>.
- Arunkumar, A., Shanavas, S., & Anbarasan, P. M. (2018). First-principles study of efficient phenothiazine-based D– π –A organic sensitizers with various spacers for DSSCs. *Journal of Computational Electronics*, 17(4), 1410–1420.
- Azeredo, H. M. C. (2009). Betalains: properties, sources, applications, and stability—a review. *International Journal of Food Science & Technology*, 44(12), 2365–2376.
- Bartolotta, A., & Calogero, G. (2020). Dye-sensitized solar cells: from synthetic dyes to natural pigments. In *Solar Cells and Light Management* (pp. 107–161). Elsevier. <https://doi.org/10.1016/B978-0-08-102762-2.00004-5>.
- Bauer, C., Boschloo, G., Mukhtar, E., & Hagfeldt, A. (2002). Interfacial Electron-Transfer Dynamics in Ru(tcterpy)(NCS)₃-Sensitized TiO₂ Nanocrystalline Solar Cells. *The Journal of Physical Chemistry B*, 106(49), 12693–12704.
- Becke, A. D. (1993). Densityfunctional thermochemistry. III. The role of exact exchange. *The Journal of Chemical Physics*, 98(492), 5648–5652.
- Becquerel, M. E. (1839). Mémoire sur les effets électriques produits sous l'influence des rayons solaires. *Comptes Rendus Hebdomadaires Des Séances De l'Académie Des Sciences*, 9, 561–567.

- Belov, G. V., Iorish, V. S., & Yungman, V. S. (1999). IVTANTHERMO for Windows — database on thermodynamic properties and related software. *Calphad*, 23(2), 173–180. [https://doi.org/10.1016/S0364-5916\(99\)00023-1](https://doi.org/10.1016/S0364-5916(99)00023-1).
- Blöchl, P. E. (1994). Projector augmented-wave method. *Physical Review B*, 50(24), 17953–17979. <https://doi.org/10.1103/PhysRevB.50.17953>.
- Born, M., & Oppenheimer, R. (1927). Zur Quantentheorie der Molekeln. *Annalen der Physik*, 389(20), 457–484. <https://doi.org/10.1002/andp.19273892002>.
- Brillouin, L. (1934). Le champ self-consistent de Fock pour les électrons des métaux. *Journal de Physique et Le Radium*, 5(8), 413–418.
- Brockington, S. F., Yang, Y., Gandia-Herrero, F., Covshoff, S., Hibberd, J. M., Sage, R. F., Wong, G. K. S., Moore, M. J., & Smith, S. A. (2015). Lineage-specific gene radiations underlie the evolution of novel betalain pigmentation in Caryophyllales. *New Phytologist*, 207(4), 1170–1180. <https://doi.org/10.1111/nph.13441>.
- Calogero, G., Bartolotta, A., Di Marco, G., Di Carlo, A., & Bonaccorso, F. (2015). Vegetable-based dye-sensitized solar cells. *Chemical Society Reviews*, 44(10), 3244–3294. <https://doi.org/10.1039/C4CS00309H>.
- Calogero, G., Di Marco, G., Cazzanti, S., Caramori, S., Argazzi, R., Di Carlo, A., & Bignozzi, C. A. (2010). Efficient dye-sensitized solar cells using red turnip and purple wild sicilian prickly pear fruits. *International Journal of Molecular Sciences*, 11(1), 254–267. <https://doi.org/10.3390/ijms11010254>.
- Calogero, G., Yum, J.-H., Sinopoli, A., Di Marco, G., Grätzel, M., & Nazeeruddin, M. K. (2012). Anthocyanins and betalains as light-harvesting pigments for dye-sensitized solar cells. *Solar Energy*, 86(5), 1563–1575.
- Cao, Y., Liu, Y., Li, F., Guo, S., Shui, Y., Xue, H., & Wang, L. (2019). Portable colorimetric detection of copper ion in drinking water via red beet pigment and smartphone. *Microchemical Journal*, 150(104176), 1–6.
- Carey, F. A., & Sundberg, R. J. (2007). *Advanced Organic Chemistry: Part A: Structure and Mechanisms*. 5th ed., pp. 1–1212. Springer New York, USA.

- Carruthers, J. E., Carruthers, W., & Coldham, I. (2004). *Modern Methods of Organic Synthesis*. 5th ed., Cambridge University Press. New York, United States of America. <https://doi.org/10.1017/CBO9780511811494>.
- Chang, H., & Lo, Y.-J. (2010). Pomegranate leaves and mulberry fruit as natural sensitizers for dye-sensitized solar cells. *Solar Energy*, 84(10), 1833–1837.
- Chapin, D. M., Fuller, C. S., & Pearson, G. L. (1954). A New Silicon p-n Junction Photocell for Converting Solar Radiation into Electrical Power. *Journal of Applied Physics*, 25(5), 676–677. <https://doi.org/10.1063/1.1721711>.
- Chattaraj, P. K. (2009). *Chemical Reactivity Theory: A Density Functional View*. CRC press. <https://doi.org/10.1201/9781420065442>.
- Chattaraj, P. K., & Giri, S. (2009). Electrophilicity index within a conceptual DFT framework. *Annual Reports Section "C" (Physical Chemistry)*, 105, 13–39.
- Chattaraj, P. K., & Roy, D. R. (2007). Update 1 of: Electrophilicity Index. *Chemical Reviews*, 107(9), PR46–PR74. <https://doi.org/10.1021/cr078014b>.
- Chen, P., Yum, J. H., Angelis, F. D., Mosconi, E., Fantacci, S., Moon, S. J., Baker, R. H., Ko, J., Nazeeruddin, M. K., & Grätzel, M. (2009). High Open-Circuit Voltage Solid-State Dye-Sensitized Solar Cells with Organic Dye. *Nano Letters*, 9(6), 2487–2492.
- Cherepy, N. J., Smestad, G. P., Grätzel, M., & Zhang, J. Z. (1997). Ultrafast Electron Injection: Implications for a Photoelectrochemical Cell Utilizing an Anthocyanin Dye-Sensitized TiO₂ Nanocrystalline Electrode. *The Journal of Physical Chemistry B*, 101(45), 9342–9351. <https://doi.org/10.1021/jp972197w>.
- Christmann, K. (1988). Interaction of hydrogen with solid surfaces. *Surface Science Reports*, 9(1), 1–163. [https://doi.org/10.1016/0167-5729\(88\)90009-X](https://doi.org/10.1016/0167-5729(88)90009-X).
- Cramer, C. J. (2013). *Essentials of Computational Chemistry: Theories and Models*. John Wiley & Sons. Chichester, England.
- Creswell, J. W. (2007). *Qualitative Inquiry & Research Design: Choosing Among Five Approaches*. 2nd ed., pp. 1–414. Sage Publications, Inc. United State of America.

- Cronquist, A., & Takhtadzhian, A. L. (1981). *An integrated system of classification of flowering plants*. pp. 1–641. Columbia University Press. New York, United State of America.
- Curtarolo, S., Hart, G. L. W., Nardelli, M. B., Mingo, N., Sanvito, S., & Levy, O. (2013). The high-throughput highway to computational materials design. *Nature Materials*, 12(3), 191–201. <https://doi.org/10.1038/nmat3568>.
- Dai, P., Yang, L., Liang, M., Dong, H., Wang, P., Zhang, C., Sun, Z., & Xue, S. (2015). Influence of the Terminal Electron Donor in D–D– π –A Organic Dye-Sensitized Solar Cells: Dithieno[3,2-b:2',3'-d]pyrrole versus Bis(amine). *ACS Applied Materials & Interfaces*, 7(40), 22436–22447. <https://doi.org/10.1021/acsami.5b06481>.
- Das, I. (2012). *An Introduction to Physical Chemistry*. New Age International. India.
- Davies, K. (Ed.). (2004). *Plant Pigments and their Manipulation*. 1st ed., Vol. 14. Blackwell Publishing Ltd. Oxford, United Kingdom. 1–369.
- Davin, T. J. (2009). *Computational Chemistry of Organometallic and Inorganic Species* [PhD Thesis] Department of Chemistry, University of Glasgow. Glasgow, United Kingdom. pp. 1–177.
- De Bièvre, P. (1997). Measurement results without statements of reliability (uncertainty) should not be taken seriously. *Accreditation and Quality Assurance*, 2, 269–269. <https://doi.org/10.1007/s007690050147>.
- DeFusco, A., Ivanic, J., Schmidt, M. W., & Gordon, M. S. (2011). Solvent-Induced Shifts in Electronic Spectra of Uracil. *The Journal of Physical Chemistry A*, 115(18), 4574–4582. <https://doi.org/10.1021/jp112230f>.
- Deogratias, G., Al-Qurashi, O. S., Wazzan, N., Pogrebnaya, T., & Pogrebnoi, A. (2020). Effects of heteroatoms in π -conjugated linkers on the optical and electronic properties of modified triphenylamine based dyes: towards DSSCs' applications. *Journal of Molecular Modeling*, 26(288), 1–15. <https://doi.org/10.1007/s00894-020-04542-x>.
- Deogratias, G., Seriani, N., Pogrebnaya, T., & Pogrebnoi, A. (2019). Tuning optoelectronic properties of triphenylamine based dyes through variation of π -conjugated units and

- anchoring groups: A DFT/TD-DFT investigation. *Journal of Molecular Graphics and Modelling*, 94, 107480, 1–13. <https://doi.org/10.1016/j.jmgm.2019.107480>.
- Devadiga, D., & Ahipa, T. (2020). Betanin: A Red-Violet Pigment-Chemistry and Applications. In S. Ashis Kumar, S. A. Nasser, & A. Hamed Majdooa (Eds.), *Chemistry and Technology of Natural and Synthetic Dyes and Pigments*, 772(10), 1–19. IntechOpen. <https://doi.org/10.5772/intechopen.88939>
- Dhananjayan, I., Kathirolu, S., Subramani, S., & Veerasamy, V. (2017). Ameliorating effect of betanin, a natural chromoalkaloid by modulating hepatic carbohydrate metabolic enzyme activities and glycogen content in streptozotocin – nicotinamide induced experimental rats. *Biomedicine & Pharmacotherapy*, 88, 1069–1079.
- Dhere, N. G. (2007). Toward GW/year of CIGS production within the next decade. *Solar Energy Materials and Solar Cells*, 91(15), 1376–1382.
- Domingo, L. R., Aurell, M. J., Arnó, M., & Sáez, J. A. (2007). Toward an understanding of the 1,3-dipolar cycloaddition between diphenylnitrone and a maleimide:bisamide complex. A DFT analysis of the reactivity of symmetrically substituted dipolarophiles. *Journal of Molecular Structure: Theochem*, 811(1), 125–133.
- Domingo, L. R., Chamorro, E., & Pérez, P. (2008). An Understanding of the Electrophilic/Nucleophilic Behavior of Electro-Deficient 2,3-Disubstituted 1,3-Butadienes in Polar Diels–Alder Reactions. A Density Functional Theory Study. *The Journal of Physical Chemistry A*, 112(17), 4046–4053.
- Dumbravă, A., Enache, I., Oprea, C. I., Georgescu, A., & Gîrțu, M. A. (2012). Toward a more efficient utilisation of betalains as pigments for dye-sensitized solar cells. *Digest Journal of Nanomaterials & Biostructures (DJNB)*, 7(1), 1–13.
- Eagar, T. W. (1995). Bringing new materials to market. *Technology Review*, 98(2), 42–49.
- Escribano, J., Cabanes, J., Jiménez-Atiénzar, M., Ibañez-Tremolada, M., Gómez-Pando, L. R., García-Carmona, F., & Gandía-Herrero, F. (2017). Characterization of betalains, saponins and antioxidant power in differently colored quinoa (*Chenopodium quinoa*) varieties. *Food Chemistry*, 234, 285–294.

- Escribano, J., Pedreño, M. A., García-Carmona, F., & Muñoz, R. (1998). Characterization of the antiradical activity of betalains from *Beta vulgaris* L. roots. *Phytochemical Analysis: An International Journal of Plant Chemical and Biochemical Techniques*, 9(3), 124–127. [https://doi.org/10.1002/\(SICI\)1099-1565\(199805/06\)9:3<124::AID-PCA401>3.0.CO;2-0](https://doi.org/10.1002/(SICI)1099-1565(199805/06)9:3<124::AID-PCA401>3.0.CO;2-0).
- Felker, P., Stintzing, F. C., Müssig, E., Leitenberger, M., Carle, R., Vogt, T., & Bunch, R. (2008). Colour inheritance in cactus pear (*Opuntia ficus-indica*) fruits. *Annals of Applied Biology*, 152(3), 307–318. <https://doi.org/10.1111/j.1744-7348.2008.00222.x>.
- Fernandes, D. L. A., Paun, C., Pavliuk, M. V., Fernandes, A. B., Bastos, E. L., & Sá, J. (2016). Green microfluidic synthesis of monodisperse silver nanoparticles via genetic algorithm optimization. *RSC Advances*, 6(98), 95693–95697.
- Fernandes, S. S. M., Mesquita, I., Andrade, L., Mendes, A., Justino, L. L. G., Burrows, H. D., & Raposo, M. M. M. (2017). Synthesis and characterization of push-pull bithiophene and thieno[3,2-b]thiophene derivatives bearing an ethyne linker as sensitizers for dye-sensitized solar cells. *Organic Electronics*, 49, 194–205.
- Finnie, K. S., Bartlett, J. R., & Woolfrey, J. L. (1998). Vibrational Spectroscopic Study of the Coordination of (2, 2'-Bipyridyl-4, 4'-dicarboxylic acid) ruthenium (II) Complexes to the Surface of Nanocrystalline Titania. *Langmuir*, 14(10), 2744–2749.
- Fock, V. (1930). Näherungsmethode zur Lösung des quantenmechanischen Mehrkörperproblems. *Zeitschrift für Physik*, 61(1), 126–148.
- Frisch, M. J., Trucks, G. W., Schlegel, H. B., Scuseria, G. E., Robb, M. A., Cheeseman, J. R., Scalmani, G., Barone, V., Petersson, G. A., Nakatsuji, H., Li, X., Caricato, M., Marenich, A. V., Bloino, J., Janesko, B. G., Gomperts, R., Mennucci, B., Hratchian, H. P., Ortiz, ... & Fox, D. J. 2019. Gaussian 16, Revision C.01
- Fthenakis, V. M. (2018). Chapter IV-1-A - Overview of Potential Hazards. In S. A. Kalogirou (Ed.), *McEvoy's Handbook of Photovoltaics (Third Edition)* (pp. 1195–1212). Academic Press. <https://doi.org/10.1016/B978-0-12-809921-6.00035-5>.

- Fu, Y., Lu, T., Xu, Y., Li, M., Wei, Z., Liu, H., & Lu, W. (2018). Theoretical screening and design of SM315-based porphyrin dyes for highly efficient dye-sensitized solar cells with near-IR light harvesting. *Dyes and Pigments*, 155, 292–299.
- Fu, Y., Shi, J., Xie, S. Y., Zhang, T. Y., Soladoye, O. P., & Aluko, R. E. (2020). Red Beetroot Betalains: Perspectives on Extraction, Processing, and Potential Health Benefits. *Journal of Agricultural and Food Chemistry*, 68(42), 11595–11611.
- Fujisawa, J. I., Eda, T., & Hanaya, M. (2017). Comparative study of conduction-band and valence-band edges of TiO_2 , SrTiO_3 , and BaTiO_3 by ionization potential measurements. *Chemical Physics Letters*, 685, 23–26.
- Gabrielsson, E. (2014). *Molecular Engineering of D- π -A Dyes for Dye-Sensitized Solar Cells* [Doctoral thesis] School of Chemical Science and Engineering, KTH Royal Institute of Technology. Stockholm, Sweden. Retrieved and Accessed on October 19, 2019 from <http://urn.kb.se/resolve?urn=urn:nbn:se:kth:diva-144874>
- Gandía-Herrero, F., Escribano, J., & García-Carmona, F. (2005a). Betaxanthins as pigments responsible for visible fluorescence in flowers. *Planta*, 222(4), 586–593.
- Gandía-Herrero, F., Escribano, J., & García-Carmona, F. (2010). Structural implications on color, fluorescence, and antiradical activity in betalains. *Planta*, 232(2), 449–460. <https://doi.org/10.1007/s00425-010-1191-0>.
- Gandía-Herrero, F., García-Carmona, F., & Escribano, J. (2005b). Floral fluorescence effect. *Nature*, 437(7057), 334–334. <https://doi.org/10.1038/437334a>.
- Gandía-Herrero, F., García-Carmona, F., & Escribano, J. (2005c). Fluorescent pigments: new perspectives in betalain research and applications. *Food Research International*, 38(8–9), 879–884. <https://doi.org/10.1016/j.foodres.2005.01.012>.
- Garzón, I. L., Michaelian, K., Beltrán, M. R., Posada-Amarillas, A., Ordejón, P., Artacho, E., Sánchez-Portal, D., & Soler, J. M. (1998). Lowest Energy Structures of Gold Nanoclusters. *Physical Review Letters*, 81(8), 1600–1603.
- Gazquez, J. L., Cedillo, A., & Vela, A. (2007). Electrodonating and electroaccepting powers. *The Journal of Physical Chemistry A*, 111(10), 1966–1970.

- Geerlings, P., De Proft, F., & Langenaeker, W. (2003). Conceptual Density Functional Theory. *Chemical Reviews*, 103(5), 1793–1874. <https://doi.org/10.1021/cr990029p>.
- Gentile, C., Tesoriere, L., Allegra, M., Livrea, M., & D'alessio, P. (2004). Antioxidant betalains from cactus pear (*Opuntia ficus-indica*) inhibit endothelial ICAM-1 expression. *Annals of the New York Academy of Sciences*, 1028(1), 481–486.
- Gliszczynska-Świgło, A., Szymusiak, H., & Malinowska, P. (2006). Betanin, the main pigment of red beet: Molecular origin of its exceptionally high free radical-scavenging activity. *Food Additives and Contaminants*, 23(11), 1079–1087.
- Gómez-Ortíz, N. M., Vázquez-Maldonado, I. A., Pérez-Espadas, A. R., Mena-Rejón, G. J., Azamar-Barrios, J. A., & Oskam, G. (2010). Dye-sensitized solar cells with natural dyes extracted from achiote seeds. *Solar Energy Materials and Solar Cells*, 94(1), 40–44. <https://doi.org/10.1016/j.solmat.2009.05.013>.
- Gonçalves, L. C. P., Da Silva, S. M., DeRose, P. C., Ando, R. A., & Bastos, E. L. (2013). Beetroot-Pigment-Derived Colorimetric Sensor for Detection of Calcium Dipicolinate in Bacterial Spores. *PLoS ONE*, 8(9), e73701.
- Gordy, W. (1946a). A New Method of Determining Electronegativity from Other Atomic Properties. *Physical Review*, 69(11–12), 604–607.
- Gordy, W. (1946b). A Relation between Bond Force Constants, Bond Orders, Bond Lengths, and the Electronegativities of the Bonded Atoms. *The Journal of Chemical Physics*, 14(5), 305–320. <https://doi.org/10.1063/1.1724138>.
- Gorelsky, S. I. (2017). *AOMix: Program for Molecular Orbital Analysis*. In (Version version 6.90) Retrieved and Accessed on November 28, 2021 from <http://www.sg-chem.net>
- Gorelsky, S. I., & Lever, A. B. P. (2001). Electronic structure and spectra of ruthenium diimine complexes by density functional theory and INDO/S. Comparison of the two methods. *Journal of Organometallic Chemistry*, 635(1), 187–196.
- Gou, F., Jiang, X., Fang, R., Jing, H., & Zhu, Z. (2014). Strategy to improve photovoltaic performance of DSSC sensitized by zinc phophrin using salicylic acid as a tridentate anchoring group. *ACS Applied Materials & Interfaces*, 6(9), 6697–6703.

- Gould, G. W. (1977). Recent Advances in the Understanding of Resistance and Dormancy in Bacterial Spores. *Journal of Applied Bacteriology*, 42(3), 297–309.
- Graf, B. L., Rojas-Silva, P., Rojo, L. E., Delatorre-Herrera, J., Baldeón, M. E., & Raskin, I. (2015). Innovations in Health Value and Functional Food Development of Quinoa (*Chenopodium quinoa* Willd.). *Comprehensive Reviews in Food Science and Food Safety*, 14(4), 431–445. <https://doi.org/10.1111/1541-4337.12135>.
- Granovsky, A. A. (2013). Firefly Version 8.2.0. Retrieved and Accessed on February 15, 2020 from <http://classic.chem.msu.su/gran/firefly/index.html>
- Grätzel, M. (2003). Dye-sensitized solar cells. *Journal of Photochemistry and Photobiology C: Photochemistry Reviews*, 4(2), 145–153.
- Grätzel, M. (2004). Conversion of sunlight to electric power by nanocrystalline dye-sensitized solar cells. *Journal of Photochemistry and Photobiology A: Chemistry*, 164(1), 3–14. <https://doi.org/10.1016/j.jphotochem.2004.02.023>.
- Grätzel, M. (2006). The advent of mesoscopic injection solar cells. *Progress in Photovoltaics: Research and Applications*, 14(5), 429–442.
- Gray, J. L. (2003). The Physics of the Solar Cell. In A. Luque & S. Hegedus (Eds.), *Handbook of Photovoltaic Science and Engineering* pp. 61–112.
- Grisorio, R., De Marco, L., Allegretta, G., Giannuzzi, R., Suranna, G. P., Manca, M., Mastroianni, P., & Gigli, G. (2013). Anchoring stability and photovoltaic properties of new D(- π -A)₂ dyes for dye-sensitized solar cell applications. *Dyes and Pigments*, 98(2), 221–231. <https://doi.org/10.1016/j.dyepig.2013.02.012>.
- Grossmann, C. (1981). Unconstrained Optimization. Practical Methods of Optimization 1. *Journal of Applied Mathematics and Mechanics/Zeitschrift für Angewandte Mathematik und Mechanik*, 61(8), 408–408.
- Grünwald, R., & Tributsch, H. (1997). Mechanisms of Instability in Ru-Based Dye Sensitization Solar Cells. *The Journal of Physical Chemistry B*, 101(14), 2564–2575.
- Guba, E. G., & Lincoln, Y. S. (1994). Competing paradigms in qualitative research. *Handbook of Qualitative Research*, 2, 105–117.

- Guerrero-Rubio, M. A., Martínez-Zapata, J., Henarejos-Escudero, P., García-Carmona, F., & Gandía-Herrero, F. (2020). Reversible bleaching of betalains induced by metals and application to the fluorescent determination of anthrax biomarker. *Dyes and Pigments*, 180, 108493. <https://doi.org/10.1016/j.dyepig.2020.108493>.
- Guesmi, A., Ladhari, N., Hamadi, N. B., Msaddek, M., & Sakli, F. (2013). First application of chlorophyll-a as biomordant: sonicator dyeing of wool with betanin dye. *Journal of Cleaner Production*, 39, 97–104. <https://doi.org/10.1016/j.jclepro.2012.08.029>.
- Guesmi, A., Ladhari, N., Hamadi, N. B., & Sakli, F. (2012). Isolation, identification and dyeing studies of betanin on modified acrylic fabrics. *Industrial Crops and Products*, 37(1), 342–346. <https://doi.org/10.1016/j.indcrop.2011.12.034>.
- Gyftopoulos, E. P., & Hatsopoulos, G. N. (1968). Quantum-thermodynamic definition of electronegativity. *Proceedings of the National Academy of Sciences of the United States of America*, 60(3), 786–793. <https://doi.org/10.1073/pnas.60.3.786>.
- Hagberg, D. P., Edvinsson, T., Marinado, T., Boschloo, G., Hagfeldt, A., & Sun, L. (2006). A novel organic chromophore for dye-sensitized nanostructured solar cells. *Chemical Communications*, 21, 2245–2247. <https://doi.org/10.1039/B603002E>.
- Hagfeldt, A., Boschloo, G., Sun, L., Kloo, L., & Pettersson, H. (2010). Dye-sensitized solar cells. *Chemical Reviews*, 110(11), 6595–6663. <https://doi.org/10.1021/cr900356p>.
- Hagfeldt, A., & Graetzel, M. (1995). Light-Induced Redox Reactions in Nanocrystalline Systems. *Chemical Reviews*, 95(1), 49–68. <https://doi.org/10.1021/cr00033a003>.
- Haid, S., Marszalek, M., Mishra, A., Wielopolski, M., Teuscher, J., Moser, J.-E., Humphry-Baker, R., Zakeeruddin, S. M., Grätzel, M., & Bäuerle, P. (2012). Significant Improvement of Dye-Sensitized Solar Cell Performance by Small Structural Modification in π -Conjugated Donor–Acceptor Dyes. *Advanced Functional Materials*, 22(6), 1291–1302. <https://doi.org/10.1002/adfm.201102519>.
- Han, D., Wu, Y., Cai, H., Pang, C., & Zhao, L. (2015). DFT/TDDFT investigation on the electronic structures and photophysical properties of a series of substituted N-heterocyclic carbene (NHC) platinum(II) complexes. *Synthetic Metals*, 209, 455–460. <https://doi.org/10.1016/j.synthmet.2015.08.029>.

- Hanwell, M. D., Curtis, D. E., Lonie, D. C., Vandermeersch, T., Zurek, E., & Hutchison, G. R. (2012). Avogadro: An advanced semantic chemical editor, visualization, and analysis platform. *Journal of Cheminformatics*, 4(1), 17.
- Hao, S., Wu, J., Huang, Y., & Lin, J. (2006). Natural dyes as photosensitizers for dye-sensitized solar cell. *Solar Energy*, 80(2), 209–214.
- Hao, Y., Yang, X., Cong, J., Tian, H., Hagfeldt, A., & Sun, L. (2009). Efficient near infrared D- π -A sensitizers with lateral anchoring group for dye-sensitized solar cells. *Chemical Communications*, 27, 4031–4033. <https://doi.org/10.1039/B908396K>.
- Haque, S. A., Palomares, E., Cho, B. M., Green, A. N. M., Hirata, N., Klug, D. R., & Durrant, J. R. (2005). Charge Separation versus Recombination in Dye-Sensitized Nanocrystalline Solar Cells: the Minimization of Kinetic Redundancy. *Journal of the American Chemical Society*, 127(10), 3456–3462. <https://doi.org/10.1021/ja0460357>.
- Hardin, B. E., Snaith, H. J., & McGehee, M. D. (2012). The renaissance of dye-sensitized solar cells. *Nature Photonics*, 6(3), 162–169.
- Hartree, D. R., & Hartree, W. (1935). Self-consistent field, with exchange, for beryllium. *Proceedings of the Royal Society of London. Series A - Mathematical and Physical Sciences*, 150(869), 9–33. <https://doi.org/10.1098/rspa.1935.0085>.
- Hay, P. J., & Wadt, W. R. (1985). Ab initio effective core potentials for molecular calculations. Potentials for the transition metal atoms Sc to Hg. *The Journal of Chemical Physics*, 82(1), 270–283. <https://doi.org/10.1063/1.448799>.
- Hempel, J., & Böhm, H. (1997). Betaxanthin pattern of hairy roots from *Beta vulgaris* var. *lutea* and its alteration by feeding of amino acids. *Phytochemistry*, 44(5), 847–852.
- Herbach, K. M., Stintzing, F. C., & Carle, R. (2006). Betalain stability and degradation—structural and chromatic aspects. *Journal of Food Science*, 71(4), R41–R50.
- Hernandez-Martinez, A. R., Estevez, M., Vargas, S., Quintanilla, F., & Rodriguez, R. (2011). New dye-sensitized solar cells obtained from extracted bracts of *Bougainvillea glabra* and *spectabilis* betalain pigments by different purification processes. *International Journal of Molecular Sciences*, 12(9), 5565–5576.

- Hernandez-Martinez, A. R., Estevez, M., Vargas, S., Quintanilla, F., & Rodríguez, R. (2012). Natural pigment-based dye-sensitized solar cells. *Journal of Applied Research and Technology*, 10(1), 38–47.
- Hinze, J., & Jaffe, H. H. (1962). Electronegativity. I. Orbital Electronegativity of Neutral Atoms. *Journal of the American Chemical Society*, 84(4), 540–546.
- Ho, C., Mu-Jung, K., Tien-Li, C., Chin-Guo, K., Kun-Ching, C., & Xiu-Ping, L. (2011). Natural Sensitizer for Dye-Sensitized Solar Cells Using Three Layers of Photoelectrode Thin Films with a Schottky Barrier. *Current Research in Nanotechnology*, 1(1), 13–22. <https://doi.org/10.3844/ajnsr.2010.13.22>.
- Hosseini, S. E., & Wahid, M. A. (2020). Hydrogen from solar energy, a clean energy carrier from a sustainable source of energy. *International Journal of Energy Research*, 44(6), 4110–4131. <https://doi.org/10.1002/er.4930>.
- Hwang, K. J., Yoo, S. J., Kim, S. S., Kim, J. M., Shim, W. G., Kim, S. I., & Lee, J. W. (2008). Photovoltaic performance of nanoporous TiO₂ replicas synthesized from mesoporous materials for dye-sensitized solar cells. *Journal of Nanoscience and Nanotechnology*, 8(10), 4976–4981. <https://doi.org/10.1166/jnn.2008.1199>.
- Iczkowski, R. P., & Margrave, J. L. (1961). Electronegativity. *Journal of the American Chemical Society*, 83(17), 3547–3551. <https://doi.org/10.1021/ja01478a001>.
- Ioannidis, E. I., & Kulik, H. J. (2015). Towards quantifying the role of exact exchange in predictions of transition metal complex properties. *The Journal of Chemical Physics*, 143(3), 034104. <https://doi.org/10.1063/1.4926836>.
- Irfan, A., & Al-Sehemi, A. G. (2012). Quantum chemical study in the direction to design efficient donor-bridge-acceptor triphenylamine sensitizers with improved electron injection. *Journal of Molecular Modeling*, 18(11), 4893–4900.
- Ismael, S. M. H. (2012). Study of the Hydrogen bonding between 1-heteroaryl-2-(1-methylpyridinium-2-yl) ethylene Cation (HME) and Some small molecules. *Journal of Basrah Researches (Sciences)*, 38(2A), 73–85. Retrieved and Accessed on October 15, 2020 from <https://www.iasj.net/iasj/download/9e6d71731b4515f2>

- Jackman, R. L., & Smith, J. L. (1996). Anthocyanins and betalains. In G. A. F. Hendry & J. D. Houghton (Eds.), *Natural Food Colorants* (pp. 244–309). Springer. Boston, MA. https://doi.org/10.1007/978-1-4615-2155-6_8.
- Jain, A., Persson, K. A., & Ceder, G. (2016). Research Update: The materials genome initiative: Data sharing and the impact of collaborative ab initio databases. *APL Materials*, 4(5), 053102. <https://doi.org/10.1063/1.4944683>.
- James, S., & Contractor, R. (2018). Study on Nature-inspired Fractal Design-based Flexible Counter Electrodes for Dye-Sensitized Solar Cells Fabricated using Additive Manufacturing. *Scientific Reports*, 8(1), 17032. <https://doi.org/10.1038/s41598-018-35388-2>.
- Janjua, M. R. S. A. (2017). Computational Study on Non-linear Optical and Absorption Properties of Benzothiazole based Dyes: Tunable Electron-Withdrawing Strength and Reverse Polarity. *Open Chemistry*, 15(1), 139–146. <https://doi.org/10.1515/chem-2017-0017>.
- Jasim, K. E. (2011). Dye Sensitized Solar Cells-Working Principles, Challenges and Opportunities. In A. K. Leonid (Ed.), *Solar Cells* (pp. 1–36). IntechOpen. <https://doi.org/10.5772/19749>
- Jensen, F. (2013). Atomic orbital basis sets. *WIREs Computational Molecular Science*, 3(3), 273–295. <https://doi.org/10.1002/wcms.1123>.
- Kalyanasundaram, K., & Grätzel, M. (1998). Applications of functionalized transition metal complexes in photonic and optoelectronic devices. *Coordination Chemistry Reviews*, 177(1), 347–414. [https://doi.org/10.1016/S0010-8545\(98\)00189-1](https://doi.org/10.1016/S0010-8545(98)00189-1).
- Kapadia, G. J., Azuine, M. A., Rao, S. G., Arai, T., Iida, A., & Tokuda, H. (2011). Cytotoxic Effect of the Red Beetroot (*Beta vulgaris* L.) Extract Compared to Doxorubicin (Adriamycin) in the Human Prostate (PC-3) and Breast (MCF-7) Cancer Cell Lines. *Anti-Cancer Agents in Medicinal Chemistry- Anti-Cancer Agents*, 11(3), 280–284. <https://doi.org/10.2174/187152011795347504>.
- Kezi, J., & Sumathy, J. H. (2014). Betalain-a boon to the food industry. *Discov*, 20(63), 51–58.

- Khan, M. I. (2016). Plant Betalains: Safety, Antioxidant Activity, Clinical Efficacy, and Bioavailability. *Comprehensive Reviews in Food Science and Food Safety*, 15(2), 316–330. <https://doi.org/10.1111/1541-4337.12185>.
- Khan, M. I., Harsha, P. S. C. S., Giridhar, P. S. C. P., & Ravishankar, G. A. (2012). Pigment identification, nutritional composition, bioactivity, and in vitro cancer cell cytotoxicity of *Rivina humilis* L. berries, potential source of betalains. *LWT*, 47(2), 315–323. <https://doi.org/10.1016/j.lwt.2012.01.025>.
- Kiehl, J. T., & Trenberth, K. E. (1997). Earth's Annual Global Mean Energy Budget. *Bulletin of the American Meteorological Society*, 78(2), 197–208.
- Kim, K., & Jordan, K. D. (1994). Comparison of Density Functional and MP2 Calculations on the Water Monomer and Dimer. *The Journal of Physical Chemistry*, 98(40), 10089–10094. <https://doi.org/10.1021/j100091a024>.
- Kishimoto, S., Maoka, T., Sumitomo, K., & Ohmiya, A. (2005). Analysis of Carotenoid Composition in Petals of *Calendula* (*Calendula officinalis* L.). *Bioscience, Biotechnology, and Biochemistry*, 69(11), 2122–2128.
- Kitchin, R. (2014). Big Data, new epistemologies and paradigm shifts. *Big Data & Society*, 1(1), 2053951714528481. <https://doi.org/10.1177/2053951714528481>.
- Knorr, F. J., Malamen, D. J., McHale, J. L., Marchioro, A., & Moser, J. E. (2014). Two-electron photo-oxidation of betanin on titanium dioxide and potential for improved dye-sensitized solar energy conversion. In *Physical Chemistry of Interfaces and Nanomaterials XIII* (Vol. 9165, pp. 48–56). SPIE. Retrieved and Accessed on February 19, 2022 from <https://core.ac.uk/download/148008318.pdf>
- Knorr, F. J., McHale, J. L., Clark, A. E., Marchioro, A., & Moser, J. E. (2015). Dynamics of Interfacial Electron Transfer from Betanin to Nanocrystalline TiO₂: The Pursuit of Two-Electron Injection. *The Journal of Physical Chemistry C*, 119(33), 19030–19041. <https://doi.org/10.1021/acs.jpcc.5b05896>.
- Kohn, W., & Sham, L. J. (1965). Self-Consistent Equations Including Exchange and Correlation Effects. *Physical Review*, 140(4A), A1133-A1138.

- Komorowski, L. (1987). Chemical Hardness and L. Pauling's Scale of Electronegativity. *Zeitschrift für Naturforschung A*, 42(7), 767–773. <https://doi.org/10.1515/zna-1987-0718>.
- Koops, S. E., O'Regan, B. C., Barnes, P. R. F., & Durrant, J. R. (2009). Parameters Influencing the Efficiency of Electron Injection in Dye-Sensitized Solar Cells. *Journal of the American Chemical Society*, 131(13), 4808–4818.
- Krajka-Kuźniak, V., Paluszczak, J., Szaefer, H., & Baer-Dubowska, W. (2013). Betanin, a beetroot component, induces nuclear factor erythroid-2-related factor 2-mediated expression of detoxifying/antioxidant enzymes in human liver cell lines. *British Journal of Nutrition*, 110(12), 2138–2149.
- Kresse, G., & Furthmüller, J. (1996a). Efficiency of ab-initio total energy calculations for metals and semiconductors using a plane-wave basis set. *Computational Materials Science*, 6(1), 15–50. [https://doi.org/10.1016/0927-0256\(96\)00008-0](https://doi.org/10.1016/0927-0256(96)00008-0).
- Kresse, G., & Furthmüller, J. (1996b). Efficient iterative schemes for ab initio total-energy calculations using a plane-wave basis set. *Physical Review B*, 54(16), 11169–11186. <https://doi.org/10.1103/PhysRevB.54.11169>.
- Kresse, G., & Hafner, J. (1993). Ab initio molecular dynamics for liquid metals. *Physical Review B*, 47(1), 558–561. <https://doi.org/10.1103/PhysRevB.47.558>.
- Kresse, G., & Hafner, J. (1994). Ab initio molecular-dynamics simulation of the liquid-metal-amorphous-semiconductor transition in germanium. *Physical Review B*, 49(20), 14251–14269. <https://doi.org/10.1103/PhysRevB.49.14251>.
- Kresse, G., & Joubert, D. (1999). From ultrasoft pseudopotentials to the projector augmented-wave method. *Physical Review B*, 59(3), 1758–1775.
- Kresse, G., Marsman, M., & Furthmüller, J. (2018). VASP the GUIDE, Computational Materials Physics. *Wien, Austria: Faculty of Physics, Universität Wien, Sensengasse*, 8(12). 1–234.
- Kuhn, T. S. (1962). *The Structure of Scientific Revolutions. International Encyclopedia of Unified Science. Foundations of the Unity of Science*. (2th ed., Vol. 1 and II pp. 1–

- 222). The University of Chicago Press. Chicago. Retrieved and Accessed on July 27, 2021 from <https://www.lri.fr/~mbl/Stanford/CS477/papers/Kuhn-SSR-2ndEd.pdf>
- Kujala, T. S., Vienola, M. S., Klika, K. D., Loponen, J. M., & Pihlaja, K. (2002). Betalain and phenolic compositions of four beetroot (*Beta vulgaris*) cultivars. *European Food Research and Technology*, 214(6), 505–510. <https://doi.org/10.1007/s00217-001-0478-6>.
- Kumara, G. R. A., Kaneko, S., Okuya, M., Onwona-Agyeman, B., Konno, A., & Tennakone, K. (2006). Shiso leaf pigments for dye-sensitized solid-state solar cell. *Solar Energy Materials and Solar Cells*, 90(9), 1220–1226.
- Leach, A. R., & Gillet, V. J. (2007). *An Introduction to Chemoinformatics* (Rev. ed., pp. 1–260). Springer Dordrecht. Dordrecht, The Netherlands. <https://doi.org/10.1007/978-1-4020-6291-9>.
- Lee, C., Yang, W., & Parr, R. G. (1988). Development of the Colle-Salvetti correlation-energy formula into a functional of the electron density. *Physical Review B*, 37(2), 785. <https://doi.org/10.1103/PhysRevB.37.785>.
- Lewars, E. (2003). Computational chemistry. In *Introduction to the Theory and Applications of Molecular and Quantum Mechanics* (2nd ed., pp. 1–669). Kluwer Academic Publishers. New York. <https://doi.org/10.1007/978-90-481-3862-3>.
- Lewis, N. S., Crabtree, G., Nozik, A. J., Wasielewski, M. R., Alivisatos, P., Kung, H., Tsao, J., Chandler, E., Walukiewicz, W., Spitler, M., Ellingson, R., Overend, R., Mazer, J., Gress, M., Horwitz, J., Ashton, C., Herndon, B., Shapard, L., & Nault, R. M. (2005). *Basic Research Needs for Solar Energy Utilization. Report of the Basic Energy Sciences Workshop on Solar Energy Utilization, April 18-21, 2005* US DOE - Office of Basic Energy Sciences. United States. pp. 1–276. <https://doi.org/10.2172/899136>.
- Li, M., Kou, L., Diao, L., Zhang, Q., Li, Z., Wu, Q., Lu, W., Pan, D., & Wei, Z. (2015). Theoretical study of WS-9-based organic sensitizers for unusual Vis/NIR absorption and highly efficient dye-sensitized solar cells. *The Journal of Physical Chemistry C*, 119(18), 9782–9790. <https://doi.org/10.1021/acs.jpcc.5b03667>.

- Li, P., Cui, Y., Song, C., & Zhang, H. (2017). A systematic study of phenoxazine-based organic sensitizers for solar cells. *Dyes and Pigments*, 137, 12–23.
- Li, Y., Liu, J., Liu, D., Li, X., & Xu, Y. (2019). DA- π -A based organic dyes for efficient DSSCs: A theoretical study on the role of π -spacer. *Computational Materials Science*, 161, 163–176. <https://doi.org/10.1016/j.commatsci.2019.01.033>.
- Lin, B. C., Cheng, C. P., You, Z. Q., & Hsu, C. P. (2005). Charge transport properties of tris (8-hydroxyquinolinato) aluminum (III): Why it is an electron transporter. *Journal of the American Chemical Society*, 127(1), 66–67. <https://doi.org/10.1021/ja045087t>.
- Lin, L. Y., Tsai, C. H., Wong, K. T., Huang, T. W., Wu, C. C., Chou, S. H., Lin, F., Chen, S. H., & Tsai, A. I. (2011). Efficient organic DSSC sensitizers bearing an electron-deficient pyrimidine as an effective π -spacer. *Journal of Materials Chemistry*, 21(16), 5950–5958. <https://doi.org/10.1039/C1JM10201J>.
- Listorti, A., O'Regan, B., & Durrant, J. R. (2011). Electron transfer dynamics in dye-sensitized solar cells. *Chemistry of Materials*, 23(15), 3381–3399.
- Liu, G. H., & Parr, R. G. (1995). On Atomic and Orbital Electronegativities and Hardnesses. *Journal of the American Chemical Society*, 117(11), 3179–3188.
- Liyanage, D., Murakami, K., & Illeperuma, O. (2013). Use of Salicylic acid as a de-aggregating agent in Dye Sensitized Solar Cells. *International Journal of Electrochemical Science*, 8, 11916–11923.
- Lowry, T. H., & Richardson, K. S. (1987). *Mechanism and Theory in Organic Chemistry*. (Vol. 294 pp. 1–760). Harper & Row Publishers. New York, United State of America.
- Ludin, N. A., Al-Alwani Mahmoud, A. M., Bakar Mohamad, A., Kadhum, A. A. H., Sopian, K., & Abdul Karim, N. S. (2014). Review on the development of natural dye photosensitizer for dye-sensitized solar cells. *Renewable and Sustainable Energy Reviews*, 31, 386–396. <https://doi.org/10.1016/j.rser.2013.12.001>.
- Luque, A., & Hegedus, S. (Eds.). (2011). *Handbook of Photovoltaic Science and Engineering*. 2nd ed., John Wiley & Sons, Ltd. United Kingdom.

- Ma, W., Jiao, Y., & Meng, S. (2014). Predicting Energy Conversion Efficiency of Dye Solar Cells from First Principles. *The Journal of Physical Chemistry C*, 118(30), 16447–16457. <https://doi.org/10.1021/jp410982e>.
- Madili, N., Pogrebnoi, A., & Pogrebnaya, T. (2018). Theoretical Design of Complex Molecule via Combination of Natural Lawsone and Synthetic Indoline D131 Dyes for Dye Sensitized Solar Cells Application. <https://doi.org/10.4236/cc.2018.64007>.
- Magee, C. L. (2012). Towards quantification of the role of materials innovation in overall technological development. *Complexity*, 18(1), 10–25.
- Makoye, A., Pogrebnoi, A., & Pogrebnaya, T. (2020). Lawsone isomers, lawsone ether and bilawsone for dye-sensitized solar cells applications: DFT and UV–Vis studies. *Journal of Molecular Graphics and Modelling*, 94, 1–10.
- Marcus, R. A. (1965). On the Theory of Electron-Transfer Reactions. VI. Unified Treatment for Homogeneous and Electrode Reactions. *The Journal of Chemical Physics*, 43(2), 679–701. <https://doi.org/10.1063/1.1696792>.
- Marinado, T., Nonomura, K., Nissfolk, J., Karlsson, M. K., Hagberg, D. P., Sun, L., Mori, S., & Hagfeldt, A. (2009). How the nature of triphenylamine-polyene dyes in dye-sensitized solar cells affects the open-circuit voltage and electron lifetimes. *Langmuir*, 26(4), 2592–2598. <https://doi.org/10.1021/la902897z>.
- Marinado, T., Nonomura, K., Nissfolk, J., Karlsson, M. K., Hagberg, D. P., Sun, L., Mori, S., & Hagfeldt, A. (2010). How the Nature of Triphenylamine-Polyene Dyes in Dye-Sensitized Solar Cells Affects the Open-Circuit Voltage and Electron Lifetimes. *Langmuir*, 26(4), 2592–2598. <https://doi.org/10.1021/la902897z>.
- Martínez, A., Vargas, R., & Galano, A. (2009). What is important to prevent oxidative stress? A theoretical study on electron-transfer reactions between carotenoids and free radicals. *The Journal of Physical Chemistry B*, 113(35), 12113–12120.
- Martínez, L., Cilla, I., Beltrán, J. A., & Roncalés, P. (2006). Comparative effect of red yeast rice (*Monascus purpureus*), red beet root (*Beta vulgaris*) and betanin (E-162) on colour and consumer acceptability of fresh pork sausages packaged in a modified atmosphere. *Journal of the Science of Food and Agriculture*, 86(4), 500–508.

- Maynard, A. T., Huang, M., Rice, W. G., & Covell, D. G. (1998). Reactivity of the HIV-1 nucleocapsid protein p7 zinc finger domains from the perspective of density-functional theory. *Proceedings of the National Academy of Sciences*, 95(20), 11578.
- Megala, M., & Rajkumar, B. J. M. (2016). Theoretical study of anthoxanthin dyes for dye sensitized solar cells (DSSCs). *Journal of Computational Electronics*, 15(2), 557–568. <https://doi.org/10.1007/s10825-016-0791-8>.
- Michaelian, K., Rendón, N., & Garzón, I. L. (1999). Structure and energetics of Ni, Ag, and Au nanoclusters. *Physical Review B*, 60(3), 2000–2010.
- Mishra, A., Pootrakulchote, N., Fischer, M. K. R., Klein, C., Nazeeruddin, M. K., Zakeeruddin, S. M., Bäuerle, P., & Grätzel, M. (2009). Design and synthesis of a novel anchoring ligand for highly efficient thin film dye-sensitized solar cells. *Chemical Communications*, 46, 7146–7148. <https://doi.org/10.1039/B912506J>.
- Monkhorst, H. J., & Pack, J. D. (1976). Special points for Brillouin-zone integrations. *Physical Review B*, 13(12), 5188–5192. <https://doi.org/10.1103/PhysRevB.13.5188>.
- Morandeira, A., López-Duarte, I., Martínez-Díaz, M. V., O'Regan, B., Shuttle, C., Haji-Zainulabidin, N. A., Torres, T., Palomares, E., & Durrant, J. R. (2007). Slow Electron Injection on Ru–Phthalocyanine Sensitized TiO₂. *Journal of the American Chemical Society*, 129(30), 9250–9251. <https://doi.org/10.1021/ja0722980>.
- Mounet, N., Gibertini, M., Schwaller, P., Campi, D., Merkys, A., Marrazzo, A., Sohler, T., Castelli, I. E., Cepellotti, A., Pizzi, G., & Marzari, N. (2018). Two-dimensional materials from high-throughput computational exfoliation of experimentally known compounds. *Nature Nanotechnology*, 13(3), 246–252. <https://doi.org/10.1038/s41565-017-0035-5>.
- Mulliken, R. S. (1934). A New Electroaffinity Scale; Together with Data on Valence States and on Valence Ionization Potentials and Electron Affinities. *The Journal of Chemical Physics*, 2(11), 782–793. <https://doi.org/10.1063/1.1749394>.
- Myrseth, V., Bozek, J. D., Kukk, E., Sæthre, L. J., & Thomas, T. D. (2002). Adiabatic and vertical carbon 1s ionization energies in representative small molecules. *Journal of Electron Spectroscopy and Related Phenomena*, 122(1), 57–63.

- Naik, P., Elmorsy, M. R., Su, R., Babu, D. D., El-Shafei, A., & Adhikari, A. V. (2017). New carbazole based metal-free organic dyes with D- π -A- π -A architecture for DSSCs: synthesis, theoretical and cell performance studies. *Solar Energy*, 153, 600–610. <https://doi.org/10.1016/j.solener.2017.05.088>.
- Nakashima, K. K., & Bastos, E. L. (2019). Rationale on the High Radical Scavenging Capacity of Betalains. *Antioxidants*, 8(7), 1–13.
- Narayan, M. R. (2012). Review: Dye sensitized solar cells based on natural photosensitizers. *Renewable and Sustainable Energy Reviews*, 16(1), 208–215.
- Nazeeruddin, M. K., Kay, A., Rodicio, I., Humphry-Baker, R., Müller, E., Liska, P., Vlachopoulos, N., & Grätzel, M. (1993). Conversion of light to electricity by cis-X₂bis (2, 2'-bipyridyl-4, 4'-dicarboxylate) ruthenium (II) charge-transfer sensitizers (X= Cl-, Br-, I-, CN-, and SCN-) on nanocrystalline titanium dioxide electrodes. *Journal of the American Chemical Society*, 115(14), 6382–6390.
- Nazeeruddin, M. K., Péchy, P., Renouard, T., Zakeeruddin, S. M., Humphry-Baker, R., Comte, P., Liska, P., Cevey, L., Costa, E., Shklover, V., Spiccia, L., Deacon, G. B., Bignozzi, C. A., & Grätzel, M. (2001). Engineering of Efficient Panchromatic Sensitizers for Nanocrystalline TiO₂-Based Solar Cells. *Journal of the American Chemical Society*, 123(8), 1613–1624. <https://doi.org/10.1021/ja003299u>.
- Nguyen, W. H., Bailie, C. D., Unger, E. L., & McGehee, M. D. (2014). Enhancing the hole-conductivity of spiro-OMeTAD without oxygen or lithium salts by using spiro (TFSI)₂ in perovskite and dye-sensitized solar cells. *Journal of the American Chemical Society*, 136(31), 10996–11001. <https://doi.org/10.1021/ja504539w>.
- Nishantha, M. R., Yapa, Y. P. Y. P., & Perera, V. P. S. (2012). Sensitization of photoelectrochemical solar cells with a natural dye extracted from Kopsia flavida fruit. <https://ips1.lk/documents/TechSession/2012/ips112-08.pdf>.
- Nogueira, F., Castro, A., & Marques, M. A. L. (2003). A Tutorial on Density Functional Theory. In C. Fiolhais, F. Nogueira, & M. A. L. Marques (Eds.), *A Primer in Density Functional Theory*. (pp. 218–256). Springer Berlin Heidelberg. Berlin, Heidelberg. https://doi.org/10.1007/3-540-37072-2_6.

- Nouemo, S., Tchoffo, F., Ndjaka, J. M. B., & Domngang, S. (2016). Global minima of iron clusters described by Gupta potential. *Journal of Taibah University for Science*, 10(3), 430–436. <https://doi.org/10.1016/j.jtusci.2015.06.014>.
- O'Regan, B., & Grätzel, M. (1991). A low-cost, high-efficiency solar cell based on dye-sensitized colloidal TiO₂ films. *Nature*, 353(6346), 737–740.
- Obasuyi, A. R., Glossman-Mitnik, D., & Flores-Holguín, N. (2019). Electron injection in anthocyanidin and betalain dyes for dye-sensitized solar cells: A DFT approach. *Journal of Computational Electronics*, 18(2), 396–406.
- Olivieri, A. C., & Escandar, G. M. (2014). Chapter 6 - Analytical Figures of Merit. In A. C. Olivieri & G. M. Escandar (Eds.), *Practical Three-Way Calibration* (pp. 93–107). Elsevier. Boston. <https://doi.org/10.1016/B978-0-12-410408-2.00006-5>.
- Olivieri, A. C., & Faber, N. M. (2009). 3.03 - Validation and Error. In S. D. Brown, R. Tauler, & B. Walczak (Eds.), *Comprehensive Chemometrics* (pp. 91–120). Elsevier. Oxford. <https://doi.org/10.1016/B978-044452701-1.00073-9>.
- Ooyama, Y., Shimada, Y., Kagawa, Y., Yamada, Y., Imae, I., Komaguchi, K., & Harima, Y. (2007). Synthesis of new-type donor–acceptor π -conjugated benzofuro[2,3-c]oxazolo[4,5-a]carbazole fluorescent dyes and their photovoltaic performances of dye-sensitized solar cells. *Tetrahedron Letters*, 48(52), 9167–9170.
- Oprea, C. I., Dumbravă, A., Enache, I., Georgescu, A., & Gîrțu, M. A. (2012). A combined experimental and theoretical study of natural betalain pigments used in dye-sensitized solar cells. *Journal of Photochemistry and Photobiology A: Chemistry*, 240, 5–13.
- Oprea, C. I., Frecuș, B., Minaev, B. F., & Gîrțu, M. A. (2011). DFT study of electronic structure and optical properties of some Ru-and Rh-based complexes for dye-sensitized solar cells. *Molecular Physics*, 109(21), 2511–2523.
- Oum, K., Lohse, P. W., Klein, J. R., Flender, O., Scholz, M., Hagfeldt, A., Boschloo, G., & Lenzer, T. (2013). Photoinduced ultrafast dynamics of the triphenylamine-based organic sensitizer D35 on TiO₂, ZrO₂ and in acetonitrile. *Physical Chemistry Chemical Physics*, 15(11), 3906–3916. <https://doi.org/10.1039/C3CP44095H>.

- Papoian, G., Nørskov, J. K., & Hoffmann, R. (2000). A Comparative Theoretical Study of the Hydrogen, Methyl, and Ethyl Chemisorption on the Pt(111) Surface. *Journal of the American Chemical Society*, 122(17), 4129–4144. <https://doi.org/10.1021/ja993483j>.
- Park, K. H., Kim, T. Y., Park, J. Y., Jin, E. M., Yim, S. H., Choi, D. Y., & Lee, J. W. (2013). Adsorption characteristics of gardenia yellow as natural photosensitizer for dye-sensitized solar cells. *Dyes and Pigments*, 96(2), 595–601.
- Parr, R. G. (1980). Density Functional Theory of Atoms and Molecules. In K. Fukui & B. Pullman (Eds.), *Horizons of Quantum Chemistry. Académie Internationale Des Sciences Moléculaires Quantiques / International Academy of Quantum Molecular Science*, (vol 3. pp. 5–15). Springer, Dordrecht. https://doi.org/10.1007/978-94-009-9027-2_2.
- Parr, R. G., Donnelly, R. A., Levy, M., & Palke, W. E. (1978). Electronegativity: The density functional viewpoint. *The Journal of Chemical Physics*, 68(8), 3801–3807.
- Parr, R. G., & Pearson, R. G. (1983). Absolute hardness: companion parameter to absolute electronegativity. *Journal of the American Chemical Society*, 105(26), 7512–7516. <https://doi.org/10.1021/ja00364a005>.
- Parr, R. G., Szentpály, L. V., & Liu, S. (1999). Electrophilicity index. *Journal of the American Chemical Society*, 121(9), 1922–1924. <https://doi.org/10.1021/ja983494x>.
- Pastore, M., & De Angelis, F. (2010). Aggregation of Organic Dyes on TiO₂ in Dye-Sensitized Solar Cells Models: An ab Initio Investigation. *ACS Nano*, 4(1), 556–562. <https://doi.org/10.1021/nn901518s>.
- Patel, D. G., Bastianon, N. M., Tongwa, P., Leger, J. M., Timofeeva, T. V., & Bartholomew, G. P. (2011). Modification of nonlinear optical dyes for dye sensitized solar cells: a new use for a familiar acceptor. *Journal of Materials Chemistry*, 21(12), 4242–4250. <https://doi.org/10.1039/C0JM03774E>.
- Pauling, L. (1932). The nature of the chemical bond. IV. The energy of single bonds and the relative electronegativity of atoms. *Journal of the American Chemical Society*, 54(9), 3570–3582. <https://doi.org/10.1021/ja01348a011>.

- Pauling, L. (1960). *The Nature of the Chemical Bond*. Cornell university press Ithaca, New York.
- Pawar, A. B., Jadhav, K. D., Wadekar, M. P., & Sarawadekar, R. G. (2011). Spectral and theoretical investigation on 2-hydroxy-1, 4-naphthoquinone (lawsone). *Journal of Pharmacy Research*, 4(6), 1745–1747. Retrieved and Accessed on July 26, 2020 from <http://citeseerx.ist.psu.edu/viewdoc/download?doi=10.1.1.735.2774&rep=rep1&type=pdf>
- Payne, M. C., Teter, M. P., Allan, D. C., Arias, T. A., & Joannopoulos, J. D. (1992). Iterative minimization techniques for ab initio total-energy calculations: Molecular dynamics and conjugate gradients. *Reviews of Modern Physics*, 64(4), 1045–1097.
- Pearce, J. M. (2002). Photovoltaics: A path to sustainable futures. *Futures*, 34(7), 663–674. [https://doi.org/10.1016/S0016-3287\(02\)00008-3](https://doi.org/10.1016/S0016-3287(02)00008-3).
- Pearson, R. G. (1997). *Chemical hardness*. Wiley-VCH Verlag GmbH. Weinheim, German. <https://doi.org/10.1002/3527606173>
- Perdew, J. P., Burke, K., & Ernzerhof, M. (1996). Generalized Gradient Approximation Made Simple. *Physical Review Letters*, 77(18), 3865–3868.
- Perera, V. P. S., & Tennakone, K. (2003). Recombination processes in dye-sensitized solid-state solar cells with CuI as the hole collector. *Solar Energy Materials and Solar Cells*, 79(2), 249–255. [https://doi.org/10.1016/S0927-0248\(03\)00103-X](https://doi.org/10.1016/S0927-0248(03)00103-X).
- Piattelli, M., Minale, L., & Protà, G. (1964). Isolation, structure and absolute configuration of indicaxanthin. *Tetrahedron*, 20(10), 2325–2329.
- Pierotti, R. A. (1976). A scaled particle theory of aqueous and nonaqueous solutions. *Chemical Reviews*, 76(6), 717–726. <https://doi.org/10.1021/cr60304a002>.
- Pinheiro, A. C., Fazzi, R. B., Esteves, L. C., Machado, C. O., Dörr, F. A., Pinto, E., Hattori, Y., Sa, J., da Costa Ferreira, A. M., & Bastos, E. L. (2021). A bioinspired nitron precursor to a stabilized nitroxide radical. *Free Radical Biology and Medicine*, 168, 110–116. <https://doi.org/10.1016/j.freeradbiomed.2021.03.030>.

- Polini, M., Guinea, F., Lewenstein, M., Manoharan, H. C., & Pellegrini, V. (2013). Artificial honeycomb lattices for electrons, atoms and photons. *Nature Nanotechnology*, 8(9), 625–633. <https://doi.org/10.1038/nnano.2013.161>.
- Preat, J., Michaux, C., Jacquemin, D., & Perpete, E. A. (2009). Enhanced efficiency of organic dye-sensitized solar cells: Triphenylamine derivatives. *The Journal of Physical Chemistry C*, 113(38), 16821–16833. <https://doi.org/10.1021/jp904946a>.
- Press, W. H., Teukolsky, S. A., Vetterling, W. T., & Flannery, B. P. (2007). *Numerical Recipes. The Art of Scientific Computing*. (3rd ed). Cambridge University Press. New York, United State of America. Retrieved and Accessed on November 24, 2021 from https://e-maxx.ru/bookz/files/numerical_recipes.pdf.
- Pritchard, H. O., & Skinner, H. A. (1955). The Concept of Electronegativity. *Chemical reviews*, 55(4), 745–786. <https://doi.org/10.1021/cr50004a005>.
- Qin, C., & Clark, A. E. (2007). DFT characterization of the optical and redox properties of natural pigments relevant to dye-sensitized solar cells. *Chemical Physics Letters*, 438(1–3), 26–30. <https://doi.org/10.1016/j.cplett.2007.02.063>.
- Raga, S. R., Barea, E. M., & Fabregat-Santiago, F. (2012). Analysis of the Origin of Open Circuit Voltage in Dye Solar Cells. *The Journal of Physical Chemistry Letters*, 3(12), 1629–1634. <https://doi.org/10.1021/jz3005464>.
- Rahimi, P., Abedimanesh, S., Mesbah-Namin, S. A., & Ostadrahimi, A. (2019a). Betalains, the nature-inspired pigments, in health and diseases. *Critical Reviews in Food Science and Nutrition*, 59(18), 2949–2978. <https://doi.org/10.1080/10408398.2018.1479830>.
- Rahimi, P., Mesbah-Namin, S. A., Ostadrahimi, A., Separham, A., & Asghari Jafarabadi, M. (2019b). Betalain- and betacyanin-rich supplements' impacts on the PBMC SIRT1 and LOX1 genes expression and Sirtuin-1 protein levels in coronary artery disease patients: A pilot crossover clinical trial. *Journal of Functional Foods*, 60, 1–8. <https://doi.org/10.1016/j.jff.2019.06.003>.
- Ramkumar, S., & Manidurai, P. (2017). Tuning the physical properties of organic sensitizers by replacing triphenylamine with new donors for dye sensitized solar cells-a

- theoretical approach. *Spectrochimica Acta Part A: Molecular and Biomolecular Spectroscopy*, 173, 425–431. <https://doi.org/10.1016/j.saa.2016.09.036>.
- Reddy, M. K., Alexander-Lindo, R. L., & Nair, M. G. (2005). Relative Inhibition of Lipid Peroxidation, Cyclooxygenase Enzymes, and Human Tumor Cell Proliferation by Natural Food Colors. *Journal of Agricultural and Food Chemistry*, 53(23), 9268–9273. <https://doi.org/10.1021/jf051399j>.
- Ren, H. S., Li, Y. K., Zhu, Q., Zhu, J., & Li, X. Y. (2012). Spectral shifts of the $n \rightarrow \pi^*$ and $\pi \rightarrow \pi^*$ transitions of uracil based on a modified form of solvent reorganization energy. *Physical Chemistry Chemical Physics*, 14(38), 13284–13291.
- Rosa, E. S., Shobih, Retnaningsih, L., Muliani, L., & Hidayat, J. (2017). The influence of the addition of dye surface modifier on the performance of transparent dye sensitized solar cells. *AIP Conference Proceedings*, 1904(1), 1–7.
- Rossetto, M., Vanzani, P., Mattivi, F., Lunelli, M., Scarpa, M., & Rigo, A. (2002). Synergistic antioxidant effect of catechin and malvidin 3-glucoside on free radical-initiated peroxidation of linoleic acid in micelles. *Archives of Biochemistry and Biophysics*, 408(2), 239–245. [https://doi.org/10.1016/S0003-9861\(02\)00561-1](https://doi.org/10.1016/S0003-9861(02)00561-1).
- Rostkowska, H., Nowak, M. J., Lapinski, L., & Adamowicz, L. (1998). Molecular structure and infrared spectra of 2-hydroxy-1, 4-naphthoquinone; experimental matrix isolation and theoretical Hartree–Fock and post Hartree–Fock study. *Spectrochimica Acta Part A: Molecular and Biomolecular Spectroscopy*, 54(8), 1091–1103.
- Rühle, S., Shalom, M., & Zaban, A. (2010). Quantum-Dot-Sensitized Solar Cells. *ChemPhysChem*, 11(11), 2290–2304. <https://doi.org/10.1002/cphc.201000069>.
- Saga, T. (2010). Advances in crystalline silicon solar cell technology for industrial mass production. *NPG Asia Materials*, 2(3), 96–102.
- Sanderson, W. T., Stoddard, R. R., Echt, A. S., Piacitelli, C. A., Kim, D., Horan, J., Davies, M. M., McCleery, R. E., Muller, P., Schnorr, T. M., Ward, E. M., & Hales, T. R. (2004). Bacillus anthracis contamination and inhalational anthrax in a mail processing and distribution center. *Journal of Applied Microbiology*, 96(5), 1048–1056.

- Sandquist, C., & McHale, J. L. (2011). Improved efficiency of betanin-based dye-sensitized solar cells. *Journal of Photochemistry and Photobiology A: Chemistry*, 221(1), 90–97. <https://doi.org/10.1016/j.jphotochem.2011.04.030>.
- Saravanan, R. R., Seshadri, S., Gunasekaran, S., Mendoza-Meroño, R., & Garcia-Granda, S. (2014). Crystallographic, experimental (FT-IR and FT-RS) and theoretical (DFT) investigation, UV–Vis, MEP, HOMO–LUMO and NBO/NLMO of (E)-1-[1-(4-Chlorophenyl) ethylidene] thiosemicarbazide. *Spectrochimica Acta Part A: Molecular and Biomolecular Spectroscopy*, 121, 268–275.
- Schleder, G. R., Padilha, A. C. M., Acosta, C. M., Costa, M., & Fazzio, A. (2019). From DFT to machine learning: Recent approaches to materials science: A review. *Journal of Physics: Materials*, 2(3), 1–47. <https://doi.org/10.1088/2515-7639/ab084b>.
- Schlegel, H. B. (1982). Optimization of equilibrium geometries and transition structures. *Journal of Computational Chemistry*, 3(2), 214–218.
- Schmidt, M. W., Baldridge, K. K., Boatz, J. A., Elbert, S. T., Gordon, M. S., Jensen, J. H., Koseki, S., Matsunaga, N., Nguyen, K. A., & Su, S. (1993). General atomic and molecular electronic structure system. *Journal of Computational Chemistry*, 14(11), 1347–1363. <https://doi.org/10.1002/jcc.540141112>
- Schrödinger, E. (1926). An Undulatory Theory of the Mechanics of Atoms and Molecules. *Physical Review*, 28(6), 1049–1070. <https://doi.org/10.1103/PhysRev.28.1049>.
- Shahid, M., Shahid ul, I., & Mohammad, F. (2013). Recent advancements in natural dye applications: A review. *Journal of Cleaner Production*, 53, 310–331.
- Sinha, K., Saha, P. D., & Datta, S. (2012). Extraction of natural dye from petals of Flame of forest (*Butea monosperma*) flower: Process optimization using response surface methodology (RSM). *Dyes and Pigments*, 94(2), 212–216.
- Skyner, R. E., McDonagh, J. L., Groom, C. R., van Mourik, T., & Mitchell, J. B. O. (2015). A review of methods for the calculation of solution free energies and the modelling of systems in solution. *Physical Chemistry Chemical Physics*, 17(9), 6174–6191.
- Slater, J. C. (1929). The Theory of Complex Spectra. *Physical Review*, 34(10), 1293–1322.

- Slater, J. C. (1930). Note on Hartree's Method. *Physical Review*, 35(2), 210–211.
- Sreeja, S., & Pesala, B. (2020). Plasmonic enhancement of betanin-lawsone co-sensitized solar cells via tailored bimodal size distribution of silver nanoparticles. *Scientific Reports*, 10(1), 8240. <https://doi.org/10.1038/s41598-020-65236-1>.
- Starzak, K., Skopińska, A., & Wybraniec, S. (2012). Research on betanidin oxidation by ABTS radicals. *Challenges of Modern Technology*, 3(4), 39–43.
- Stephens, P. J., Devlin, F. J., Chabalowski, C. F., & Frisch, M. J. (1994). Ab Initio Calculation of Vibrational Absorption and Circular Dichroism Spectra Using Density Functional Force Fields. *The Journal of Physical Chemistry*, 98(45), 11623–11627. <https://doi.org/10.1021/j100096a001>.
- Stintzing, F. C., & Carle, R. (2007). Betalains—emerging prospects for food scientists. *Trends in Food Science & Technology*, 18(10), 514–525.
- Strack, D., Vogt, T., & Schliemann, W. (2003). Recent advances in betalain research. *Phytochemistry*, 62(3), 247–269. [https://doi.org/10.1016/S0031-9422\(02\)00564-2](https://doi.org/10.1016/S0031-9422(02)00564-2).
- Subalakshmi, K., Senthilselvan, J., Kumar, K. A., Kumar, S. A., & Pandurangan, A. (2017). Solvothermal synthesis of hexagonal pyramidal and bifrustum shaped ZnO nanocrystals: natural betacyanin dye and organic Eosin Y dye sensitized DSSC efficiency, electron transport, recombination dynamics and solar photodegradation investigations. *Journal of Materials Science: Materials in Electronics*, 28(20), 15565–15595. <https://doi.org/10.1007/s10854-017-7445-x>.
- Suhaimi, S., Shahimin, M. M., Alahmed, Z., Chyský, J., & Reshak, A. (2015). Materials for enhanced dye-sensitized solar cell performance: Electrochemical application. *International Journal of Electrochemical Science*, 10(4), 2859–2871.
- Sutariya, B., & Saraf, M. (2017). Betanin, isolated from fruits of *Opuntia elatior* Mill attenuates renal fibrosis in diabetic rats through regulating oxidative stress and TGF- β pathway. *Journal of Ethnopharmacology*, 198, 432–443.

- Sutthanut, K., Sripanidkulchai, B., Yenjai, C., & Jay, M. (2007). Simultaneous identification and quantitation of 11 flavonoid constituents in *Kaempferia parviflora* by gas chromatography. *Journal of Chromatography A*, 1143(1), 227–233.
- Syzgantseva, O. A., Gonzalez-Navarrete, P., Calatayud, M., Bromley, S., & Minot, C. (2011). Theoretical investigation of the hydrogenation of (TiO₂) N clusters (N= 1–10). *The Journal of Physical Chemistry C*, 115(32), 15890–15899.
- Tao, J., Perdew, J. P., Staroverov, V. N., & Scuseria, G. E. (2003). Climbing the Density Functional Ladder: Nonempirical Meta-Generalized Gradient Approximation Designed for Molecules and Solids. *Physical Review Letters*, 91(14), 146401.
- Timoneda, A., Feng, T., Sheehan, H., Walker-Hale, N., Pucker, B., Lopez-Nieves, S., Guo, R., & Brockington, S. (2019). The evolution of betalain biosynthesis in Caryophyllales. *New Phytologist*, 224(1), 71–85. <https://doi.org/10.1111/nph.15980>.
- Tiwari, A., & Pal, U. (2015). Effect of donor-donor- π -acceptor architecture of triphenylamine-based organic sensitizers over TiO₂ photocatalysts for visible-light-driven hydrogen production. *International Journal of Hydrogen Energy*, 40(30), 9069–9079. <https://doi.org/10.1016/j.ijhydene.2015.05.101>.
- Todkary, A. V., Dalvi, R., Salunke-Gawali, S., Linares, J., Varret, F., Marrot, J., Yakhmi, J. V., Bhadbhade, M., Srinivas, D., & Gejji, S. P. (2006). SOM assembly of hydroxynaphthoquinone and its oxime: Polymorphic X-ray structures and EPR studies. *Spectrochimica Acta Part A: Molecular and Biomolecular Spectroscopy*, 63(1), 130–138. <https://doi.org/10.1016/j.saa.2005.04.054>.
- Tokarev, K. L. (2007–2009). OpenThermo v. 1.0 Beta 1 (C) ed Retrieved and Accessed on September 25, 2018 from <http://openthermo.software.informer.com/>
- Tomasi, J., & Mennucci, B. (2002). Self-consistent Reaction Field Methods. In P. V. R. Schleyer, N. L. Allinger, T. Clark, J. Gasteiger, P. A. Kollman, H. F. Schaefer, & P. R. Schreiner (Eds.), *Encyclopedia of Computational Chemistry*.
- Tomasi, J., Mennucci, B., & Cammi, R. (2005). Quantum Mechanical Continuum Solvation Models. *Chemical Reviews*, 105(8), 2999–3094. <https://doi.org/10.1021/cr9904009>.

- Torres-García, E., Galano, A., & Rodriguez-Gattorno, G. (2011). Oxidative desulfurization (ODS) of organosulfur compounds catalyzed by peroxo-metallate complexes of $\text{WO}_x\text{-ZrO}_2$: Thermochemical, structural, and reactivity indexes analyses. *Journal of Catalysis*, 282(1), 201–208. <https://doi.org/10.1016/j.jcat.2011.06.010>.
- Tripathi, A., & Prabhakar, C. (2018). Impact of replacement of the central benzene ring in anthracene by a heterocyclic ring on electronic excitations and reorganization energies in anthratetrathiophene molecules. *Journal of the Chinese Chemical Society*, 65(8), 918–924. <https://doi.org/10.1002/jccs.201700448>.
- Tripathi, A., & Prabhakar, C. (2020). Optical and charge transport properties of chalcogen (O, S and Se) based acene molecules. *Journal of Molecular Structure*, 1203, 127397. <https://doi.org/10.1016/j.molstruc.2019.127397>.
- Ulahannan, R. T., Kannan, V., Vidya, V., & Sreekumar, K. (2020). Synthesis and DFT studies of the structure - NLO activity evaluation of 2-(4-methoxyphenyl)-1,4,5-triphenyl-2,5-dihydro-1H-imidazole. *Journal of Molecular Structure*, 1199, 1–7.
- Upadhyaya, H. M., Senthilarasu, S., Hsu, M. H., & Kumar, D. K. (2013). Recent progress and the status of dye-sensitised solar cell (DSSC) technology with state-of-the-art conversion efficiencies. *Solar Energy Materials and Solar Cells*, 119, 291–295.
- Vessecchi, R., Emery, F. S., Galembeck, S. E., & Lopes, N. P. (2012). Gas-phase reactivity of 2-hydroxy-1, 4-naphthoquinones: a computational and mass spectrometry study of lapachol congeners. *Journal of Mass Spectrometry*, 47(12), 1648–1659.
- Vieira Teixeira da Silva, D., dos Santos Baião, D., de Oliveira Silva, F., Alves, G., Perrone, D., Mere Del Aguila, E., & M. Flosi Paschoalin, V. (2019). Betanin, a Natural Food Additive: Stability, Bioavailability, Antioxidant and Preservative Ability Assessments. *Molecules*, 24(3), 161–175.
- Vosko, S. H., Wilk, L., & Nusair, M. (1980). Accurate spin-dependent electron liquid correlation energies for local spin density calculations: A critical analysis. *Canadian Journal of Physics*, 58(8), 1200–1211. <https://doi.org/10.1139/p80-159>.

- Vovna, V. I., Kazachek, M. V., & L'vov, I. B. (2012). Excited states and absorption spectra of β -diketonate complexes of boron difluoride with aromatic substituents. *Optics and Spectroscopy*, 112(4), 497–505. <https://doi.org/10.1134/S0030400X12030228>.
- Wang, H., Bao, B., Hu, X., & Fang, J. K. (2017). Efficient Small Molecule Organic Dyes Containing Different Bridges in Donor Moieties for Dye-Sensitized Solar Cells. *Electrochimica Acta*, 250, 278–284. <https://doi.org/10.1016/j.electacta.2017.08.089>.
- Wang, J., Li, H., Ma, N. N., Yan, L. K., & Su, Z. M. (2013). Theoretical studies on organoimido-substituted hexamolybdates dyes for dye-sensitized solar cells (DSSC). *Dyes and Pigments*, 99(2), 440–446. <https://doi.org/10.1016/j.dyepig.2013.05.027>.
- Wang, Q., Ito, S., Grätzel, M., Fabregat-Santiago, F., Mora-Seró, I., Bisquert, J., Bessho, T., & Imai, H. (2006). Characteristics of High Efficiency Dye-Sensitized Solar Cells. *The Journal of Physical Chemistry B*, 110(50), 25210–25221.
- Wazzan, N., & Irfan, A. (2018). Theoretical study of triphenylamine-based organic dyes with mono-, di-, and tri-anchoring groups for dye-sensitized solar cells. *Organic Electronics*, 63, 328–342. <https://doi.org/10.1016/j.orgel.2018.09.039>.
- Wendel, M., Nizinski, S., Gierszewski, M., Pukala, D., Sikorski, M., Starzak, K., Wybraniec, S., & Burdzinski, G. (2016). Chemical quenching of singlet oxygen by betanin. *Photochemical & Photobiological Sciences*, 15(7), 872–878.
- Wendel, M., Nizinski, S., Pukala, D., Sikorski, M., Wybraniec, S., & Burdzinski, G. (2017). Ultrafast internal conversion in neobetanin in comparison to betacyanins. *Journal of Photochemistry and Photobiology A: Chemistry*, 332, 602–610.
- Wendel, M., Nizinski, S., Tuwalska, D., Starzak, K., Szot, D., Pukala, D., Sikorski, M., Wybraniec, S., & Burdzinski, G. (2015). Time-resolved spectroscopy of the singlet excited state of betanin in aqueous and alcoholic solutions. *Physical Chemistry Chemical Physics*, 17(27), 18152–18158.
- Wenger, S., Bouit, P. A., Chen, Q., Teuscher, J., Censo, D. D., Humphry-Baker, R., Moser, J.-E., Delgado, J. L., Martín, N., Zakeeruddin, S. M., & Grätzel, M. (2010). Efficient Electron Transfer and Sensitizer Regeneration in Stable π -Extended

- Tetrathiafulvalene-Sensitized Solar Cells. *Journal of the American Chemical Society*, 132(14), 5164–5169. <https://doi.org/10.1021/ja909291h>.
- West, W. (1974). Proceedings of vogel centennial symposium. *Photographic Science and Engineering*, 18, 35.
- Williams, D. R. (2018). Sun Fact Sheet. NASA Official: Ed Grayzeck, Last Updated: 23 February 2018, DRW. Greenbelt, MD 20771. Retrieved and Accessed on February 28, 2022 from <https://nssdc.gsfc.nasa.gov/planetary/factsheet/sunfact.html>
- Wongcharee, K., Meeyoo, V., & Chavadej, S. (2007). Dye-sensitized solar cell using natural dyes extracted from rosella and blue pea flowers. *Solar Energy Materials and Solar Cells*, 91(7), 566–571. <https://doi.org/10.1016/j.solmat.2006.11.005>.
- Wyler, H., & Dreiding, A. S. (1957). Kristallisiertes Betanin. Vorläufige Mitteilung. *Helvetica Chimica Acta*, 40(1), 191–192.
- Xu, Y., Li, M., Fu, Y., Lu, T., Hu, Y., & Lu, W. (2019). Theoretical study of high-efficiency organic dyes with the introduction of different auxiliary heterocyclic acceptors based on IQ1 toward dye-sensitized solar cells. *Journal of Molecular Graphics and Modelling*, 86, 170–178. <https://doi.org/10.1016/j.jmgm.2018.10.001>.
- Yoshikawa, K., Kawasaki, H., Yoshida, W., Irie, T., Konishi, K., Nakano, K., Uto, T., Adachi, D., Kanematsu, M., Uzu, H., & Yamamoto, K. (2017). Silicon heterojunction solar cell with interdigitated back contacts for a photoconversion efficiency over 26%. *Nature Energy*, 2(5), 17032. <https://doi.org/10.1038/nenergy.2017.32>.
- Zeng, W., Cao, Y., Bai, Y., Wang, Y., Shi, Y., Zhang, M., Wang, F., Pan, C., & Wang, P. (2010a). Efficient Dye-Sensitized Solar Cells with an Organic Photosensitizer Featuring Orderly Conjugated Ethylenedioxythiophene and Dithienosilole Blocks. *Chemistry of Materials*, 22(5), 1915–1925. <https://doi.org/10.1021/cm9036988>.
- Zeng, W., Liu, T., Wang, Z., Tsukimoto, S., Saito, M., & Ikuhara, Y. (2010b). Oxygen adsorption on anatase TiO₂ (101) and (001) surfaces from first principles. *Materials transactions*, 51(1), 171–175. <https://doi.org/10.2320/matertrans.M2009317>.

- Zhang, C. R., Liu, L., Zhe, J. W., Jin, N. Z., Yuan, L. H., Chen, Y. H., Wei, Z. Q., Wu, Y. Z., Liu, Z. J., & Chen, H. S. (2013). Comparative study on electronic structures and optical properties of indoline and triphenylamine dye sensitizers for solar cells. *Journal of Molecular Modeling*, 19(4), 1553–1563. <https://doi.org/10.1007/s00894-012-1723-6>.
- Zhang, D., Lanier, S. M., Downing, J. A., Avent, J. L., Lum, J., & McHale, J. L. (2008). Betalain pigments for dye-sensitized solar cells. *Journal of Photochemistry and Photobiology A: Chemistry*, 195(1), 72–80.
- Zhang, D., Yamamoto, N., Yoshida, T., & Minoura, H. (2002). Natural dye sensitized solar cells. *Transactions of the Materials Research Society of Japan*, 27(4), 811–814.
- Zhang, H., Lu, Y., Han, W., Zhu, J., Zhang, Y., & Huang, W. (2020). Solar energy conversion and utilization: Towards the emerging photo-electrochemical devices based on perovskite photovoltaics. *Chemical Engineering Journal*, 393, 1–13.
- Zhang, J., & Dolg, M. (2015). ABCluster: The artificial bee colony algorithm for cluster global optimization. *Physical Chemistry Chemical Physics*, 17(37), 24173–24181.
- Zhang, J., Kan, Y. H., Li, H. B., Geng, Y., Wu, Y., & Su, Z. M. (2012). How to design proper π -spacer order of the D- π -A dyes for DSSCs? A density functional response. *Dyes and Pigments*, 95(2), 313–321. <https://doi.org/10.1016/j.dyepig.2012.05.020>.
- Zhang, J., Zhu, H. C., Zhong, R. L., Wang, L., & Su, Z. M. (2018). Promising heterocyclic anchoring groups with superior adsorption stability and improved IPCE for high-efficiency noncarboxyl dye sensitized solar cells: A theoretical study. *Organic Electronics*, 54, 104–113. <https://doi.org/10.1016/j.orgel.2017.12.023>.
- Zhang, J., Zhu, L., & Wei, Z. (2017). Toward Over 15% Power Conversion Efficiency for Organic Solar Cells: Current Status and Perspectives. *Small Methods*, 1(12), 1–14.
- Zhurko, G. A., & Zhurko, A. D. (2015). ChemCraft graphical program for visualization of computed results. Retrieved and Accessed on February 28, 2020 from <http://www.chemcraftprog.com/.2015>

APPENDICES

Appendix 1: Optimised geometrical structure of the Bd-b, Bd-p and dBd dye molecules; Cartesian coordinates of atoms in Å

Atom	Bd-b			Atom	Bd-p			Atom	dBd		
	x	y	z		x	y	z		x	y	z
O	-0.3945	-0.0195	1.4373	C	-6.0230	4.5516	0.4356	O	-6.2502	2.0915	-2.1419
O	-0.3821	1.9659	2.5565	C	-7.3465	4.2212	0.1477	O	-5.3377	-0.3398	-1.5523
O	-6.228	2.0724	-1.6441	C	-5.0549	3.5516	0.4231	O	0.4490	-3.9858	2.4763
O	-5.1486	-0.0051	-2.9082	C	-7.6933	2.8848	-0.1588	O	2.4525	-4.9886	2.2453
O	0.0557	-2.2303	2.8734	C	-5.4188	2.2376	0.1222	O	6.2027	-2.6767	0.9020
O	1.7599	-3.6696	3.1202	C	-6.7370	1.8776	-0.1763	O	6.2224	-0.6050	-0.0030
O	6.0107	-2.7149	1.4087	H	-5.7765	5.5846	0.6572	N	-0.9279	1.6332	-0.6335
O	6.3626	-1.3822	-0.3825	H	-7.0236	0.8608	-0.4291	N	3.5490	-2.7980	1.0543
N	-0.8225	1.1675	-0.9387	C	-3.5768	3.6194	0.6965	C	-0.5019	2.9123	-0.6976
N	3.4018	-2.2829	1.4087	C	-3.0751	2.2356	0.2663	C	-1.5853	3.8406	-1.1455
C	-0.4781	2.0799	0.1822	H	-3.3814	3.8215	1.7578	C	-2.7465	2.8923	-1.3024
C	-1.6207	3.1089	0.2071	H	-3.0516	4.3714	0.1000	C	-2.3216	1.6010	-0.9994
C	-2.7235	2.3955	-0.5350	N	-4.2727	1.4017	0.1760	C	-0.2421	0.4946	-0.3211
C	-2.2125	1.2819	-1.2035	C	-2.2764	2.2630	-1.2008	C	-4.0653	3.1082	-1.6979
C	-0.0452	0.1669	-1.2919	H	-2.3641	1.7879	0.9631	C	-3.1599	0.4927	-1.0816
C	-4.0785	2.6990	-0.6556	O	-2.3289	1.1725	-1.7893	C	1.2941	-1.9119	0.7033
C	-2.9952	0.4632	-2.0195	O	-1.7310	3.3496	-1.4101	C	2.2490	-2.6416	1.6716
C	1.3914	-1.9779	0.1038	C	-4.2873	0.0860	0.0290	C	1.9200	-0.6099	0.2348
C	2.0030	-1.9031	1.5141	C	-3.1681	-0.7660	0.1365	C	1.1552	0.4603	-0.1905
C	2.0983	-0.8620	-0.6458	H	-5.2705	-0.3424	-0.1286	C	-4.9274	2.0170	-1.7724
C	-0.4157	1.2402	1.5643	C	-3.2205	-2.1408	0.0470	C	-4.4809	0.7134	-1.4666
C	1.3829	0.1805	-1.1811	H	-2.1935	-0.3090	0.2507	C	3.3458	-0.5577	0.1988
C	-4.8844	1.8828	-1.4450	C	-4.4870	-2.9160	-0.2845	C	4.1260	-1.6211	0.5743
C	-4.3475	0.7683	-2.1313	C	-2.0248	-2.9151	0.1637	C	1.7584	-4.0021	2.1344
C	3.5292	-0.8981	-0.5339	C	-4.4357	-4.3213	0.3444	C	5.5853	-1.5431	0.4461
C	4.1218	-1.7017	0.4223	H	-4.5685	-3.0125	-1.3757	H	0.4905	3.1796	-0.3752
C	1.2625	-2.7007	2.5826	H	-5.3899	-2.4145	0.0672	H	-1.3539	4.3594	-2.0916
C	5.6050	-1.8902	0.4143	C	-2.0424	-4.2846	0.0727	H	-1.7896	4.6369	-0.4108
H	0.5072	2.5224	0.0314	N	-3.2099	-4.9898	-0.0284	H	-0.8531	-0.3853	-0.1948
H	-1.3503	4.0450	-0.2988	H	-1.0642	-2.4269	0.2742	H	-4.4215	4.1056	-1.9462
H	-1.8564	3.3451	1.2473	H	-3.1951	-6.0000	-0.0104	H	0.3424	-1.7344	1.2124
H	-0.5543	-0.6950	-1.7186	C	-0.7612	-5.0406	0.0828	H	1.0893	-2.5703	-0.1527
H	-4.5053	3.5573	-0.1421	C	-5.6080	-5.2199	-0.0172	H	-2.8401	-0.5201	-0.8712
H	0.3183	-1.8214	0.1555	H	-4.4834	-4.1893	1.4431	H	2.3060	-2.0202	2.5890
H	1.6105	-2.9617	-0.3287	O	-5.5062	-6.3895	-0.3104	H	1.7036	1.3488	-0.5024
H	-2.6062	-0.3897	-2.5638	O	0.3414	-4.5464	0.1739	H	4.1695	-3.4530	1.5100
H	1.9524	-0.8495	1.8291	O	-6.7891	-4.5747	0.0795	H	3.8518	0.3281	-0.1693
H	1.8968	1.1090	-1.4224	H	-7.4801	-5.2290	-0.1233	H	-6.4876	3.0042	-2.3481
H	3.7983	-2.9212	2.0855	O	-0.9684	-6.3801	-0.0180	H	-6.1988	0.0037	-1.8363
H	4.1686	-0.3145	-1.1844	H	-0.0902	-6.7958	-0.0147	H	0.2457	-4.8801	2.8001
H	-6.5446	2.8174	-1.1172	O	-8.3022	5.1851	0.1568	H	7.1519	-2.5264	0.7654
H	-6.0493	0.3500	-2.8534	H	-9.1439	4.7735	-0.0933				
H	-0.1418	-1.3470	2.4309	O	-9.0279	2.6934	-0.4286				
H	6.9757	-2.7969	1.3294	H	-9.1822	1.7942	-0.7440				

Appendix 2: Thermodynamic functions of the Bd-b, Bd-p, and dBd dyes in the gas phase

T K	$C_p^\circ(T)$ J.mol ⁻¹ .K ⁻¹	$S^\circ(T)$ J.mol ⁻¹ .K ⁻¹	$\Phi^\circ(T)$ J.mol ⁻¹ .K ⁻¹	$H^\circ(T)-H^\circ(0)$ kJ.mol ⁻¹
Bd-b				
298.15	406.054	705.575	481.266	66.878
300	408.174	708.093	482.657	67.631
400	514.904	840.522	555.722	113.920
500	603.684	965.304	625.294	170.005
600	674.874	1081.910	691.797	234.068
Bd-p				
298.15	411.524	739.893	508.457	69.003
300	413.614	742.445	509.892	69.766
400	519.284	876.297	584.930	116.547
500	607.024	1001.940	655.906	173.017
600	677.334	1119.070	723.457	237.368
dBd				
298.15	374.104	679.205	472.011	61.775
300	376.064	681.526	473.297	62.469
400	474.834	803.604	540.752	105.141
500	556.854	918.693	604.953	156.870
600	622.624	1026.260	666.315	215.967
L0				
298.15	359.554	675.548	476.420	59.370
300	361.634	677.779	477.655	60.037
400	467.504	796.667	542.622	101.618
500	555.884	910.830	604.944	152.943
600	626.654	1081.680	665.007	212.204
L0-1-Bd				
298.15	738.614	1177.580	771.365	121.113
300	742.724	1182.170	773.893	122.483
400	951.644	1425.150	906.535	207.446
500	1126.414	1656.950	1033.642	311.654
600	1266.714	1875.200	1155.910	431.574
L0-2-Bd				
298.15	737.094	1166.980	762.395	120.627
300	741.214	1171.560	764.913	121.994
400	950.444	1414.150	897.095	206.822
500	1125.514	1645.710	1023.866	310.922
600	1266.014	1863.810	1145.878	430.759
L0-1-dBd				
298.15	707.504	1138.440	750.364	115.705
300	711.474	1142.830	752.770	117.018
400	912.944	1375.790	879.588	198.481
500	1080.914	1598.220	1001.278	298.471
600	1215.514	1807.650	1118.407	413.546
L0-2-dBd				
298.15	710.284	1151.710	760.719	116.574
300	714.254	1156.110	763.137	117.892
400	915.254	1389.810	890.137	199.610

T	$C_p^\circ(T)$	$S^\circ(T)$	$\Phi^\circ(T)$	$H^\circ(T)-H^\circ(0)$
K	J.mol ⁻¹ .K ⁻¹	J.mol ⁻¹ .K ⁻¹	J.mol ⁻¹ .K ⁻¹	kJ.mol ⁻¹
500	1082.714	1612.700	1013.088	299.806
600	1216.914	1822.420	1130.685	415.041

Appendix 3: Total energies of the dyes in neutral and ionised states (a.u.)

Dye	$E^+(g_0)$	$E^+(g_+)$	$E^0(g_+)$	$E^-(g_0)$	$E^-(g_-)$	$E^0(g_-)$	$E^0(g_0)$
Bd-b	-1405.854	-1405.861	-1406.098	-1406.163	-1406.179	-1406.089	-1406.107
Bd-p	-1405.869	-1405.927*	-1406.096	-1406.158	-1406.172	-1406.091	-1406.104
dBd	-1217.415	-1217.425	-1217.596	-1217.613	-1217.627	-1217.588	-1217.604
L0	-1107.040	-1107.043	-1107.282	-1107.312	-1107.324	-1107.273	-1107.285
L0-1-Bd	-2436.767	-2436.771	-2436.999	-2437.068	-2437.082	-2436.983	-2437.002
L0-2-Bd	-2436.775	-2436.779	-2437.004	-2437.081	-2437.091	-2436.995	-2437.010
L0-1-dBd	-2248.318	-2248.327	-2248.491	-2248.549	-2248.562	-2248.486	-2248.500
L0-2-dBd	-2248.317	-2248.326	-2248.491	-2248.549	-2248.560	-2248.487	-2248.499

*The $E^+(g_+)$ corresponds to the system where the cation Bd-p decomposes with CO_2 (Appendix 1), resulting in the decarboxylated betanidin cation.

RESEARCH OUTPUTS

(i) Publications

Costa, R., Pogrebnoi, A., & Pogrebnaya, T. (2021). Betanidin isomerisation and decarboxylation, thermodynamic and charge transfer dye properties towards dye sensitised solar cells application. *Journal of Physical Organic Chemistry*, 34(6), 1–21. <https://doi.org/10.1002/poc.4185>

Costa, R., Al-Qurashi, O. S., Wazzan, N., Pogrebnoi, A., & Pogrebnaya, T. (2022). Designed complexes based on betanidin and L0 Dyes for DSSCs: Thermodynamic and optoelectronic properties from DFT study. *Molecular Simulation*, 48(8), 1–15. <https://doi.org/10.1080/08927022.2022.2042531>

(ii) Conferences/Workshops

Costa, R., Pogrebnoi, A., & Pogrebnaya, T. (2021). *Betanidin isomerisation and decarboxylation, thermodynamic and charge transfer dye properties towards dye-sensitised solar cells application*. Initial part of the work was presented as a poster at the 32nd Workshop for the electronic structure, hosted by the University of California, Merced, Virtual Poster Session I, 3–5 June 2020, workshop sessions <https://physics.ucmerced.edu/electronic-structure-workshop/>, Presenter see Session I 10:30 am–11:30 am PDT (17:30–18:30 GMT), Name number 14. <https://physics.ucmerced.edu/electronic-structure-workshop/virtual-poster-session>, Accessed on September 25, 2021.

Costa, R., Al-Qurashi, O. S., Wazzan, N., Pogrebnoi, A., & Pogrebnaya, T (2021). *Designed Complexes Based on Betanidin and L0 Dyes for DSSCs: Thermodynamic and Optoelectronic Properties from DFT study*. Initial part of the work was presented as a poster at the 1st 2021 workshop for the US-Africa initiative in electronic structure, hosted by the ICTP–EAI FR, University of Rwanda, Kigali, Rwanda, Virtual, June 14–18, 2021. <https://usafraicainitiative.org/JuneWorkshop2021/>, Accessed on September 25, 2021.

Costa, R., Al-Qurashi, O. S., Wazzan, N., Pogrebnoi, A., & Pogrebnaya, T (2021). *Zwitterionic or non-ionic conformer structures of betanidin influence to*

thermodynamic, charge transfer and reactivity indices property towards DSSCs applications. Initial work presented as a poster at the 33rd 2021 workshop on recent developments in electronic structure methods, hosted by the Flatiron Institute, Center for Computational Quantum Physics, Simons Foundations, New York, United States of America, Virtual, Monday, July 12th – Thursday, July 15th, 2021, <https://www.simonsfoundation.org/international-workshop-on-recent-developments-in-electronic-structure-es21/>, and <https://s3.amazonaws.com/sf-web-assets-prod/wp-content/uploads/2021/07/01113524/Rene-Costa.pdf> to the Poster Session #1, Accessed on September 25, 2021.

Costa, R., Al-Qurashi, O. S., Wazzan, N., Pogrebnoi, A., & Pogrebnaya, T (2021). *Betanidin zwitterionic and non-ionic dimer conformers towards DSSCs application: interrelation between the structure, thermodynamics and reactivity indices*, in SPTEch 2021 conference. Book of abstracts international conference on solar power technologies – SPTEch2021 [version 1; not peer reviewed]. F1000Research 2021, **10**:1041 (document) (<https://f1000research.com/documents/10-1041>). Applied through the link <https://www.rsc.org/events/detail/47124/international-solar-power-technologies-sptech-conference>, Accessed on September 25, 2021.

Costa, R., Al-Qurashi, O. S., Wazzan, N., Pogrebnoi, A., & Pogrebnaya, T (2022). *Betanidin zwitterionic and nonionic dimer conformers towards DSSCs application: A DFT investigation to optoelectronic and charge transfer properties.* Conference Proceedings, <https://greeniupac2022.org/>, Book of abstract 9th IUPAC International Conference on Green Chemistry via the link https://greeniupac2022.org/wp-content/uploads/9th_ICGC_Conference_Proceedings.pdf, page 591, 5-9 September 2022, Athens, Greece, Venue: Zappeion Megaron, Physical and Virtual

Costa, R., Al-Qurashi, O. S., Wazzan, N., Pogrebnoi, A., & Pogrebnaya, T (2022). *Zwitterionic/nonionic conformer structures of betanidin help tailor the optoelectronic properties and understand using DFT for DSSCs application.* IUMRS-ICYRAM 2022, <https://icyram2022.wixsite.com/official-site>, 3-6 August 2022, Fukuoka, Japan, Hybrid Meeting, <https://www.iumrs-icyram2022.org/en/prg/index.php>, Entry no 2149, Presentation C-P3-005, Accessed via the link https://www.iumrs-icyram2022.org/en/prg/programList_poster.php?id=C

Costa, R., Al-Qurashi, O. S., Wazzan, N. (2022). *Betacyanin geometrical isomers and their conformers with a selected organic sensitiser (L0) in forming complexes dye towards dye-sensitised solar cell application*. Conference Proceedings, <https://www.greenchemistry.school/the-school/>, Book of Abstract Proceedings of the 14th Green Chemistry Postgraduate Summer School. Accessed via the link https://www.greenchemistry.school/wpcontent/uploads/2022/07/PROCEEDINGS_2022-2.pdf, page 52, poster page 126, Editors: Mirabbos Hojamberdiev, Fabio Aricò, Aurelia Visa and Pietro Tundo GSSD Foundation ISBN: 978-88-945537-2-7, [Online/in-person], 3-8 July 2022, Venice, Italy

(iii) Poster presentation



Combination of natural betanidin dye with synthetic organic sensitiser towards dye-sensitised solar cell application

Rene Costa^{1,2}

Alexander Pogrebnoi¹

Tatiana Pogrebnaya¹

¹Department of Materials and Energy Science and Engineering, School of Materials, Energy, Water and Environmental Sciences, The Nelson Mandela African Institution of Science and Technology, Arusha, Tanzania

²Department of Physical and Environmental Sciences, Faculty of Science, Technology and Environmental Studies, The Open University of Tanzania, Dar es Salaam, Tanzania



Introduction

- Renewable energy sources are the most easily exploitable, limitless, silent and adaptable to massive uses
- Semiconducting materials can be used to turn sunlight into useable electricity.
- The critical issue is the dye sensitisation principle for large band-gap semiconductor electrodes.
- Small band-gap is achieved by covering the internal TiO₂ electrode with dye molecules capable of absorbing the incident photons.
- The structure of the dye employed as sensitiser impacts the stability, performance and efficiency of DSSCs.
- Simple adjustments and greater purification of existing natural pigments is essential in improving the device's efficiency and stability

Results

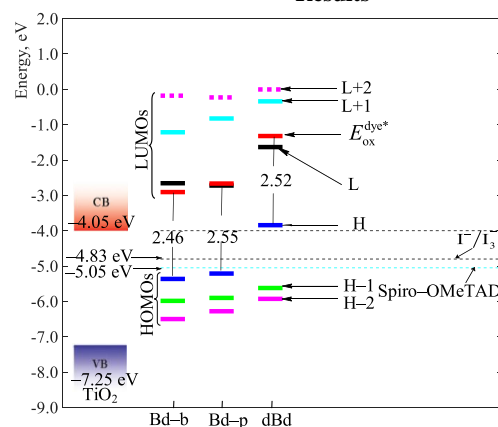


Figure 3: Energy level diagram of relevant MOs

Reference

Qin, C., & Clark, A. E. (2007). DFT characterization of the optical and redox properties of natural pigments relevant to dye-sensitized solar cells. *Chemical Physics Letters*, 438(1-3), 26-30.
<https://doi.org/10.1016/j.cplett.2007.02.063>

Conclusions

- Bd-b is more stable than Bd-p
- Both betanidin structure are suitable for regeneration
- Thermal instability of CO₂ detachment is realized
- L0-Bd complexes satisfy the requirement to sensitise the TiO₂ semiconductor
- L0-dBd complexes are stable but they challenge regeneration

Recommendations

- Dimerisation of the betanidin to increase number of anchoring groups
- Synthesis of the proposed designed molecules better to be realised
- Grafting to the bond structure of the betanidin molecule
- Experimental measurements to the absorption and emission spectral is of significance

Statement of the Problem

- Limited information from practical experiments
- Insufficient information to the theoretical simulation and modelling
- Limited reliable data to the thermodynamic and optoelectronic properties about betanidin
- Investigation of betanidin materials for energy harvesting reduce unfriendly emiss



Figure 1: Beet root fruit

Methodology

